Organization and crystallography of the microstructures of bryozoans (Phylum Bryozoa) and serpulids (Phylum Annelida)

UNIVERSIDAD
DE GRANADA

PhD Thesis 2024

Christian Grenier Romero

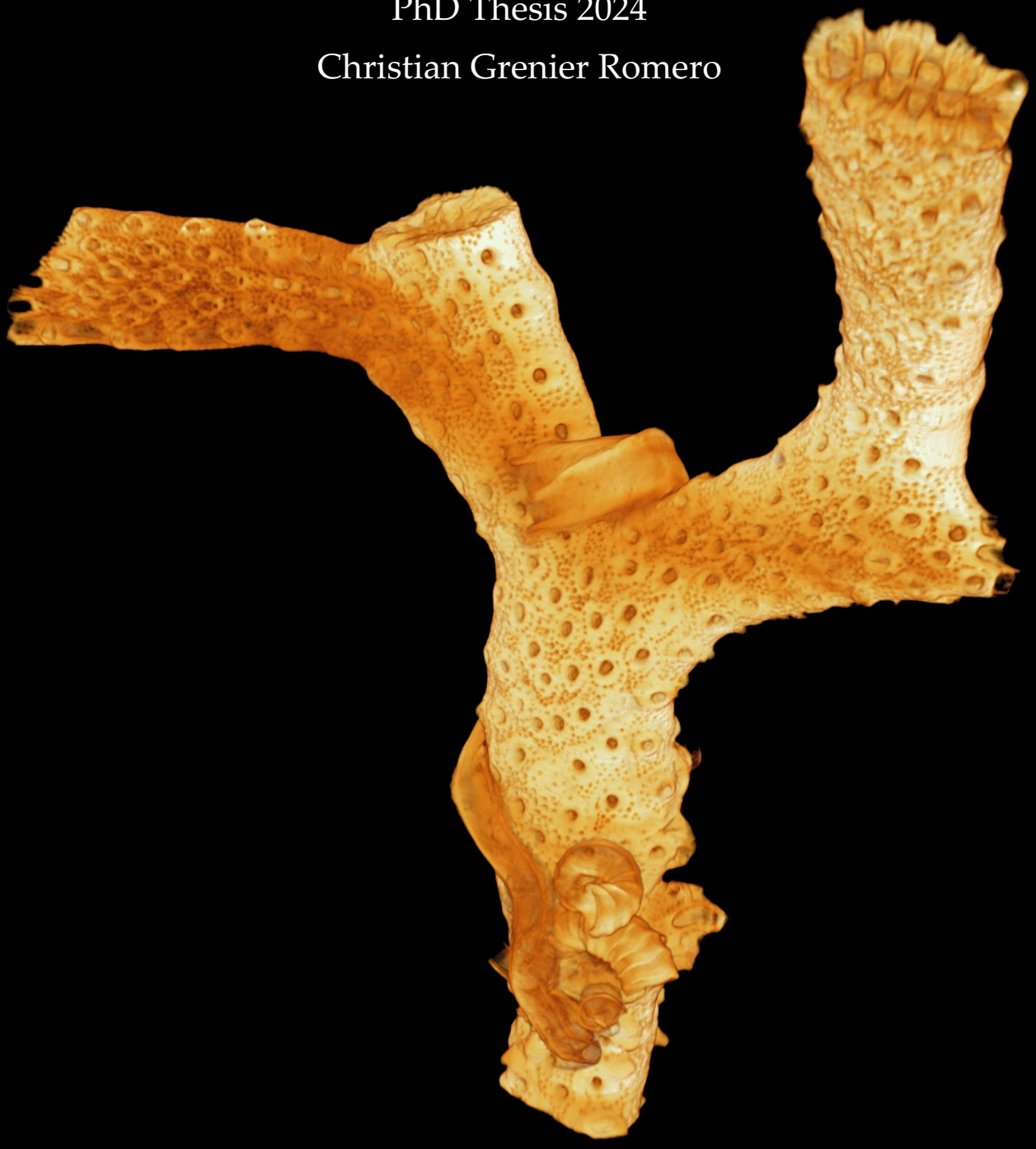

Director:

Antonio G. Checa González

UNIVERSIDAD
DE GRANADA

Faculty of Science

Department of Stratigraphy and Palaeontology

Organization and crystallography of the microstructures of bryozoans (Phylum Bryozoa) and serpulids (Phylum Annelida)

Christian Grenier Romero

PhD Thesis 2024

Director:

Antonio G. Checa González

Programa Doctorado
Ciencias de la Tierra

Editor: Universidad de Granada. Tesis Doctorales
Autor: Cristian Greiner Romero
ISBN: 978-84-1195-452-5
URI: https://hdl.handle.net/10481/95033

To my family,

the pillar on which my whole life rests.

"As long as the circle of their compassion does not embrace all living beings, humans will not find peace on their own"

Albert Schweitzer

(Adapted from the original version)

This quote emphasizes the interconnectedness of humanity and the natural world. True peace and fulfillment can only be achieved when one extends compassion and care not only to fellow human beings but also to all living beings as well as the environment that surrounds us. It reflects my deepest belief in the importance of universal compassion and respect for all life forms.

Disclaimer of liability

All illustrations on the covers of the chapters and subchapters are copyright-free.

Some are part of Ernst Haeckel's collection of lithographs, published in 1904 in his book *Kunstformen der Natur* (Art Forms in Nature):

- Chapter III: *plate 23, Bryozoa*
- Chapter III, part 2: *plate 33, Bryozoa*
- Chapter IV: *plate 96, Chaetopoda*

Other have been generated by a free use AI (Gencraft):

- Chapters I, II, III part 1, IV (subchapter), and V.

Some photos from the introduction chapter belong to the Dr. Luís Sánchez Tocino and can be found in the link https://litoraldegranada.ugr.es/

All the photos from the Chapter II "Material and Methods" were taken from the internet. In the caption of each figure, a link to the site is attached.

Table of contents

List of abbreviations

AFM: Atomic Force Microscope

ANSI: American National Standards Institute

BC: Band Contrast

BSE: Backscattered Electron

Ca^{2+}: Calcium ion

$CaCO_3$: Calcium carbonate

CAMI: Coated Abrasive Manufacturers Institute

CDD: Charge Coupled Device

CIC: Centro de Instrumentación Científica

DSC: Differential Scanning Calorimetry

EBSD: Electron Backscattered Diffraction

EDTA: Ethylenediaminetetraacetic acid

EDX or EDS: Electron Dispersive X-Ray Spectroscopy

FEI: Field Electron and Ion (FEI Company)

FESEM: Field Emission Scanning Electron Microscopy

FIB: Focused Ion Beam

FTIR: Fourier Transform Infrared

HEPES: Hydroxyethylpiperazineethanesulfonic acid

HRSEM: High-Resolution Scanning Electron Microscopy

IOM: Insoluble Organic Matter

IPF: Inverse Pole Figures

Kv: Kilovolt

Mg^{2+}: Magnesium ion

Micro-CT: Micro-Computed Tomography

μm: micrometer

MUD: Multiple of Uniform Distribution

nA: nanoAmpere

nm: nanometer

PBCs: Periodic Bond Chains

PFs: Pole Figures

SCAI: Servicios Centrales de Apoyo a la Investigación

SE: Secondary Electrons

SEM: Scanning Electron Microscopy

SMT: Semiconductor Manufacturing Technology (Carl Zeiss)

SOM: Soluble Organic Matter

Sr / Sr^{2+}: Strontium ions

t-EBSD: Transmission-Electron Backscattered Diffraction

TGA: Thermogravimetric Analysis

UGR: Universidad de Granada

UMA: Universidad de Málaga

XRD: X-Ray Diffraction

Acknowledgments

Perhaps, the most enlightening aspect of undertaking this doctoral thesis has been the realization that the results are not the most important factor, nor even the line of research, but rather the continuous process of developing as a researcher. This ongoing formation is crucial for sustaining an independent academic career. Integral to this formative journey is the role of a thesis advisor, someone who not only guides and corrects your work but also educates and shapes you as a researcher. For all of this, I feel fortunate and wish to express my deepest gratitude to my advisor, Antonio Checa, for being both a referent and a mentor to me.

I would like to express my gratitude to my tutor Gonzalo Jiménez, for always being available to lend me a hand with the thesis bureaucracy.

Likewise, I am grateful to all the Professors and researchers who have directly assisted me throughout my thesis: Alejandro Rodríguez-Navarro (University of Granada), Kasia Berent (Akademickie Centrum Materiałów i Nanotechnologii, AGH, Krakow), and Erika Griesshaber and Wolfgang Schmahl (Ludwig-Maximilians-Universität, Munich). Thank you for welcoming me, training me, and assisting me with the complex and essential techniques required for this thesis.

For their time and kindness in reviewing this doctoral thesis, I would like to thank the international reviewers Dr. Nelson A. Lagos Suárez (Centro de Investigación e innovación para el Cambio Climático, Universidad de Santo Tomás, Chile) and Dr. Michael Vendrasco (Pasadena City College, Department of Geology, USA).

At the institutional level, I would like to thank the Spanish Ministry of Science and Innovation: MCIN/AEI/10.13039/501100011033. This doctoral thesis has been funded by National projects CGL2017-85118-P and PID2020116660GB-I00. Also, by "FEDER Una manera de hacer Europa" and PCM 00092 (Consejería

de Economía, Innovación, Ciencia y Empleo, Junta de Andalucía). Further, I would like to thank the Research Group RNM363 and the Unidad Científica de Excelencia UCE-PP2016-05 (University of Granada). Funding for open Access was provided by Universidad de Granada/Consorcio de Bibliotecas Universitarias de Andalucia (CBUA).

From a more personal point of view, I would like to extend my gratitude to all my colleagues at the "Paleobecaría" for their warmth and efforts to integrate me as one of their own: Bob, Santi, Willy, Javi, Jon, Ernesto, Sergio, Carlos, and Paola. And especially to Pablo and Raef, thank you for your hospitality, unconditional help, kindness, and, in essence, for your friendship.

To my colleagues at the "Minebecaría": Luís, Julia, Clara, Laura, Migue, Aurelia, María(s), Núria, Irene, … thank you all for the many years together and the shared experiences. With special affection, I will remember the discussion and all the funny moments with Igor, Sarah, Teodora, Paulina, and Aurélie. And for all the time we spent together as a padel partner, thank you Francesco (a.k.a. Paco), also for giving me a new perspective on how to approach science.

In particular, to Mercedes and Natalia, thank you for your care, active listening, and close companionship over these years, which has inevitably led to a sincere and profound friendship which I hope will last over time.

To all the Professors and postdocs of the Stratigraphy and Palaeontology Department, who make it an inclusive place in which to develop education and science, thank you.

I would not like to conclude without reminding that during these years I have had the opportunity to work in different Departments, allowing me to give a multidisciplinary approach to my thesis. Therefore, many thanks to Professors Carlos, Kerstin, Jorge, and Conchi, for welcoming me as if I were part of the family. And in the same way, thanks to the technicians from the Scientific Instrumentation Center (CIC): Isa, Alicia, Fátima, Lola, Dani, Juande, Nazaret,

Bendi… for making it possible to achieve fascinating results with such advanced and complex techniques.

And lastly, to my family, who has been a fundamental pillar in my life: Dad, Mom, Carmen, Ignacio, Marta, and all my wonderful nieces and nephews! André, Paloma, María, Amelia, Maya, Alejandro, and Vera. Without your love, I would not have come this far.

Extended abstract

Marine calcifying organisms have a great significance in the biodiversity and stability of the ecosystems they inhabit. They play a key role as global carbon dioxide reservoirs and are of major economic relevance, both in food production and biotechnology applications.

The investigation of their microstructures, mineralogy, and crystallography holds paramount importance for a comprehensive understanding of their biomechanical properties, their biomineralization processes, and their susceptibility to the intrinsic factors associated with climate change (e.g., variations in ocean acidity and temperature). However, while major marine calcifying taxa (such as corals, mollusks, echinoderms, and foraminifera) have garnered considerable attention and research in recent decades, other groups, albeit less recognized but equally important, have been comparatively understudied.

This is the case of the two principal classes of bryozoans (stenolaemates and gymnolaemates) and of the serpulid polychaetes. Both are marine calcifying animals that belong to different phyla. They build calcium carbonate skeletons and are pivotal in marine ecosystems worldwide. They produce sophisticated microstructures for which little to nothing is known regarding their crystallography or their biomineralization processes.

The present Ph.D. work aims at elucidating the mineralogy and crystallography of the main microstructures found in bryozoans and serpulids. Further, we unravel the biomineralization processes inherent to each group considering the morphology of the microstructures, their growth dynamics, and the theoretical position of the secretory epithelium.

For this purpose, we have applied high-resolution techniques such as scanning electron microscopy (SEM) and associated techniques: energy dispersive spectroscopy (EDX), focused ion beam (FIB), and electron backscatter

diffraction (EBSD). We have completed the micro and nano-structural analysis with micro-computed tomography (micro-CT) and atomic force microscopy (AFM), respectively. Likewise, we have studied the mineralogy and characterized the organic fraction using X-ray diffraction (XRD), RAMAN and Fourier transform infrared spectroscopy (FTIR), and thermogravimetric analysis (TGA).

To achieve the aforementioned objectives, this Ph.D. study is divided into three main lines of research:

- Bryozoan class **Stenolaemata**. We have studied the microstructures, mineralogy, and crystallography of three extant species (*Fasciculipora ramosa*, *Hornera robusta,* and *Cinctipora elegans*). We have differentiated two sophisticated microstructures: foliated calcite and tabular calcite. For each one, we have established consistent models of their crystallography. Foliated calcite is present in *Fasciculipora ramosa* and *Cinctipora elegans* and consists of co-oriented laths arranged with their c-axes aligned to their elongation axis and parallel to their main surfaces. One of the a*-axis is perpendicular to the main surfaces. The foliated calcite displays a well-defined sheet texture. In contrast, the tabular calcite is only present in *Hornera robusta* and consists of polygonal tablets with the c-axis as the fiber axis, perpendicular to the tablet surface. Thus, tabular calcite displays a characteristic axial texture.
- Bryozoans class **Gymnolaemata**. We have studied the microstructures, mineralogy, and crystallography of eight extant cheilostome species (*Calpensia nobilis*, *Schizobrachiella sanguinea*, *Rhynchozoon neapolitanum*, *Schizoretepora serratimargo*, *Pentapora fascialis*, *Adeonella pallasii*, *Schizomavella cornuta*, and *Smittina cervicornis*). We have distinguished five basic microstructures, three calcitic (tabular, irregularly platy and granular) and two aragonitic (granular-platy and fibrous). The calcitic microstructures consist of crystal aggregates that transition from tabular or irregularly platy to granular assemblies toward the interior of the zooid chambers. Fibrous aragonite consists of fibers arranged into

spherulites. In all cases, the crystallographic textures are axial, and stronger in aragonite than in calcite, with the c-axis as the fiber axis. We reconstruct the biomineralization sequence in the different species by taking into account the distribution and morphology of the growth fronts of crystals and the location of the secretory epithelium.

- **Serpulid** polychaetes. We have reviewed the microstructures of seven different serpulid species (*Cruzigera websteri, Spirobranchus triqueter*, *Serpula vermicularis, Spirobranchus giganteus, Serpula crenata, Crucigera zygphora,* and *Floriprotis sabiuraensis*), and studied their mineralogy and crystallography. We have identified three main microstructures: granular-prismatic and lamello-fibrillar calcite, and fibrous aragonite. The granular-prismatic may present two different appearances: finely unoriented and coarsely oriented prisms. Serpulids generally have a high amount of organic matter within the tube structure, consisting of chitin + proteins. Calcite is always present as medium to high magnesium calcite. Except for the finely granular-prismatic, which displays a scattered texture for all their crystallographic axes, the rest of the microstructures display axial textures, with the c-axis aligned with the crystal elongation axis.

We conclude that stenolaemate bryozoans, despite being an older group and currently having less evolutionary success, present more sophisticated microstructures than gymnolaemates. This is due to the secretory epithelium being close to the forming shell in the former. The foliated calcite of stenolaematans is homeomorph to that of bivalves but has significantly different crystallography. As for the tabular calcite, it lacks the spiral morphology of the tablet-shaped calcite of craniiform brachiopods, differing also in their crystallography. Conversely, except for the tabular calcite, the biomineralization in gymnolaematans is remote and occurs within a relatively wide extrapallial space, which is consistent with the inorganic-like appearance of the microstructures, whose surfaces show signs of free growth.

In serpulids, recrystallization processes are widespread. Only the external coarse prismatic layer and the lamello-fibrillar are primary (i.e. directly secreted by the animal) microstructures. Secondary (i.e. substitution) microstructures grow within the primary calcitic microstructures and retain remnants of the original structures, such as vestigial crystals or major growth increments. We conclude that the absence of a proper extrapallial space in serpulids and their characteristic growth by episodic increments is directly related to the biomineralization by high-magnesium calcite, which eventually favors the recrystallization processes. The high-ordered arrangement of the lamello-fibrillar microstructure may be explained by a previous cholesteric liquid crystal phase of the organic precursors, which would serve as a template for the fiber's crystallization by oriented nucleation.

Resumen extendido

Los organismos calcificadores marinos tienen una gran importancia en la biodiversidad y la estabilidad de los ecosistemas que habitan. Desempeñan un papel clave como reservorios globales de dióxido de carbono y tienen una gran relevancia económica, tanto en la producción de alimentos como en aplicaciones en biotecnología.

La investigación de sus microestructuras, mineralogía y cristalografía es de capital importancia para conocer en profundidad sus propiedades biomecánicas, sus procesos de biomineralización y su susceptibilidad a los factores intrínsecos asociados al cambio climático (como, por ejemplo, las variaciones de acidez y temperatura del océano). Mientras que los principales taxones calcificadores marinos (como corales, moluscos, equinodermos y foraminíferos) han sido objeto de considerable atención e investigación en las últimas décadas, otros grupos menos reconocidos, pero igualmente importantes, han sido comparativamente poco estudiados.

Éste es el caso de las dos clases principales de briozoos (estenolemados y gimnolemados) y de los poliquetos serpúlidos. Ambos son animales marinos calcificadores que pertenecen a filos diferentes. Construyen esqueletos de carbonato cálcico y son fundamentales en los ecosistemas marinos de todo el mundo. Producen sofisticadas microestructuras de las que poco o nada se sabe sobre su cristalografía o sus procesos de biomineralización.

El presente trabajo de doctorado tiene como objetivo dilucidar la mineralogía y cristalografía de las principales microestructuras encontradas en briozoos y serpúlidos. Además, desentrañamos los procesos de biomineralización inherentes a cada grupo considerando la morfología de las microestructuras, su dinámica de crecimiento y la posición teórica del epitelio secretor.

Para ello, hemos aplicado técnicas de alta resolución como la microscopía electrónica de barrido (SEM) y técnicas asociadas a ella, como la espectroscopia de energía dispersiva (EDX), el haz de iones focalizado (FIB) y la difracción de electrones retrodispersados (EBSD). Además, hemos completado el análisis macro y nanoestructural usando tomografía microcomputerizada (micro-CT) y la microscopía de fuerza atómica (AFM), respectivamente. Asimismo, para estudiar la mineralogía y la caracterización de la fracción orgánica, hemos utilizado difracción de rayos X (DRX), RAMAN y espectroscopia infrarroja por transformada de Fourier (FTIR), y análisis termogravimétrico (TGA).

Para alcanzar los objetivos mencionados, este estudio de doctorado se dividió en tres investigaciones principales:

- Briozoos clase **Stenolaemata**. Hemos estudiado las microestructuras, mineralogía y cristalografía de tres especies actuales (*Fasciculipora ramosa*, *Hornera robusta* y *Cinctipora elegans*). Diferenciamos dos microestructuras altamente sofisticadas: calcita foliada y calcita tabular. Para cada una de ellas hemos establecido modelos coherentes de su cristalografía. La calcita foliada está presente en *Fasciculipora ramosa* y *Cinctipora elegans* y consiste en láminas coorientadas dispuestas con sus "ejes c" alineados al eje de elongación y paralelos a las superficies principales de los cristales. Uno de los "ejes a*" es perpendicular a dichas superficies. La calcita foliada presenta una textura en láminas bien definida. En cambio, la calcita tabular sólo está presente en *Hornera robusta* y consiste en tabletas poligonales con el "eje c" como eje de fibra, perpendicular a la superficie de la tableta, mostrando una característica una textura axial.
- Briozoos clase **Gymnolaemata**. Hemos estudiado las microestructuras, la mineralogía y la cristalografía de ocho especies actuales *(Calpensia nobilis*, *Schizobrachiella sanguinea*, *Rhynchozoon neapolitanum*, *Schizoretepora serratimargo*, *Pentapora fascialis*, *Adeonella pallasii*, *Schizomavella cornuta* y *Smittina cervicornis*). Hemos distinguido cinco microestructuras básicas, tres calcíticas (tabular, foliada irregular y granular) y dos aragoníticas (granular-laminar y fibrosa). Las

microestructuras calcíticas consisten en agregados de cristales que pasan de tabulares o irregularmente laminares a conjuntos granulares hacia el interior de las cámaras de los zooides. El aragonito fibroso consiste en fibras dispuestas en esferulitos. En todos los casos, las texturas cristalográficas son axiales, y más fuertes en el aragonito que en la calcita, con el "eje c" como eje de elongación de las fibras. Hemos reconstruido la secuencia de biomineralización en las diferentes especies teniendo en cuenta la distribución y morfología de los frentes de crecimiento de los cristales y la localización del epitelio secretor.

- Poliquetos **serpúlidos**. Hemos revisado las microestructuras de siete especies diferentes de serpúlidos (*Cruzigera websteri*, *Spirobranchus triqueter*, *Serpula vermicularis*, *Spirobranchus giganteus*, *Serpula crenata, Crucigera zygphora* y *Floriprotis sabiuraensis*), y hemos estudiado su mineralogía y, por primera vez, su cristalografía. Identificamos tres microestructuras principales: calcita granular-prismática y lamello-fibrillar, y aragonito esferulítico. La granular-prismática puede presentar dos apariencias diferentes: prismas finamente desorientados y prismas gruesamente orientados. Los serpúlidos presentan generalmente una elevada cantidad de materia orgánica, constituida por proteínas y polisacáridos sulfatados. La calcita está siempre presente como calcita media o alta en magnesio. Excepto los prismas pequeños de la granular-prismática, que muestran una textura dispersa para todos sus ejes cristalográficos, el resto de las microestructuras muestran texturas axiales, con el "eje c" alineado con el eje de elongación del cristal.

Concluimos que los briozoos estenolemados, a pesar de ser un grupo más antiguo y con menor éxito evolutivo en la actualidad que los gimnolemados, presentan microestructuras más sofisticadas, hecho que puede estar relacionado con un contacto más estrecho del epitelio secretor en los estenolemados. La calcita foliada de los estenolemados es homeomorfa a la de los bivalvos, pero tiene una cristalografía diferente. En cuanto a su calcita tabular, carece de la morfología espiral de la calcita tabular de los braquiópodos craniiformes, difiriendo también

en su cristalografía. Por el contrario, la biomineralización en los gimnolemados es remota y se produce en un espacio extrapaleal relativamente amplio, lo que concuerda con el aspecto inorgánico de las microestructuras, cuyas superficies presentan indicios de un crecimiento libre (excepto para el caso de la calcita tabular). En los serpúlidos, los procesos de recristalización están muy extendidos. Sólo la capa prismática gruesa externa y la lamello-fibrillar son microestructuras primarias (es decir, secretadas directamente por el animal). Las microestructuras secundarias (es decir, de sustitución) crecen a partir de las microestructuras calcíticas primarias y conservan restos de las estructuras originales, como cristales vestigiales o sus incrementos de crecimiento. Concluimos que la ausencia de un espacio extrapaleal aislado del medio externo en serpúlidos y su característico crecimiento por incrementos episódicos está directamente relacionado con la biomineralización de calcita alta en magnesio, lo que eventualmente favorecería los procesos de recristalización. La disposición altamente ordenada de la microestructura lamello-fibrillar podría explicarse por una fase colestérica de cristal líquido de los precursores orgánicos, que serviría de plantilla para la cristalización de las fibras a partir de un proceso de nucleación orientada.

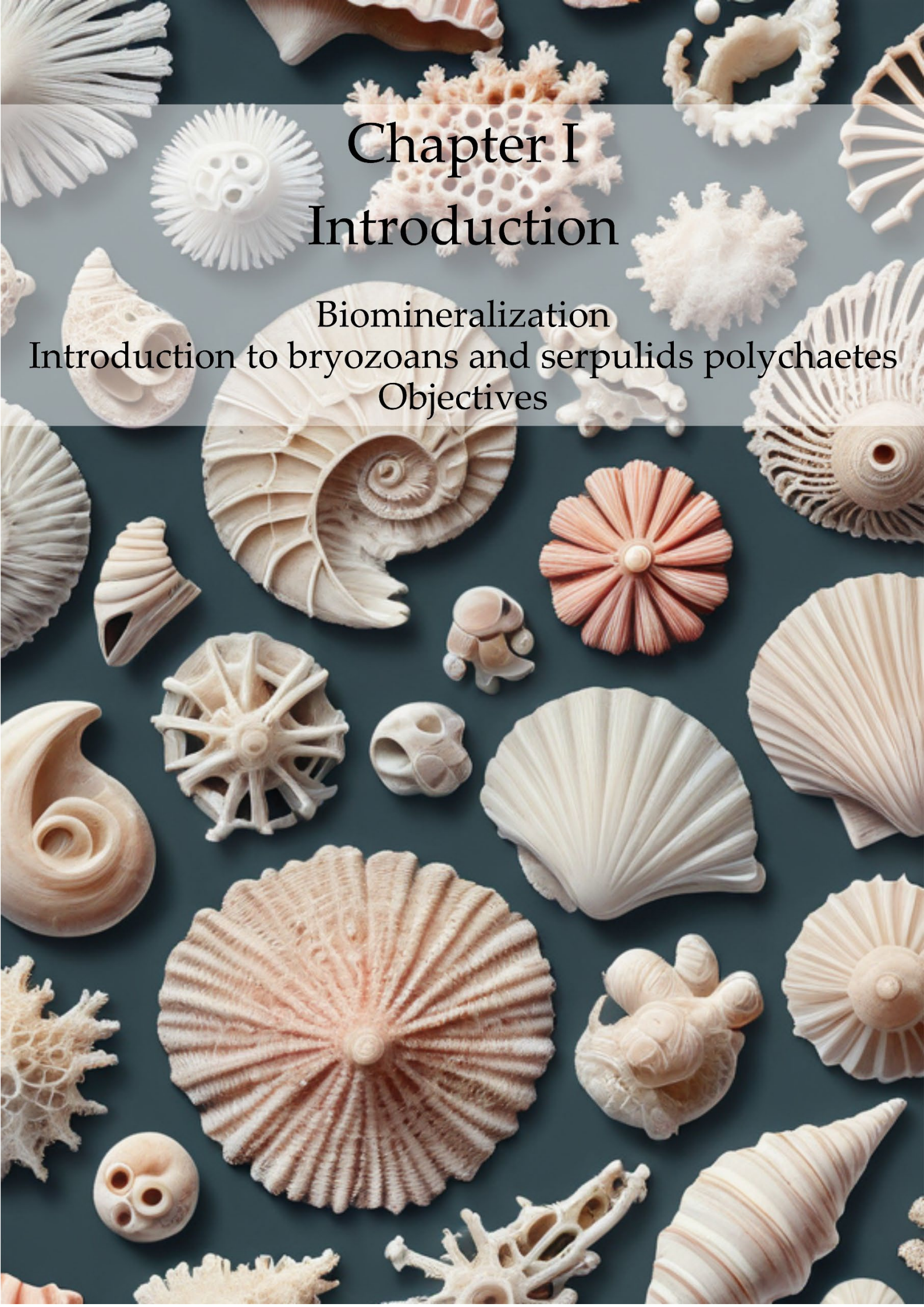

Chapter I
Introduction

Biomineralization
Introduction to bryozoans and serpulids polychaetes
Objectives

1. Introduction

1.1. Biomineralization

Biomineralization is a complex process whereby living organisms control the synthesis of mineralized tissues. This phenomenon is essential for several biological functions, including skeletal formation and tooth enamel production in vertebrates (Kovacs et al. 2021), otoliths (Hüssy et al. 2020) and guanine crystals in fishes (Levy-Lior et al. 2008; Zhang et al. 2019), and the secretion of shells in a broad variety of invertebrates such as mollusks, corals, brachiopods, bryozoans, foraminifers, and many other biocalcifying organisms (Checa et al. 2021; Coronado et al. 2019; Crippa et al. 2020; Simonet Roda et al. 2022; Yin et al. 2021) (Fig. 1). As a whole, biomineralization plays a significant role in carbon sequestration and climate change mitigation by transforming the dissolved carbon dioxide (CO_2) into solid mineral forms, thereby reducing the amount of CO_2 in the atmosphere.

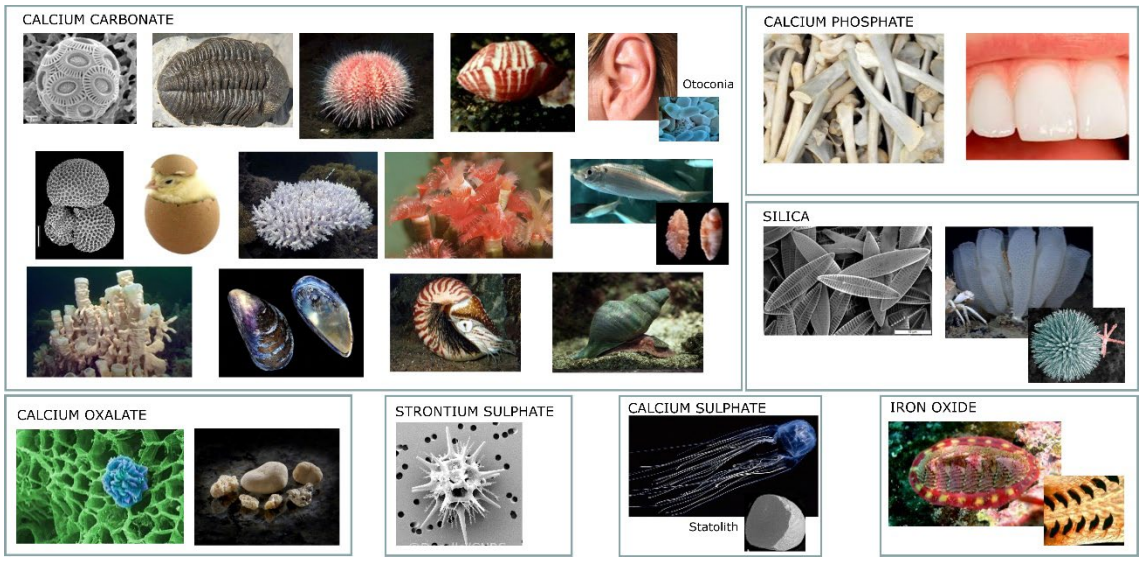

Figure 1. Examples of the different varieties of biominerals present in nature.

Biomineralization occurs through the interaction of organic molecules, often proteins and polysaccharides, with inorganic minerals, leading to the controlled nucleation and growth of mineral phases. Both organic and inorganic precursors are secreted by a specialized epithelium (e.g. the calcifying cells of the

mantle in mollusks), and released into an extracellular medium space (that can be an enclosed space or not), where the mineral precipitation takes place. Studies conducted by Addadi and Weiner (1992) elucidated the role of organic matrix proteins in controlling calcium carbonate mineralization in mollusk shells, highlighting the importance of interfacial interactions in biomineralization processes. In vertebrate animals, proteins such as collagen and osteocalcin play crucial roles in bone mineralization. These biomolecules often possess specific amino acid sequences or structural motifs that interact with mineral ions, facilitating their deposition and organization of hydroxyapatite crystals into ordered structures (Mann 1983, 2001).

It is precisely due to these interactions between organic and inorganic components that biominerals exhibit a wide variety of morphologies with remarkable biomechanical properties, such as elasticity and fracture toughness, which exceed by far that of the homologous inorganic minerals (Currey 1977; Currey and Taylor 1974) (Fig. 2).

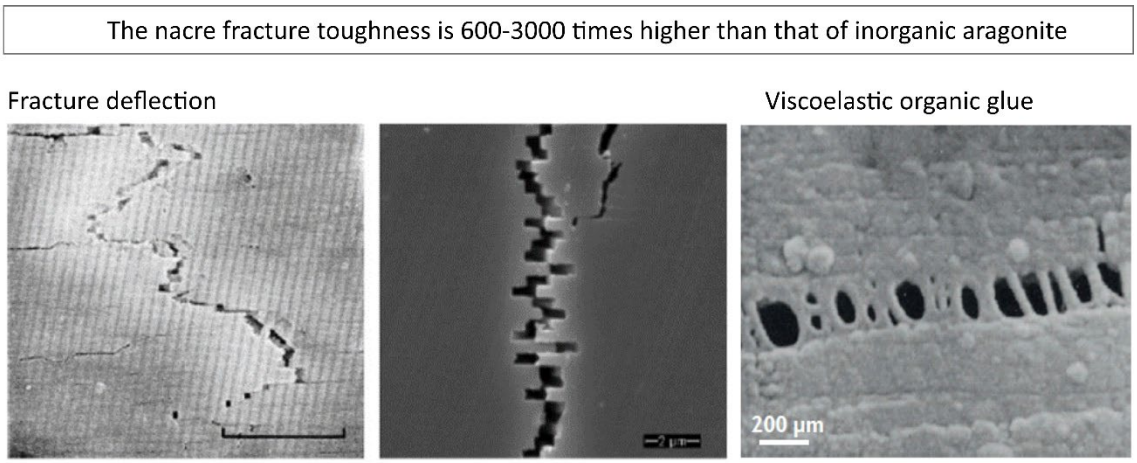

Figure 2. Nacre fracture. the zig-zag arrangement of the tablets and the organic membranes promote fracture line dispersion. Adapted from Chen et al. 2012.

The morphological diversity exhibited by shells and skeletal structures of marine invertebrates has captivated biologists for centuries (Haeckel 1899), serving also as a guiding principle for geologists and paleontologists in unraveling the Earth's history. This pursuit was initially suggested by Georges

Cuvier (1797-98) and further implemented by Leopold von Buch (1839), who advocated for the utilization of fossils, particularly shell morphology, as a stratigraphic dating tool.

Fossil skeletal remains harbor tangible evidence of environmental conditions from geological epochs in the past. With the emergence of modern high-resolution microscopy and thanks to the advances in chemical element and isotope analytical techniques, fossils have emerged as primary proxy objects for paleoenvironmental reconstructions (Brand et al. 2003; Lowenstam 1981; Urey et al. 1951; Veizer et al. 1999, 2000). The generation of geochemical models building on isotopic and trace element signatures that the shell material acquires during its formation or diagenesis is one of the prime objects of sclerochronology, which uses this natural material database to study climatic events with a precision of a year or even for sub-annual events (Hudson et al. 1976; Schöne & Gillikin 2013; Peharda et al. 2021).

Thus, the understanding that all these aforementioned characteristics of biominerals are strictly related to their microstructures and crystallographic textures makes their study even more relevant. It contributes not only to our knowledge of a fundamental biological phenomenon involved in the growth, development, and survival of individuals, but also holds promise for unraveling the paleoenvironmental reconstructions and for applications in material science and engineering, regenerative medicine, and environmental protection face to climate change.

Based on all these premises, the present PhD research is intended to shed light on two completely different phyla of calcifying organisms that have not been exhaustively studied yet: the bryozoans and serpulid polychaetes.

The following sections provide a general introduction to both groups of animals (classification, biology, skeletal morphology, and mineralogy). Additional information on microstructures and crystallography found in the

scientific literature is reported in the introduction of chapters III (parts 1 and 2) and IV.

1.2. Introduction to the Phylum Bryozoa

Bryozoans comprise an entire phylum of aquatic, exclusively colonial animals that occur worldwide in freshwater as well as in marine environments, and from shallow to deep waters (Ryland 1977; Taylor 2020) (Fig. 3).

Figure 3. Gymnolaemate bryozoan *Pentapora fascialis* from the Mediterranean Sea (Granada coastline), found at a depth of 15 m. Photo by Prof. Luís Sánchez Tocino (Department of Zoology, Faculty of Sciences, University of Granada). https://litoraldegranada.ugr.es/el-litoral/el-litoral-sumergido/fauna/briozoos/briozoos-del-litoral-granadino/.

The total number of living bryozoan species is currently estimated at 6,461, distributed among the classes Gymnolaemata (5,805 species), Stenolaemata (654 species), and Phylactolaemata (<100 species) (WoRMS Editorial Board 2024).

Except for the class Phylactolaemata, all the bryozoans live in seawater (only a few of them in brackish water) and secrete calcium carbonate skeletons, which makes them an important fossil group (Hageman et al. 2003; O'Dea et al. 2011; Taylor and Allison 1998). Together with their importance in the fossil record, they also register the effects of climate change in the marine environment, and constitute a significant CO_2 fixation reservoir, along with many other marine calcifying proto- and metazoans (e.g., corals, mollusks, foraminifera) (Taylor and

Allison 1998). Due to the absence of calcium carbonate skeleton in the class Phylactolaemata, the present Ph.D. research focuses on the study of species belonging to the classes Stenolaemata and Gymnolaemata.

Bryozoans form colonies composed of clone individuals, called zooids. The zooids are small, typically measuring under a millimeter in length. However, because colonies can contain a large number of zooids, colonies can vary in size from a few centimeters to more than one meter (composed of tens of thousands of zooids, e.g. in *Pentapora fascialis*, Fig. 3). The basic bryozoan zooid consists of a body wall (cystid) containing a fluid-filled cavity (coelom) within which is suspended a polypide with a lophophore (feeding organ) and gut. (Fig. 4).

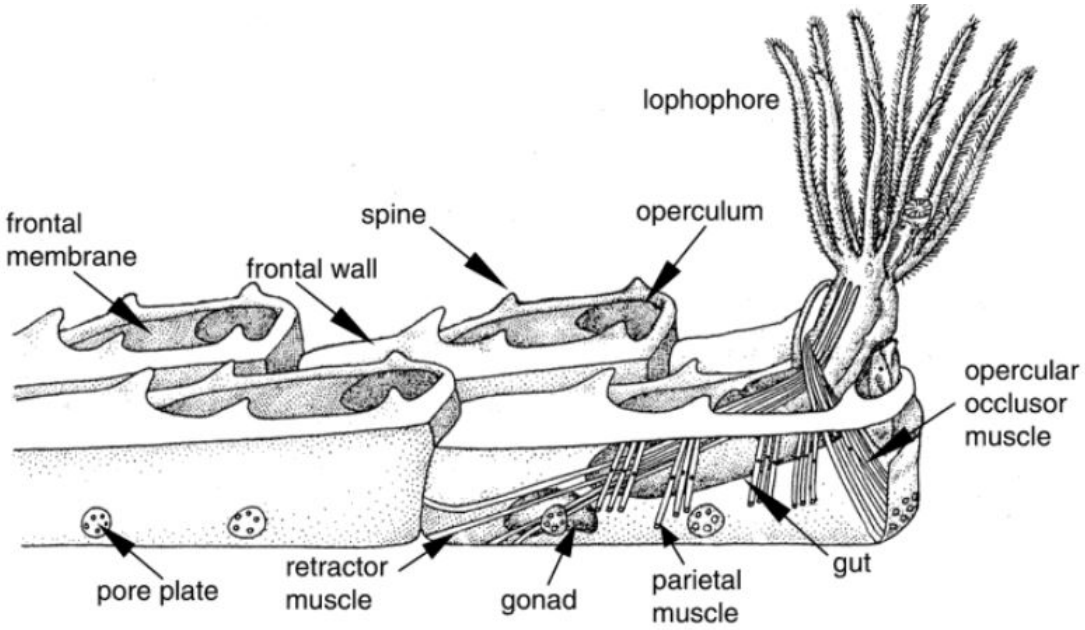

Figure 4. Schematic drawing of a basic cheilostome bryozoan, pointing out some of the most important anatomical features of the zooids (from Taylor 2020).

The mineralized skeletons are covered by an organic layer, the cuticle. The cuticle forms at the growing edge of the colony where newly budded zooids originate. It is secreted by an epithelium consisting of palisade, fusiform, and vesicular cells, and serves as a template for the nucleation of calcium carbonate crystals during the early stages of skeleton formation (Tavener-Smith and Williams 1972) (Fig. 5).

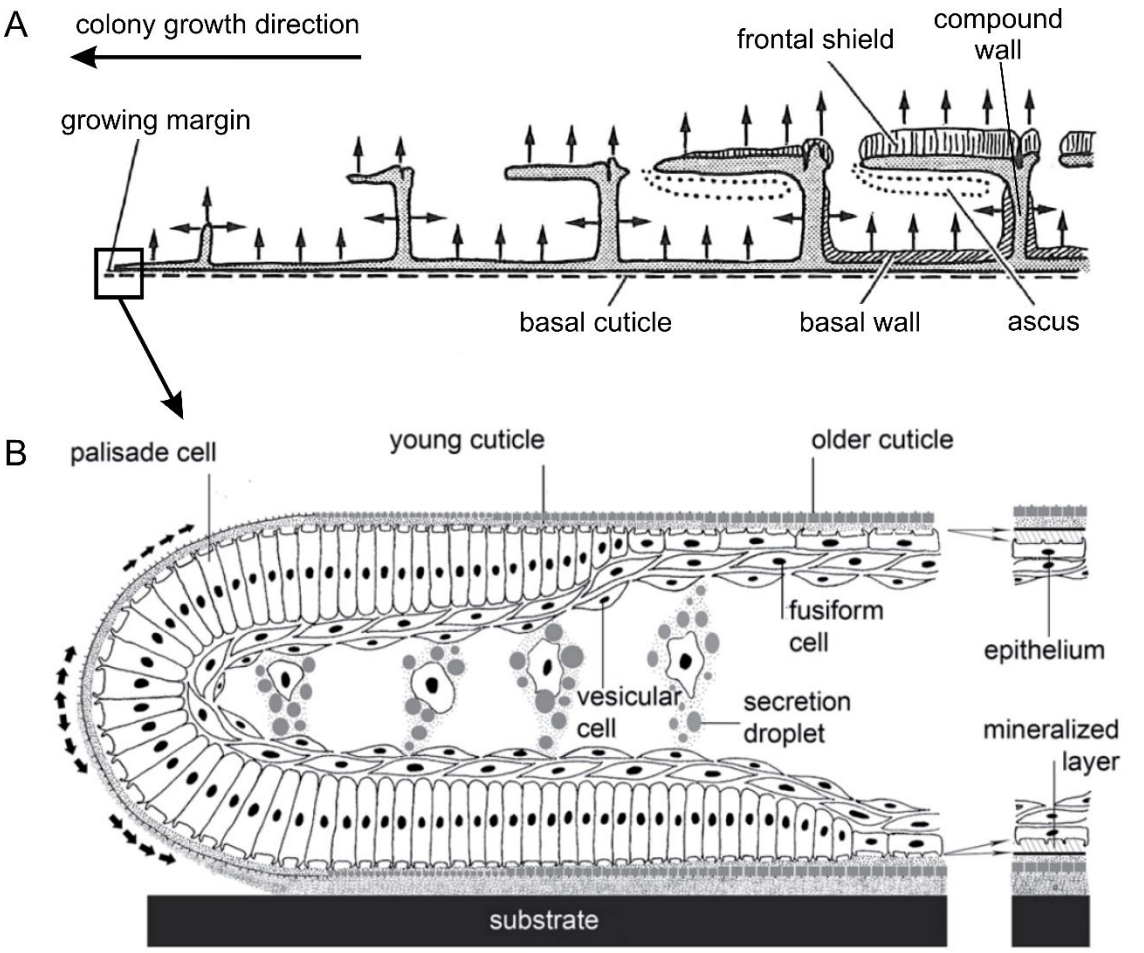

Figure 5. Schematic drawing of a cheilostome colony growth. A. Longitudinal section of the skeletal at the growing edge. The black arrows indicate the direction of expansion. B. Sagittal section of the secretory epithelium at the tip edge. The principal cells responsible for the organic cuticle and the mineralized skeleton formation are depicted (after Sandberg 1983 and Taylor et al. 2015).

As mentioned above, depending on the species, each colony can be formed by a few to many thousands of zooids. Nevertheless, despite their identical genetic pool, zooids can have diverse morphologies (polymorphism) due to either a different developmental stage (ontogeny and astogeny) or because of functional differentiation depending on their role within the colony: feeding lophophorate zooids (autozooids), brooding zooids (gonozooids), defensive zooids (avicularia), and structural zooids (kenozooids) (see Ryland 1977 and Taylor 2020 for a biological introduction to the phylum) (Fig. 6). This phenotypic plasticity has played a fundamental role in the evolutionary and adaptive success of this phylum throughout its history (Shack et al. 2019).

The different zooids that make up a colony are interconnected by a network of channels known as "the funicular system" (Bobin 1977; Bone and Keough 2010; Carle and Ruppert 1983). This network promotes the exchange of nutrients and oxygen from the feeding autozooids to the remaining polymorphic individuals of the colony.

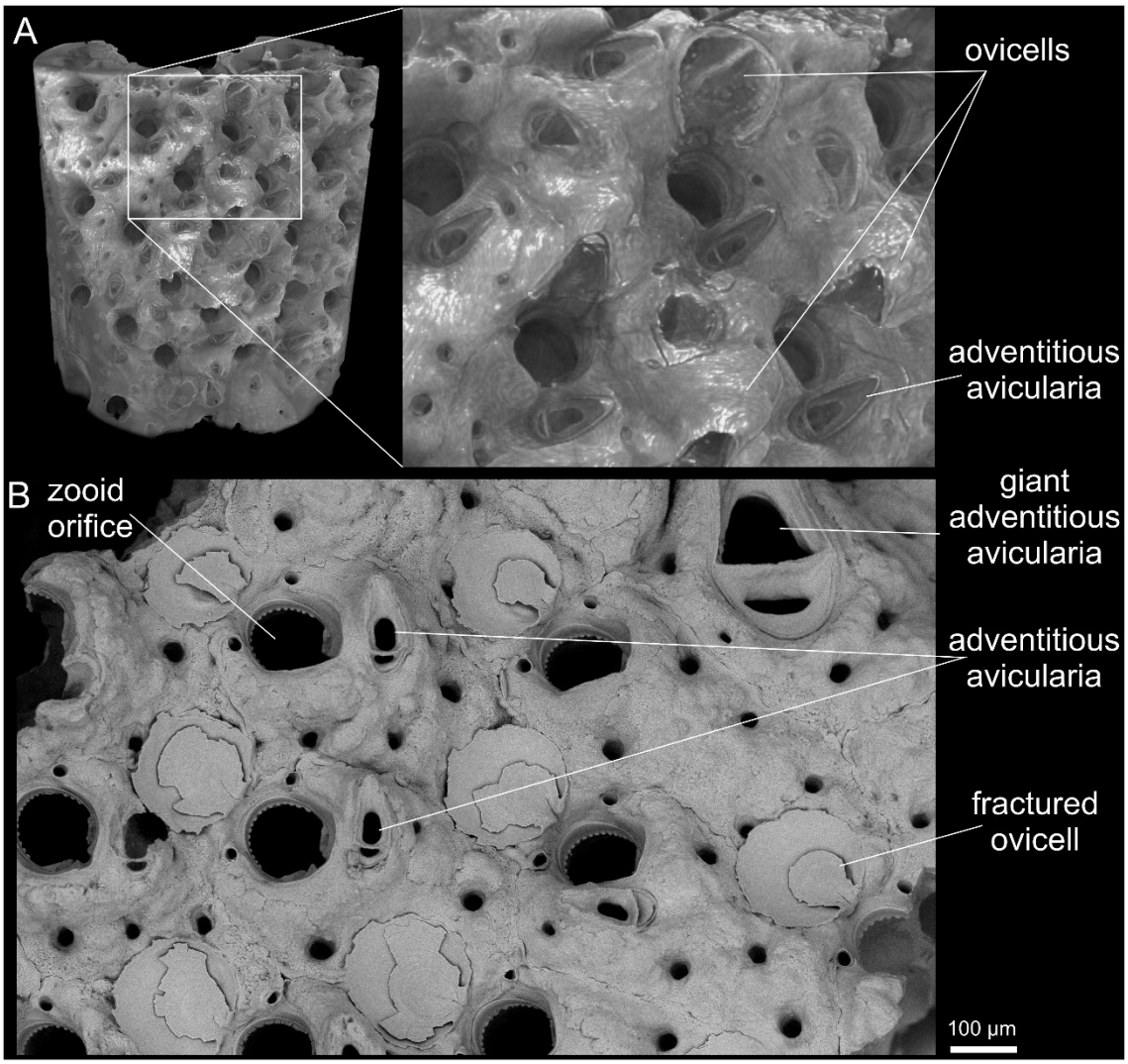

Figure 6. Zooid polymorphism present in the cheilostome *Schizoretepora serratimargo*. A. Micro-CT image of a colony fragment. The framed area is magnified, showing different types of zooids: autozooids, ovicells, and adventitious avicularia. B. SEM image of a fragment of the same sample. It can be observed the double-layered wall of the (fractured) ovicells and a giant adventitious avicularium (top right).

The species belonging to the class Stenolaemata account for about 10% of the living bryozoans. They inhabit only marine environments, produce mineralized skeletons consisting exclusively of calcite, and have a characteristic "tubular-shaped" zooid chamber (Figs. 7 and 9). They are currently represented by a single order, Cyclostomata. They were the first bryozoans to appear, present already in the Early Cambrian (Cambrian Age 3), and participated in the Cambrian Radiation (Zhang et al. 2021). They spread their diversity during the Great Ordovician Biodiversity Event (Harper 2006) and remained the dominant group of bryozoans until the Upper-Jurassic radiation of the gymnolaematans (Taylor 1994) (Fig. 9).

Figure 7. Stenolaemate bryozoan *Tubulipora aperta* from Granada coastline (La Herradura, at 5 m depth). It can be appreciated the characteristic tubular-shaped zooid chambers. Photo by Prof. Luís Sánchez Tocino (Department of Zoology, Faculty of Sciences, University of Granada). https://litoraldegranada.ugr.es/el-litoral/el-litoral-sumergido/fauna/briozoos/briozoos-del-litoral-granadino/tubulipora-aperta/.

On the other hand, gymnolaematans represent more than 89% of the extant bryozoan species. They all live in marine environments (except a few species that can live in brackish conditions) (Fig. 8). The Order Cheilostomatida, which appeared in the Late Jurassic (Taylor 1994) and diversified from the mid-Cretaceous on (Jablonski et al. 1997), became the dominant group of bryozoans

☛ **Figure 8.** Different cheilostomes species found on Granada coastline: A. *Myriapora truncata*. B. *Adeonella calveti*. C. *Chartella tenella*. D. *Schizobrachiella sanguinea*. Photo by Prof. Luís Sánchez Tocino. https://litoraldegranada.ugr.es/el-litoral/el-litoral-sumergido/fauna/briozoos/briozoos-del-litoral-granadino/.


A
B
C
D

until today, comprising more than 94% of the species of the group (Taylor 2020). All cheilostomes have a characteristic box-shaped zooidal chamber (Figs. 4, 8, and 9). They have three types of zooidal walls: basal, vertical (parallel or transverse to the elongation axis), and frontal (Figs. 10 and 11).

Unlike stenolaematans, the skeletons of cheilostomes can be made of two calcium carbonate polymorphs: calcite and aragonite. Some species are either entirely calcitic or, much less often, entirely aragonitic, and others can secrete both polymorphs (bimineralic) (Lowenstam 1954; Sandberg 1977; Smith et al. 2006; Taylor et al. 2009).

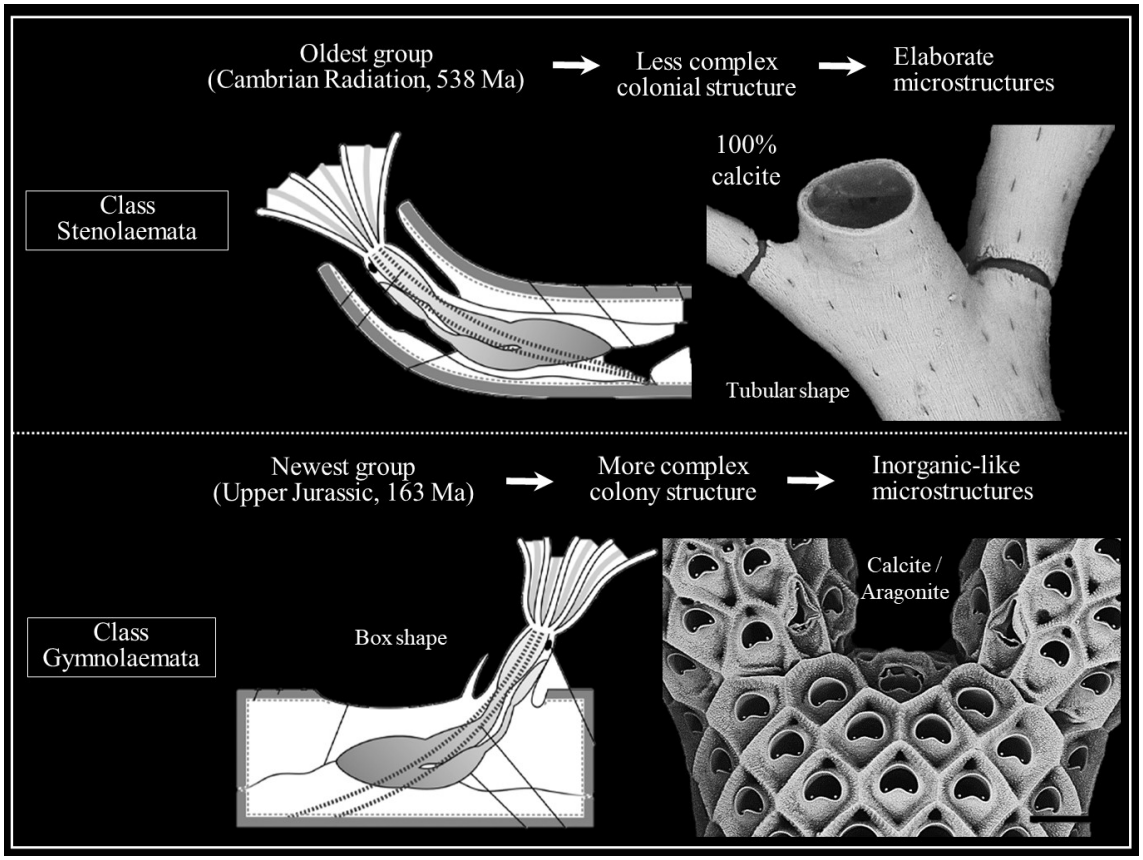

Figure 9. Schematic comparison of the principal features representative of the two major groups of bryozoans: stenolaemates (up) and gymnolaemates (down).

Among cheilostomes, the greatest differences are found in the structure of the frontal wall, which may be either wholly membranous or underlain by a calcified cryptocyst in some taxa (e.g. in the informal group Anasca), or calcified to form an external wall called "frontal shield" (e.g. in the informal group Ascophora) (Dick et al. 2009) (Fig. 10). It is also important to consider whether the walls are interior walls (internal partitions where secretory epithelia are found on both sides of the surfaces) or exterior walls (secretory epithelium on one side and the cuticle on the opposite side). Additionally, two external walls separating adjacent zooids, with their cuticles placed side by side in the center, are defined as compound walls (Figs. 10 and 11).

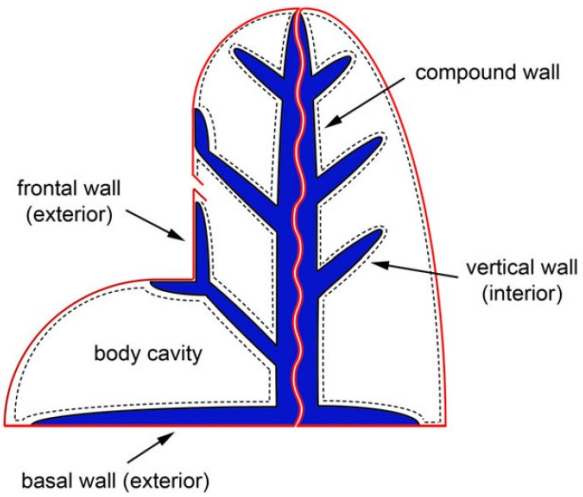

Figure 10. Stylized vertical section scheme of a hypothetical bryozoan colony. The cuticle is in red. The calcified epithelium is depicted by the dashed lines. The different wall types are indicated (from Taylor et al. 2015).

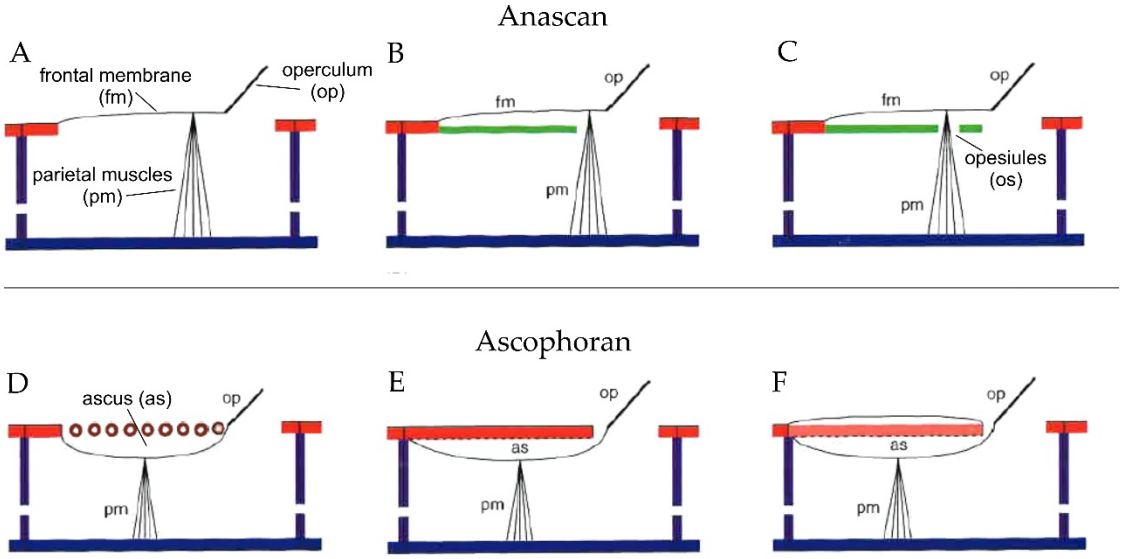

Figure 11. Longitudinal cross-section schemes of different cheilostome frontal wall types. A-C. Anascan group, with the cryptocyst under the frontal membrane (green color). D-F. Ascophoran group, with the external frontal wall (frontal shield, in red color) and the underlying ascus. (from Taylor 2020).

Finally, regarding cheilostome mineralogy, numerous studies performed on a large number of species (summarized in Taylor et al. 2009, 2015) have demonstrated a strong latitudinal pattern: calcitic bryozoans are dominant at high latitudes (around the polar circles), while towards the equator, the number of aragonitic and bimineralic species increases until reaching a proportion similar to the calcitic ones (Fig. 12).

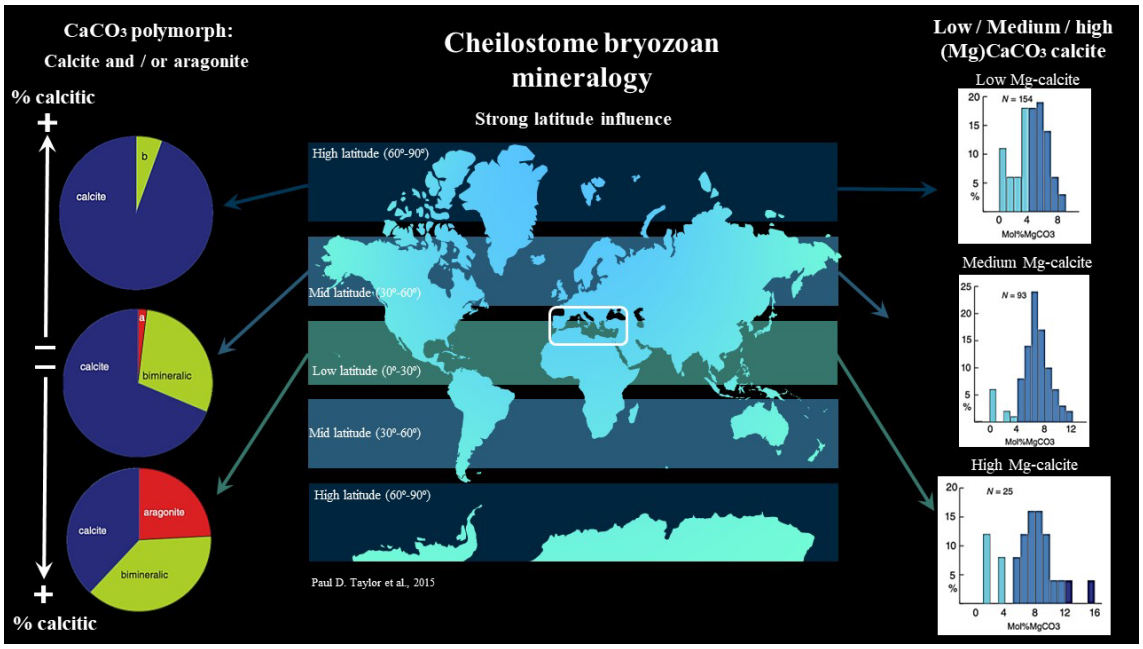

Figure 12. Mineralogy of cheilostome bryozoans. There is a strong latitudinal influence: at high latitudes (60º-90º) predominate calcitic bryozoans with low Mg-calcite. At mid-latitude (30º-60º) the is an increase of bimineralic and aragonitic bryozoans, and calcite appears as medium Mg-calcite. At low latitudes (0º-30º) the is a more or less equal proportion between calcitic, bimineralic, and aragonitic bryozoans, and calcite appears as high Mg-calcite (data from Taylor et al. 2015).

Other studies based on scanning electron microscopy and electron microprobe (Taylor et al. 2008) determined the location of both calcium carbonate polymorphs within the skeleton of some bimineralic bryozoans. The aragonite is restricted to the outer layer of the frontal shield (in ascophorans) or the cryptocyst (in anascans), while the rest of the skeletal walls are usually made of calcite (Fig. 13). On rare occasions, aragonite is located in adventitious avicularia in *Odontionella cyclops* and *Stylopoma inchoans*, or in the outermost part of the basal walls in *Pentapora foliacea* (Taylor et al. 2008).

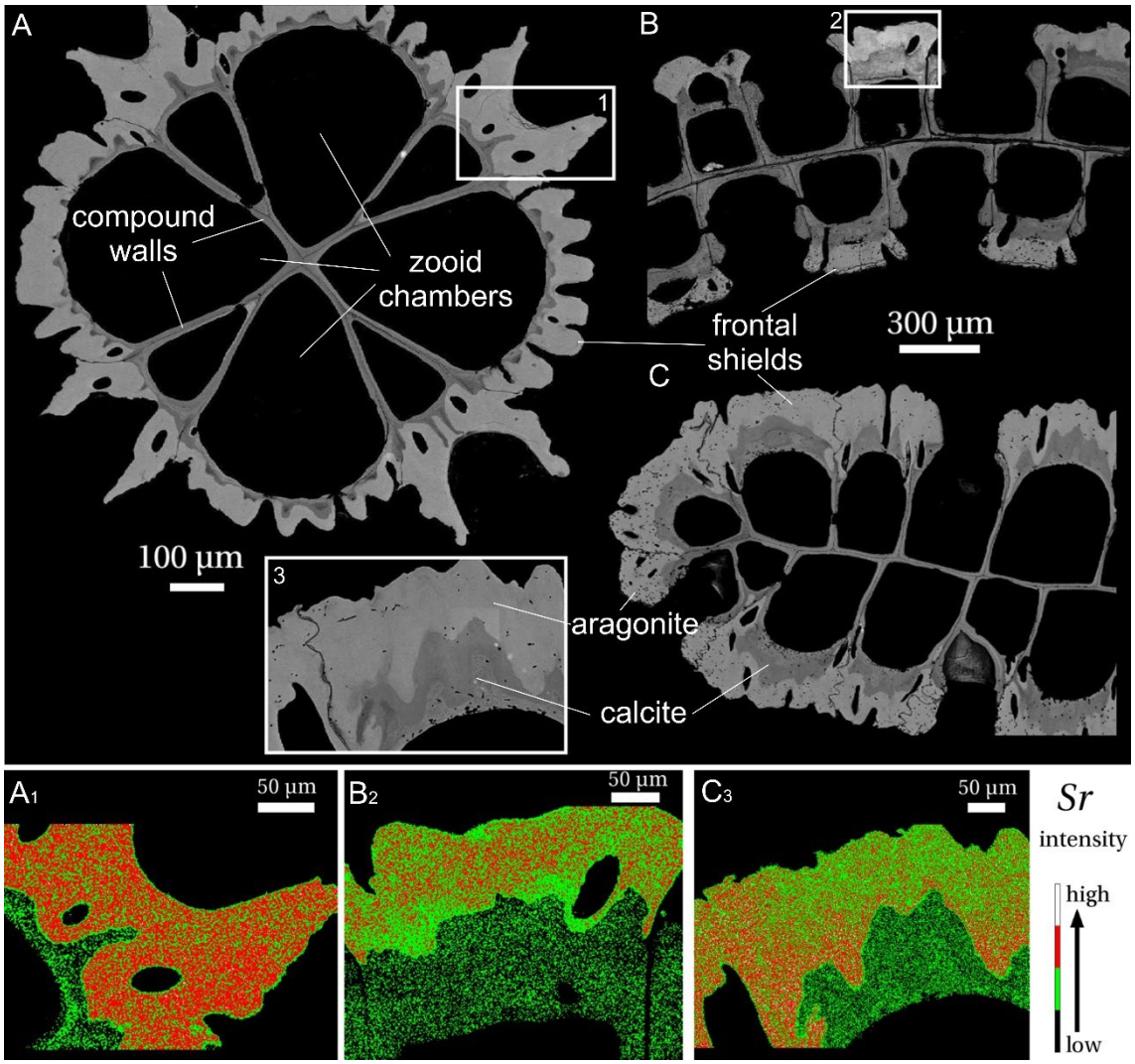

Figure 13. Calcite and aragonite distribution in bimineralic cheilostome bryozoans. A-C. SEM images (backscattered mode) of three different cross-sectioned colony samples: *Margaretta cereoides* (A), *Odontionella cyclops* (B), and *Pentapora fascialis* (C). Light grey corresponds to aragonite and dark grey to calcite. Aragonite is restricted to the frontal shields, whereas calcite comprises the interior basal and compound walls. The framed areas (A_1, B_2. C_3) were selected from each species to perform electron microprobe maps of strontium (Sr). As the Sr is only incorporated by the aragonite phase mineral, the maps show the presence of aragonite at the frontal shields. The intensity of the Sr signal is given by the color key bar (from Benedix et al. 2014).

1.3. Introduction to serpulid polychaetes (Phylum Annelida)

The family Serpulidae (Rafinesque, 1815) comprises a diverse group of sedentary marine tubeworms that belong to the class Polychaeta (phylum Annelida). The current number of known serpulid species is 568 (WoRMS Editorial Board 2024) and they are widely distributed, from shallow to deep waters (Hove and Kupriyanova 2009; Kupriyanova et al. 2014). Except for the sabellid genus *Glomerula* and some cirratulid species, serpulids are the only family that secretes calcium carbonate tubes, where they live in (Hedley 1958; Fischer et al. 2000; Vinn et al. 2008a; Vinn 2009). They are commonly known as "feather duster worms" because of their characteristic organ for suspension feeding and respiration called

the radiolar crown, which can be completely retracted inside the tube (Tilic et al. 2021) (Fig. 14).

Because of their ability to attach to hard substrates and their invasive habits (Kupriyanova et al. 2016), serpulids contribute to biofouling impact (Charles et al. 2018; Lacoste and Gaertner-Mazouni 2015), along with other sessile organisms (such as sponges, barnacles, bryozoans, calcareous algae or bivalves). Nevertheless, they also play an important ecological role in structuring diverse marine ecosystems. They provide new habitats for other species by occasionally building reefs, which promote biodiversity (Rossbach et al. 2021). Serpulids contribute significantly in terms of biomass productivity and sediment formation, acting as carbonate sinks (Montefalcone et al. 2022). They are useful as metal pollution indicators (Xie et al. 2005) and as hypoxic events markers related to anthropogenic activity (Jewett et al. 2005). Serpulids are vulnerable to ocean acidification, which adversely alters the biomechanical properties (hardness and elasticity) of the tube structure (Chan et al. 2012).

Regarding serpulid life's cycle, they reproduce sexually and generate a trochophore larva. The larva swims away and, after metamorphosing into a juvenile stage, settles on a new substrate (Nelson et al. 2017). The secretion of the tube begins a few days after the juvenile serpulid settles (e.g., five days in *Galeolaria hystrix*, Nelson et al. 2017) (Fig. 15).

☚ **Figure 14.** Pictures of three different serpulids polychaetes from the Granada coastline. A. *Serpula vermicularis*. B. *Protula tubularia*. C. *Protula intestinum*. It can be appreciated how the radiolar crown can be protruded or retracted inside the calcium carbonate tube. Photos by Prof. Luís Sánchez Tocino. https://litoraldegranada.ugr.es/el-litoral/el-litoral-sumergido/fauna/anelidos/poliquetos/poliquetos-del-litoral-granadino/.

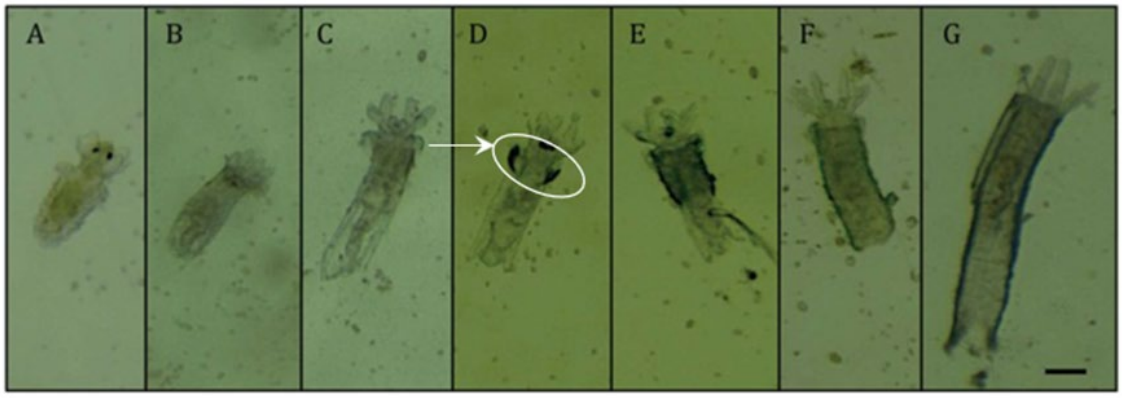

Figure 15. Settlement and juvenile growth of *Galeolaria hystrix* (days 22-27). A. Settled individual at the end of trochophore lava metamorphosis (after 19 days). B-C. The presence of a transparent tube can be appreciated. D-G. The initial site of calcification (dark bands framed in D) starts after 5 days of settlement in the substrate (after Nelson et al. 2017).

Calcification is carried out by the neck folds (anatomically named "peristomial collar", situated just below the radiolar crown), where the calcium-secreting tubular-racemose glands are located, surrounded by a secretory epithelium composed of mucus cells (Hedley 1956). As a whole, a mix of calcium carbonate precursors and a sulphomucopolysaccharide matrix is secreted and deposited at the growing edge of the tube (Hedley 1956; Neff 1969) (Fig. 16).

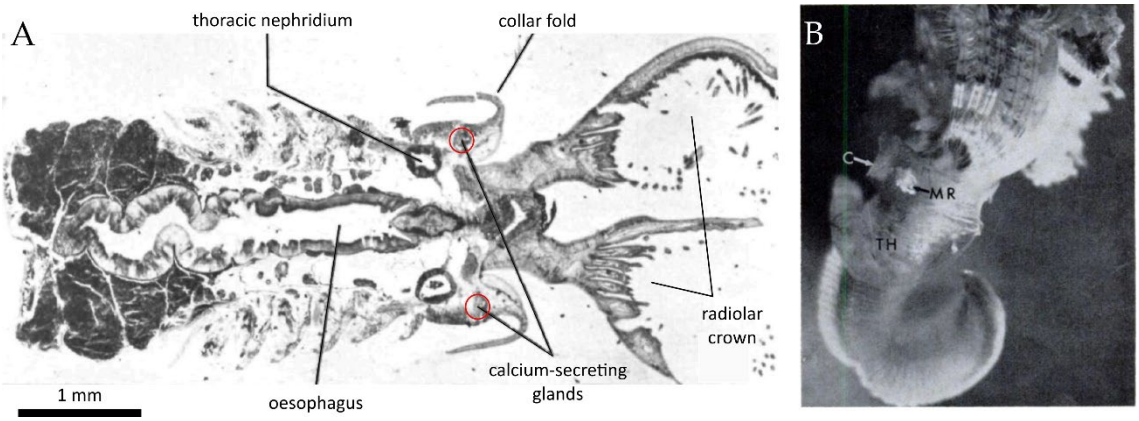

Figure 16. A. Longitudinal thin section of *Spirobranchus triqueter* soft body, showing the radiolar crown, the thorax, and the anterior region of the abdomen. The calcium secretory glands are indicated, located below the collar folds (from Hedley, 1956). B. An image of *Eupomatus dianthus* removed from its tube and allowed to regenerate calcium carbonate mineral for about 4 hours. A small mineral concretion lies under the fold of the collar and directly over the opening of the calcium-secreting glands. (20x). C, collar; MR, mineral regenerate; TH, thoracic membrane (from Neff, 1969).

Concerning their mineralogy, serpulids can secrete calcite, aragonite, or both calcium polymorphs within a single tube (Lowenstam 1954; Ten Hove and Van den Hurk 1993; Vinn et al. 2008c, b). Although the mineralogy of most species is unknown, the majority of serpulids studied are calcitic (around 40%), followed by bimineralic (36%) and aragonitic (24%) (Smith et al. 2013). Calcite is always medium to high magnesium calcite (7-15 wt% $MgCO_3$) (Smith et al. 2013) (Fig. 17A). Based on a review of a large number of previous studies, these authors concluded that latitude accounts only part of the variations in both calcite percentage and Mg-calcite content, with most of the variation attributable to phylogenetic diversity among specimens (Fig. 17B)

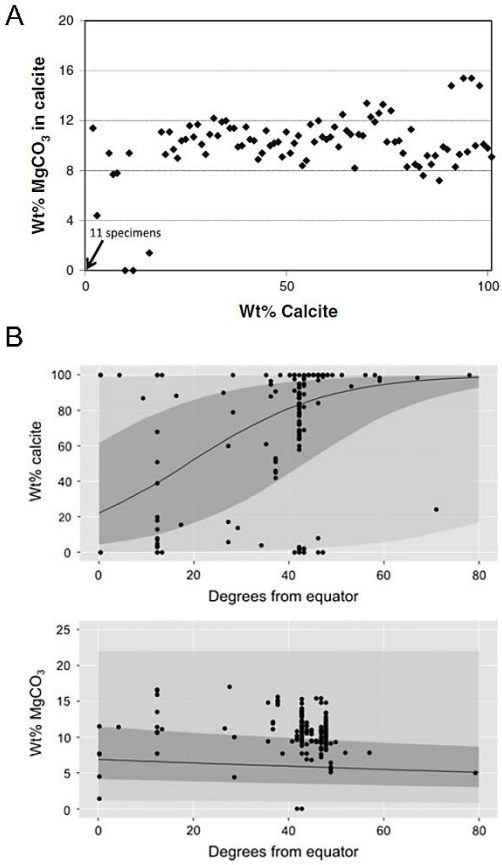

Figure 17. A. Skeletal mineralogy of 155 specimens of serpulids from which both wt% calcite and wt% $MgCO_3$ are known, including the tube structure and the opercula. B. Effect of latitude on serpulid mineralogy. Latitude explains only a small proportion of variation in calcite and Mg content (dark grey area represents 50% of credible intervale and light grey 95%) (Smith et al. 2013).

Finally, another important aspect to consider is that the tube structure of serpulids contains a significant amount of organic matter, which occurs primarily as membranes marking the different growth increments (Vinn 2011). The organic fraction can be separated into soluble and insoluble organic matter (SOM and IOM), which are mainly composed of carboxylate and sulfated polysaccharides (Tanur et al. 2010).

1.4. Objectives

Within the framework of a major research project on diverse marine calcifying organisms (I+D Spanish National Project CGL 2017-85118-P) the present Ph.D. thesis (FPI fellowship PRE-2018-085419) focuses on applying high-resolution techniques to perform an in-depth study to elucidate the microstructures and crystallography of the bryozoans and serpulid polychaetes skeletons.

Therefore, the main objective of the present Ph.D. work is to determine the degree of organization and the physical and biological factors operating on the microstructures of bryozoans and serpulids polychaetes.

To achieve this objective, the following goals were established:

- Characterize the organization and crystallography of bryozoan microstructures:
  - Study the calcitic microstructures of stenolaemate bryozoans.
  - Identify the calcitic and aragonitic microstructures of gymnolaemate bryozoans.
  - Analyze the membranes and organic matrices involved in the biomineralization process.
  - Establish the relationship between the position of the calcifying epithelium, the morphology of the microstructures, and the growth mechanisms.
- Determine the organization and crystallography of microstructures of serpulid polychaetes:
  - Identify the calcitic and aragonitic microstructures of the different genera selected.
  - Study the membranes and organic matrices involved in the biomineralization process.
  - Investigate the relationship of the calcifying epithelium at the growing edge of the tube.
  - Elucidate the biomineralization processes that occur in serpulids.

Chapter II
Materials and Methods

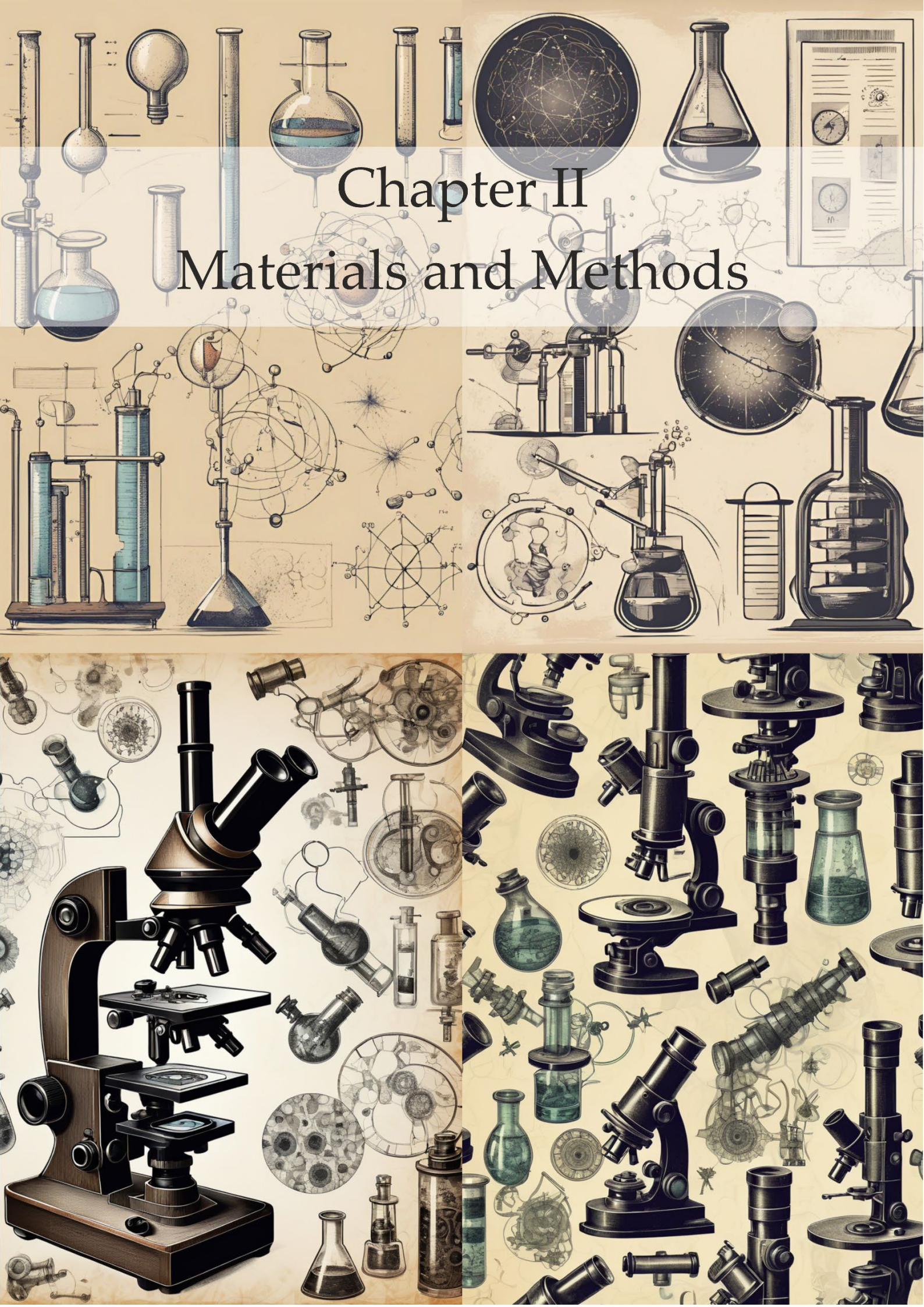

2. Material and Methods

2.1. Samples preparation for SEM and EBSD

For SEM and EBSD measurements, all the bryozoans and serpulids analyzed were prepared according to the following protocol:

1. **Cleaning**. All the samples studied in this Ph.D. were cleaned by immersion in commercial bleach (~ 5% active chlorine) for 2 h in a stirring set. Then, the bleach solution was removed by several sonicated washes (2-3 min each). The fragments were dried in a laboratory oven at 40ºC for 24h.

2. **Embedding**. Selected fragments of each sample were embedded in epoxy resin (EpoFix, Struers). The epoxy resin must be mixed with a hardening solution (Hardener EpoFix, Struers) (Fig. 1). For our samples, the proportion used was [7:1]. For instance, for a final volume of 50 ml, taking into account the resin density, we mixed around 58 gr of resin with 8.28 gr of hardener. The mixture should be done in a plastic pot and heated up to about 50ºC while moving for 5 min until reaches transparency and liquid texture. It is highly recommended to carry out the whole process under safety measures: all the samples were manipulated wearing laboratory gloves and the embedding was performed in a laminar flow air extractor.

Figure 1. Epoxy resin "EpoFix" and hardener from Struers. https://www.struers.com.

3. **Vacuum**. To avoid air bubbles inside or surrounding the samples, it is highly recommended to put the samples in a vacuum chamber just after embedding (60 pa / 10min) (Fig. 2). After 24-48h for hardening, the samples are ready to start directly the grinding and polishing steps or to be firstly cut.

Figure 2. Vacuum pump coupled with a glass desiccator. https://www.labbox.eu/product/vacuum-pump-ibx-instruments-v-series/.

4. **Cutting**. The samples were sectioned longitudinally or transversally, mostly just along the equatorial plane, using a precision sectioning saw (IsoMet® 1000, Buehler) (Fig. 3). After cutting, if necessary to fill the voids, the resulting surface is re-embedded again following the same process explained before.

5. **Sanding**. The surface of interest of the different samples was sanded in successive steps with electroplated diamond discs: 360, 600, and 1200; ANSI/CAMI US grit number). It is important to rotate the sample 90º to avoid titled surfaces and to have all scratches in the same direction as we progress to finer sanded stages.

Figure 3. IsoMet® 1000 precision sectioning machine. From Buehler. https://www.buehler.com/products/sectioning/precision-cutters/isomet-1000-precision-cutter/.

6. **Polishing**. To eliminate the scratches of the sanding steps, the samples were firstly polished with silicon carbide powder (9µm, 4,5µm and 3µm) mixed with water, performing smooth circular or infinitum ("∞") movements against a glass surface. Between each step, the samples were washed with sonicated distilled water to remove silicon carbide. Then, the samples were polished with high-density wool felt pads (adding 1 µm and ¼ µm of polycrystalline diamond suspension, Struers), until reaching a mirror surface (Fig. 5). Both grinding and polishing steps were carried out with the Hi-Tech Diamond machine (All-U-Need model) (Fig. 4). For EBSD analyses, a final manual polishing step was done using Aluminum Oxide or Silica Oxide (¼ µm) in order to eliminate amorphized layers on the surface, formed during the final polishing steps.

Figure 4. Hi-Tech Diamond polishing machine "All-U-Need" (rock/mineral model). https://hitechdiamond.com/products/all-u-need-rock-mineral-model.

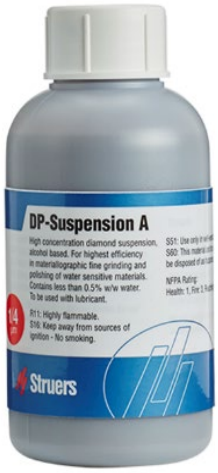

Figure 5. ¼ µm Polycrystalline diamond suspension, Struers. https://www.struers.com/en/Products/Grinding-and-Polishing/Grinding-

7. **Decalcification**. Only for SEM observations, some of the polished samples were immersed in an etching and decalcifying solution (2.5% glutaraldehyde, 0.25M HEPES buffer, and 0.05M EDTA), for 1 minute in an orbital shaker (Fig. 6). This step sharpens and highlights the microstructures by clearing the surface of amorphous layers.

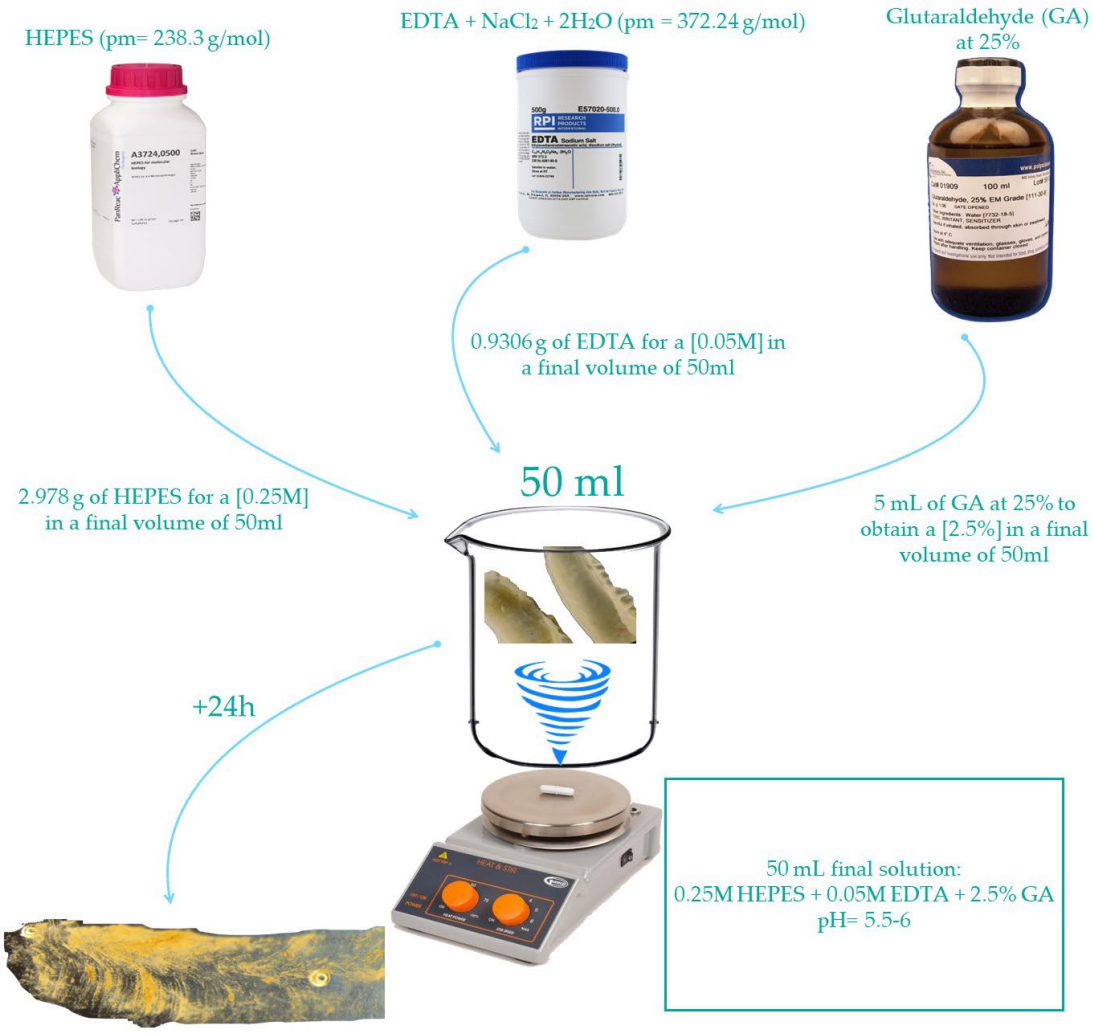

Figure 6. Protocol of etching and decalcifying samples using 2.5% glutaraldehyde, 0.25M HEPES buffer, and 0.05M EDTA solution.

2.2. Guide to EBSD data Processing by AZtec and Project Manager (CHANNEL5)

2.2.1. AZtec

1º: On the home screen, we can choose between using the interface for EDS-SEM or for EBSD (choose EBSD).

2º: Initiate a new Project or open a previously created project (e.g., "Specimen 1").

3º: On the vertical bar to the left of the screen, a vertical menu called "data tree" is displayed, where all the analyses performed are saved (SEM photos, EBSD and/or EDS maps, etc.).

4º: In the "scan images" or "acquire map" tab, we can view the maps in larger size and export them (simply right-click in the mouse and select "copy image").

5º: Once the specimen with the EBSD maps has been selected, go to the horizontal toolbar, click "Files" and "Export to CHANNEL5". Save in the corresponding folder (Fig. 7).

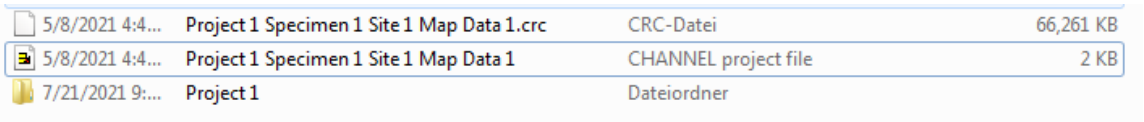

Figure 7. Files exported from Aztec to CHANNEL5.

IMPORTANT: Two files are exported, the "CHANNEL5 project file" and another one in "CRC" format, both must be saved in the same folder and must have the same name, including spaces; otherwise, it will not be possible to open them.

2.2.2. Project Manager (HKL CHANNEL5)

1º: Open the exported file and select our profile (previously created with the preestablished parameters). A narrow "Project Manager" window will open with the downloaded applications (we will only use Tango and Mambo). Drag the open project to one of the two applications: first to "Tango" to process the map and then to "Mambo" for the creation of pole figures (Fig. 8).

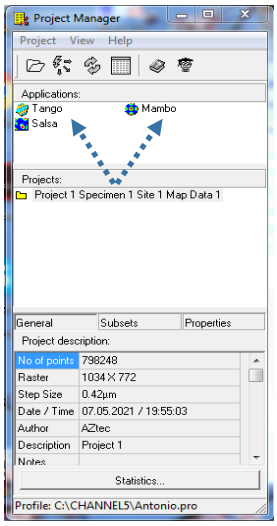

Figure 8. Project Manager interface "general".

2º: In the menu bar, under "view", we can see different options that we will use later:

- Statistics.
- Record Browser.
- Misorientation and angle distribution.
- 3D Crystal orientation (unit cell) —> check the "acquire surface" box.
- Virtual chamber (Fig. 9).

2.2.3. Tango (mapping)

1º: Go to the horizontal toolbar and select "Edit —> Noise Reduction": first, click on "Extrapolate Wild spikes" and then on "Extrapolate Zero solutions" (medium level). Repeat it only twice (two clicks in each one) (Fig. 10).

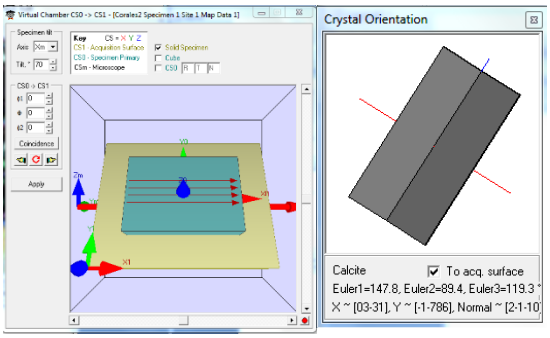

Figure 9. Examples of "virtual chamber" and "3D crystal orientation" user interfaces.

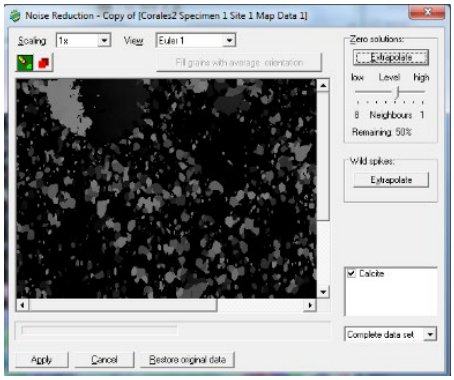

Figure 10. User interface of noise reduction tool.

2º: Edit —> Map properties: Drag the "Band contrast" component (take into account to check or uncheck the "Semi-Transparency" box for different combinations).

3º: View —> Legend. In the graph, right-click and select "properties." Choose "user defined" and define the range of the histogram.

4º: View —> Zero solutions (optional if there are many non-indexed areas).

5º: Edit —> Map properties: Open different tabs (copy map) with different map components selected (Band Contrast, Phase, and IPFz) (Fig. 11).

6º: Capture screenshots of the different maps and export them to a PowerPoint or click on the map with the right mouse button —> export —> to Clipboard (bmp) in a Word document. For each map, attach the corresponding legend with the adjusted parameters as explained earlier. Obtain results from each analysis with SEM and AZtec images from the map area, Band Contrast and Phase map, IPFx, IPFy, or IPFz color orientation maps with their corresponding Pole Figures. Attach the corresponding legend to each map (Fig. 12).

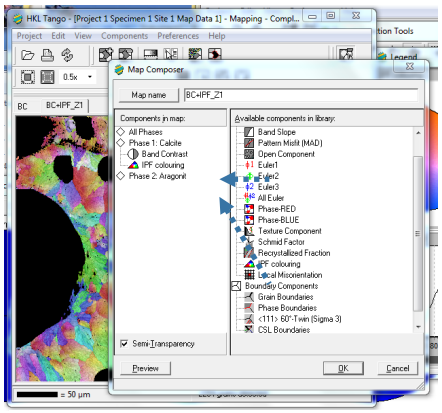

Figure 11. User interface of map composer tool. You can select different components by dragging them (from the right column) to the phase selected (to the left column).

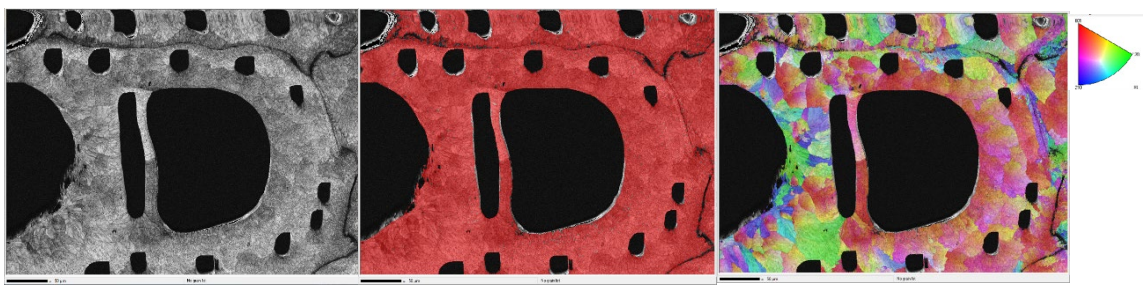

Figure 12. Screenshots of band contrast, phase, and IPFz maps (from left to right).

2.2.4. Mambo (Pole Figures):

1º: Drag the project to the Mambo application (Fig. 8).

2º: In the horizontal toolbar, choose "Sheet properties" —> Select the phase you wish to plot (in this case, calcite or aragonite) (Fig. 13).

3º: Edit —> "Template properties" or click the right button of the mouse and choose "Template properties" —> "General" —> Coordinate system CS0.

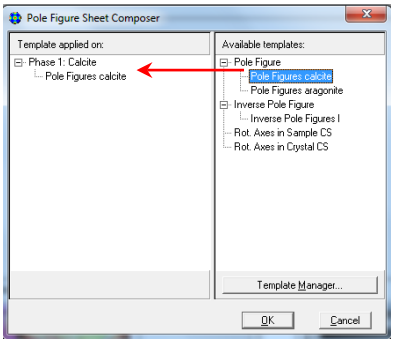

Figure 13. Pole Figure sheet composer. You can select different templates by dragging them (from the right column) to the phase selected (to the left column).

4º: Previously, the characteristics of each PF (planes and crystallographic faces of each phase) have been established. Right-click "Template properties" —> "Items":

- Aragonite: a, b and c-axes: (100), (010), (001)
- Calcite: (direction) c-axis <001> and planes (100) and (104).

5º: Mouse right-click "Template properties" —> "Projection" and select "Stereographic". You can choose to plot the "lower or upper hemispheres" (Fig. 14).

6º: Right-click on the pole figures and select "New Contouring" to obtain the contour version with the MUD value (Fig. 15). Select the following parameters:

- Half width: 5º
- Data Clustering: 3º

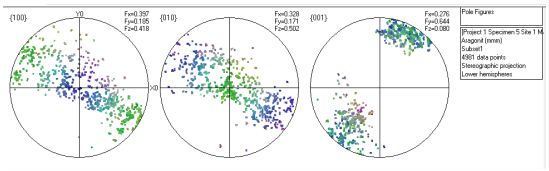

Figure 14. Screenshot of aragonite Pole Figures. The "a, b and c-axes" has been plotted.

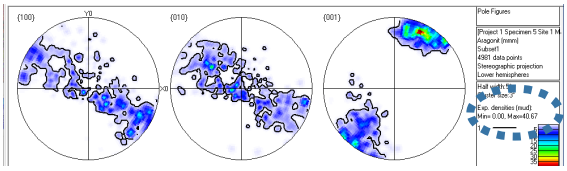

Figure 15. Screenshot of the contouring version of the same aragonite Pole Figures. The MUD value (40.67) is provided.

7º: Preferences —> General —> Display:

- Scheme: rainbow o extended rainbow

- PF axis: select the first option (Y0, X0, Z0).

8º: Toolbar —> Shortcut: click on "Subset selection" to add or remove values directly in the PF projection.

2.2.5. Tango (advanced options)

1º: Edit —> Detect Grains (or use the "Grain click" shortcut on the toolbar). For the detected grain size, indicate a "Critical misorientation = 2°" (increase to values of 10°, 20°, or 30° if you want to capture larger areas, for example, to select an area of interest and create a "subset").

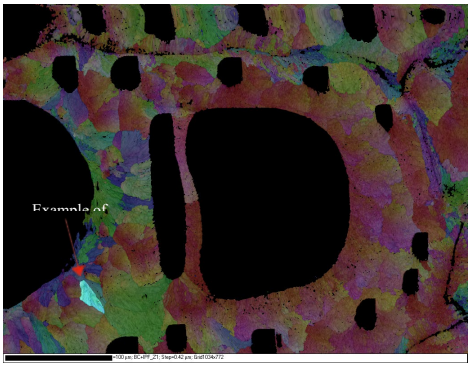

Figure 16. IPFz map screenshot showing the selected subset of a grain.

2º: Edit —> Subset Selection (or use the "Subset selection" toolbar). Select the different options to create a "new subset". Alternatively, click on a specific area, then right-click and select "into current subset —> Highlighted grain or Neighbours grain") (Fig. 16).

IMPORTANT: For the selected subset to stand out on the map:

- Tango: Preferences —> General —> Subsets —> Pixel transformation: select "Tone Down" for Anti-subset and "No transformation" for Subset.

- The map magnification must be "1x or greater". If it is 0.5x or lower, the highlighted "subset" does not appear.

3º: Select a map from any created subset and continuous as follow:

- Mambo: Preferences —> General —> Display (change color, grain size, etc...) (Fig. 17).

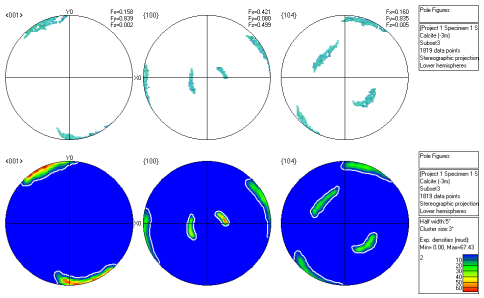

Figure 17. Pole figures and its contoured version of a selected grain.

- Project Manager —> View: obtain information from Statistics, Record Browser, Misorientation and angle distribution, 3D Crystal orientation.

4º: If you want to remove any region from the general map, select a subset and in the "Project Manager" window —> Subset tab —> "Nullify" and then "Delete".

5º: Toolbar —> Shortcut: click on "Misorientation Profile" and create a misorientation profile in the desired area. Important: select the option "Relative to the first point" (Fig. 18).

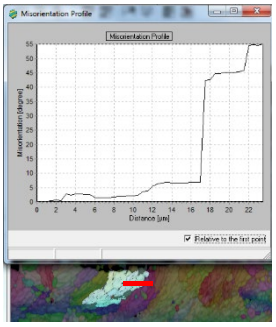

Figure 18. Misorientation profile traced along two grains.

6º: Edit —> Map properties —> Local disorientation (click on the icon to open the "properties for components" window):

- Color scheme: rainbow.

- Local Misorientation: “Filter size” (3x3) and “Subgrain angle” (5º)

2.3. Techniques

2.3.1. Micro-computed tomography (Micro-CT)

Micro-CT is a non-destructive three-dimensional imaging modality that employs X-rays to penetrate and visualize internal structures of objects, layer by layer. Micro-CT operates at a miniature scale, offering high-contrast images at a significantly enhanced resolution (e.g. limit of 0.7 μm in the equipment used).

Micro-CT works by rotating a sample and acquiring a series of x-ray projections from multiple angles. Each projection provides information about the attenuation of X-rays as they pass through the sample, revealing variations in density and composition. By reconstructing these 2D projections, a 3D volumetric image of the sample is generated. Standard Micro-CT setup includes an X-ray source, a sample stage, and a detector (Fig. 19)

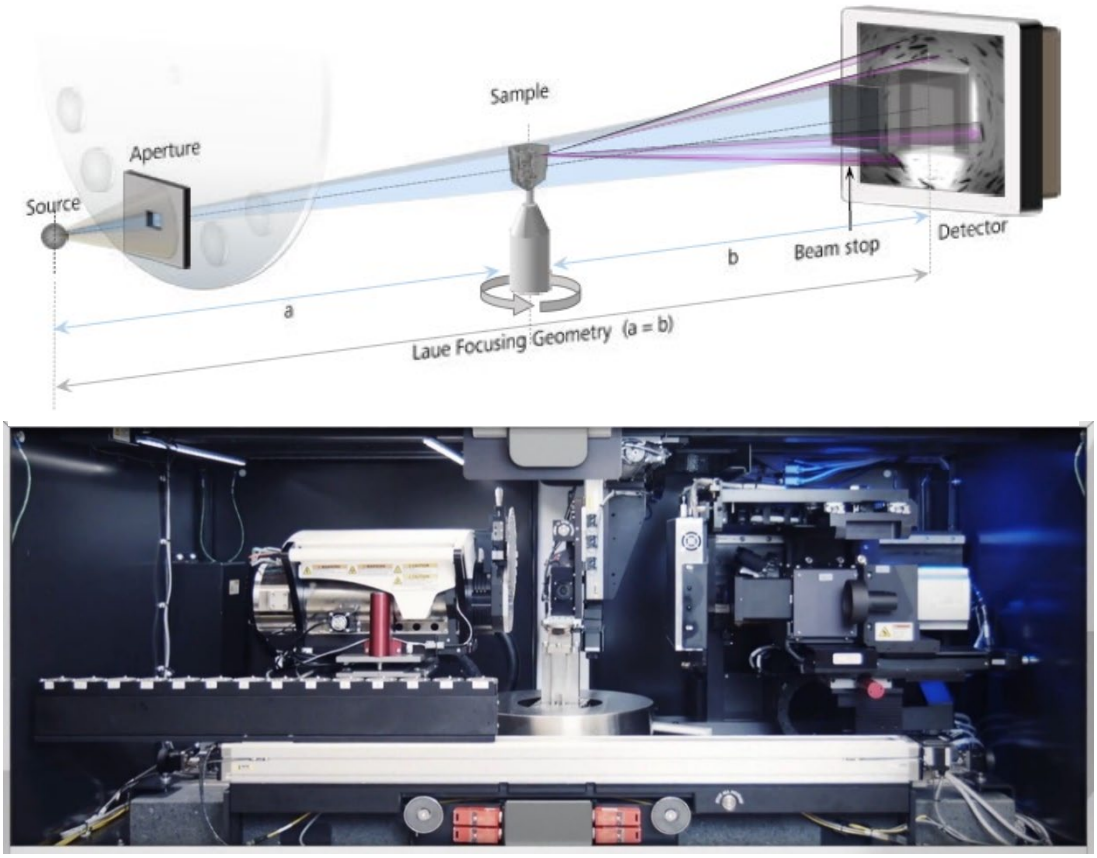

Figure 19. Principle of Micro-CT technique. The diagram above is a schematic representation of the operating module. Below, is the interior setup. From left to right: X-ray source, sample stage, and contrast-optimized detectors. https://siemindustrial.com/product/zeiss-xradia/.

With the aim of studying the complex morphology and arrangement of zooids in the different types of colonies, samples from the two main groups of bryozoans were selected for this technique. Therefore, it was not considered necessary to perform micro-CT on serpulid tube samples, whose tubular structure is less complex. The scans were performed in an X-ray microtomograph Xradia 510 VERSA Zeiss (CIC, UGR) (Fig. 20).

Figure 20. Micro-CT Xradia 510 VERSA Zeiss (CIC, UGR). https://intranet-cic.ugr.es/servicios-y-unidades/ficha.php?codServicio=6&unidad=103.

2.3.2. Scanning Electron Microscopy (SEM)

The SEM is a powerful technique used for imaging the surface morphology and composition of materials at high resolution. It operates on the principle of scanning a focused electron beam across the sample surface and detecting various signals generated by interactions between the electron beam and the atoms in the sample (Fig. 21). For instance, in these interactions, several signals are emitted, including secondary electrons (SE), backscattered electrons (BSE), and characteristic X-rays (Fig. 22).

The electron source typically consists of a tungsten filament or a field emission gun (Fig. 23). Electromagnetic lenses are used for focusing the electron beam. A scanning system is in charge of moving the beam across the sample. Finally, detectors are placed to capture the emitted signals from the sample, all placed in a vacuum chamber to prevent electron scattering by air molecules.

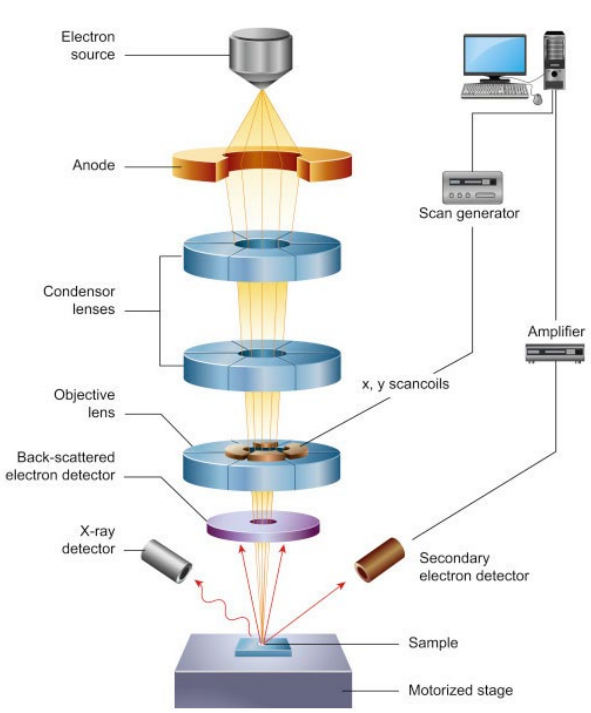

Figure 21. Schematic principles of a SEM. DOI: http://doi.org/10.5772/intechopen.91438.

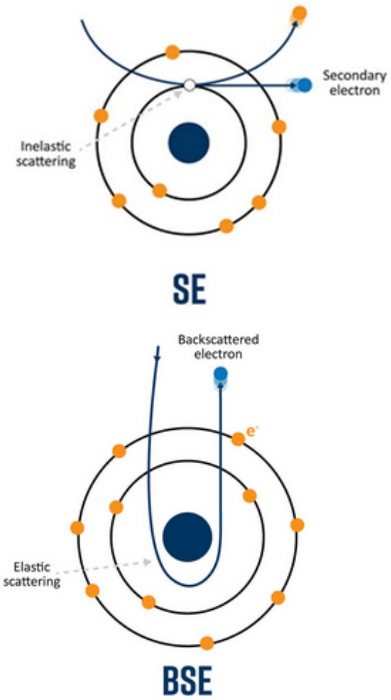

Figure 22. Diagram of the principles of secondary electrons and backscattered electrons. https://www.nanoscience.com/blogs/which-electron-detector-is-right-for-your-application/.

There are two principal imaging modes and one associated technique:

- Secondary Electron (SE): provides topography information by detecting low-energy electrons emitted from the sample surface.
- Backscattered Electron (BSE): offers compositional contrast, where the intensity of backscattered electron correlates with the atomic number of the elements in the samples.
- Energy-Dispersive X-ray Spectroscopy (EDS): provide information about elemental composition and quantification of a sample by detecting X-ray

Figure 23. Tungsten filament. https://www.deltamicroscopies.com/.

(characteristic for each element) emitted from the sample when it is bombarded with the electron beam in the SEM.

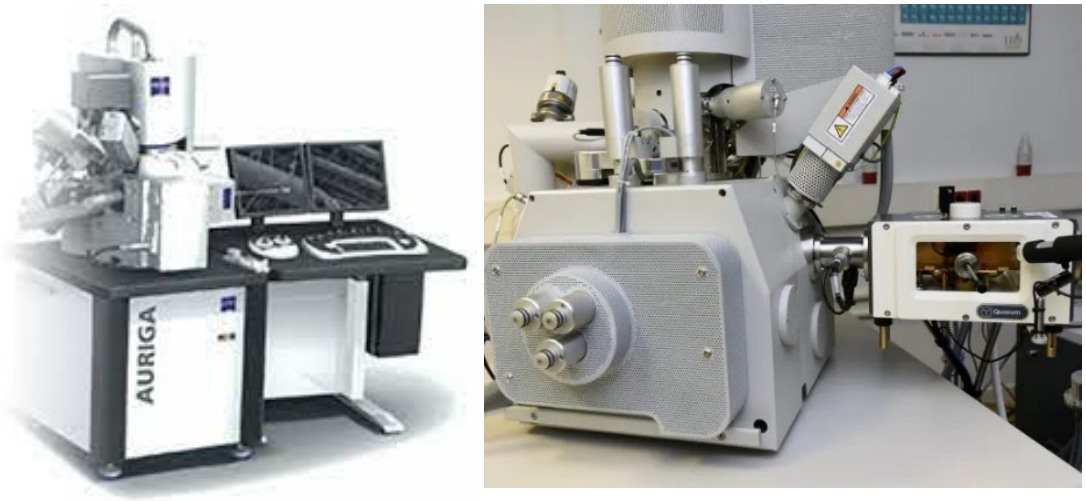

Figure 24. Carl Zeiss AURIGA (FIB-FESEM) work station (left) and SEM FEI Quanta 400 (right). https://cic.ugr.es/servicios/servicios-unidades#contenido7

2.3.3. Electron backscattered diffraction (EBSD)

EBSD is a powerful technique used for analyzing the crystallography structure, orientation, and microstructure of crystalline materials at the micrometer to nanometer scale. It operates on the principle of detecting electrons backscattered from a sample surface and analyzing the diffraction patterns (known as "Kikuchi bands") (Fig. 25) produced by interactions between the incident electron beam and the crystal lattice. These diffraction patterns contain information about the crystal orientation, phase, grain size, grain boundaries, and other microstructural features of the material (Fig. 26). To perform the technique, the SEM has to be equipped with an EBSD detector. It consists of a phosphor screen coupled with a charge-coupled device (CCD) camera, which captures the diffraction patterns formed by the backscattered electrons. To obtain the best diffraction patterns, the sample has to be tilted at

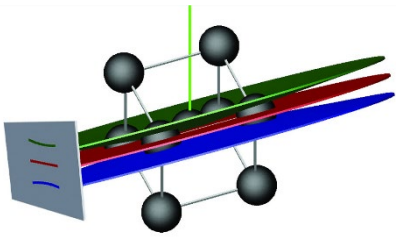

Figure 25. Diagram of the formation of a Kikuchi band in an electron backscattered diffraction pattern. https://www.ebsd.com/ebsd-explained/pattern-formation .

an angle of 70º and at a predetermined distance to the electron beam and the EBSD detector (Fig. 27).

Information obtained from EBSD diffraction measurements was processed by CHANNEL 5 HKL software (as explained in section 2.3). The results are presented as band contrast measurement images and as Inverse Pole Figure (IPF) maps. White or dark regions in the band contrast maps correspond to higher or weaker signal strengths, respectively, of the EBSD Kikuchi diffraction patterns. The IPF maps are color-coded crystal orientation images, where similar colors indicate similar orientations. The term "texture" relates to the orientation of the crystallographic axes within a material. The texture is represented by the pole figures (PFs) corresponding to each EBSD map. The PFs are presented either as individual data points or, in the contoured version, as the densities of poles. In the latter case, we use the lowest possible degree for half-width (5°) and cluster size (3°). The half-width controls the extent of the spread of the poles over the surface of the project sphere. A cluster comprises data with the same orientation. We also provide the Multiple of Uniform Distribution (MUD) values. Low MUD values point to random orientation or low crystal co-orientation, while a high MUD value indicates high crystal co-orientation. Very high values (MUD> 700) indicate a single-crystal nature.

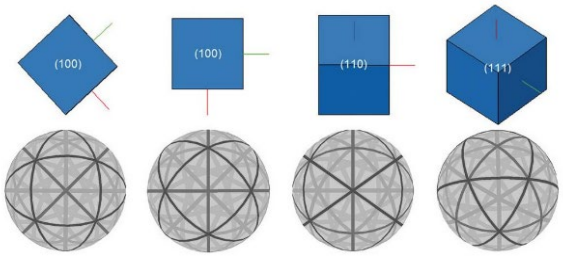

Figure 26. Schemes of spherical diffraction patterns generated by different orientations of a cubic structure. https://www.ebsd.com/ebsd-explained/interpreting-the-diffraction-pattern.

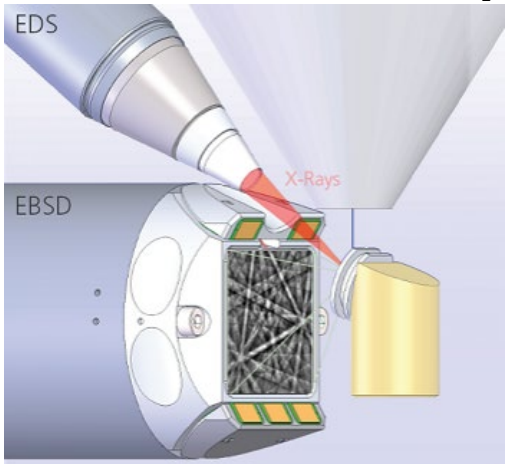

Figure 27. Diagram of the operating of EBSD technique, showing the tilted sample and the EBSP projected onto a phosphor screen at the end of the EBSD detector https://www.ebsd.com/how-does-ebsd-work.

2.3.4. Transmission-electron backscatter diffraction t-EBSD (t-EBSD) and Focused Ion Beam (FIB)

Transmission Kikuchi Diffraction (TKD) technique, also known as transmission-electron backscatter diffraction (t-EBSD), operates on the same principle of electron diffraction (as explained in section 2.4.3). But now, the electron beam is transmitted through a thin sample. The sample must be prepared using FIB technique as a thin foil with a thickness on the order of tens to hundreds of nanometers to allow for electron transmission. FIB is an advanced nanofabrication and characterization technique that operates on the principle of directing a focused ion beam of ions, typically gallium ions (Ga^+) onto the sample surface. The high-energy ions interact with the sample, causing various effects such as sputtering, milling, deposition, and imaging. By controlling the beam intensity and scanning patterns, FIB can selectively remove material, fabricate nanostructures, or analyze samples with high spatial resolution (Fig. 28).

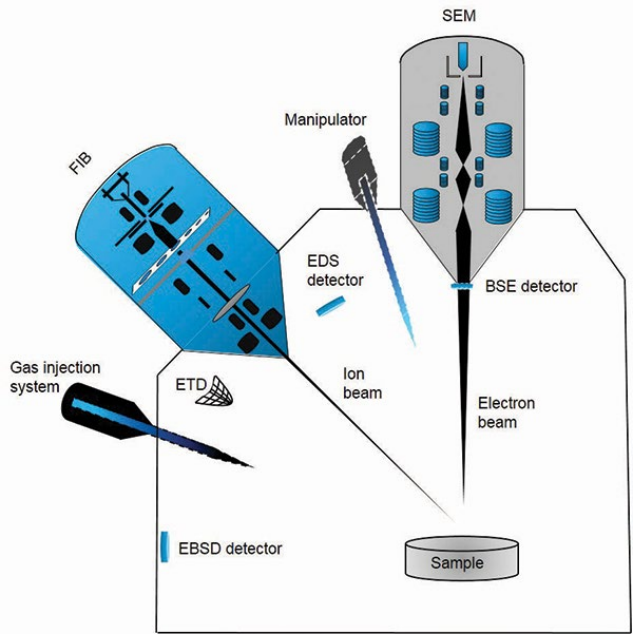

Figure 28. Schematic diagram of a typical FIB-SEM setup. It combines a SEM and a FIB single device, often equipped with multiple detectors (ETD, BSE, EDS, EBSD). Gas injection systems as well as manipulators are also commonly included in the same equipment.
https://analyticalscience.wiley.com/content/article-do/focused-ion-beams-overview-technology-and-its-capabilities.

2.3.5. Atomic Force Microscope (AFM)

AFM is a high-resolution imaging and characterization technique used in various scientific and engineering fields to investigate surface topography, mechanical properties, and interactions at the nanometer scale. AFM operates by scanning a sharp probe tip, located at the end of a cantilever, over the sample surface. The tip interacts detecting interaction forces, such as van der Waals, electrostatic, and chemical bonding forces (Fig. 29).

These interactions cause the cantilever to deflect, and the deflection is measured by a laser providing information about the sample's topography and mechanical properties (Fig. 30). Finally, a feedback system controls the tip-sample interaction forces.

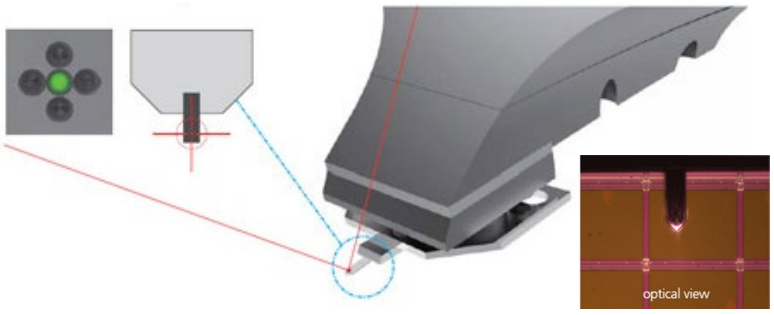

Figure 30. AFM cantilever. A laser measures the cantilever deflection. https://m.parksystems.com/.

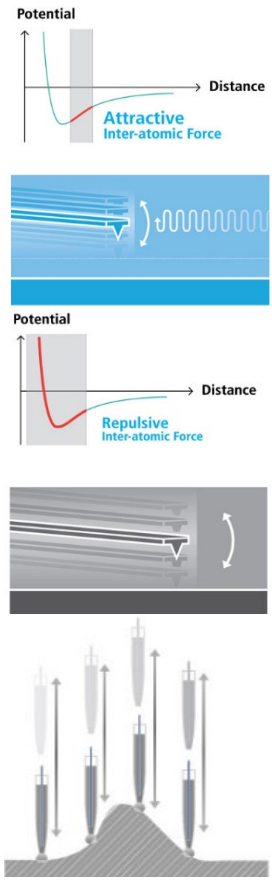

Figure 29. AFM tip probe interacts with the sample surface, experiencing attraction or repulsion forces. https://m.parksystems.com/.

2.3.6. Fourier Transform Infrared Spectroscopy (FTIR)

FTIR spectroscopy is a useful, non-destructive analytical technique used to identify chemical bonds and functional groups in a wide variety of materials. FTIR spectroscopy measures the absorption of infrared radiation at specific frequencies corresponding to the vibrational modes of their chemical bonds, providing valuable information about its molecular composition and structure. The sample's absorption spectrum is obtained by Fourier transforming the measured interferogram, which is plotted as absorbance versus wavenumber (Fig. 31).

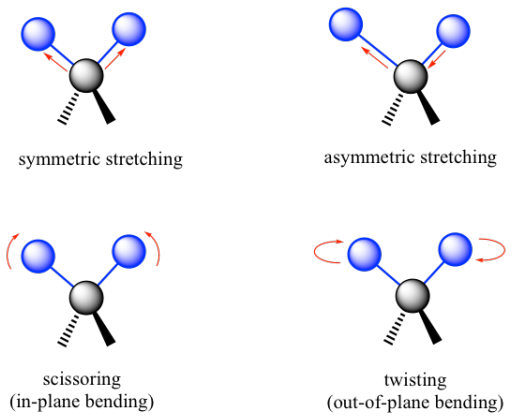

Figure 31. Vibration modes of molecules bonds: stretching, scissoring and twisting. https://kpu.pressbooks.pub/organicchemistry/chapter/6-2-infrared-ir-spectroscopy/.

The technique is conducted by an FTIR spectrometer, which emits a broadband infrared light source (Fig. 32). In this Ph.D., an Attenuated Total Reflection (ATR) module has been used to accommodate the samples. The ATR consists of a platform that contains a flat surface called IRE (Internal Reflection Element). The surface is typically made of a high-refractive-index material (e.g., diamond, as used in this Ph.D.). The sample is brought into contact with the IRE surface, and infrared light is directed through the IRE at an angle greater than the critical angle for total internal reflection. As the infrared light interacts with the sample at the IRE surface, it undergoes multiple reflections, resulting in an evanescent wave that penetrates a few micrometers (Fig. 33).

Figure 32. Infrared spectrometer. https://www.jasco-global.com/solutions/high-sensitivity-atr-unit-for-ftir-spectroscopy/.

Finally, The interferometer modulates the infrared light, producing an interferogram that contains information about the sample's absorption spectrum, which is Fourier transformed to yield the sample's infrared absorption spectrum to identify chemical bonds and functional groups.

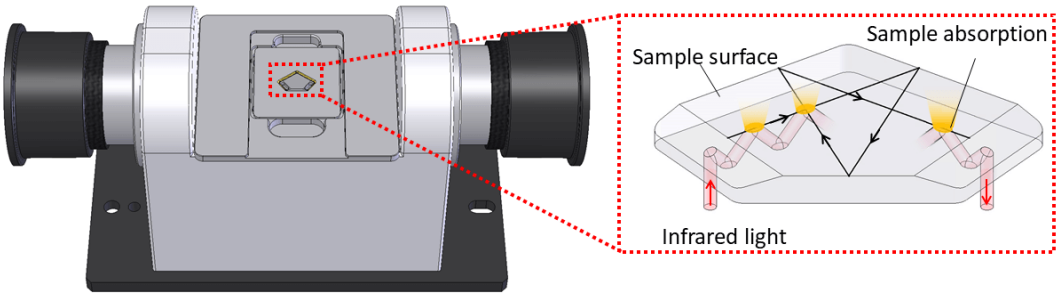

Figure 33. Schematic diagram of an ATR module, showing the reflections of the infrared light on the IRE surface. https://www.jasco-global.com/solutions/high-sensitivity-atr-unit-for-ftir-spectroscopy/.

2.3.7. RAMAN Spectroscopy

RAMAN spectroscopy, similarly to FTIR spectroscopy, is a non-destructive, analytical technique used to provide information about molecular vibrations, rotational modes, and other low-frequency excitations within a sample. It is based on the inelastic scattering of monochromatic light (usually laser light) by molecules of a sample. When a photon interacts with a molecule, most of the scattered light retains the same energy (Rayleigh scattering). However, a small fraction undergoes energy exchange with the molecules, resulting in a frequency

Figure 34. RAMAN spectroscopy setup, equipped with an optical microscope. https://cic.ugr.es/servicios/servicios-unidades/analisis-y-determinacion-estructuras/espectroscopia-microraman-y-ftir.

shift known as the RAMAN shift. This shift corresponds to the energy gained or lost by the molecule due to changes in its vibrational or rotational modes, constituting unique signatures of each functional group.

RAMAN spectroscopy setup consists of a laser light source (commonly in the visible or near-infrared range) fitted to an optical microscope. Then, a monochromator or filter is used to select the desired wavelength. Finally, a detector (often a charge-coupled device or CCD) captures the Raman-scattered light, which is analyzed to generate a RAMAN spectrum (Fig. 34).

2.3.8. X-ray Diffraction (XRD)

XRD is a widely used analytical technique for determining the crystallographic structure, phase composition, and preferred orientation of crystalline materials. XRD relies on the principle of X-ray diffraction by the atomic planes of a crystalline material. The diffraction follows Bragg's law, which describes the relationship between the angle of incidence, the wavelength of X-rays, and the spacing between crystallographic planes. The reflected rays undergo constructive interference when the distance between adjacent crystal planes is equal to an integer multiple of the X-ray wavelength. This results in the scattering of X-rays in specific directions which produces characteristic peaks in the X-ray diffraction pattern (Fig. 35).

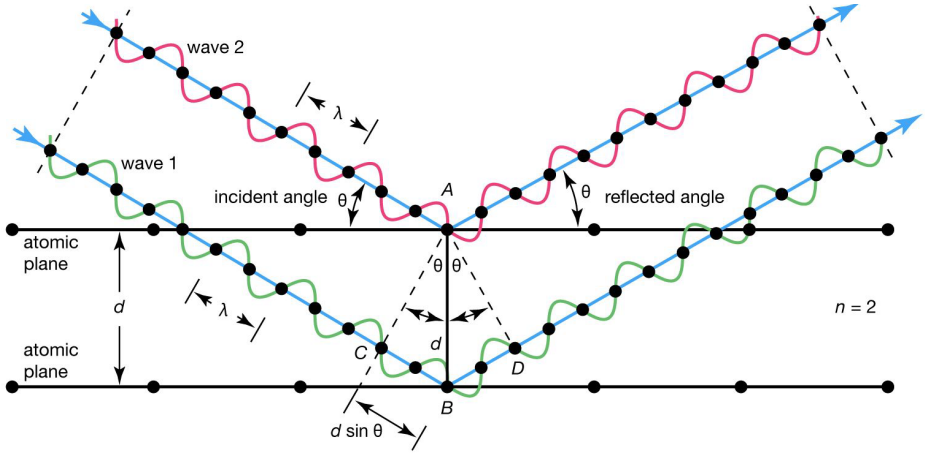

Figure 35. Scheme of the basic principles of X-ray diffraction and Bragg's Law. https://doi.org/10.1007/978-981-19-1562-8_2.

The technique is carried out in an X-ray diffractometer, which consists of an X-ray source, a sample holder, an X-ray detector, and a goniometer for rotating the sample (Fig. 36). By rotating the sample and measuring the intensity of diffracted X-rays at different angles, a complete X-ray diffraction pattern is obtained.

Figure 36. X'pert Pro θ-θ system in reflection Bragg-Brentano geometry for powder measurements. Petrology and Mineralogy Department, Facultad de Ciencias, UGR.

2.3.9. Thermogravimentric Analysis (TGA)

TGA is a thermal analysis technique used to characterize the thermal stability, composition, and mass changes of materials as a function of temperature or time. It monitors the weight change of a sample as it is heated or cooled under controlled conditions. The temperature varies at a constant rate, in an inert or oxidative atmosphere, while weight is continously recorder in a high sensitive balance. Changes in sample weight result from processes such as decomposition, desorption, oxidation, phase transitions, and chemical reactions occurring within the sample. TGA instruments may include additional features such as gas flow controllers, mass spectrometers, and differential scanning calorimetry (DSC) modules for simultaneous analysis.

Figure 37. Thermic analyser instrument. https://www.mt.com/es/es/home/products/Laboratory_Analytics_Browse/TA_Family_Browse/ta-instruments/thermal-analysis-system-TGA-DSC-3-plus.html.

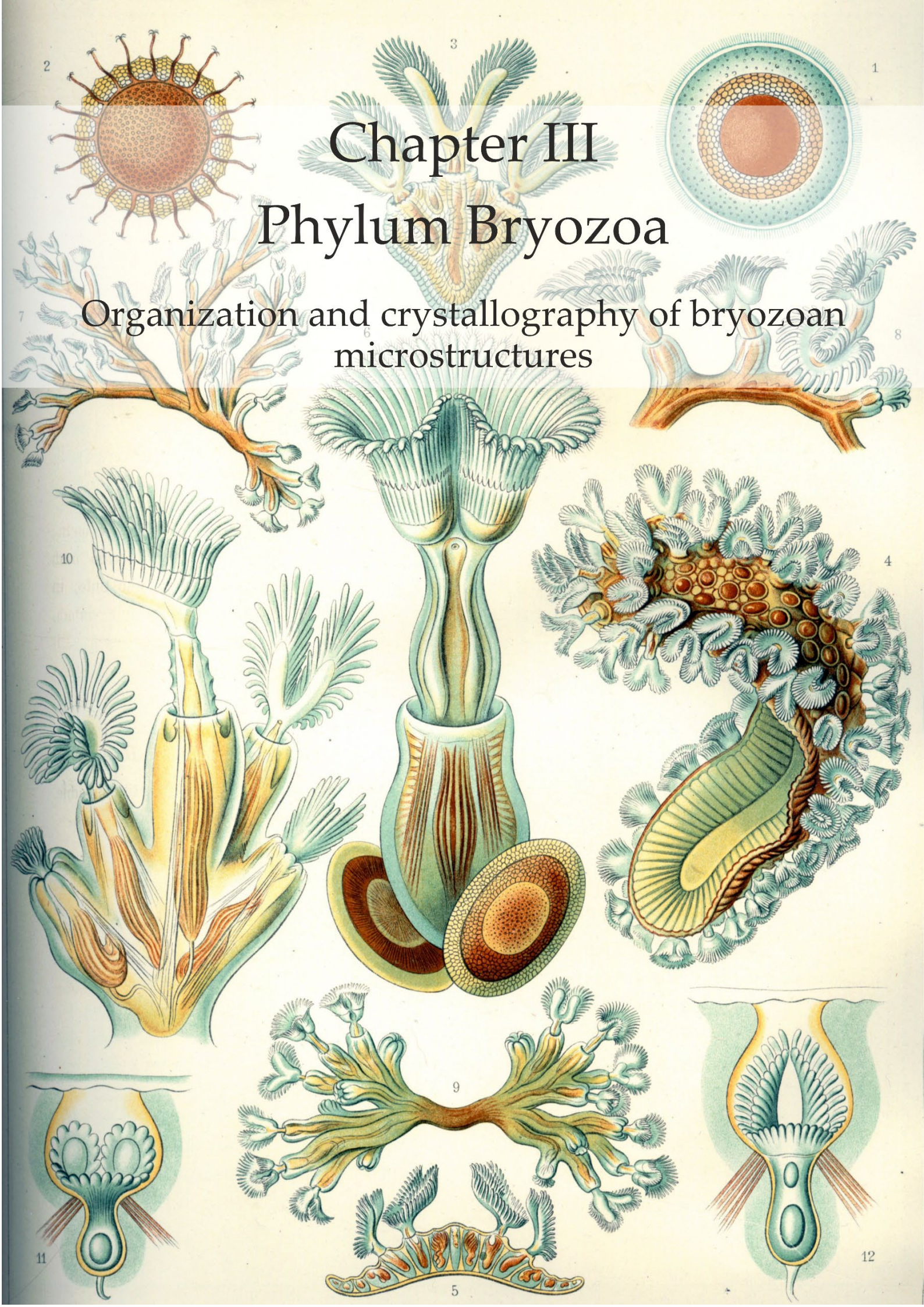

Chapter III
Phylum Bryozoa

Organization and crystallography of bryozoan microstructures

PART 1

Class Stenolaemata

Microstructure and crystallographic characteristics of stenolaemate bryozoans

Microstructure and crystallographic characteristics of stenolaemate bryozoans (Phylum Bryozoa, Class Stenolaemata)

Christian Grenier[1], Erika Griesshaber[3], Wolfgang Schmahl[3], Antonio G. Checa[1,2]*

[1]Departamento de Estratigrafía y Paleontología, Universidad de Granada, 18002 Granada, Spain

[2]Instituto Andaluz de Ciencias de la Tierra, CSIC-Universidad de Granada, 18100 Armilla, Spain

[3]Department of Earth and Environmental Sciences, Ludwig-Maximilians Universität, 80333 Munich, Germany

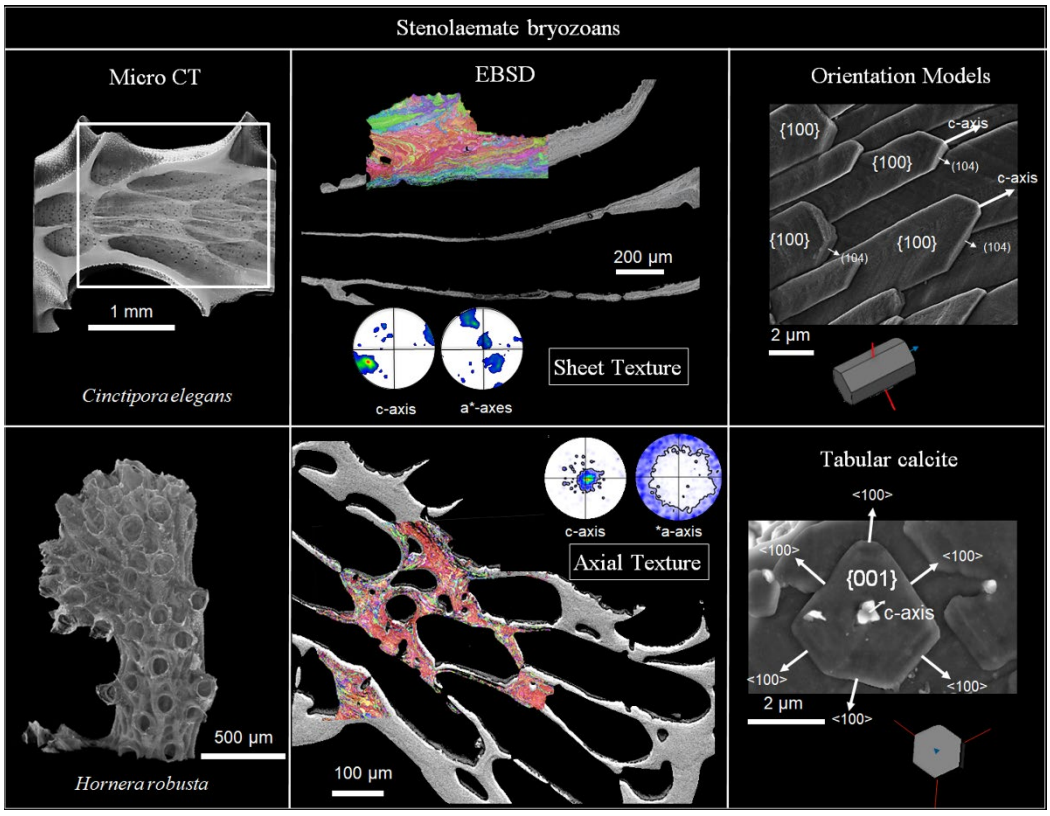

Submitted: 11/10/2022
Accepted: 29/12/2022
Published online: 9/01/2023

ABSTRACT

The bryozoan Cass Stenolaemata is currently represented by the Order Cyclostomata. They produce skeletons made exclusively of calcite crystals assembled into different microstructures. Despite extensive previous research, no appropriate crystallographic techniques have been applied to decipher their crystallographic organization. We present an in-depth crystallographic study of the microstructures of three extant species (*Fasciculipora ramosa*, *Hornera robusta*, and *Cinctipora elegans*) using scanning electron microscopy and associated techniques (energy-dispersive spectroscopy and electron backscatter diffraction), together with atomic force microscopy and micro-computed tomography. We differentiate two microstructures, foliated and tabular calcite, and establish consistent models of their crystallography. Foliated calcite of *F. ramosa* and *C. elegans* consists of co-oriented laths arranged with their *c*-axes parallel to their elongation axis and to their main surfaces, and one *a**-axis perpendicular to the latter (sheet texture). Tabular calcite of *H. robusta* consists of polygonal tablets with the *c*-axis as fiber axis (axial texture), perpendicular to the tablet surface. The foliated calcite of bryozoans is homeomorph to that of bivalves but has a significantly different crystallography. The tabular calcite of bryozoans lacks the spiral morphology of the tablet-shaped calcite of craniiformis brachiopods and has a different orientation of the *c*-axis with respect to the constituent tablets.

1. Introduction

In the last decades, numerous studies based on SEM imaging have described different types of microstructures in both fossil and recent genera of stenolaemate bryozoans. These authors highlighted the widespread presence of **granular**, **laminar**, or **tabular** fabrics. They established primary, secondary, and even tertiary layers based on their chronological secretion sequence (from earliest to latest, respectively) by the secretory epithelium (Fig. 1). A summary of the foremost studies conducted in the last decades is presented below.

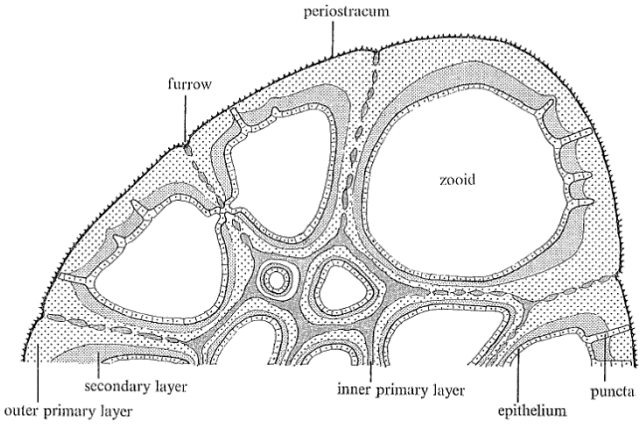

Figure 1. Cross-section of tubular-shaped zooid chambers of a cyclostome bryozoan (*Entalophora*) colony. The locations of the successive primary and secondary layers are depicted (from Tavener-Smith 1972).

Söderqvist (1968) was the first to image the microstructure of cyclostome bryozoans with SEM and noted the presence of two calcite layers: a thin **outer prismatic** layer and a thicker **inner lamellar** layer. In the same year, Boardman and Cheetham (1968) reviewed, from both thin sections and SEM imaging, the colony structure, the zooid arrangement, and the skeletal fabrics of bryozoans. They confirmed the existence of **laminated lath-like fibers** in "tubular" (i.e., stenolaemate) bryozoans. Later, Tavener-Smith and Williams (1972) studied the

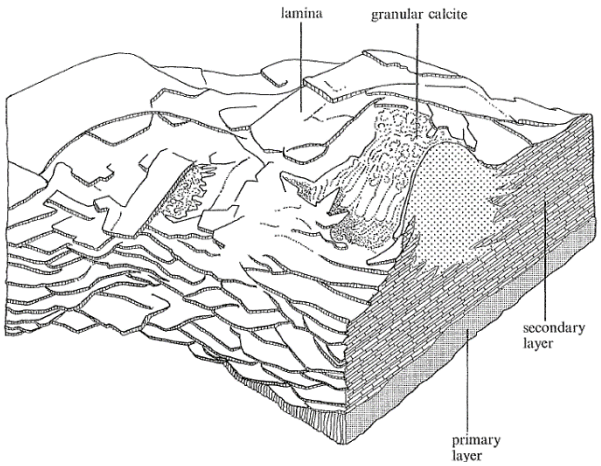

Figure 2. Diagram showing the distribution and morphology of the primary and secondary layers in the cyclostome bryozoan *Lichenopora* (from Tavener-Smith 1972).

walls of cyclostome (i.e., stenolaemate) genera of different extant and fossil species, determining that they are generally constituted of a **primary (outer) granular calcite** layer succeeded by a s**econdary (inner) laminated layer** (Figs. 1 and 2). Brood (1976), in trying to use the skeletal structures (constituting single or double walls) as a new character in phylogeny, reported three different layers in the walls cross-sections of the order Cyclostomatida: a **primary granular layer** bounded by two **secondary laminar layers** on both sides (Fig. 3). More recently, Boardman et al. (1992) described the shell ultrastructure of their new stenolaemate family Cinctiporidae, demonstrating the presence of an inner layer of **transverse fibrous crystallites** covered by a l**aminated layer made of lath-like crystals**. Later, Taylor and Jones (1993) described the microstructure of *Hornera robusta* as made up of **polygonal tablets**. Finally, in a complete review of the skeletal ultrastructure of the Cyclostomata, Taylor and Weedon (2000) summarized a total of six fundamental ultrastructural fabrics based on SEM images of 87 different species: **granular**, **planar spherulitic**, **transverse fibrous**, **foliated**, **rhombic semi-nacreous** and **hexagonal semi-nacreous** (according to their terminology, see Fig. 4).

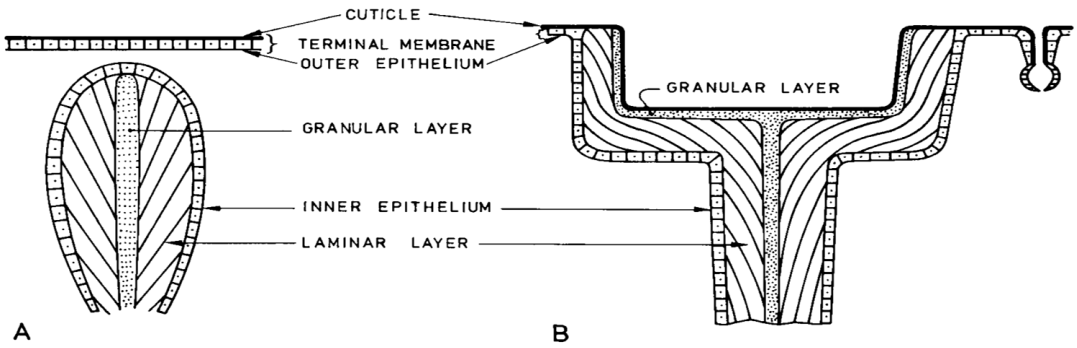

Figure 3. Diagram showing two examples of interzooidal walls at different stages. The primary granular layer and the secondary laminar layer are depicted. A. The growing edge of an invagination of the secretory epithelium, creating a new inner wall. B. Already formed inner wall. From Brood 1976.

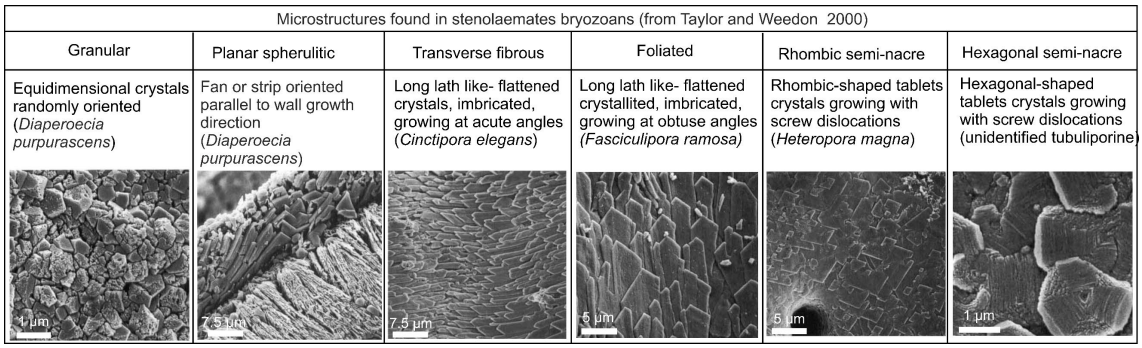

Figure 4. Summary table of the six different microstructures described by Taylor and Weedon (2000) in stenolaemate bryozoans.

Although Carter and Clark (1985) had previously used the term "Semi-nacre calcite" to name the rhombic and hexagonal platelets in bryozoans, this "calcitic semi-nacre" term was first described in craniid brachiopods to refer to "calcitic laminae that grow spirally from single or double screw dislocations" (Williams 1970; Williams and Wright 1970). However, Simonet Roda et al. (2022) disregarded the term "semi-nacre" because of their lack of affinity with nacre (mineralogically, microstructurally, and crystallographically) and considered this microstructure as being formed by tablet-shaped calcitic elements. Following Simonet Roda et al. (2022), we will adopt the term **tabular calcite** for the "semi-nacre" of bryozoans from here on.

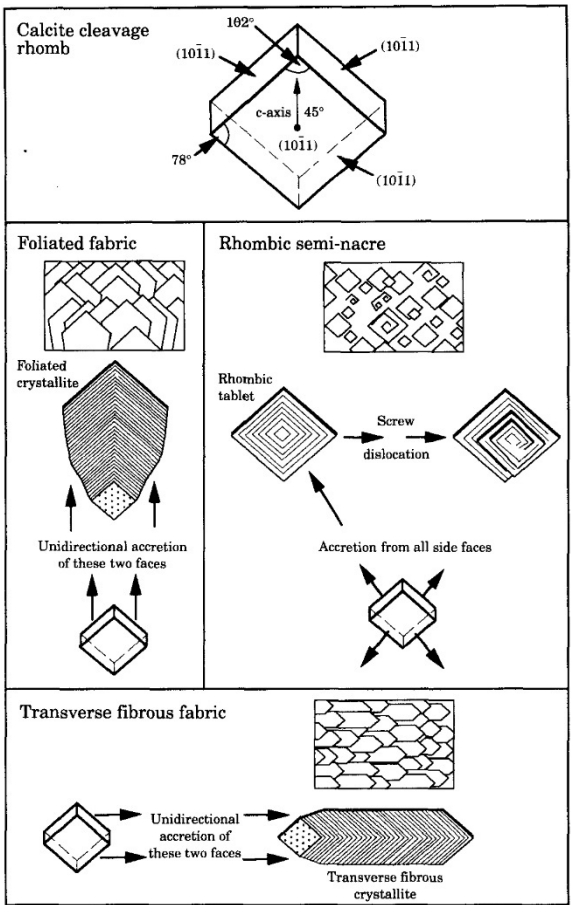

Figure 5. Diagram of the crystallography and growth by accretion of the calcite cleavage rhomb of the foliated, the transverse fibrous, and the rhombic semi-nacre fabrics by Taylor and Weedon (2000). The c-axis is at 45º to the surface and the main crystal's faces correspond to {104}.

Previous studies have described bryozoan microstructures in detail based on SEM images, but very few have provided crystallographic data on the prevailing crystal orientations. Based on SEM images, Taylor and Weedon (2000) suggested that the laths of the foliated fabric had a main external surface of the {104} type ({10$\bar{1}$1} in their notation), and the c-axis was inclined by 45° in the direction of elongation (growth) of the laths. The elongation proceeded by accretion of the {104} faces looking in that direction. They differentiated a second variety, their transverse microstructure, which was made by laths growing along a direction perpendicular to that of the foliated microstructure (Fig. 5).

In their "rhombic semi-nacre" (tabular microstructure), the tablets also had the same distribution of crystallographic axes but they grew at their periphery in all directions.

Additionally, they explained the hexagonal variety of semi-nacre as platy crystals growing at their periphery, where the c-axis is perpendicular to the top surface, which would then be a {001} surface, with oblique {104} lateral faces (Fig. 6).

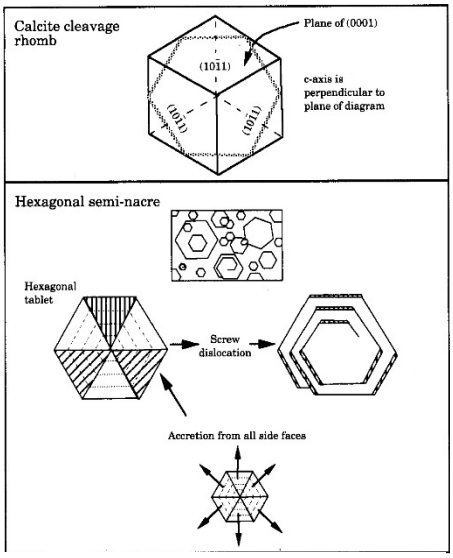

Figure 6. Diagram of the crystallography and growth by accretion of the calcite cleavage rhomb of the hexagonal semi-nacre fabric according to Taylor and Weedon (2000). The c-axis is perpendicular to the surface and the main crystal's face corresponds to {001}.

To date, only two studies based on the electron backscatter diffraction (EBSD) technique have provided crystallography data. Batson et al. (2021) and Negrini et al. (2022) examined the "laminated calcite" (i.e. **tabular calcite**) of the cyclostome bryozoans *Hornera currieae* and *Hornera robusta*, concluding, in line with the interpretation of the "hexagonal semi-nacre" by Taylor and Weedon (2000), that the c-axes were oriented perpendicular to the

skeletal walls, whereas the a*-axes were randomly oriented "laying predominantly in the plane of the wall" (Fig. 7).

Contrary to other groups of biomineralizers such as corals, mollusks, and brachiopods, where numerous and complete crystallographic studies of their microstructures have been carried out (Checa et al. 2021; Crippa et al. 2020; Simonet Roda et al. 2022; yin et al. 2021), there is still much to learn about in bryozoans. Accordingly, we decided to conduct a thorough study of the distribution and crystallography of the microstructures of the two main groups of bryozoans: cheilostomes and cyclostomes.

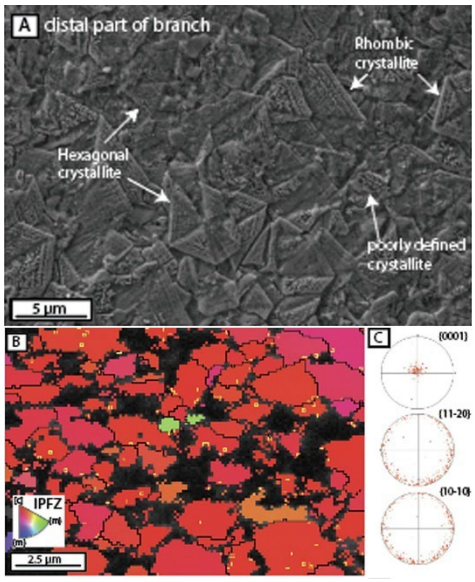

Figure 7. Crystallography data of the "laminate calcite" (i.e. tabular calcite) microstructure of *Hornera currieae* (adapted from Negrini et al. 2022). A. SEM image of the tabular calcite displaying rhombic and hexagonal shape. B. IPFz map showing the c-axis perpendicular to the surface.

In this study, we provide new crystallographic data for three cyclostome species: *Fasciculipora ramosa*, *Hornera robusta*, and *Cinctipora elegans*. We studied their microstructures using SEM imaging, energy dispersive spectroscopy (EDS), and EBSD. Additional data were obtained with atomic force microscopy (AFM) and micro-computed tomography (Micro-CT). For the first time, we provide **specific modes of crystal orientations** for the foliated and tabular calcite and compare their similarities and differences with homeomorphic microstructures of other phyla.

2. Materials and methods

2.1. Material

We analyzed three different species of Stenolaemata, order Cyclostomatida: *Fasciculipora ramosa* (d'Orbigny, 1842), *Hornera robusta* (MacGillivray, 1883), and *Cinctipora elegans* (Hutton, 1873). Fragments of colonies were obtained from the palaeontological and zoological reference collections of the Natural History Museum (London).

2.2. Micro-computed tomography (Micro-CT)

Fragments of colonies from both *Cinctipora elegans* and *Hornera robusta* were selected for micro-CT analyses. The fragments were fixed to the tip of a needle holder with glue. The measurements were performed in an X-ray microtomograph Xradia 510 VERSA ZEISS (CIC, UGR) with a maximum resolution of 0.7 μm. The established parameters were as follows: 60 kV acceleration voltage, 4 W power, and 4x magnification objective. The binning used was "bin 1" for the CDD camera detector, with a voxel size of 0.9951 μm. The distance from the source to the sample was 25 mm and the distance from the detector to the sample was 60 mm. The exposure time (per projection) and the source filter were adjusted at 30 seconds and a LE1 filter for both *C. elegans* and H. *robusta* samples. The total number of projections was 3201. For center shift and beam hardening effect corrections, images were processed using Reconstructor Scout and Scan™ (Zeiss, Oberkochen, Germany). We used 3D image analysis Dragonfly Pro™ (Object Research System, slice registration method SSD) for advanced post-processing.

2.3. Scanning Electron Microscopy (SEM)

Fragments of the three stenolaemate species studied were prepared for SEM observation as explained in section 2.1. Once the fragments were cleaned and

oven-dried, some of them were directly selected for observation, whereas others were embedded in epoxy resin. Once the resin solidified, the samples were sanded and polished in serial steps until reaching a mirror surface (Hi-Tech Diamond polishing machine, All-U-Need model). Some samples, both polished and unpolished, were immersed in an etching and decalcifying solution (2.5% glutaraldehyde, 0.25 M HEPES buffer, and 0.05 M EDTA) for 2-5 min in an orbital shaker. SEM observations were performed after carbon coating (Emitech K975X carbon evaporator) using Secondary Electron (SE) and Back Scatter Electron (BSE) detectors in a field emission SEM FEI QemScan 650 F (Centro de Instrumentación Científica, CIC, University of Granada, UGR).

2.4. Atomic Force Microscope (AFM)

Two colony fragments of *Fasciculipora ramosa* and *Hornera robusta* were cleaned by immersion in commercial bleach (~5%, 1h) and subsequently reduced to small fragments oriented so that the inner chamber surfaces were exposed. For imaging, an AFM Park Systems NX20 equipped with a cantilever MikroMasch ACTA (K = 40 N/m, F = 320 kHz) (CIC, UGR) was used in Tapping and PinPoint modes to record height, amplitude, and phase signals. Images were obtained with Smart Scan v12 and processed using XEI software (4.3.0. Build2, Park Systems).

2.5. Electron Backscattered Diffraction (EBSD)

Shell samples were embedded in epoxy resin, sectioned, and subjected to several sequential mechanical grinding and polishing steps (as explained in section 2.1). For EBSD analysis, the samples were coated with 4 to 6 nm of carbon (Leica EM ACE200). Measurements were taken on a Hitachi SU5000 field emission SEM, equipped with an Oxford Instruments NordlysNano II EBSD detector. The SEM was operated at 20 kV, and Kikuchi patterns were indexed with the CHANNEL

5 HKL software. EBSD measurements were performed in step increments between 200 and 500 nm.

3. Results

3.1. Colony structure and zooid arrangement

The colony of *Cinctipora elegans* (Fig. 8) presents a cylindrical erect morphology. In the fragment analyzed, two levels of concentrically disposed zooids can be observed (Fig. 8A). In the inner central region, we can see smaller, disordered chambers of different sizes that may correspond to enclosed dormant autozooids (kenozooids) (Fig. 8A). In the longitudinal section (Fig. 8B), the autozooids have a conical tubular shape, which is significantly wider at the aperture. The zooids are connected to each other through interzooidal pores, which are more abundant toward their central region. The interzooidal walls, which separate two generations of autozooids, are interconnected by special pores called hypostegal pores (white arrows, Fig. 8B). 3D reconstruction reveals the inner volumes of the zooids, the hypostegal pores, and the funicular system (white arrows) (Fig. 8C).

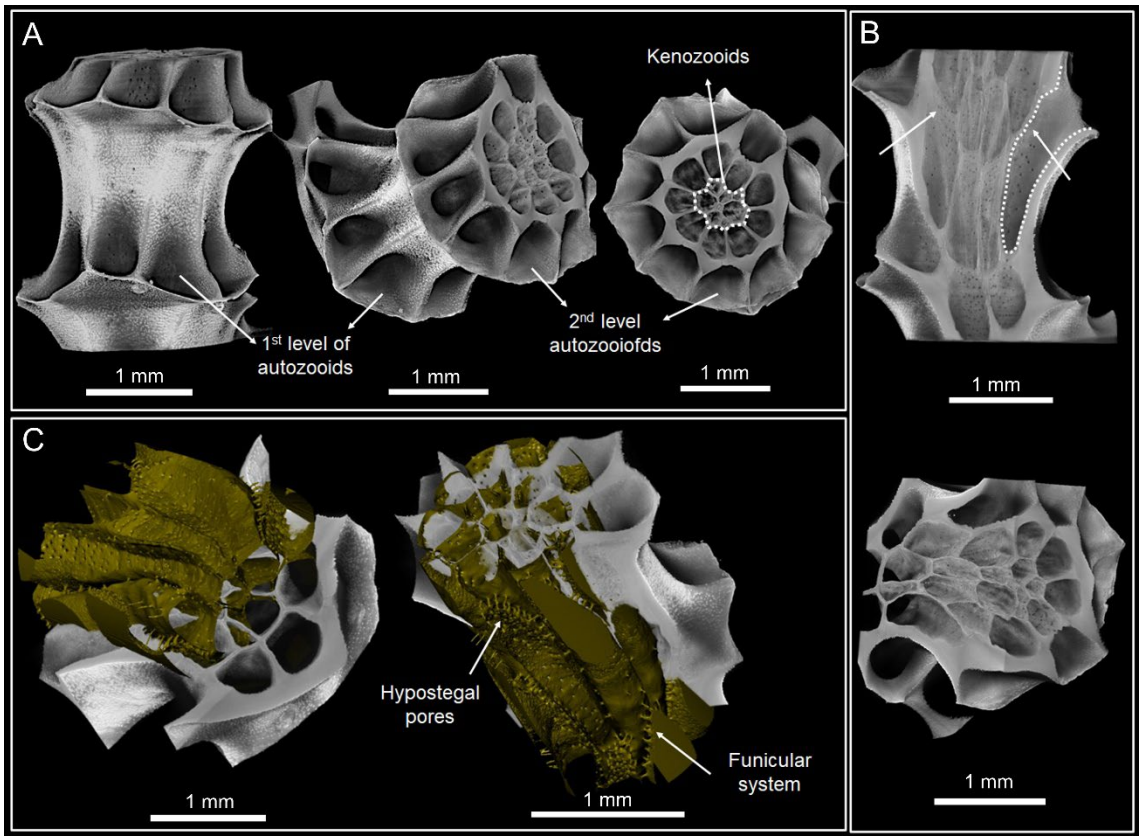

Figure 8. Micro CT images from *Cinctipora elegans.* A. From left to right: frontal, oblique and zenithal views of the cylindrical colony fragment analyzed. Concentrically disposed 1st and 2nd level autozooids (indicated) can be observed. In the central region, the structural kenozooids are delimited with white dashed lines. B. Longitudinal (top) and oblique (bottom) views of the colony. The conical-tubular-shaped zooid chambers (wider at the aperture) are concentrically arranged. They are connected to each other through interzooidal pores, which are more numerous towards the kenozooids. Interzooidal walls (indicated with white arrows) separate two generations of autozooids that remain connected by the hypostegal pores. C. Oblique views of a longitudinal section of the colony. The reconstructed interior volumes of the zooid chambers are interconnected by channels (funicular system). The hypostegal pores, through which budding growth proceeds, are indicated.

The zooids of *Hornera robusta* build branched erect colonies, arranged in a fan-like manner. The free-walled zooids present long tubular chambers, slightly widening toward the aperture (Fig. 9). The branch has an abfrontal (posterior) part from which the lateral autozooids bud and grow (Fig. 9A). Autozooids curve towards their frontal part. The boundaries between adjacent zooids and the skeleton (shown with cyan and gold colours in Fig. 9B) can be distinguished. The communicative channels (funicular system, shown in Fig. 9C) connect two adjacent zooids along the entire length of the chamber. New generations of autozooids grow through parental budding (dashed circles, Fig. 9C). They are

separated by the interzooidal walls, but are, however, connected through the hypostegal pores (white arrows, Fig. 9C).

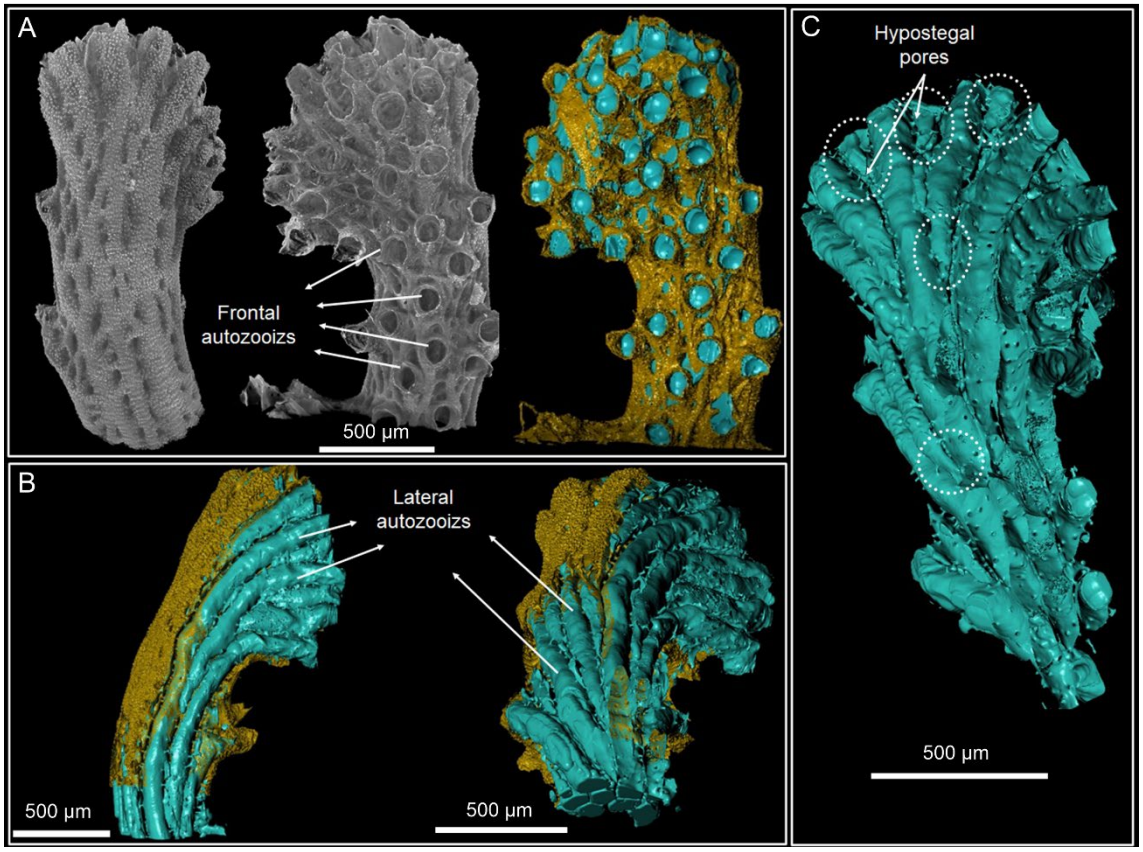

Figure 9. Micro CT images of *Hornera robusta.* A. Abfrontal (left) and frontal (center) views of the colony fragment analyzed. The micro-CT reconstruction (right) shows the inner volume of the zooid chambers (cyan) and the skeleton (gold). B. Same reconstruction in lateral (left) and oblique (right) views, with the skeleton partially removed to show the long tubular shape and the disposition of the lateral autozooids (white arrows), projected toward the front. They are connected to each other through the interzooidal pores (funicular system). C. Inner volume reconstruction of a partly sectioned colony in posterior view. New generations of autozooids, connected with to the parental autozooids by hypostegal pores, are indicated (dashed circles).

3.2. Microstructures

In the three investigated stenolaemates species we have identified two calcite microstructures: foliated and tabular.

3.2.1. Foliated calcite

Foliated calcite was found in *Fasciculipora ramosa* (Fig. 10) and *Cinctipora elegans* (Fig. 11), and formed, for both species, the skeleton of the entire colony. From the

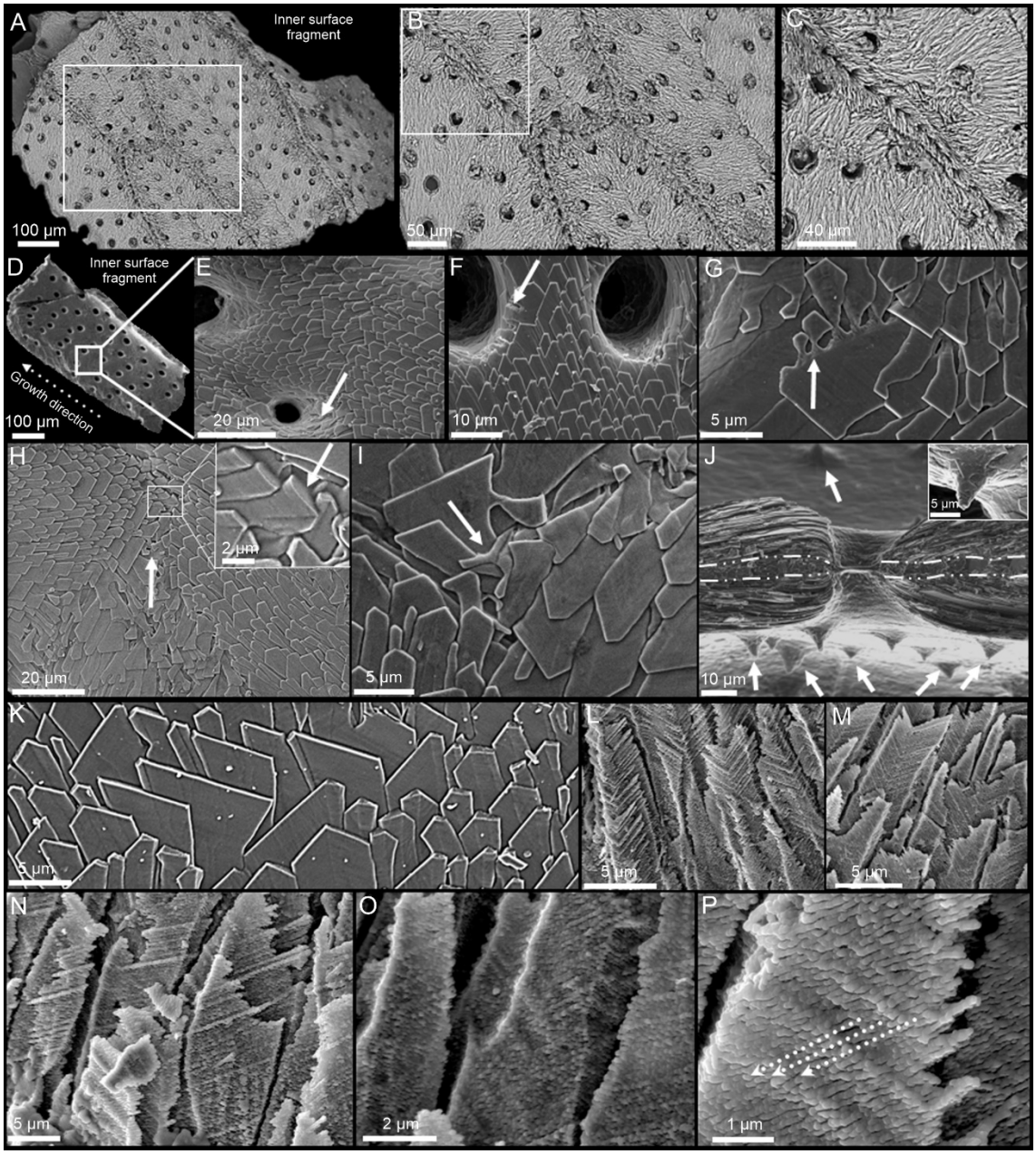

Figure 10. Foliated calcite of *Fasciculipora ramosa*. A-C. Views, at increasing magnifications, of the inner surface of a few zooid chambers from unpolished and slightly decalcified colony fragments. D-K. Unpolished bleached surfaces. D. Representative fragment of a zooidal chamber. E-K. Foliated calcite of the inner surface of the chamber. Note the ordered arrangement of the calcite laths, with their characteristic arrowhead endings. Arrows in E, F, G, H and I point to regions where laths adapt to changes in the surface topography by bending and/or bifurcating. Inset in H shows the highly inclined smooth surfaces of the lath endings (arrow). J. Cross-section of an interzooidal wall showing a central granular layer (delimited by white dashed lines). Laths are parallel to the inner surfaces of both chambers. The wall is interrupted by a mural pore that connects two adjacent zooids. Mural spines are widely distributed over the inner surfaces (arrows). The inset shows a mural spine. L-P. Slightly etched surfaces with highly marked growth lines. The close-up views (N-P) of the laths display a patent surface nanoroughness. Nanoprotrusions are arranged in particular directions (dashed lines in P).

SEM images of unpolished fragments (Figs 10 and 11), we can observe that the calcite laths are co-oriented and, in general, elongate in the growth direction of the zooidal chambers. The main planar crystal faces are parallel to the chamber surface. The laths show some degree of imbrication and their exposed part ranges in length from a few to several tens of microns. Their width ranges from one to ten microns, being longer and thinner in *Cinctipora elegans*. The characteristic arrowhead ending of the laths can be acute or obtuse, sometimes truncated by a transversal surface (Figs. 10A-K and 11A-I). Although laths tend to show a predominant growth direction, it is not uncommon that they change their orientation by bending, sometimes accompanied by bifurcation (white arrows Figs. 10E, F, G, H, I and 11E, F). This feature allows them to adapt to changes in the topography, such as protuberances, pores, transversal walls, depressions (Figs. 10F, I, J and 11F) and internal mural spines (inset in Fig. 10J). At higher magnification, the growth lines are visible on the main planar surfaces of the laths (Figs. 10I, K and 11E, F, G, I), becoming clearly discernible after decalcification (*Fasciculipora ramose*, Fig. 10L-P; *Cinctipora elegans*, Fig. 11J-L). This same treatment reveals the rough nanostructure of the laths (Figs. 10O, P, and 11K). On polished colony fragments of *F. ramosa* and *C. elegans* (Fig. 12A and G, respectively), the aspect of calcite laths differs depending on whether they are sectioned parallel (e.g., solid arrow in Fig. 12B) or transversal (empty arrows in Fig. 12B) to their main upper surfaces. The laths demonstrate their whole width in sections parallel to their main surfaces (i.e., to the zooid surfaces) (Fig. 12C, D),

☛ **Figure 11.** Foliated calcite from unpolished surfaces of *Cinctipora elegans*. A-B. Lateral and oblique views (micro-CT images) of the cylindrical colony fragment analysed (see also Fig. 8). C-I. Unpolished bleached inner surfaces. C. Representative fragment of a zooidal chamber, similar to the area framed in B. The growth direction is indicated by the bottom dotted arrow. D-I. Detailed views of the foliated calcite. D. Close up of C showing preferential alignment of the laths. E, F. Calcite laths exhibit a high growth plasticity (arrows), by tightly adapting to the surface protuberances. G is an anaglyph of a surface protuberance (to appreciate the 3D effect, red-cyan glasses have to be used). H, I. The terminal and highly inclined surfaces of the laths are smooth (arrows). J, K. Slightly etched surfaces. Some growth lines are highly marked and can be correlated across different laths (solid arrows), even between laths resulting from splitting of a parental lath (empty arrows). The surface nanoroughness is clearly exposed in K. L. Cross-sectional view of the laths, revealing their space-filling arrangement.

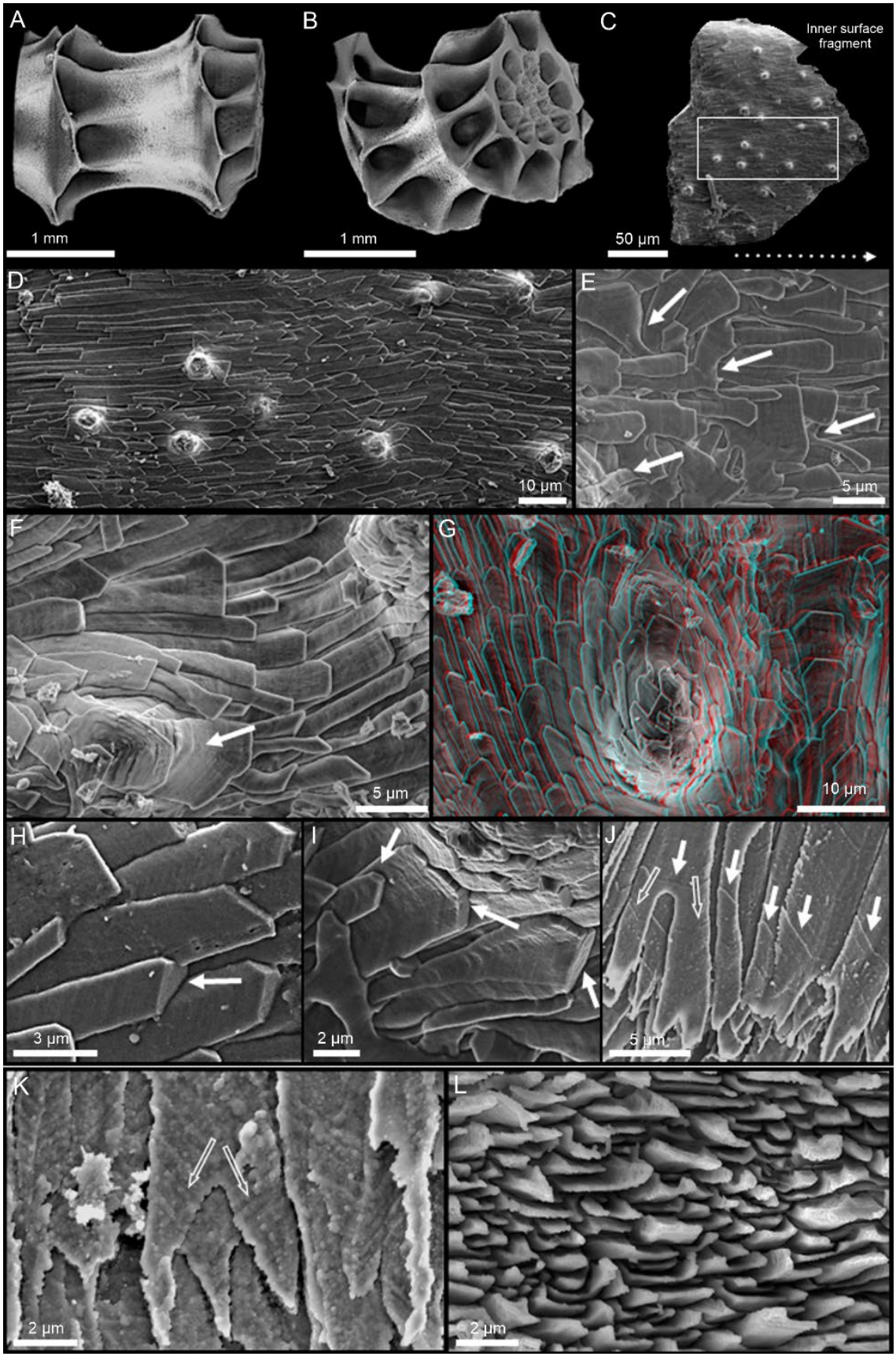
A
1 mm
B
1 mm
C
Inner surface fragment
50 µm
D
10 µm
E
5 µm
F
5 µm
G
10 µm
H
3 µm
I
2 µm
J
5 µm
K
2 µm
L
2 µm

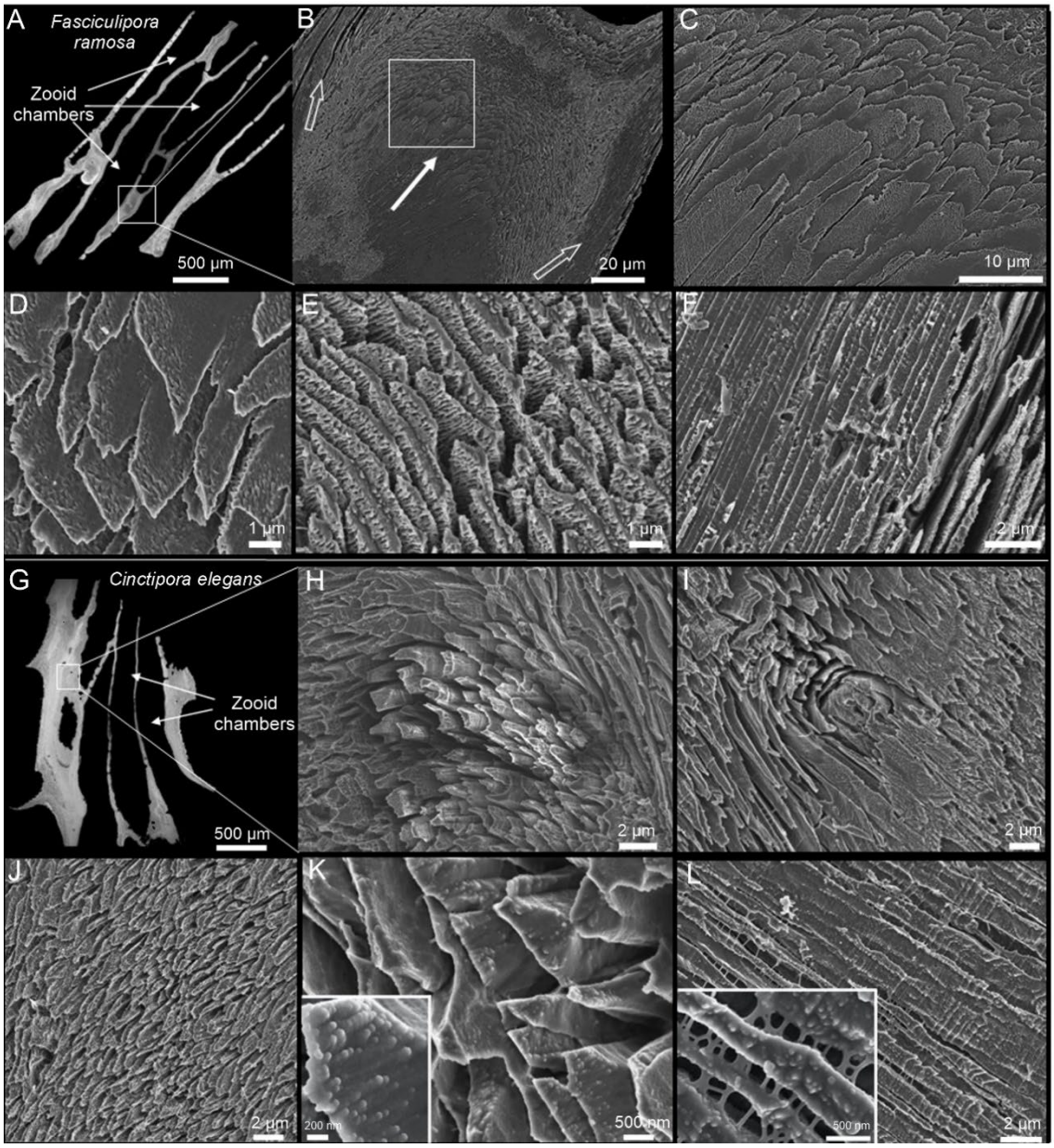

Figure 12. Polished and slightly decalcified colony fragments of *Fasciculipora ramosa* (A-F) and *Cinctipora elegans* (G-L). A, G. General views of the colonies. B. Detail of a sectioned chamber. Laths exhibit different morphologies depending on how they have been sectioned: parallel to their main surfaces in the center of the chamber (solid arrow) and perpendicular to it toward the sides (empty arrows). C, D. Details of the central area (framed in B). E, F. Details of the margins of the chamber. Laths have been sectioned transversal (E) and parallel (F) to their growth axes. H, I. Sections of two protuberances, showing the disposition of the calcite laths inside and around them. J, K. Laths sectioned transversal to the growth axis. Their space-filling behaviour is evident. The surface nanoroughness is neat in K (inset). L. Laths sectioned parallel to the growth axis. Organic threads extend between them (inset).

whereas they have rectangular, narrow shapes when cut transversely (Fig. 12E, F). In cross sections, their space-filling disposition can be appreciated, even within the interior of protuberances (Fig. 12H, I, J, and K). Upon decalcification,

the presence of very thin intervening organic threads is revealed (i.e., in *Cinctipora elegans*, Fig. 12L).

3.2.2. Tabular calcite

Tabular calcite, formerly described as semi-nacre (Carter and Clark 1985), is only present in *Hornera robusta* (Figs. 13, 14, 15, and 16), and constitutes the bulk of the skeleton of the entire colony. Calcite tablets completely carpet the inner surface of the zooidal chambers (Fig. 13D, E). They have polygonal morphologies and are arranged parallel to the surface, stacked onto each other and unevenly distributed (Fig. 13E, F). Their number of sides ranges from three to six. The range of tablet diameters is between 3 and 10 μm and their average thickness is ~150 nm (Figs. 13G-J and 15). The edges of the tablets may be straight or irregular. Adjacent tablets tend to overlap, except when their edges are at the same height (white arrows in Fig. 15B, C, E, F). Under high magnification, the main surfaces of the polygonal tablets reveal a rough nanostructure (Fig. 13G-I), similar to the surface of the laths that form the foliated calcite. Concentric growth lines, mainly parallel to the edges of the tablets, are also observable on their main surfaces (Figs. 13F, H-J, M and 15B, D-N). In the cross-section of the inner walls, that separate adjacent zooidal chambers (Fig. 13K), we can discern a thin central layer made of irregular, sometimes polyhedral, calcite grains (delimited by a dashed line in Fig. 13K). Immediately adjacent, in both growth directions, the tabular layer becomes organized and the tablets align parallel to the central granular layer, which is arranged in laminae. As previously described (Taylor and Jones 1993), virtually all the tablets in *Hornera robusta* have a "triple-spiked" outgrowth in the center. This structure is characteristic of the tabular calcite of *Hornera robusta*, and consists of a short stem that trifurcates into three pointed branches that are evenly separated from each other by angles of 120º (Figs. 13H-J, M, and 15C-N). The spikes have variable heights, usually 100-300 nm, only occasionally reaching up to 1 μm (Figs. 13J and 15I). The profiles of the triple spikes can be

observed on both sides of the growth surfaces in fractures across the inner walls (white arrows, Fig. 13K).

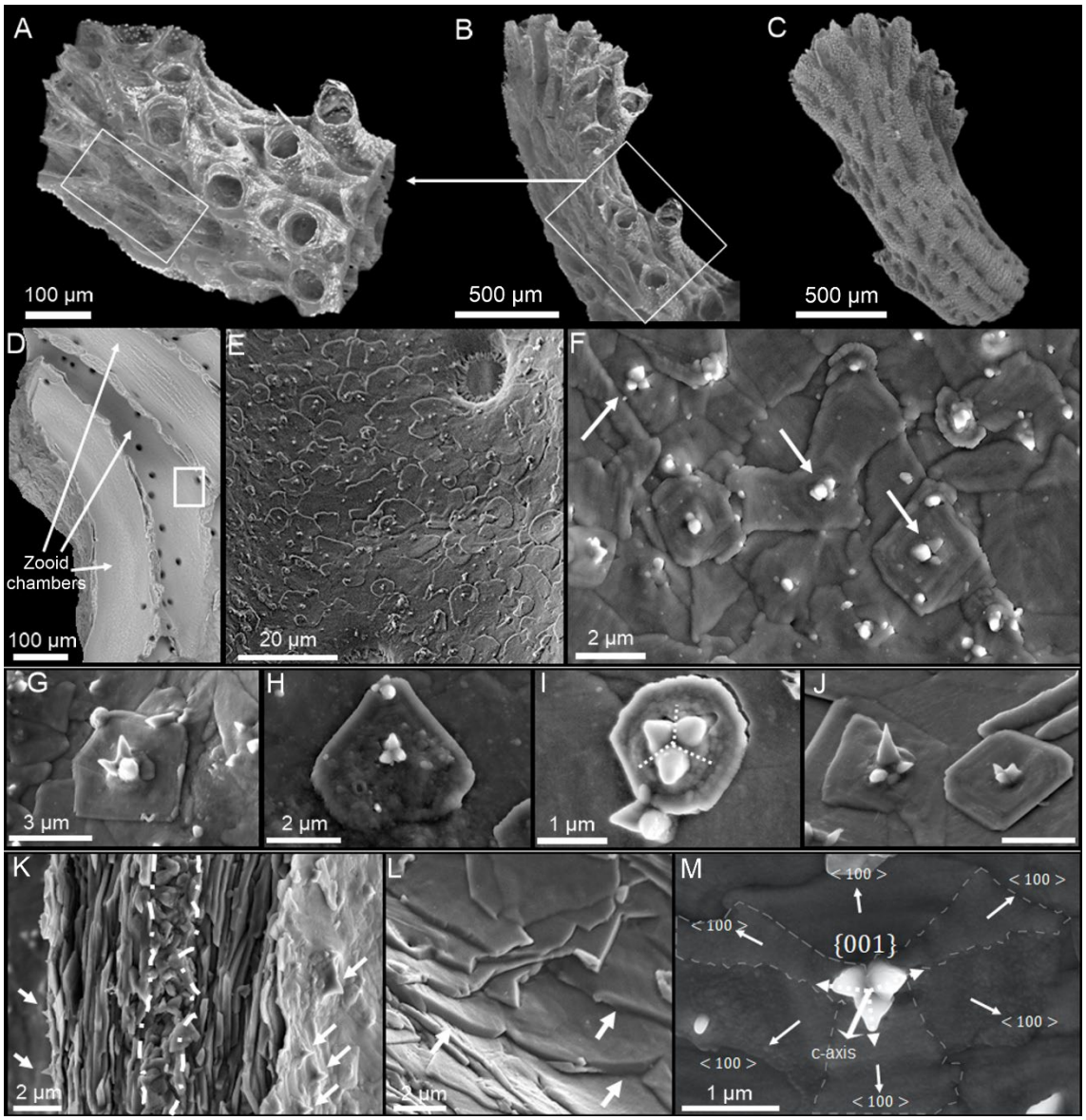

Figure 13. Tabular calcite of the interior of a colony fragment of *Hornera robusta*. A-C. Oblique (partly sectioned) (A, B) and posterior (C) views (micro-CT images) of the colony fragment analyzed (see also Fig. 9). D. Fractured fragment showing the characteristic tubular shape of the zooids, which are connected by interzooidal pores. E. Inner surface of a zooidal chamber covered by polygonal tablets. F. Close-up of the inner surface. The white dots correspond to triple-spiked structures at the centers of the tablets (arrows). G-J. Close-up views of polygonal calcite tablets. Growth lines and nanoroughness on the surfaces of the tablets are clearly discernible. The triple-spiked outgrowths measure from 100 nm to 300 nm in height, exceptionally up to 1 µm (J). K. Cross-section of an inner wall separating two zooid chambers. A central granular layer (marked by dashed lines) can be appreciated. The tablets are parallel to both surfaces and the spikes point perpendicularly (arrows). L. Fracture showing the smooth lateral surfaces of the tablets (white arrows). M. Single tablet with central triple-spike. Crystallographic faces have been tentatively indexed. The spikes diverge at equal angles (they appear distorted in the present view due to the tablet being slightly inclined with respect to the plane of the image).

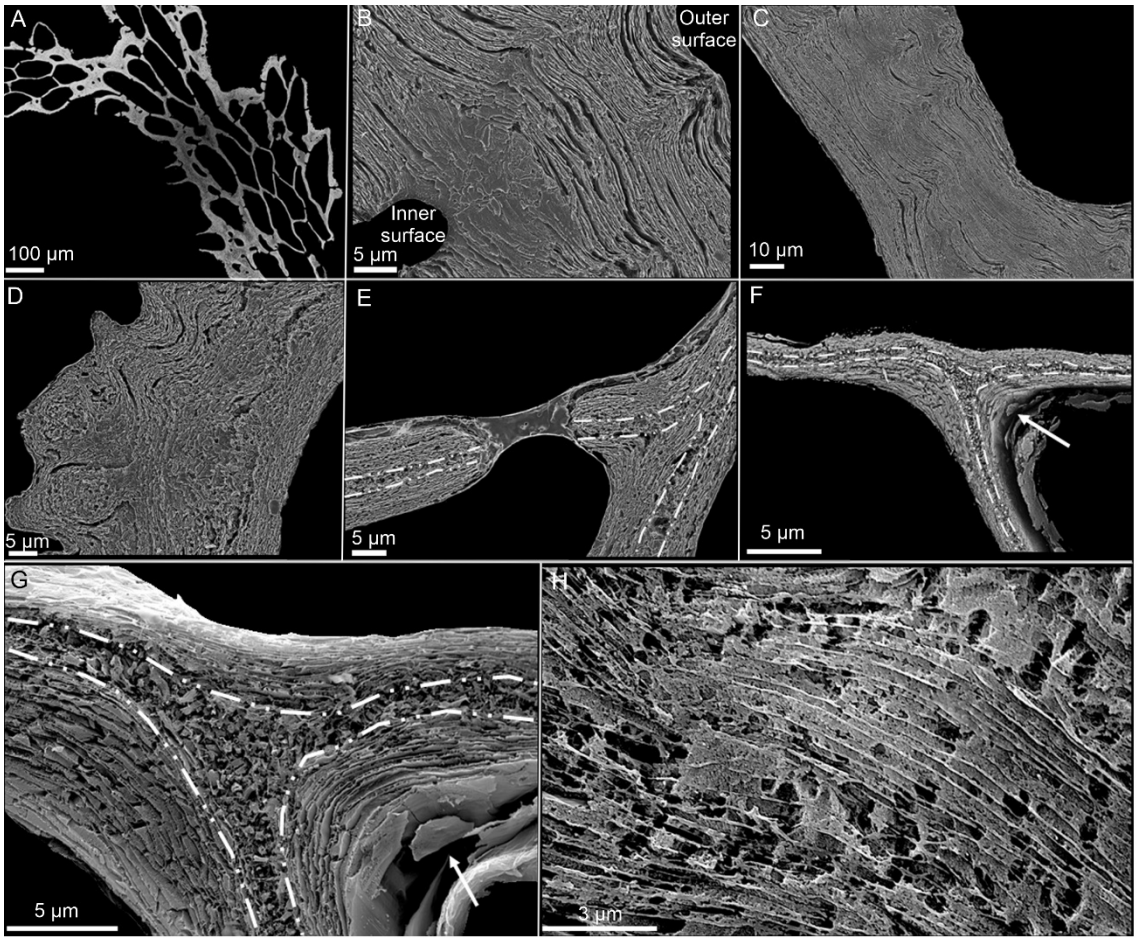

Figure 14. Cross-section views of the tabular calcite of *Hornera robusta* A. Polished and partly decalcified colony. B-D. The external wall section shows the multi-layered undulated patterning that flattens progressively toward the inner surface. The peaks correspond to the external protuberances. E-G. Cross-section of an inner wall. The sections are entirely composed of tabular calcite (arrow in F), except for the central granular layer (marked with dashed lines). H. Detail showing the organic membranes running uninterruptedly between lamellae of polygonal tablets.

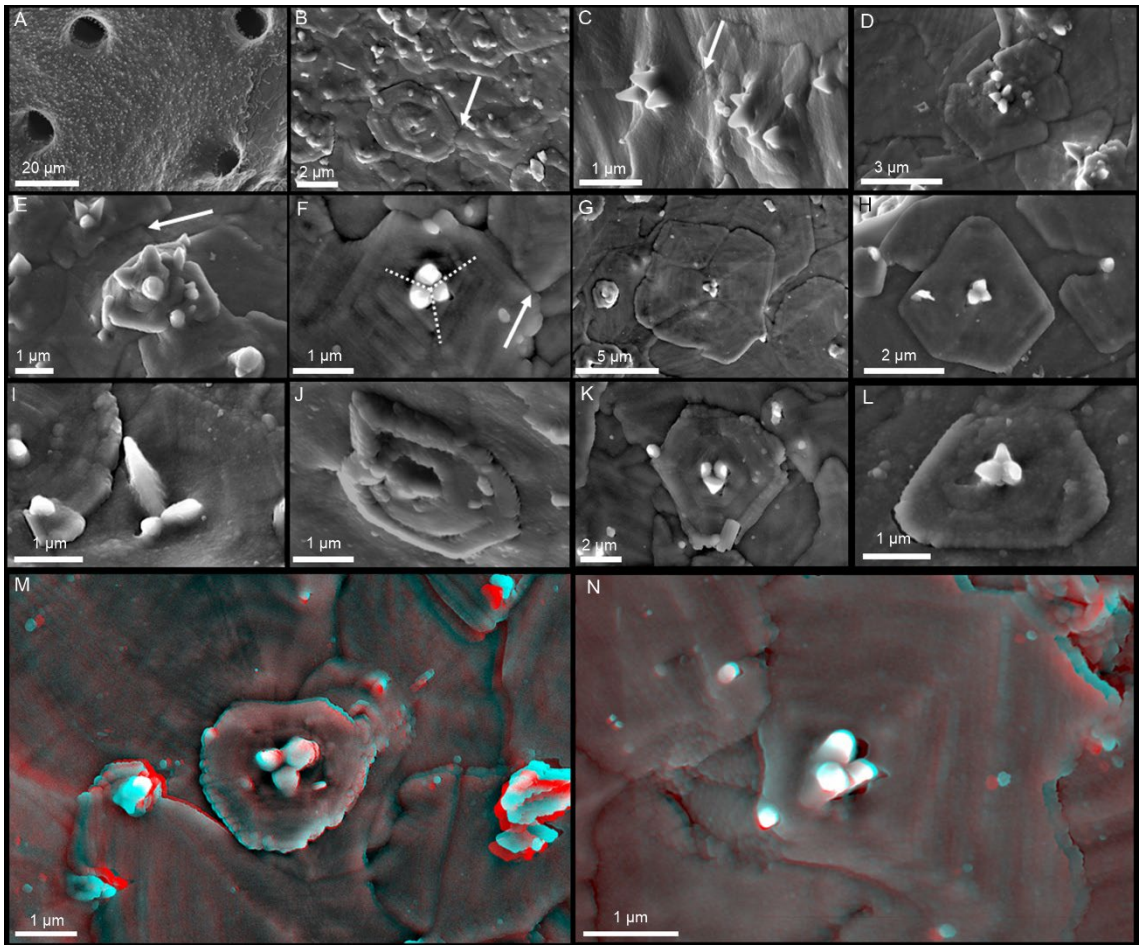

Figure 15. Tabular calcite of *Hornera robusta.* All images are from the inner surface of the zooidal chambers, previously cleaned with commercial bleach (5%, 1h). A, B. Overviews of the inner surface. C-L. Close-up views of different examples of tabular calcite. The polygonal tablets that are at the same level cease to grow when their margins collide (arrows in B, C, E and F). New tablets overlap previous ones, except for their spikes (E, H, K). Polygonal outlines vary from triangular to hexagonal. Growth lines and nanoroughness on the surfaces of the tablets are clearly discernible. The triple-spiked outgrowths are from 100 nm to 300 nm in height, exceptionally up to 1 micron (e.g., I). The three spikes are oriented at 120º from each other (e.g., F). M and N are anaglyphs. To appreciate the 3D effect, red-cyan glasses have to be used.

The external surface (Fig. 16C) shows the same tabular calcitic fabric that covers the entire internal surface, as described above, though moulded to the complex topography of the external surface, studded with protuberances (Fig. 16A). Here, the tablets display a certain degree of imbrication (Fig. 16B, C), which led them to be described as a different microstructure ("pseudofoliated calcite", Taylor and Jones 1993). This plasticity is a feature shared with the foliated calcite of *Fasciculipora ramosa* and *Cinctipora elegans* (see above). In cross-section of the external wall (Fig. 16D), the polygonal tablets form a multi-layered, undulated

wall, where the crests of the undulations correspond to the external protuberances (Fig. 14A-D and 16D). The undulations flatten progressively toward the inner surface. Polished and slightly decalcified cross-sectional surfaces from colony fragments of *Hornera robusta* (Fig. 14) clearly show the arrangement of calcite tablets and the granular central layer in the interzooidal walls (marked with dashed lines in Fig. 14E-G). Details of the decalcified tablets display the network of thin organic membranes separating the laminae (Fig. 14H). Organic membrane thickness has been estimated at ~70 nm.

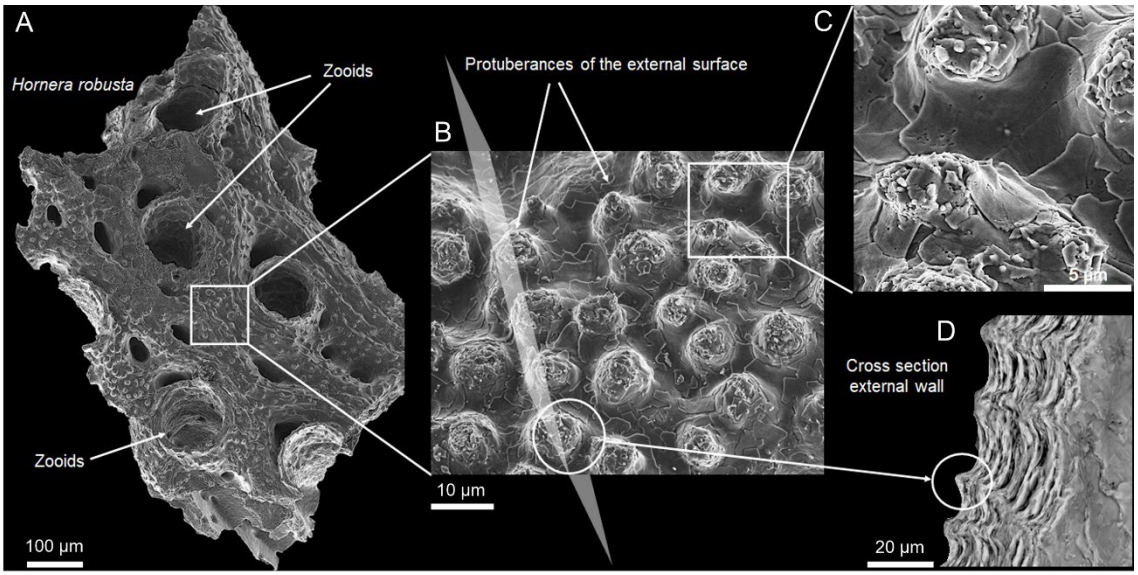

Figure 16. A. *Hornera robusta* colony fragment. B. Closer view of the outer surface studded by numerous protuberances. The white semi-transparent area represents the cross-sectional plane of the fragment shown in D. C. Detail of the outer surface showing the microstructure, constituted by the same polygonal tablets as found in the zooidal chamber's interior. The calcite tablets are partly imbricate and appear heavily distorted due to surface irregularities. D. External wall section where the protuberances have been cut transversely, showing the multi-layered undulated wall where the crests of the waves coincide with the protuberances.

3.3. Morphological analysis and surface nanoroughness

The foliated calcite of *Fasciculipora ramosa* displays the partially imbricated arrangement of the laths, as well as their characteristic arrowhead endings (Fig. 17A, B). The lath surfaces are irregular, which is more visible in the height and amplitude images (Fig. 17A). The phase signal does not show any consistent change in composition related to those irregularities. Laths vary greatly in size, orientation and morphology across small areas (Fig. 17B), as revealed also by SEM (Figs. 1 and 2). Laths vary greatly in size, orientation and morphology across small areas (Fig. 17B), as revealed also by SEM (Figs. 1 and 2). The laths are at a small angle to the growth surface (less than 15º). Their irregular and inclined surfaces can be seen in the profile graphs across selected laths (height images in Figs. 17A and B). The same graphs indicate lath thicknesses at the tip between 0.2 and 0.4 μm. The polygonal shapes of the calcite tablets of *Hornera robusta* can be observed in the height and amplitude images, together with the growth lines seen on their surfaces (Fig. 17C). In a close-up view of the surface (Fig. 17D), we can clearly observe its marked nano-roughness. The phase signal does not show significant changes in contrast.

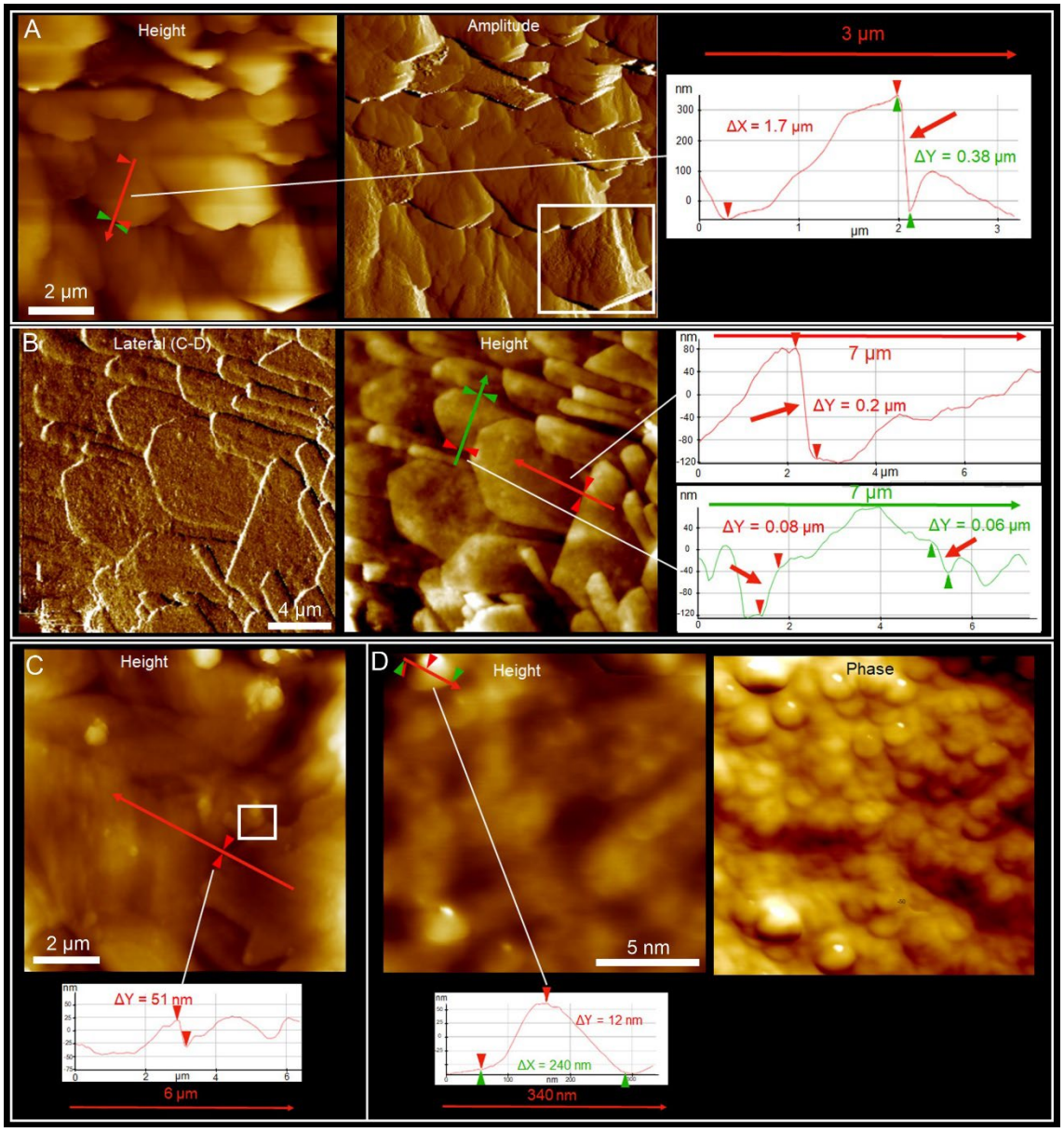

Figure 17. AFM analysis of the foliated and tabular calcite of *Fasciculipora ramosa* (A and B) and *Hornera robusta* (C and D). A. Height and amplitude images of a set of calcite laths. They display characteristic arrowhead endings and are partly imbricated. The irregular surfaces of laths are evident in the amplitude image (see framed lath). The profile graph of the transect marked both in the height shows a smooth highly sloped surface (red arrow) at the tip of the lath, with an unevenness of 0.38 µm. B. PinPoint mode of lateral strength and height images from another region. The profiles of the transects delineated in the height image show that the lateral and terminal facets (red arrows) of the laths are subvertical. C. Height image of the calcite tablets, where the polygonal contours and the growth lines are visible. D. Height and phase images of the area framed in C. The nanoprotrusions of the tablet's surface can be appreciated. The profile graph of a selected nanoprotrusion (red transect in the height image) indicates a height of 12 nm and a length of 240 nm.

3.4. Crystallography

A total of 27 EBSD maps were taken on the three studied species of stenolaemate bryozoans (between 8-10 maps per species). All EBSD phase maps indicate that the skeletons are always made of calcite.

The crystallographic arrangement of the foliated calcite of *F. ramosa* can be appreciated in the selected map of Fig. 18. The shapes of the calcite laths are discernible in the band contrast map (Fig. 18A). The central granular layer of the interzooidal walls (e.g., SEM image Fig. 10G) appears darker (white arrows in Fig. 18A) as a result of a weaker diffraction signal strength. The EBSD map (Fig. 18B) shows similar colors across large regions, alternating between green and purple, which indicates a slight variation in the orientation of the crystal laths (see color key for orientations). The corresponding contoured pole figures display defined clusters for both the c and a*-axes, which indicate that all the crystallographic axes are co-oriented. This is known as a sheet texture (Fig. 18B). The MUD values are relatively high (44 for the example of Fig. 18B). The c-axis is oriented parallel to the main surfaces and to the direction of elongation of the laths. The a*-axis pole figures display one maximum in the center of the stereographic projection, which indicates that the main planar surface of the laths corresponds to a prismatic (100) calcite face. The isolated crystal highlighted in Fig. 18B, with a MUD value of 585, provides a representative example of such an orientation. The distribution of crystallographic axes inferred from EBSD data is illustrated in Fig. 18C. The c-axis is contained within the main surfaces of the laths and parallel to the growth direction (arrow). There is an a-axis contained within the main surface, and the other two a-axes at 60° to that surface. Accordingly, this surface is of the (100) type. The different laths generally display a good coorientation, hence the sheet texture.

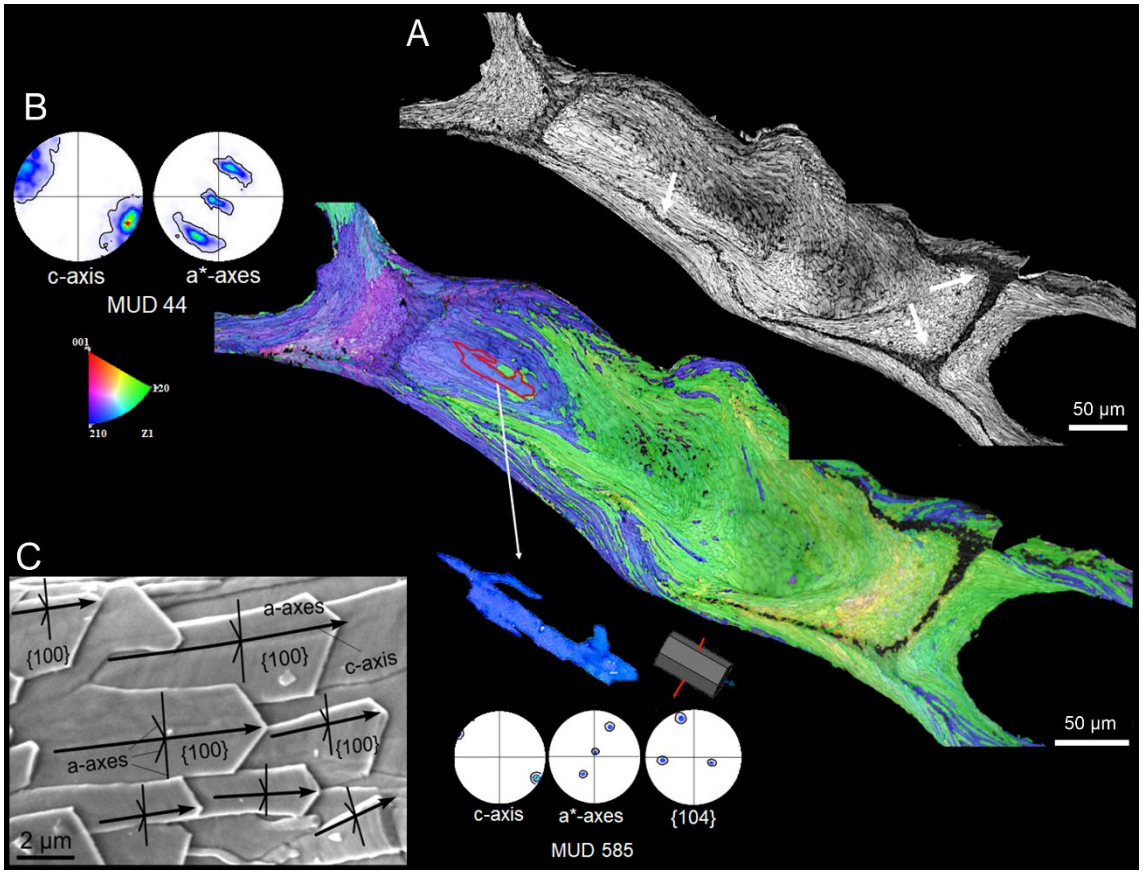

Figure 18. EBSD analysis of the foliated calcite of *Fasciculipora ramosa.* A. EBSD band contrast map in grey-scale, where the shapes of the calcite laths are discernible. Darker regions (white arrows) indicate a lower diffraction signal strength, matching the central granular layer between two inner walls. B. EBSD map of the same area as in A. The top pole figures (contoured version) show good co-orientation of the calcite laths, as also indicated by the relatively high MUD value. The orientation of the selected calcite lath (in blue) is provided by the pole figures and the unit cell, where the c-axis is parallel to the surface and to the elongation axis of the laths, and one a*-axis (intermediate between two a-axes) is perpendicular to the main surface. The extremely high MUD value is indicative of its single-crystal nature. C. The distribution of crystallographic axes inferred from EBSD pole figures is illustrated on a set of laths. The color triangle in C is the color key for orientation in all cases.

The foliated calcite of *C. elegans* presents a distribution of crystallographic axes similar to that of *F. ramosa*. The region analyzed in Fig. 19A comprises an entire wall cross-section, from the exterior to the interior of the zooid chamber. The EBSD color orientation map (right map in Fig. 19A) shows a variation in the orientation of the central region with respect to the lateral regions. This indicates a change in the orientation of the c-axes of the laths with respect to the sectioning plane, from being at a high angle (red colors) in the central area to close to parallel (green, purple, and blue colors) toward the internal and external surfaces.

In Fig. 19B we have cropped the areas corresponding to the external and internal walls. The contoured pole figures reveal good co-orientation of the calcite laths (MUD values of 72 and 50 in Fig. 19B), with defined clusters for all crystallographic axes. The c-axes are oriented parallel to the surface, while the *a-axes display maxima that are less well-defined than in *F. ramosa*. A clear example of such orientations is depicted by an isolated single-crystal lath (MUD of 506) and its 3D unit cell (Fig. 19B). The SEM image provides a representative example of such an orientation, inferred from EBSD data, in which the c-axis is oriented parallel to the elongation direction of the lath (Fig. 19C)

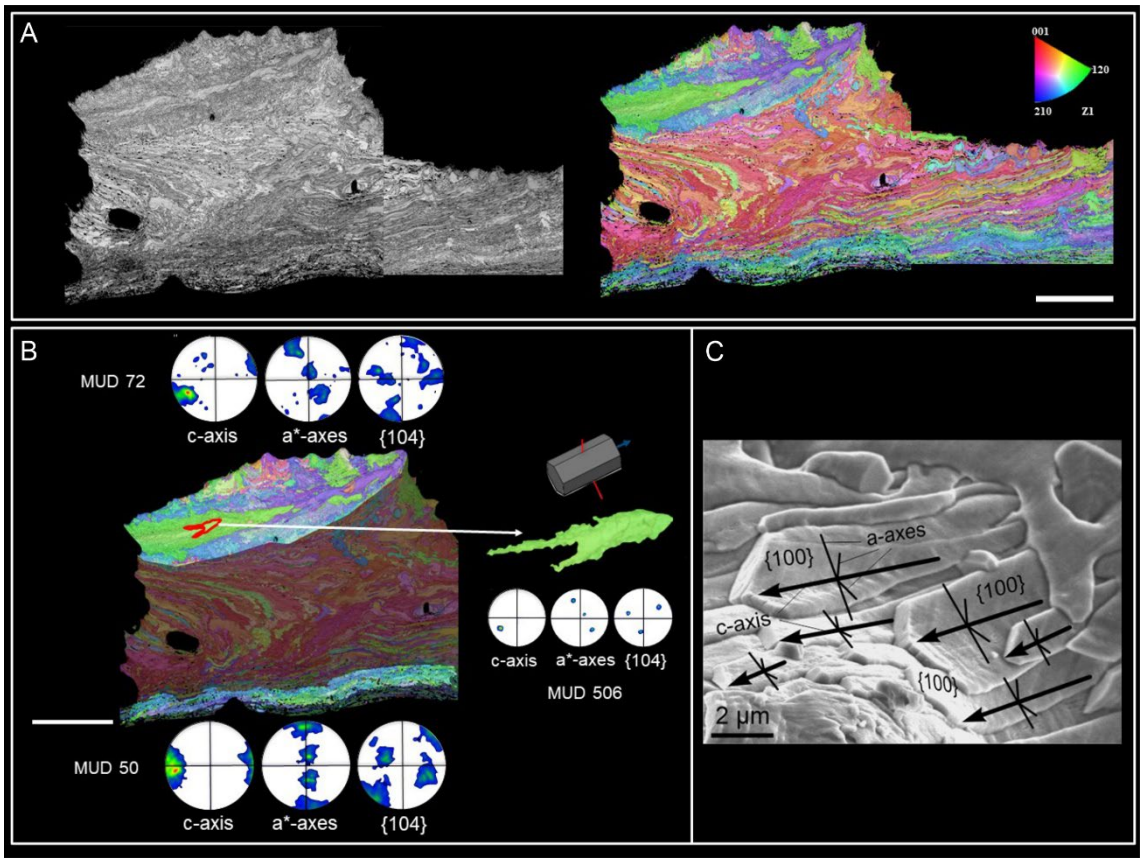

Figure 19. EBSD analysis of the foliated calcite of *Cinctipora elegans.* A. EBSD band contrast map (grey scale) and color orientation map. B. Pole figures (contoured version) of the two areas highlighted in the EBSD map. They correspond to the lateral margins of the chamber. The pole figures demonstrate good co-orientation (relatively high MUD values) and a sheet texture, with the c-axis in plane and the *a-axes having defined maxima. The orientation of the selected calcite lath (in green) is provided by the pole figures and the unit cell; the c-axis is parallel to the surface and to the elongation axis of the laths, and there is one a*-axis (intermediate between two a-axes) perpendicular to the main surface. The extremely high MUD value is indicative of its single-crystal nature. C. The distribution of crystallographic axes determined from EBSD pole figures is illustrated on a set of laths. The color triangle in A is the color key for orientation in all cases.

As occurs in *F. ramosa*, there is an a-axis contained within the main surface and the other two are at 60° to that surface. Accordingly, these surfaces are of the (100) type. The laths display a certain coorientation, hence the diffuse sheet texture.

EBSD measurements performed on *H. robusta* are from both a cross-section of the external wall (Fig. 20A, C, and E) and a section through several zooid chambers at a low angle to the wall (Fig. 20B, D, and F). Despite the smaller size of the calcite tablets compared to the calcite laths of *F. ramosa* and *C. elegans*, we can observe good signal strength in the band contrast maps (Fig. 20A, B). The EBSD maps come in multiple colors, which indicate different crystal orientations (Fig. 20C, D). In the section across the wall (Fig. 20C), the c-axis is broadly oriented in plane and perpendicular to the external surface (Fig. 20E). In this kind of section, the tablets are sectioned perpendicular to their main surfaces (Figs. 13K and 14B, G, H) and parallel to the outer shell surface. In the section parallel to the wall (Fig. 20D), where the tablets are sectioned parallel to their main surfaces, the c-axes are broadly perpendicular to the cutting plane. All this implies that the c-axes are perpendicular to their main surfaces. The pole figures indicate an axial texture, given the ring-like distribution of the a*-axes (Fig. 20E, F). The low MUD values (less than 10), confirm the low co-orientation of the crystals. The two single crystals selected, each from a different section (Fig. 20E, F), confirm that the c-axis is subperpendicular to the main surfaces of the tablets. Accordingly, these surfaces are of the (001) type. The a-axes are approximately contained within the main surfaces and change in orientation across individual tablets (Fig. 20G). In this way, an axial texture is obtained.

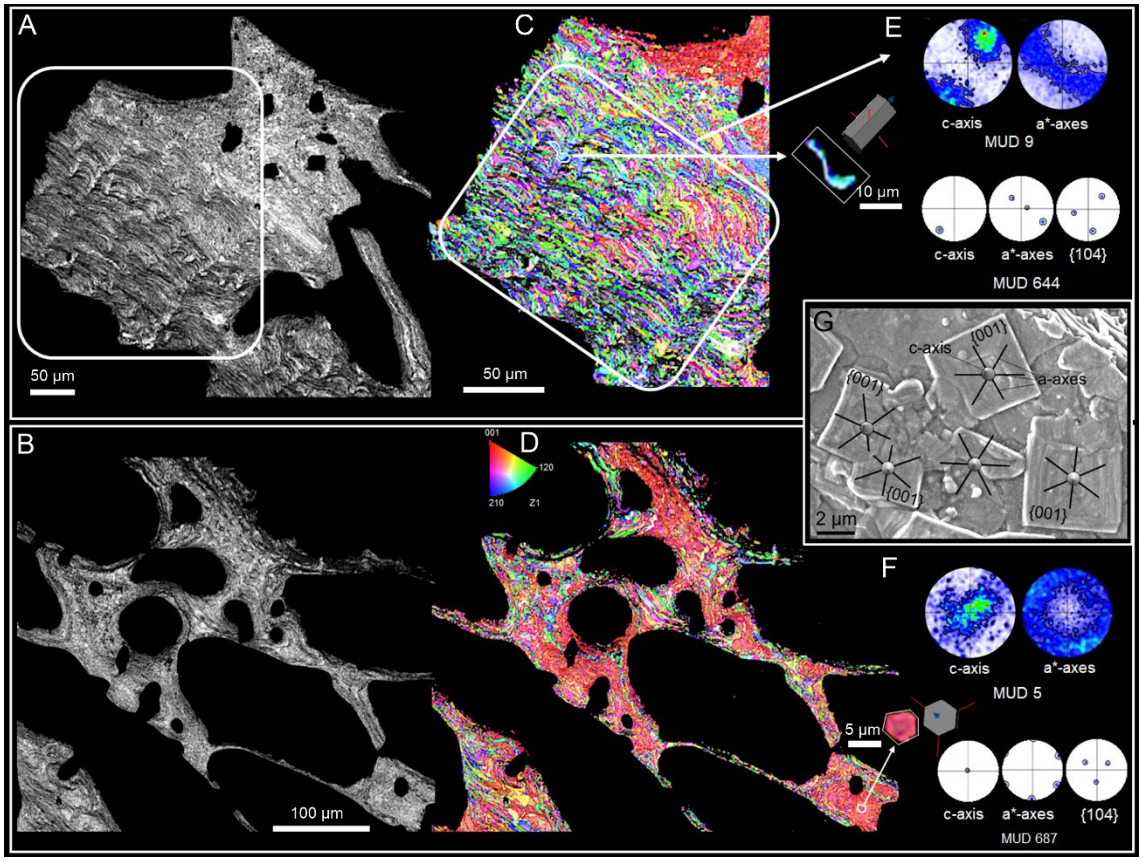

Figure 20. EBSD analysis of the tabular calcite of *Hornera robusta* from two different regions: a cross-section of the external wall (A and C) and a section of the colony wall at a low angle (B and D). A, B. Band contrast maps in grey-scale, showing good signal strength and recognizable structures, like the undulated layered wall in A. C, D. Color orientation maps. In both cases, there is low crystal co-orientation (low MUD values). E, F. Pole figures (contoured version) display an axial texture, where the c-axis is roughly perpendicular to the tablets, while the a*-axes spread in all directions. Data for individual tablets (small frames in C and D) from both maps are provided. The pole figures and the extremely high MUD values confirm that they are single crystals. G. The distribution of crystallographic axes inferred from EBSD pole figures is illustrated on a set of tablets. The orientations of the a-axes are tentative, based on the sketches of Fig. 10B. Their disorientations across tablets are inferred from those of the tablet edges. The color triangle in D is the color key for orientation in all cases.

4. Discussion

4.1. Zooid arrangement and funicular system

Micro-CT results show a different colony structure for the species *Cinctipora elegans* and *Hornera robusta*. While *C. elegans* has a cylindrical erect colony structure, where the zooids are arranged concentrically, *H. robusta* forms erect polyfurcate branched colonies, where the zooids are arranged in a fan-like manner and are curved toward the front. Autozooid chambers of *C. elegans* are more conic and wider at the aperture (Fig. 8). Nevertheless, they seem to be proportionally shorter than the long tubular-shaped chambers of the autozooids of *H. robusta* (Fig. 9). Kenozooids are present in the inner central region of *C. elegans*. Their structural function is that of a pillar for the cylindric colony (dashed line, Fig. 8A). Both species present a highly interconnected channel network, the funicular system, which goes through the interzooidal pores of the inner walls and provides oxygen and nutrients from the feeding autozooids to the rest of the colony (Bobin 1977). According to Batson et al. (2021; 2022), the interzooidal walls, which separate the new zooid generations from the parental ones, are interconnected by special pores called "hypostegal pores", through which growth by budding takes place through the transmission of the coelomic cavity (Figs. 8C and 9C).

4.2. Central granular layer

According to our observations, foliated calcite constitutes the bulk of the entire colony skeleton of both *Fasciculipora ramosa* and *Cinctipora elegans*, whereas tabular calcite is the principal microstructure of *Hornera robusta.* In all the samples analyzed, there is a central granular layer located in the center of the interzooidal walls, made up of randomly oriented polyhedral crystals (Figs. 10J, 13K, 14E-G) from which the main microstructures soon organize. This granular layer was previously described as a "primary layer consisting of granules or prisms of

calcite that occurs medially in interzooecial walls in cyclostomate bryozoans" (Brood 1976; Tavener-Smith and Williams 1972). Nevertheless, evidence of this layer was not found in the species of *H. hornera*, *H. robusta*, and *H. squamosa* (Taylor and Jones, 1993). In the EBSD band contrast map of *F. ramosa*, the central granular layer comes in dark colors (Fig. 18A), which indicates a weak diffraction signal strength, likely due to either the small crystal size or the presence of organic matter.

4.3. Foliated calcite

Our EBSD results show that the foliated calcite of both *F. ramosa* and *C. elegans* has a sheet texture, with the c-axes oriented parallel to the surface (Figs. 18 and 19), and the a*-axes perpendicular to the main surfaces of the laths, which, in this way, would roughly correspond to {100} prismatic faces. The arrowhead endings are bounded by {104} planes sectioned along the main {001} surfaces (see Figs. 10H inset, 11H, I, 21, and 22). However, whereas the terminal, highly inclined surfaces of the lath endings are smooth, their main upper surfaces are rough (Figs. 11F, G, I, J, and Figs. 17A, 21, and 22). This indicates that the former are true {104} faces. The main upper surfaces lack the smoothness typical of crystallographic faces. Accordingly, they are not true {100} faces but very close surfaces.

Conversely, Taylor and Weedon (2000) hypothesized, based on SEM observations, that the c-axis was inclined at 45º to the main lath surfaces. They distinguished between the foliated calcite of *F. ramosa* and the "transverse fibrous fabric" present in *C. elegans*, according to the obtuse or acute angles of the lath endings, respectively. In our EBSD-based model, the coexistence of acute or obtuse angles is explained by the bifurcations and switches in the elongation direction of laths that occur at constant crystallographic orientation. The changes in the growth direction of the laths with respect to the c-axis explain the

differences in the displacement of the arrowhead tip with respect to the central axis of the laths, and even its disappearance, with the development of single terminal faces (Fig. 21A). The fact that the arrowhead endings may or may not be truncated by additional flat surfaces can be explained by differences in the way in which the {104} rhombohedron is sectioned: 1) above or below the c-axis, and 2) parallel or at a certain angle to the c-axis (Fig. 21B). Accordingly, we do not consider Taylor and Weedon's (2000) as a valid argument.

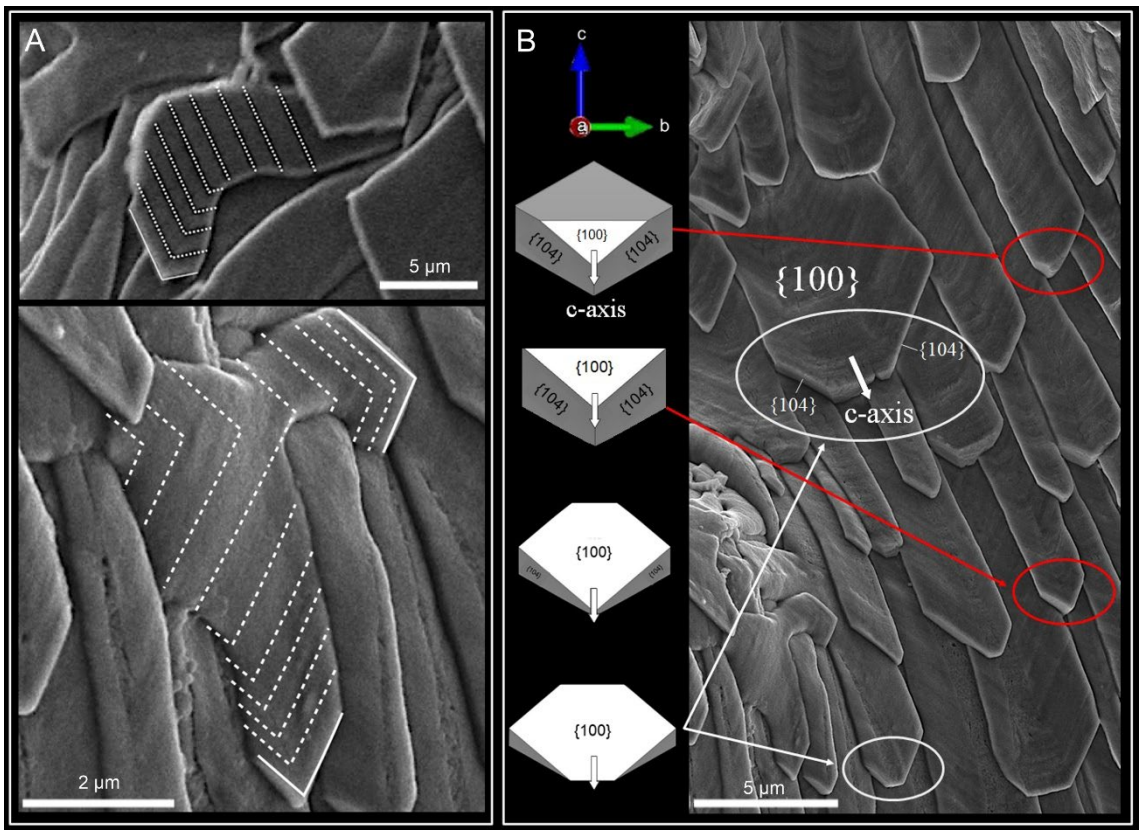

Figure 21. Crystallographic explanation of the morphological changes of lath endings. A. The displacement of the arrowhead tips (white dashed lines) with respect to the growth axis of the laths is a consequence of switches in growth direction, sometimes due to bifurcations (bottom image) that occur at constant crystal lattice orientation. B. Sketches of the calcite {104} rhombohedron oriented with one a-axis perpendicular to the plane of the image and the c-axis parallel to it (orientation key is provided on top). The crystallographic orientation of the foliated calcite has been determined from EBSD results (see schemes in Figs. 6C and 7C). The different rhombohedra are sectioned along the {100} planes at different heights, explaining the transition from sharp arrowheads to truncated terminal faces of the laths (dashed circles in the SEM image). The foliated calcite crystallography.

This ability to change the growth direction and bifurcate indicates that the foliated calcite has a high ability as filling material, in much the same way as described for the homoeomorphic foliated calcite of bivalves (Checa et al. 2007; Checa et al. 2019). Nevertheless, the foliated calcite of bryozoans is crystallographically different from that of bivalves, where the c-axis is at a great angle to the main surface of laths (Checa et al. 2019). Interestingly, the terminal faces of the laths in bivalves are also {104} faces, but their main surfaces are different from {100} as in bryozoans, of the type {10l}, with l being a high to very high Miller index, within the tentative range 8 to 25 (Checa et al. 2019).

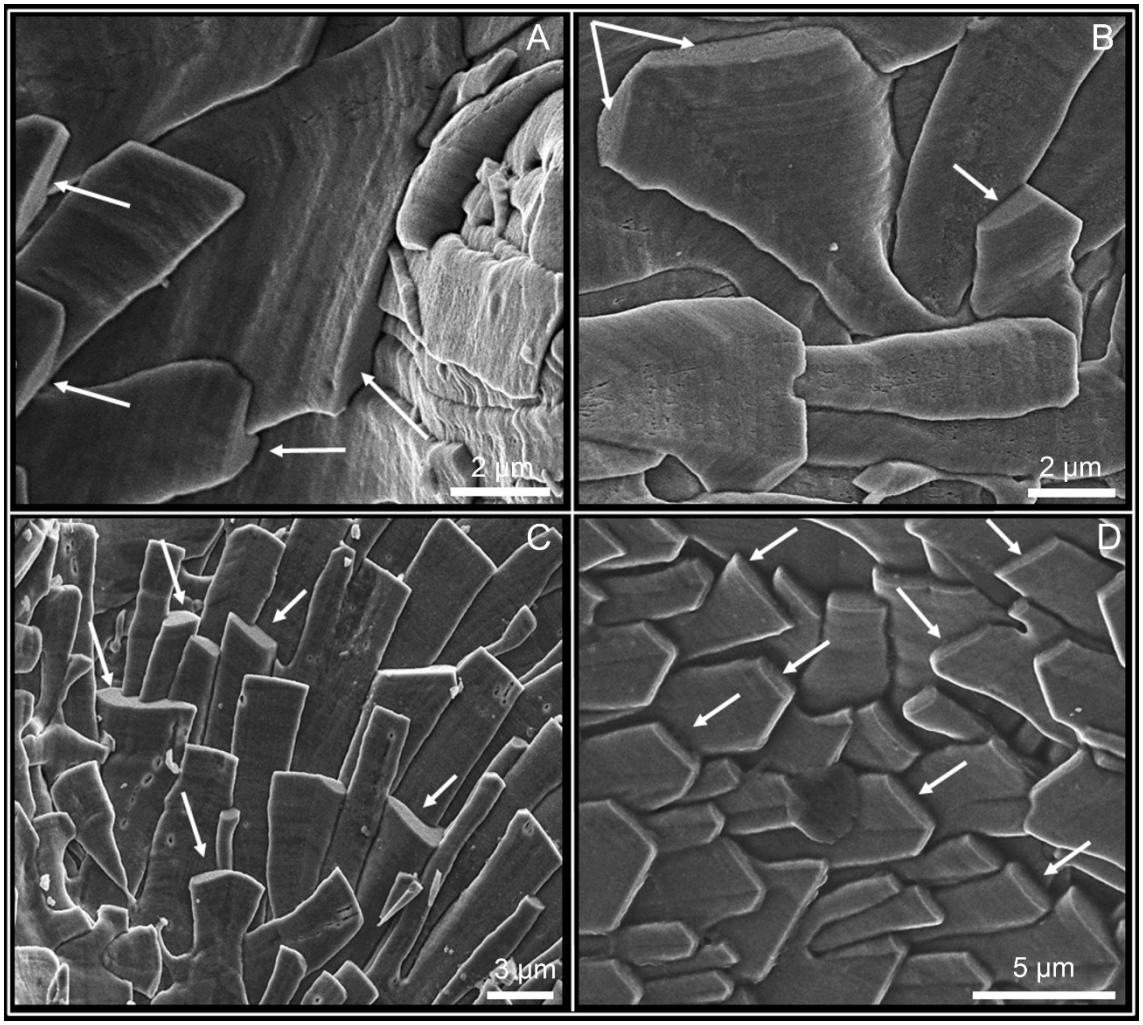

Figure 22. Views of the foliated calcite of *C. elegans* (A-C) and *F. ramosa* (D). The main surfaces of the laths are rough, with visible growth lines, whereas the highly inclined terminal surfaces are smooth (arrows).

4.4. Tabular calcite

Our EBSD results show that the microstructure of *Hornera robusta* has an axial texture, where the c-axis is oriented perpendicular to the surface of the tablets (Fig. 20C, D). A similar texture was found with EBSD measurements in *H. curriae* (Batson et al. 2021). Thus, the main flat surfaces of tabular calcite are approximately {001} planes (Fig. 23A). The edges then correspond to the intersection of the {001} plane with the calcite rhombohedron (Fig. 23A). This is supported by the smoothness of the lateral facets when seen in oblique view (arrows in Figs. 13L and 24A, B), typical of {104} rhombohedral faces. In the images of tubuliporine bryozoans of Taylor and Weedon (2000) (their figure 8B, E), calcite plates are particularly thick and extensive, and adequately oriented rhombohedral faces are evident. Depending on the level at which the rhombohedron is sectioned, the number of edges will be three (either {104} or $\{10\bar{4}\}$ planes) or six (both {104} and $\{10\bar{4}\}$ planes) (Fig. 23B). If we introduce small changes in the inclination of the sectioning plane with respect to the c-axis, we may find the whole range from three to six edges. In any case, the edges will advance along <100> directions (Figs. 13M and 23A). Our crystallographic model is similar to that proposed by Taylor and Jones (1993) and Taylor and Weedon (2000), based on SEM observations. Nevertheless, these authors only explained the existence of six-edged tablets (hexagonal semi-nacre fabric).

The term "calcite semi-nacre" was first used to refer to the "spiral laminae" present in the secondary layer of craniid brachiopods (Williams and Wright 1970). It was later extended to bryozoans (Carter and Clark 1985) and, subsequently, to the polygonal tablets of *H. robusta* (Taylor and Jones 1993). Simonet Roda et al. (2022) proposed to replace the term semi-nacre with tabular calcite, based on the lack of any relation with molluscan nacre. In this study, we also adopt the term "tabular calcite" instead of semi-nacre in bryozoans, because, in addition, the units display a tabular habit without any consistent spiral or

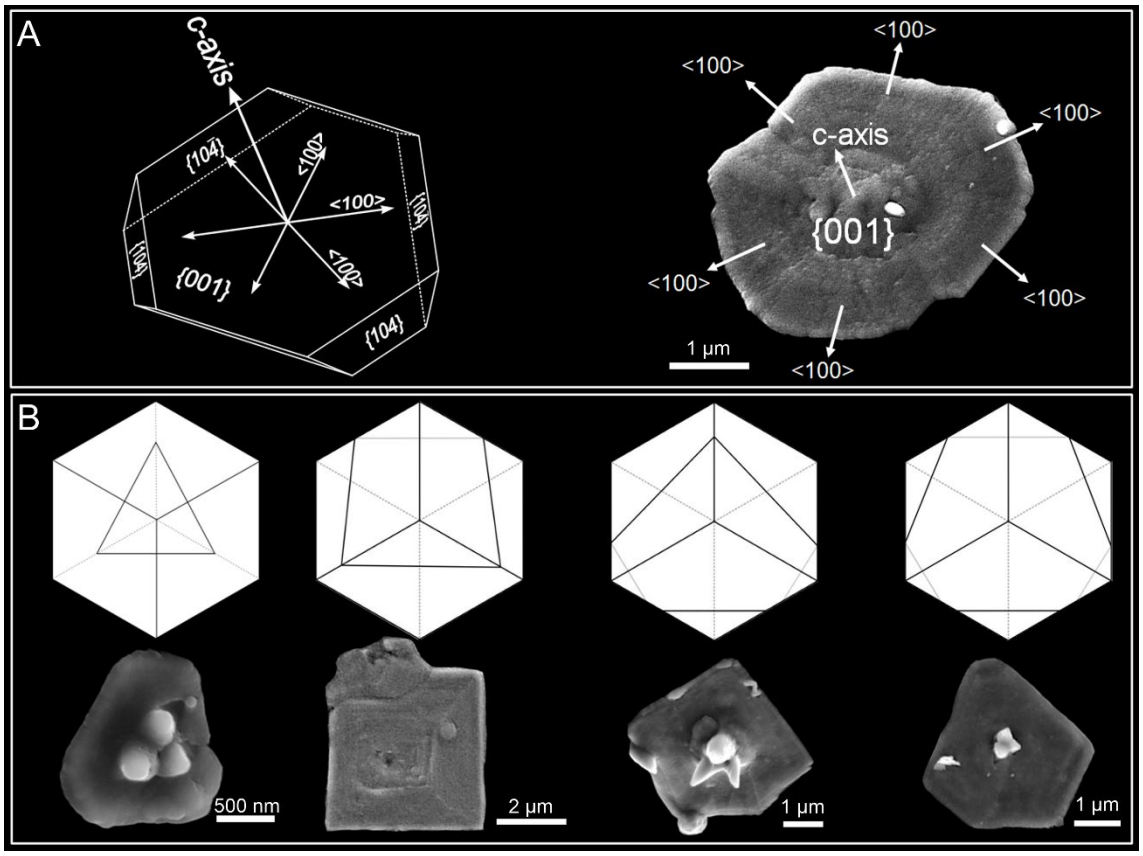

Figure 23. A. Hypothetical indexation of an ideal hexagonal calcite tablet from *H. robusta* (left), and of an actual hexagonal tablet (right). The crystallographic orientation of the tabular calcite has been established according to our EBSD results (see scheme in Fig. 8G). The main flat surfaces roughly correspond to {001} planes, with the c-axis oriented perpendicular to them. The highly inclined and smooth edges are (104) faces that advance along the <100> directions. B. Sketches of the calcite rhombohedron oriented with the c-axis perpendicular to the surface. Depending on the level at which the rhombohedron is sectioned, the number of edges is either three or six. Small changes in the inclination of the sectioning plane concerning the c-axis provide us the whole range of edges, from three to six. The lower SEM images are tentative examples of each case.

"screw dislocation-like" growth. The tabular calcite of bryozoans differs in its crystallographic arrangement from that of craniid brachiopods, where the c-axis is at a low angle to the tablet surface (Checa et al. 2009; Simonet Roda et al. 2022). Another microstructure formerly described for the external surface of *Hornera* was "pseudofoliated calcite" (Taylor and Jones 1993). According to our observations, this is merely a variety of tabular calcite composed of imbricated calcite tablets (Fig. 16).

As previously described (Taylor and Jones 1993), virtually every tablet develops a "triple-spiked" outgrowth in the center. This seems to be a particular feature of the tabular calcite of *Hornera robusta* (Figs. 13 and 15), since it did not appear in the tabular calcite of the rest of cyclostome bryozoans (Taylor and Weedon 2000). This structure consists of a short to negligible stem that trifurcates into pointed branches (spikes) that diverge from each other at an estimated angle of ~120°. Comparable, though much larger, three-branched structures (aerials) were observed on the shell surface of the glass scallop bivalve *Catillopecten* (Kamenev 2018). Checa et al. (2022) interpreted that the branches of the aerials were aligned with the edges of the {104} calcite rhombohedron, that is, the <$\bar{4}$41> directions, being at a high angle (63.64°) to the c-axis. These are the strongest periodic bond chains (PBCs) of calcite (Aquilano et al. 2011; Massaro et al. 2008), and their growth can hardly be inhibited by the action of organic molecules. The minute size of the triple-spike branches of *H. robusta* has prevented us to analyse them by EBSD, but we hypothesize that, likewise, their growth directions might well be along the edges of the rhombohedron corresponding to the underlying calcite tablet.

4.5. Surface nanoroughness

High-resolution SEM and AFM images allow us to observe that both the foliated and tabular calcites have a marked surface roughness (Figs. 10N-P, 11K, 13H, I, M and Fig. 17), which is characteristic of almost all biominerals (Dauphin 2006; Rodríguez-Navarro 2015; Sethmann et al. 2006). From AFM analysis, biominerals typically present two phases with different contrasts: a light phase forming the bulk of the material and a dark phase distributed within the light phase in the form of pellicles (Bruet et al. 2005; Dauphin 2001; Dauphin 2008). Our AFM observations have not revealed the existence of the dark phase. According to our SEM observations of etched samples of foliated calcite, the nanoprotrusions

elongate and align parallel to the terminal edges of the laths, i.e., along directions contained within the {104} faces (Fig. 10P). In the rhombohedral calcite of the barnacle *Austromegabalanus psittacus* the nanoprotrusions were oriented along the <$\bar{4}$41> crystallographic directions, i.e., the calcite PBCs (see above) (Checa et al. 2020). We hypothesize a similar orientation for the observed alignments of nanoprotrusions of foliated calcite.

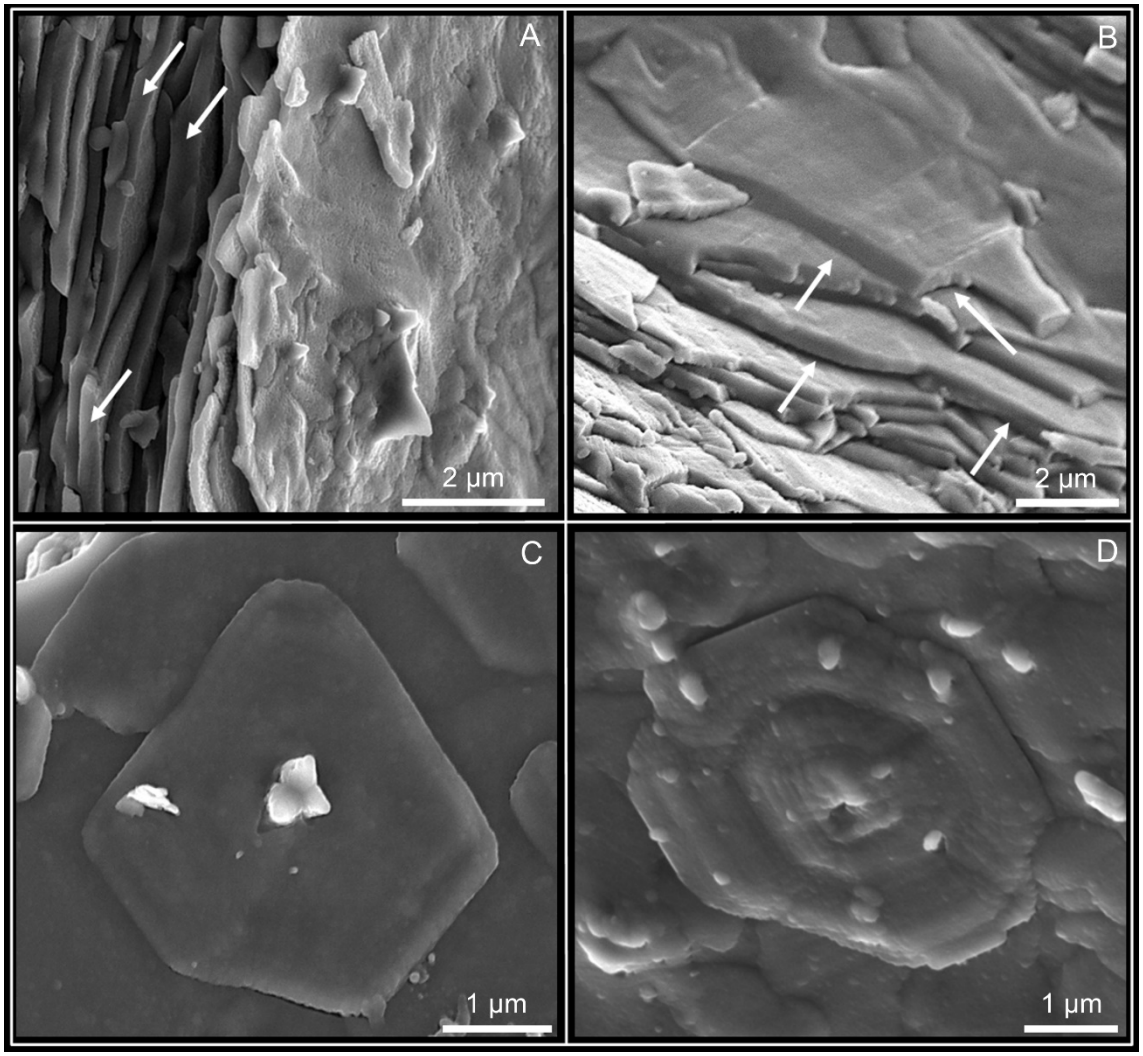

Figure 24. Close-up view of calcite tablets of *H. robusta*. A, B. Lateral views, showing the highly inclined lateral surfaces. They are smooth and straight (white arrows). C, D. Top views of the rough main surfaces of the tablets, with visible growth lines.

4.6. Final remarks

Previous research, primarily based on SEM and TEM, show that the periostracum, which is secreted by an initial stratum of palisade cells, acts as the seeding sheet for the early crystals. Calcium carbonate is secreted and released into the extrapallial space by the adjacent epithelial cells, which contain an abundance of intracellular electron-dense vesicles (Nielsen and Pedersen 1979; Tavener-Smith and Williams 1972). According to the images of Nielsen and Pedersen (1979), the extrapallial space between the secretory epithelium and the periostracum is very reduced (100-200 nm), and is traversed by tonofilamens which connect the soft body to the shell at hemidesmosomes. This pattern is similar to that found by Simonet Roda et al. (2019a,b) in articulate brachiopods. Most possibly, bryozoans follow the route of the rest of metazoans, by which calcite formation proceeds from an amorphous calcium carbonate (ACC) precursor phase (Gal et al. 2014; Weiner et al. 2009). Indirect evidence for this is the surface nanoroughness observed with AFM, which is usually interpreted as resulting from the aggregation of ACC nanoparticles (De Yoreo et al. 2015; Gal et al. 2014), although other studies (Checa et al. 2020; Macías-Sánchez et al. 2017) see it as an indication of crystallization from the previous amorphous phase across an irregular front.

Seawater chemistry at the time when clades first acquired their skeletons has been invoked as a factor influencing the skeletal mineralogy (calcite or aragonite), since it favors the production of the most stable polymorph, thus reducing the physiological costs of biomineralization (Hardie and Stanley 1997). Later on, seawater chemistry has little influence on the mineralogy because biomineralization takes place in a controlled and enclosed environment, isolated from seawater (Porter 2007; Weiner and Dove 2003). Accordingly, the fact that stenolaemate bryozoans only produce calcite could be seen as an evolutionary constraint, dating back to the origin of the group, in the Early Cambrian Stage 3

(Zhang et al. 2021), after the switch from "aragonitic" to 'calcitic' seas within the Early Cambrian Stage 2 (Maloof et al. 2010; Porter 2007). They continued to produce calcite despite the two subsequent aragonitic sea intervals II and III (late Mississippian to late Triassic or early Jurassic, and early or mid-Cenozoic to the present) (Sandberg, 1983).

The biomechanical properties of the foliated and tabular calcite of stenolaemate bryozoans have never been studied. The homeomorph foliated calcite of bivalves performs poorly in tension, compression, and bending, particularly compared to aragonitic microstructures, such as nacre and crossed-lamellar (Currey 1976). Possibly, the same can be applied to the calcitic microstructures of bryozoans. Despite this, foliated and tabular calcite have their own adaptive value due to their filling-space behavior, enabled by their high morphological versatility.

PART 2

Class Gymnolaemata

Skeletal microstructures of cheilostome bryozoans (Phylum Bryozoa, Class Gymnolaemata): Crystallography and secretion patterns

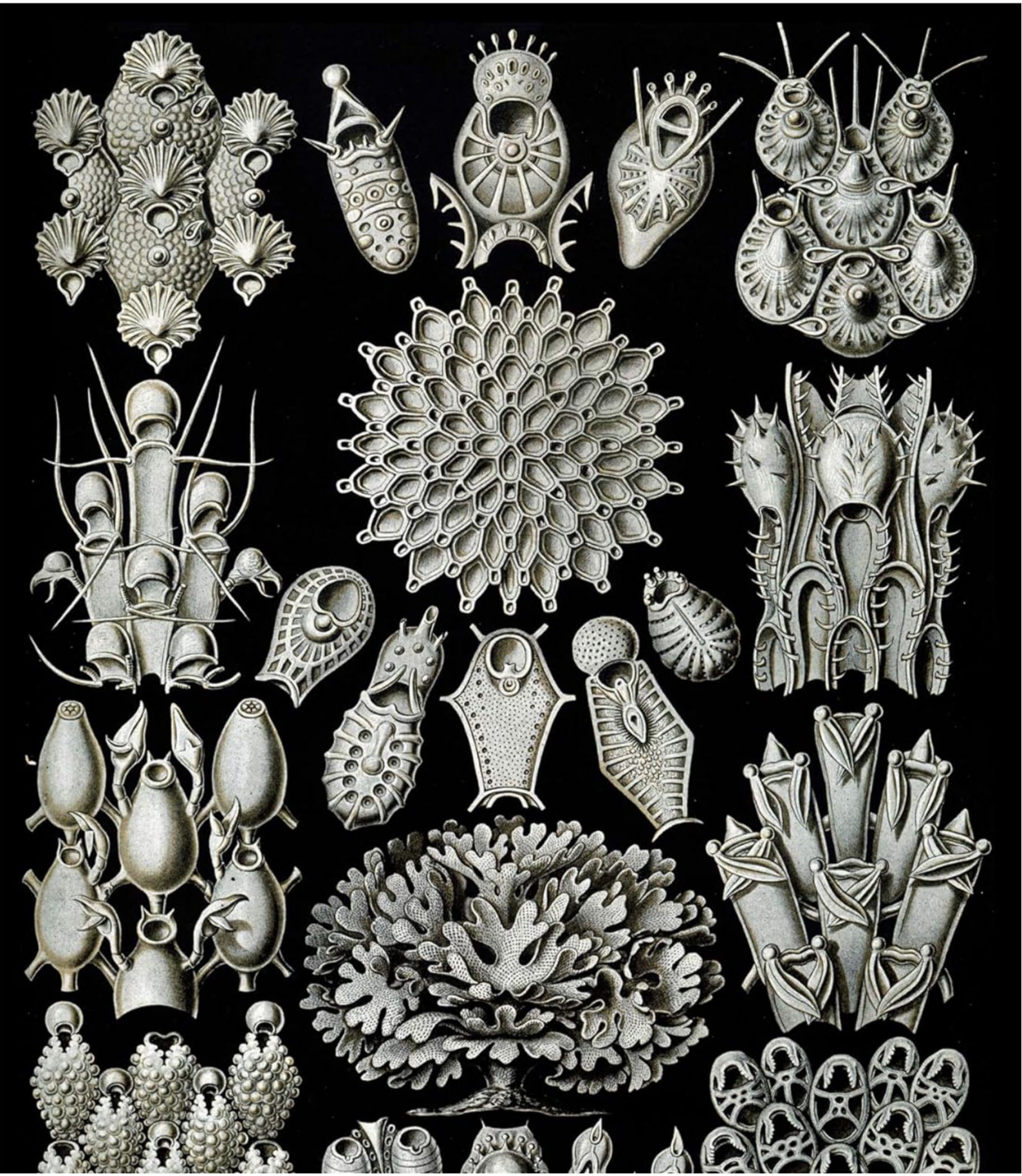

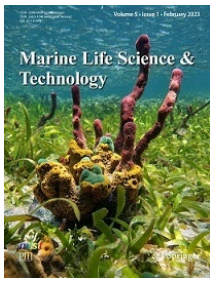

Skeletal microstructures of cheilostome bryozoans (Phylum Bryozoa, Class Gymnolaemata): Crystallography and secretion patterns

Christian Grenier[1], Erika Griesshaber[3], Wolfgang Schmahl[3], Björn Berning[4], Antonio G. Checa[1,2]*

[1]Departamento de Estratigrafía y Paleontología, Universidad de Granada, 18002 Granada, Spain

[2]Instituto Andaluz de Ciencias de la Tierra, CSIC-Universidad de Granada, 18100 Armilla, Spain

[3]Department of Earth and Environmental Sciences, Ludwig-Maximilians Universität, 80333 Munich, Germany

[4]Institute for Geology, University of Hamburg, 20146 Hamburg, Germany

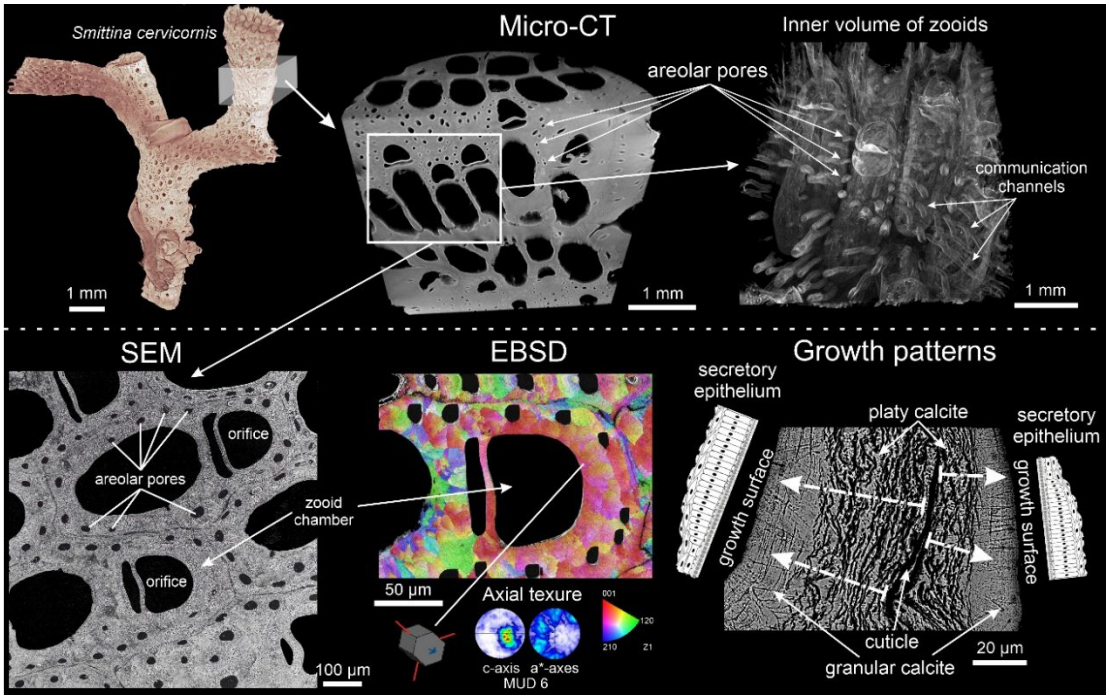

Submitted 30/11/2023
Accepted: 30/04/2024
Published online: 07/06/2024

ABSTRACT

Gymnolaemata bryozoans produce $CaCO_3$ skeletons of either calcite, aragonite, or both. Despite extensive research, their crystallography and biomineralization patterns remain unclear. We present a detailed study of the microstructures, mineralogy, and crystallography of eight extant cheilostome species using scanning electron microscopy, electron backscatter diffraction, atomic force microscopy, and microcomputed tomography. We distinguished five basic microstructures, three calcitic (tabular, irregularly platy, and granular) and two aragonitic (granular-platy and fibrous). The calcitic microstructures consist of crystal aggregates that transition from tabular or irregularly platy to granular assemblies. Fibrous aragonite consists of fibers arranged into spherulites. In all cases, the crystallographic textures are axial, and stronger in aragonite than in calcite, with the c-axis as the fiber axis. We reconstruct the biomineralization sequence in the different species by considering the distribution and morphology of the growth fronts of crystals and the location of the secretory epithelium. In bimineralic species, calcite formation always predates aragonite formation. In interior compound walls, growth proceeds from the cuticle toward the zooecium interior. We conclude that, with the exception of tabular calcite, biomineralization is remote and occurs within a relatively wide extrapallial space, which is consistent with the inorganic-like appearance of the microstructures. This biomineralization mode is rare among invertebrates.

1. Introduction

As was described for the stenolaemate bryozoans, previous research in gymnolaematans has described different microstructures arranged in distinct layers, either primary, secondary or even tertiary, according to the secretion sequence during skeletal wall growth. As explained in the general introduction (section 1.2), the box-shaped zooid chamber of gymnolaemates leads us to

distinguish principally between the inner walls and the frontal wall. The inner walls can be **basal** or **vertical**, and two vertical walls separating adjacent zooids with the cuticle in the middle are called "**inner compound walls**". It is important to highlight that in the group of anascans, the frontal wall is named as "**cryptocyst**" and in the group of ascophorans is known as the "**frontal shield**" (explained in the introduction chapter, section 1.2).

Regarding the microstructures of cheilostomes, the vast majority of studies have focused on bimineralic species (Taylor et al. 2015). The first studies based on SEM images and X-ray diffraction were performed on the genus *Metrarabdotos* by Boardman and Cheetham 1969 and Cheetham et al. 1969. According to their results, a **primary calcitic** "lamellar layer" constitutes the interior basal and vertical walls, as well as the inner layer of the frontal shields. While a **secondary aragonitic** "fibrous or wavy-lamellar layer" formed the outermost layer of the frontal shields (Figs. 1 and 2).

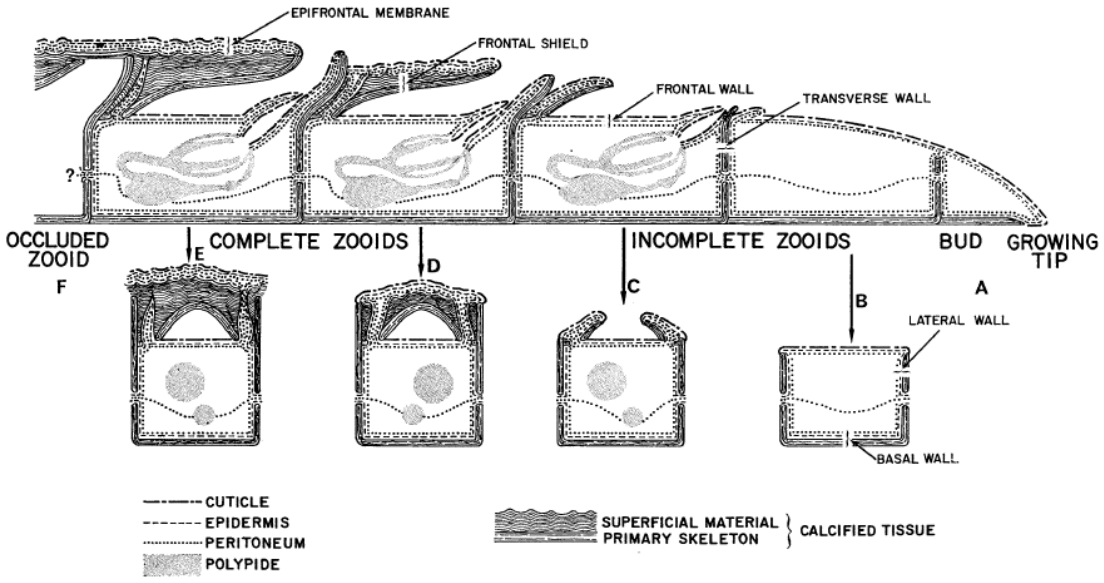

Figure 1. Longitudinal (above) and transversal (below) cross-section of an ascophoran "umbonuloid type" cheilostome bryozoan. The diagram shows different ontogenetic stages of the growing edge of a colony. Note the characteristic box-shaped zooid chambers. The inner walls (basal and vertical) are the first to be formed, and are constituted by parallel lamellar-like microstructures. The frontal shield is subsequently formed, firstly by a basal lamellar layer and later by fibrous or wavy layers. From Boardman and Cheetham (1969).

Later, in an in-depth study with fossil and recent specimens, Sandberg (1971) recognized the same aragonitic microstructure in the frontal shield, which he named "transverse fibrous". He also described a total of six different calcitic microstructures grouped into "parallel layers" (lamellar, massive internal, fibrous, and crystal stacks) and "transverse layers" (columnar or "cell-mosaic" and transverse fan).

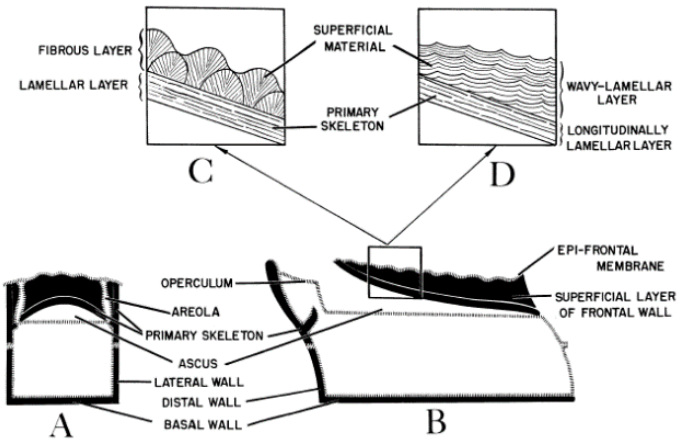

Figure 2. Diagram of transversal (A) and longitudinal (B) cross-section of *Metrarabdotos* (ascophoran "umbonuloid type") cheilostome bryozoan. Detailed views (C and D) of the primary and secondary layers of the frontal shield. From Cheetham et al. (1969).

More recently, Weedon and Taylor (2000) recognized **seven different fabric suites** in sixteen extant anascan (with primitive organization) cheilostome species (Fig. 3). All these microstructures can be grouped into both "**platy or lamellar-like microstructures**", where the plates are arranged into irregular lamellae parallel to the surface, and "**perpendicular fibrous aragonitic microstructure**", formed by perpendicular fibers arranged into spherulites in the frontal shield (Benedix et al. 2014; Sandberg 1977; Smith and Girvan 2010).

In entirely calcitic cheilostomes, the same **platy layer** was found by Bader and Schäfer (2004). Additionally, they described a secondary inner layer defined

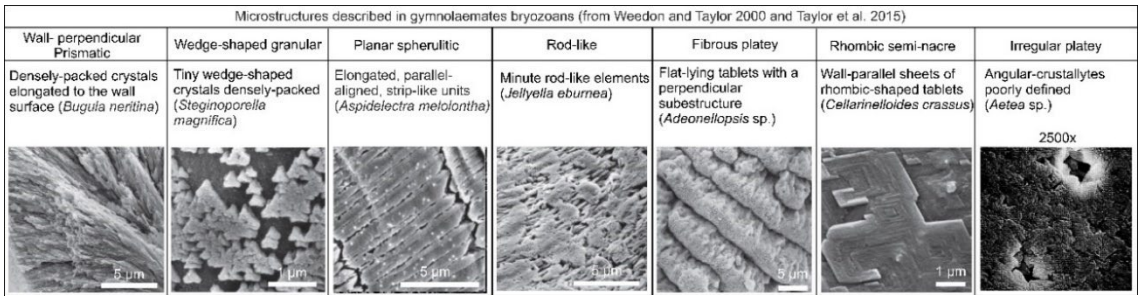

Figure 3. Summary table of the seven different microstructures described by Weedon and Taylor (2000) in gymnolaemate bryozoans.

as "densely packed crystallites" (i.e., **granular layer**). There have been fewer studies done exclusively on aragonitic bryozoans. This is most likely due to their lower abundance (notable examples are the free-living genera *Cupuladria* and the hermit crab-symbiont *Hippoporidra*; see Taylor et al. 2015). However, their microstructures are similar to those found in bimineralic bryozoans: **elongated thin fibers arranged into spherulites**.

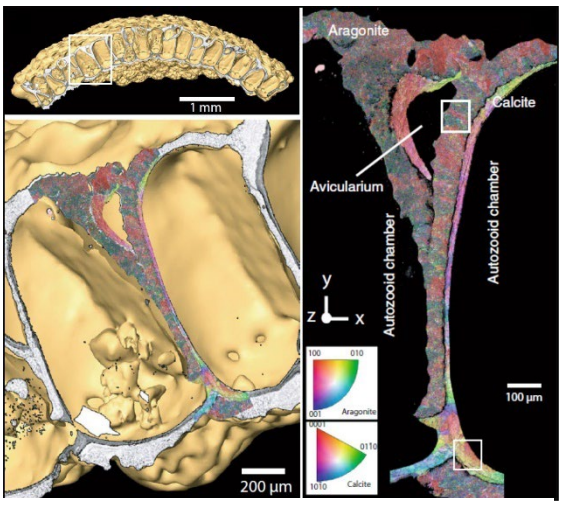

Figure 4. EBSD analysis of the skeletal structure of *Anoteropora latirostris*. The superimposed EBSD maps over the micro-CT image show the distribution of the inner calcitic layer and the external aragonitic layer. Adapted from Jacob et al. (2019).

Despite the relevance of cheilostome bryozoans as calcifiers, only one study has dealt with the crystallography of the microstructures. Examining the bimineralic *Anoteropora latirostris*, Jacob et al. (2019) (Fig. 4) determined by SEM-EBSD that calcite grain aggregates showed a stronger texture ("5–7,4 multiples of uniform distribution") than those of aragonite ("2,4 multiples of uniform distribution"). Both calcite and aragonite aggregates displayed a significant intragrain misorientation (identified by Jacob et al. 2019, as "mesocrystals") and ~ 45% of aragonite grains were twinned on the {110} plane. However, regarding cheilostome bryozoans, there is a lack of in-depth studies that elucidate the repertoire and crystallography of microstructures, in a way similar to those conducted on other calcifying groups such as molluscs, brachiopods, corals, and foraminifera (Checa et al. 2021; Coronado et al. 2019; Crippa et al. 2020; Simonet Roda et al. 2022; Yin et al. 2021).

Here, we analyze the mineralogy, crystallography, and distribution of the calcitic and aragonitic microstructures present in eight cheilostome bryozoan species by SEM, energy dispersive spectroscopy (EDS) and electron backscattered diffraction (EBSD). Additional data were obtained with atomic

force microscopy (AFM) and micro-computed tomography (Micro-CT). Taking into account the growth directions of crystal aggregates and the morphology and distribution of growth lines, we unravel the sequence of biomineralization in the different species.

2. Materials and methods

2.1. Material

Eight species of cheilostomate bryozoans were analyzed: the anascan *Calpensia nobilis* (Esper, 1796), Fam. Microporidae (though the recent molecular studies of Orr et al. 2022, and Grant et al. 2023 suggest that *Calpensia* is closely related to Thalamoporellidae and Steginoporellidae) and the ascophorans *Schizobrachiella sanguinea* (Norman, 1868), Fam. Schizoporellidae, *Rhynchozoon neapolitanum* (Gautier, 1962), Fam. Phidoloporidae, *Schizoretepora serratimargo* (Hincks, 1886), Fam. Phidoloporidae, *Pentapora fascialis* (Pallas, 1766), Fam. Bitectiporidae, *Adeonella pallasii* (Heller, 1867), Fam. Adeonidae, *Schizomavella cornuta* (Heller, 1867), Fam. Bitectiporidae, and *Smittina cervicornis* (Pallas, 1766), Fam. Smittinidae. Samples were collected at depths between 3 and 20 m in the Adriatic Sea (Korčula and Lombarda Island, Croatia) in 2008 and stored in 97% ethanol.

2.2. Micro-computed tomography (Micro-CT)

Fragments of colonies of four species (*Calpensia nobilis, Schizoretepora serratimargo*, *Schizomavella cornuta*, and *Smittina cervicornis*) were selected for micro-CT analyses. The scans were performed in an X-ray microtomograph Xradia 510 VERSA Zeiss (CIC, UGR). The fragments were fixed to the tip of a needle holder with glue and calibrated with the following parameters: 80 kV acceleration voltage, 7 W power, 75 μA beam current, and 4x magnification objective. The binning used was “bin 1” for the CDD camera detector, with a voxel size of 0.9951

μm. The total number of projections was 3201. The distance from the source to the sample was 25 mm, and the distance from the detector to the sample was 60 mm. The exposure time (per projection) and the source filter were adjusted for each sample: 14 s and LE2 filter for *C. nobilis*, 20 s and LE2 filter for *S. serratimargo*, 24 s and LE3 filter for *S. cornuta*, and 22 s and LE4 filter for *S. cervicornis*. For center shift and beam hardening effect corrections, images were processed using Reconstructor Scout and Scan™ (Zeiss, Oberkochen, Germany). We used 3D image analysis, Dragonfly Pro™ (Object Research System, slice registration method SSD) for advanced post-processing.

2.3. Scanning electron microscopy (SEM)

Fragments of each species were cleaned by immersion in commercial bleach (~ 5% active chlorine) for 2 h in a stirring set. Then, the bleach solution was removed by several sonicated washes in ultrapure water, for 2-3 min each. Once oven-dried at 40 °C for 24 h, some fragments were selected for observation, whereas others were embedded in epoxy resin (EpoFix, Struers). After 48 h of hardening, each sample section was exposed by successive grinding steps with 360, 600, 1200, and 3000 (ANSI/CAMI US grit numbers) electroplated diamond discs. Subsequently, the surfaces were polished with high-density wool felt pad discs (adding first 1 μm, followed by 0.25 μm polycrystalline diamond suspension, Struers), until reaching a mirror surface. A Hi-Tech Diamond polishing machine (All-U-Need model) was used both for grinding and polishing. Finally, an etching and decalcifying solution (2.5% glutaraldehyde, 0.25 M HEPES buffer, and 0.05 M EDTA) was applied directly to the exposed surfaces for 1 min in a stirring module. SEM observations were performed after carbon coating (Emitech K975X carbon evaporator) using secondary electron (SE) and back scatter electron (BSE) detectors in a field emission SEM FEI QemScan 650 F, a Helios Nanolab 650, and a Carl Zeiss SMT AURIGA Crossbeam Station. All the

equipment was housed in the Centro de Instrumentación Científica (CIC, University of Granada, UGR) and in the Servicios Centrales de Apoyo a la Investigación (SCAI, University of Málaga, UMA).

2.4. Electron backscattered diffraction (EBSD)

EBSD (61) maps were performed on the eight species studied. The same samples prepared for SEM observation were finished with a manual etch-polishing step, applying colloidal alumina for 3 min. The samples were coated with 4 to 6 nm of carbon (Leica EM ACE200). Measurements were taken on a Hitachi SU5000 field emission SEM, equipped with an Oxford Instruments NordlysNano II EBSD detector. The SEM was operated at 20 kV, and Kikuchi patterns were indexed with the CHANNEL 5 HKL software. EBSD measurements were performed in step increments between 200 and 500 nm.

2.5. Atomic Force Microscope (AFM)

Colony fragments of *Rhynchozoon neapolitanum*, *Pentapora fascialis*, and *Smittina cervicornis* were cleaned by immersion in commercial bleach (~5% active Cl, 8h). The bleach solution was then removed by 2 to 3 washes in MilliQ water by sonication, for 2-3 min each. Once oven-dried at 40 °C for 24 h, samples were reduced to small fragments, oriented and placed on flat metal discs for AFM observation, so that the external surfaces and walls sections were exposed. Additionally, the samples of these species prepared for SEM (embedded in resin and polished as explained above) were analyzed. An AFM Park Systems NX20 equipped with a cantilever MikroMasch ACTA (K = 40 N/m, F = 320 kHz) (CIC, UGR) was used in Tapping and PinPoint modes to record height, amplitude, and phase signals. Images were obtained with Smart Scan v12 and processed using XEI software (4.3.0. Build2, Park Systems).

3. Results

3.1. Colony structure and zooid arrangement

The bryozoans were analyzed from either encrusting unilaminar (e.g., *Calpensia nobilis* and *Schizomavella cornuta*; Fig. 5A-E) or erect ramose bilaminar colonies (e.g., *Schizoretepora serratimargo* and *Smittina cervicornis*; Fig. 6A-F). In the encrusting colonies, the basal wall attaches directly to the substratum (Fig. 5A and B) while in the erect colonies, the zooids are disposed in a bilaminar layer, with back-to-back basal walls (Fig. 6C and E).

Some of the species studied exhibit a well-developed polymorphism. For instance, avicularia can be distinguished in both *S. cornuta* and *S. serratimargo*. *S. cornuta* has only small suboral avicularia (Fig. 5D) and *S. serratimargo* has numerous adventitious avicularia, some of which are larger than others (Fig. 6A). Intact and fractured ovicells (calcified brooding capsules for the embryos) can be found distally from the orifice in some autozooids (rounded and darker depressions in Fig. 6A).

An example of the inner volume occupied by the zooids and the funicular system is shown for *S. cervicornis* (Fig. 6F). The areolar pores connect the inner zooidal coelom with the hypostegal coelom (between the frontal shield and the frontal cuticle). Additionally, the communication pores that cross the compound lateral walls of two neighboring zooids are highlighted in the framed area of Fig. 6F.

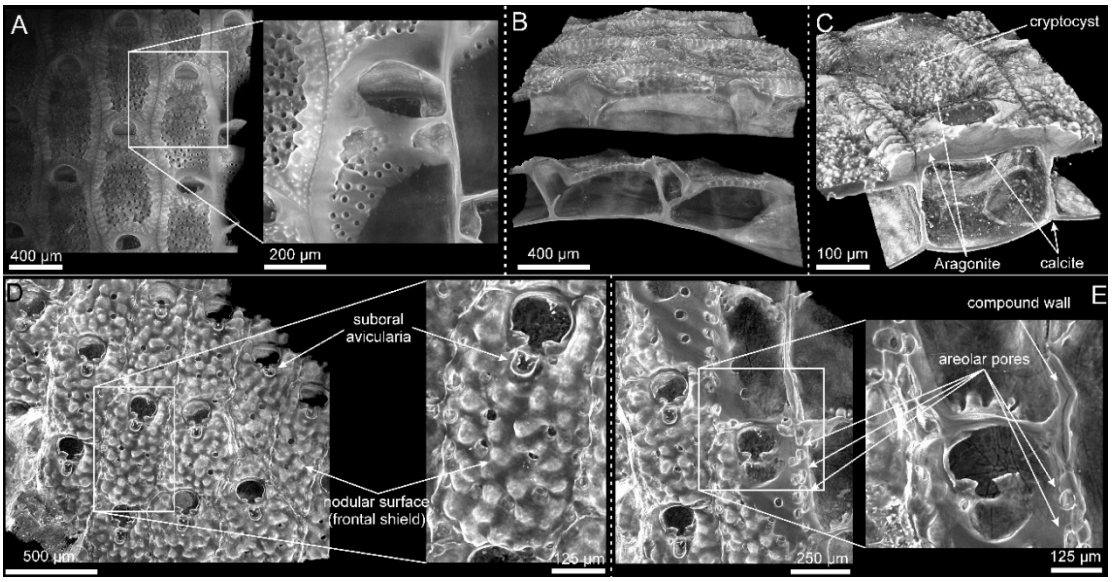

Figure 5. Micro CT images of the encrusting colonies of *Calpensia nobilis* (A-C) and *Schizomavella cornuta* (D-E). A. Frontal view of the colony fragment. The zooids are arranged in a single layer; they are aligned in rows and offset with respect to the zooids of the neighboring rows. The orifices display a semicircular shape and the cryptocyst, which lies below the frontal membrane in the living organism, is perforated by pores. The interior of the chambers of the zooid is progressively exposed toward the bottom (zoomed view of the framed area), revealing the thin interior walls. B. Two lateral views of the same fragment sectioned at different depths. The unilaminar encrusting colony structure can be seen. C. Oblique view of an isolated zooid. There is a slight contrast between the calcitic interior walls (darker) and the aragonitic cryptocyst (lighter) (indicated). D. Frontal view of a colony fragment. The orifices display a semicircular shape and all zooids have small suboral avicularia. The frontal shield exhibits a nodular surface (close-up view to the right). The zooids are slightly offset to each other. E. Fragment sectioned slightly oblique to the frontal surface; the areolar pores can be seen along the interior compound walls.

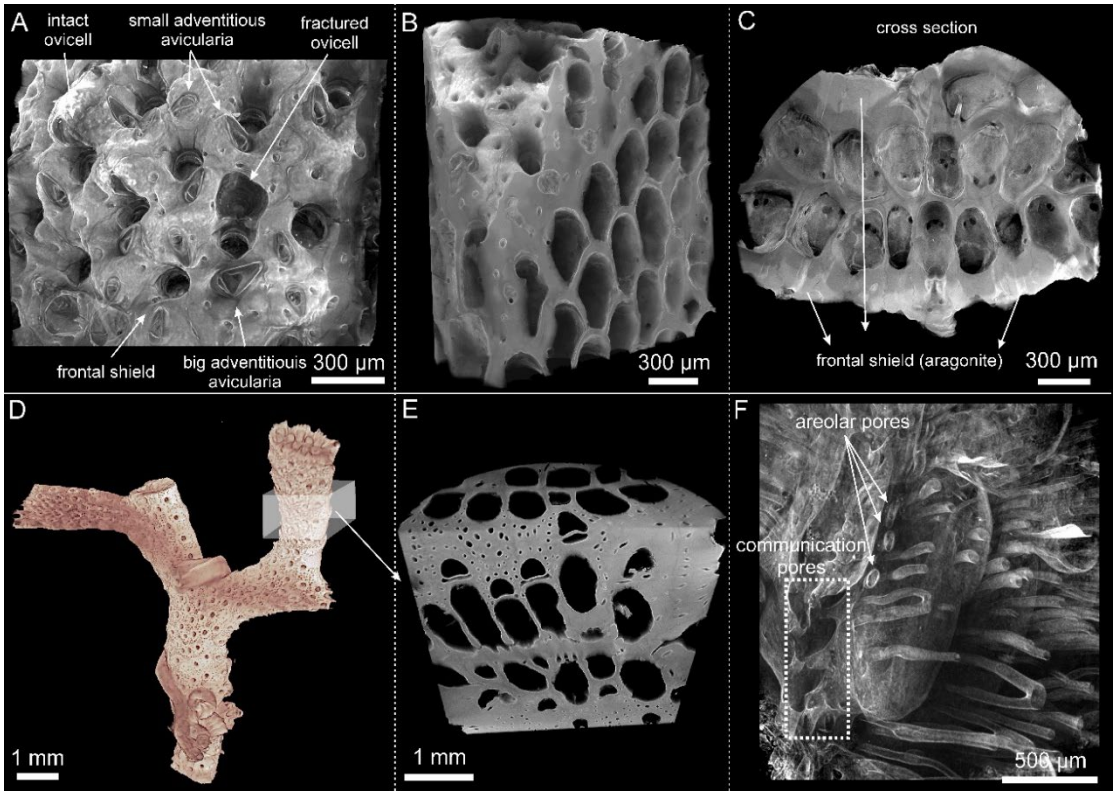

3.2. Mineralogy

The distribution of calcium carbonate polymorphs (calcite and aragonite) was determined by EBSD phase maps and Mg/Sr EDX maps (Figs. 7, 8, and 9). We grouped the eight cheilostome species into (1) bimineralic (*Schizobrachiella sanguinea*, *Calpensia nobilis*, *Schizoretepora serratimargo*, *Pentapora fascialis* and *Adeonella pallasii,* Fig. 7), (2) calcitic (*Smittina cervicornis,* Fig. 8), and (3) predominantly aragonitic (*Rhynchozoon neapolitanum* and *Schizomavella cornuta,* Fig. 9). In bimineralic bryozoans, calcite constitutes the main structures of the zooecium: interior vertical and compound walls and the first basal layers of the frontal shield (or cryptocyst in *C. nobilis*), while aragonite is only present in the outermost layer of the frontal shield (or cryptocyst in *C. nobilis*). We identified five main microstructures: three calcitic (tabular calcite, irregularly platy calcite, and granular calcite) and two aragonitic (fibrous aragonite and granular-platy aragonite).

☚ **Figure 6.** Micro CT images of the erect ramose colonies of *Schizoretepora serratimargo* (A-C) and *Smittina cervicornis* (D-F). A. Frontal view of the colony fragment. Different polymorphic zooids can be observed (autozooids and avicularia). B. Same fragment as in A sectioned longitudinally, exposing the interior of the zooids and the thick interior vertical walls (compound walls). The zooids are arranged in a zigzag pattern. C. Cross-sectional view, showing the double-layer arrangement of the zooids. D. Erect-branched colony. E. Close-up of a branch sectioned along two perpendicular planes, demonstrating the zooid disposition and the thick external frontal shields. F. Image of the inner volume occupied by the zooidal polypides, revealing the areolar channels oriented toward the frontal shield.

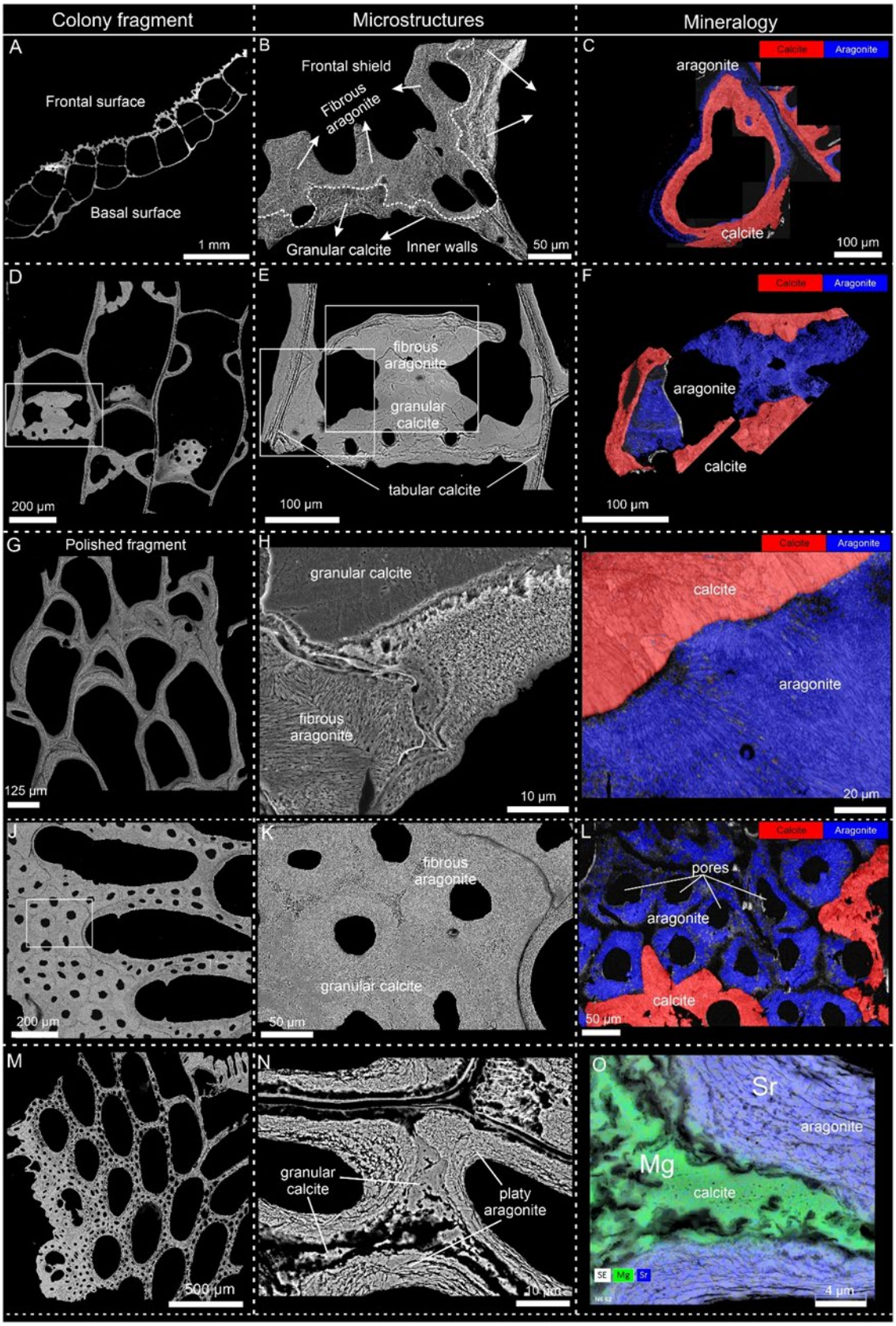

Figure 7. Microstructures and calcium carbonate polymorph distributions of the bimineralic bryozoans analyzed. A-C. *Schizobrachiella sanguinea*. D-F. *Calpensia nobilis*. H-I. *Schizoretepora serratimargo*. J-L. *Pentapora fascialis*. M-O. *Adeonella pallasii.* The left and intermediate columns are representative SEM images. The right columns are EBSD phase (C, F, I and L) and EDX (O) maps performed in each sample.

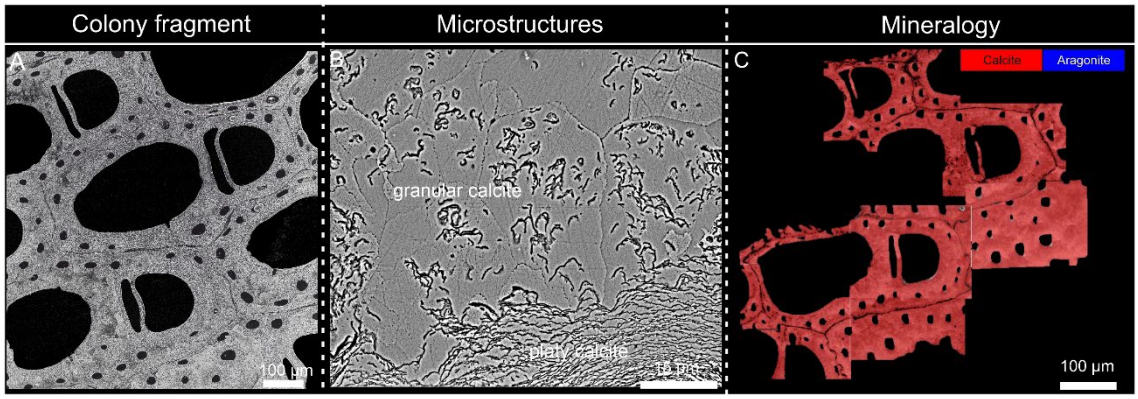

Figure 8. Microstructures and calcium carbonate polymorph distribution of the fully calcitic bryozoan analyzed, *Smittina cervicornis*. A and B. SEM images of representative areas. C. EBSD phase map.

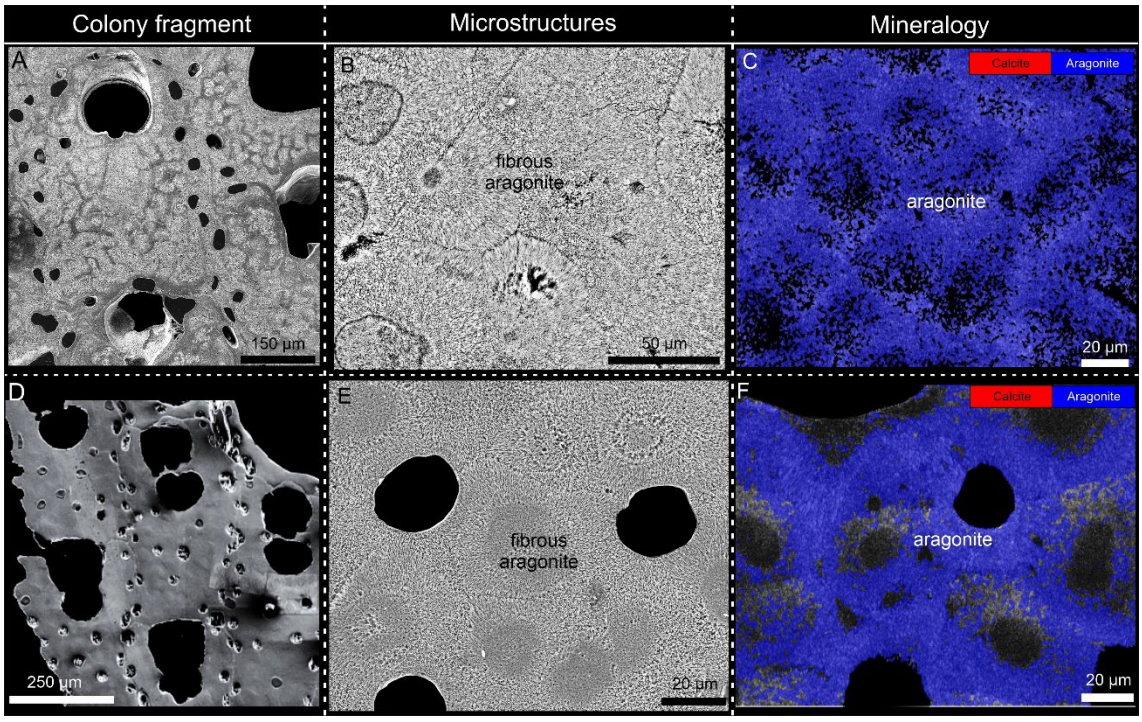

Figure 9. Microstructures and calcium carbonate polymorph distribution of the aragonitic bryozoans analyzed. A-C. *Rhynchozoon neapolitanum*. D-F. *Schizomavella cornuta.* The left and center columns are SEM images of representative areas. The right columns are EBSD phase maps (C and F).

3.3. Microstructures of the bimineralic bryozoans

3.3.1. Calcite microstructures

Tabular calcite is only present in the center of the interior vertical and compound walls of *Calpensia nobilis* (Fig. 10A-C). It consists of thin flat rhomboidal crystals that are tightly stacked and parallel to the inner surface (Fig. 10A). The tablets are typically spiral-shaped and the step size is the thickness of one tablet (see inset in Fig. 10B). The number of sides ranges from 4 to 6, and their diameters can reach up to 10 μm, depending on the growth stage. In a cross-section view, the thickness of the tablets ranges between 100 nm to 300 nm, and the boundaries are marked by abundant organic threads (Fig. 10C). At high magnification, the growth lines and the surface nano-roughness of the polygonal tablets, are visible (Fig. 10B). Growth lines indicate that tablets spread laterally until colliding with other tablets growing at the same level (Fig. 10B).

Irregularly platy calcite is made up of lamellar crystals that constitute the central part of the interior vertical and compound walls in *Schizoretepora serratimargo, Schizobrachiella sanguinea,* and *Pentapora fascialis*, arranged parallel to each other and to the inner surface (Fig. 10D-G). The thickness of individual lamellae is not constant because of the undulate morphology of their boundaries, and wedging out of lamellae is also frequent (Fig. 10E, F, and G). The thickness ranges from 0.2 μm to 3 μm, while the lateral extensions can vary from 10 μm to several tens of micrometers. Hence the name “irregularly platy”. Slight etching and decalcification treatment on polished surfaces reveals the dense distribution of organic threads encasing the crystals (inset in Fig. 10D).

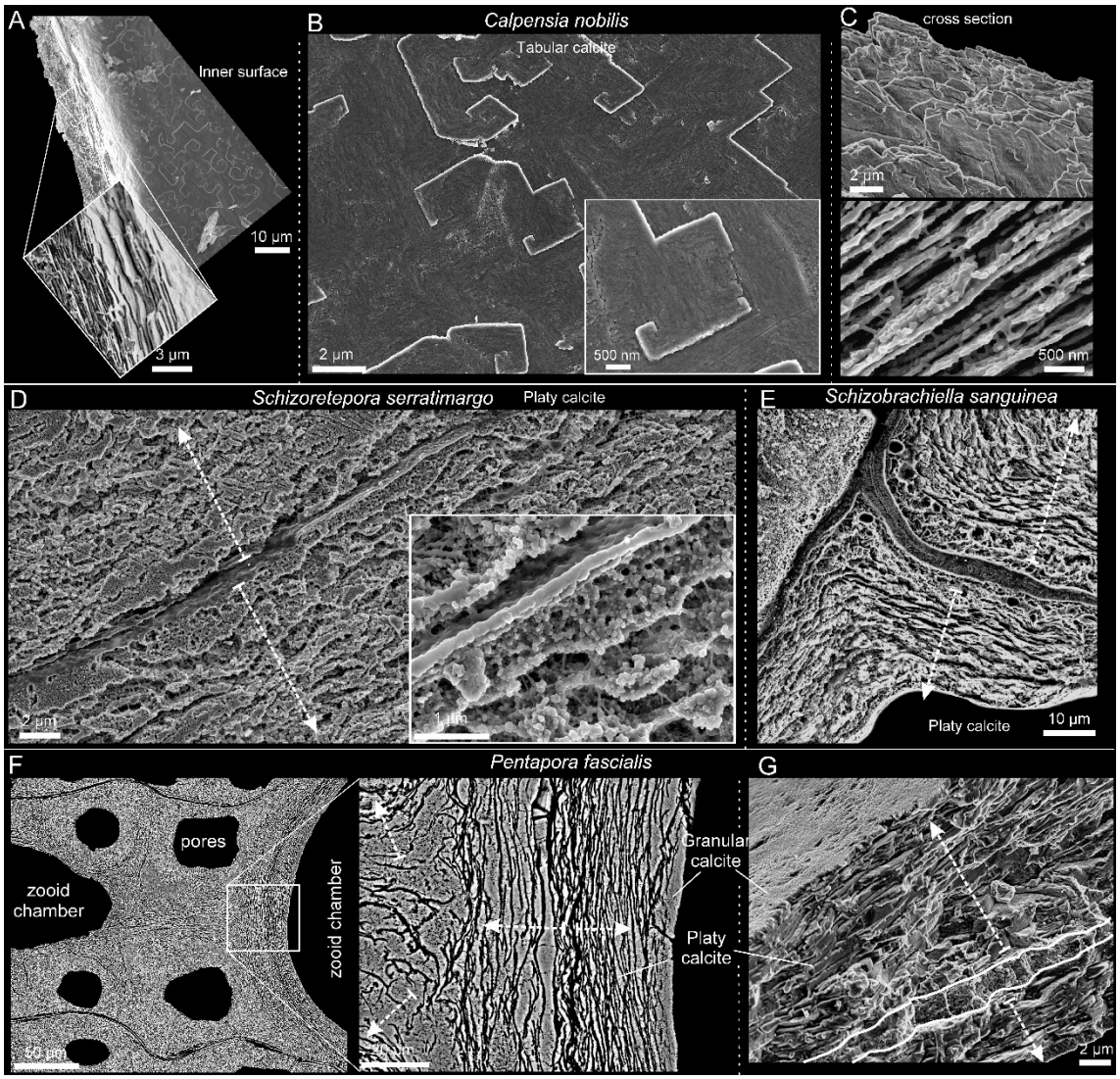

Figure 10 SEM images of the tabular (A-C) and platy (D-G) calcites. A-C. *Calpensia nobilis*. A. Fragment of interior vertical and basal walls, composed entirely of tabular calcite (inset) in an early stage of development. B. Detailed view of an unaltered inner surface. The spiral-shaped polygonal tablets cover the entire surface. The surface nano-roughness and the growth lines are visible (inset). C. Cross-section of a wall showing the stacking of tablets, which produces a lamellar arrangement. The organic threads between the crystals are visible in the bottom image. D. Polished and slightly decalcified compound wall of *Schizoretepora serratimargo* made of irregularly platy calcite. The crystals grow from the cuticle inwards in both directions (arrows). The inset shows the organic threads that surround the crystals. E. Polished-etched section through compound walls of *Schizobrachiella sanguinea*, showing the irregular and sinuous outlines of the laminae of the irregularly platy calcite. The lamellar crystals are arranged parallel to the inner surface, adapting tightly to the curvature at the corners. Dashed arrows indicate the growth directions of the layers. F, G. *Pentapora fascialis*. F. Polished section along two zooid chambers. The zoomed area shows the irregularity of the platy calcite. The dashed white arrows indicate the growth directions. G. Fracture of an interior vertical wall. The platy calcite becomes organized and grows from a finely granular central region (outlined) in both directions (white arrows). A thin granular layer covers the innermost surface.

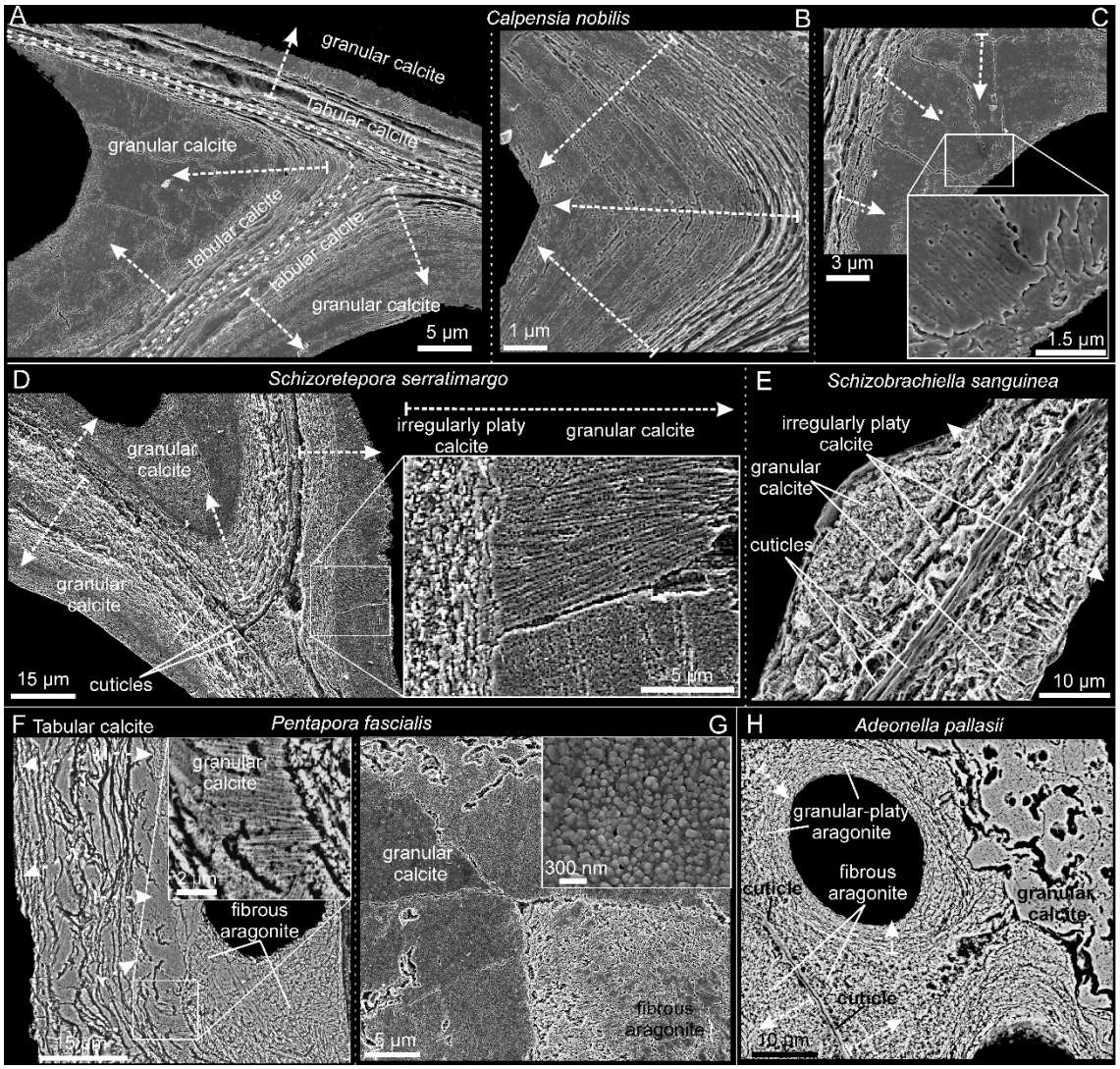

Figure 11. Relationship between calcitic microstructures in bimineralic bryozoans. A-C. Polished sections of compound walls of *Calpensia nobilis*. A. Compound wall. Tabular calcite is present from the center (dashed lines) and extends on both sides. As the wall thickens, the tablets become more and more compact until they finally grade into a thick granular calcite layer. B, C. Interior walls at the corners. Granular calcite covers the innermost surface of the zooecium, becoming thicker at the corners. The grains display an internal fibrosity coincident with the marginal serrated teeth (inset in C). D. Polished sections of a compound wall of *Schizoretepora serratimargo*. Similar to tabular and granular calcite, the irregularly platy calcite becomes progressively more compact until changing into granular calcite. The close-up view of the framed area demonstrates that the fibrosity is continuous across both microstructures. E. Polished and slightly decalcified section of a thin compound wall of *Schizobrachiella sanguinea*. The transition from irregularly platy to granular calcite is barely perceptible. F, G. Polished compound wall sections of *Pentapora fascialis*. As usual, the transition from irregularly platy to granular calcite is gradual. The internal fibrosity of crystals is also continuous across both layers and can be traced up to the boundary with the aragonite layer (see inset in F). A magnified view (inset in G) shows the surface nano-roughness of the granular calcite. H. Polished compound wall section of *Adeonella pallasii.* Granular calcite is found at the interior walls of the zooecium. Fibrous aragonite spreads from the cuticle inwards and between the pores, which are in turn surrounded by granular-platy aragonite in a concentric disposition. White dashed arrows indicate the growth directions.

Granular calcite was found in all bimineralic bryozoans analyzed. It constitutes a relatively coarse layer that is always at the interior of the zooecial chambers or below the outer aragonite layers of the frontal shield (Figs. 11 and 13). In cross-section, the grains range from 3 to 10 μm in width, and from less than 5 to more than 20 μm in length (Fig. 11A-H; Fig. 12A and B), becoming particularly large in the curvature zones (i.e., at the angles) of the interior walls. They extend in the direction of growth and demonstrate irregular boundaries (pseudodendritic) with neighboring grains (Fig. 11A-C). When conveniently etched, the granular crystals display an internal fibrosity. The individual fibers are closely spaced, oriented towards the growth direction, and terminate into the small teeth of the serrated margins (Fig. 11C, D and inset in F). This internal fibrosity can also be appreciated in fractures (granular layer in Fig. 13C and inset in G). In a magnified view, the characteristic surface nano-roughness is revealed (inset in Fig. 11G). The AFM phase signal (Fig. 12C) does not show any consistent change in composition. The size of the nanoprotrusions ranges from several tens to more than 100 nm (Fig. 12C).

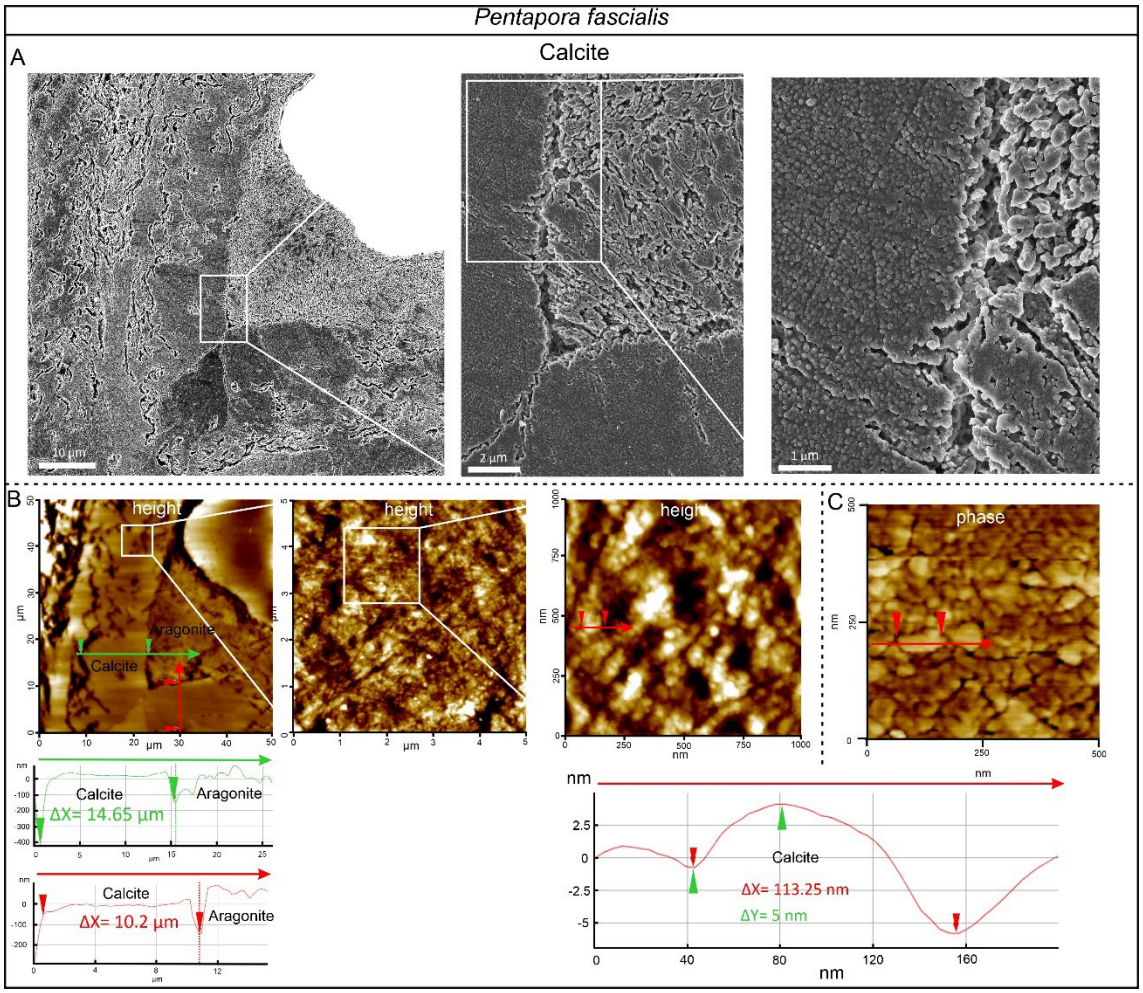

Figure 12. AFM analysis of the granular calcite of the frontal shield of *Pentapora fascialis*. A. From left to right, SEM images at increasing magnifications of a region similar to that scanned with the AFM. The surface nanoroughness can be appreciated in the right image. B. AFM height images at increased magnifications (framed areas) of the granular calcite. The profiles of the transects outlined in the height images indicate sizes of the calcite grains ranging from 10 µm to 14 µm in width. The selected nano-protrusion has a diameter of 113 nm and a height of 5 nm (see the graphs). C. The phase image shows dark/light contrast between different areas.

3.3.2. Aragonite microstructures

In bimineralic species, **fibrous aragonite** forms the outermost layer of either the cryptocyst (in *Calpensia nobilis*, Fig. 13A-B) or the frontal shield (in all other bimineralic species, e.g., *Schizoretepora serratimargo* and *Pentapora fascialis*, Fig. 13C-H), which is secreted onto a basal calcitic layer (tabular, platy, or granular) (Fig. 13B and D). Fibrous aragonite is made of thin and long crystals arranged into spherulites (Fig. 13C, F, and H), whose growth surfaces protrude toward the frontal surface, giving it a nodular aspect (Fig. 13C). This nodularity is enhanced

when the frontal shield is perforated by the frontal or areolar pores (Fig. 13E and F). The size of the fibers of the cryptocyst of *C. nobilis* is smaller (60-150 nm in width, 2-4 μm in length, Fig. 13A) than those of the frontal shields of the ascophoran species. For instance, in *P. fascialis* the fibers range from 200 nm to 600 nm in width and from 2.5 μm to >10 μm in length (Fig. 14A-C). The nanoroughness of the surface can be seen at higher magnification (Fig. 14B and C) but no contrast differences were detected in the AFM phase signal (Fig. 14D). The size of the nanoprotrusions may vary from several tens to over 150 nm, slightly larger than those analyzed in the granular calcite (see Fig. 14C).

Granular-platy aragonite was only found in *Adeonella pallasii*, surrounding the pores of the frontal shield (Figs. 7M-O, 11H, and 13I-K). In cross-section, irregularly platy aragonite units can be confused with those of the irregularly platy calcite. Nevertheless, the platy aspect is less well-developed and the crystals often appear subdivided transversely, leading to the formation of granular units with angular outlines (Fig. 13I, J and K), sometimes reminiscent of crystal faces (Fig. 13K, inset). The sizes of grains vary from less than 1 μm to more than 5 μm in length and from less than 200 nm to 1 μm in width.

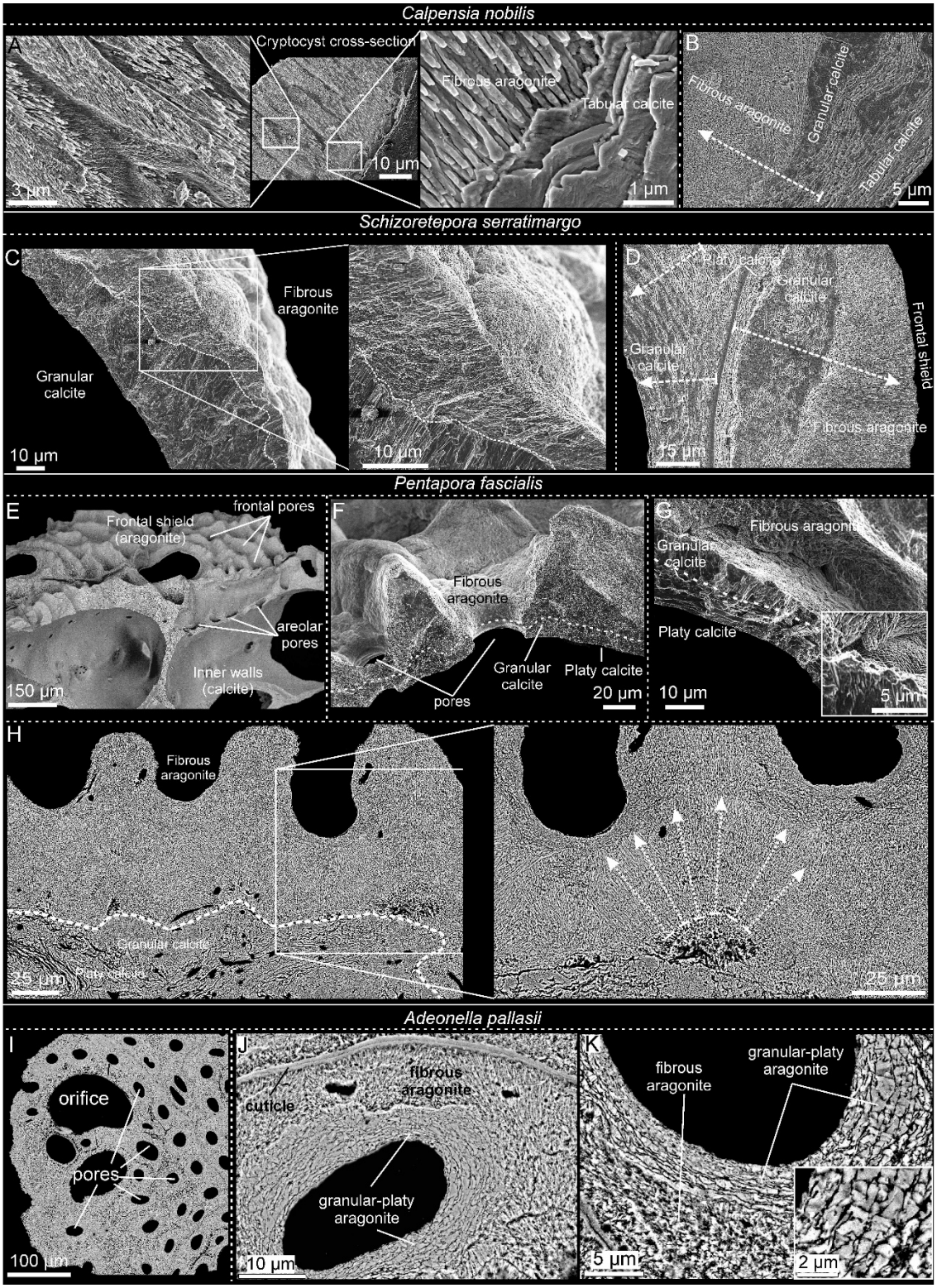
Calpensia nobilis
A
Cryptocyst cross-section
3 µm
10 µm
Fibrous aragonite
Tabular calcite
1 µm
B
Fibrous aragonite
Granular calcite
Tabular calcite
5 µm
Schizoretepora serratimargo
C
Fibrous aragonite
Granular calcite
10 µm
10 µm
D
Platy calcite
Granular calcite
Granular calcite
Frontal shield
Fibrous aragonite
15 µm
Pentapora fascialis
E
Frontal shield (aragonite)
frontal pores
areolar pores
Inner walls (calcite)
150 µm
F
Fibrous aragonite
Granular calcite
Platy calcite
pores
20 µm
G
Fibrous aragonite
Granular calcite
Platy calcite
10 µm
5 µm
H
Fibrous aragonite
Granular calcite
Platy calcite
25 µm
25 µm
Adeonella pallasii
I
orifice
pores
100 µm
J
fibrous aragonite
cuticle
granular-platy aragonite
10 µm
K
fibrous aragonite
granular-platy aragonite
5 µm
2 µm

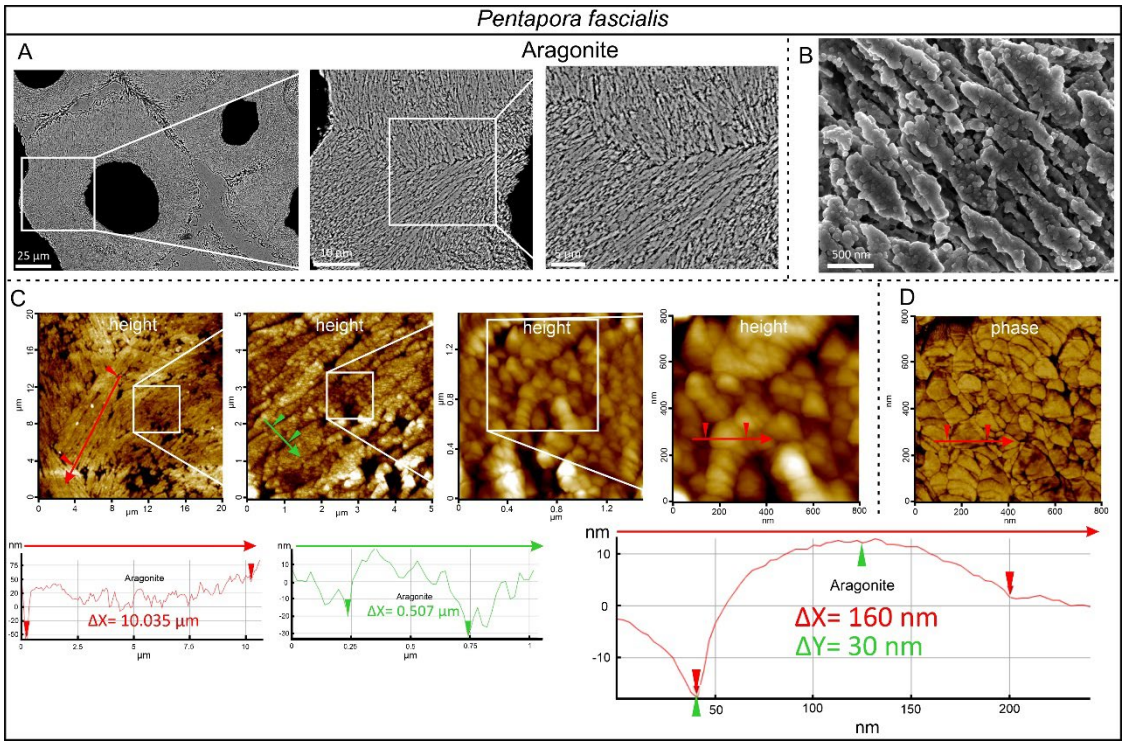

Figure 14. AFM analysis of the fibrous aragonite that surrounds the pores of the frontal shield of *Pentapora fascialis*. A. From left to right, SEM images at increasing magnifications (framed areas) of a region similar to that scanned with AFM. B. High-magnification view of a set of fibers where the surface nano-roughness can be appreciated. C. From left to right, AFM height images of the fibrous aragonite at increasing magnifications (framed areas). The profiles of the transects drawn at the height images give fiber lengths of 10 µm and close to 0.6 µm in width. The transects of the highest resolution images indicate that the diameter of the selected nano-protrusion is 160 nm and a height of 30 nm. D. The phase map appears homogeneous, indicating no changes in the composition.

☚ **Figure 13.** Fibrous aragonite in bimineralic bryozoans. A. Fractured cross-section of the cryptocyst of *Calpensia nobilis*. The aragonitic fibers directly overlie the basal layer of tabular calcite. B. Polished cross-section of the cryptocyst, showing the transition from tabular to granular calcite, and the change to fibrous aragonite (growth direction indicated by the dashed white arrow). C. Fracture of a frontal shield of *Schizoretepora serratimargo*. The basal layer of granular calcite predates the fibrous aragonite layer. The close-up of the framed area (right) shows the spherulites of aragonite, which give a nodular appearance to the outer surface. D. Polished section of the frontal shield, displaying the same sequence of microstructures as in the cryptocyst of *C. nobilis*: irregularly platy calcite, granular calcite, and fibrous aragonite. The white dashed arrows indicate growth direction. E. Lateral view of several fractured zooecia of *Pentapora fascialis* showing their frontal shields, the vertical walls, and the smooth interior skeletal surfaces. F, G. Close-up views of the frontal shield. The aragonite spherulites grow onto the calcite layers (inner platy and middle granular), forming the protuberances of the frontal surface around the pores. The granular calcite displays toothed external surfaces (inset in G). H. Polished longitudinal section of a frontal shield, showing the basal layers of platy and granular calcite and the outer layer of fibrous aragonite. The aragonite fibers display a fan-shaped arrangement (close up). The dashed arrows indicate growth directions. I. Longitudinal cross-section of the frontal shield of a zooid of *Adeonella pallasii*, showing the numerous frontal pores. J. View of a compound wall with the cuticle at the top, the granular-platy aragonite surrounding the pore, and the fibrous aragonite spreading in between, in a fan-shaped arrangement. K. Detailed view of the granular-platy and fibrous aragonites. The platy units are subdivided, forming angular grains (inset).

3.4. Microstructures of the calcitic bryozoans

The only bryozoan analyzed that possessed a wholly calcitic skeleton was *Smittina cervicornis* (Figs. 8A-C and 15). The microstructures that are secreted are irregularly platy and granular calcite (Fig. 15A and B), identical to those found in bimineralic bryozoans. The layer adjacent to the cuticle in compound walls is made of irregularly platy calcite (Fig. 15C and D), while a granular calcite layer covers the inner surfaces of the zooecium. As the frontal shield thickens, there is a smooth transition from a platy to a granular microstructure (of the kind described in bimineralic bryozoans). Towards the surface, the irregularly platy calcite becomes more undulated, and the growth increments become more marked (Fig. 15E). Fibers reveal a surface nanoroughness under high magnification (Fig. 16A). The phase signal shows changes in contrast, indicating variations in composition. Nanoprotrusions range from a few tens to more than 100 nm (see Fig. 16B and C), similar to those from granular calcite in bimineralic bryozoans (Fig. 12B).

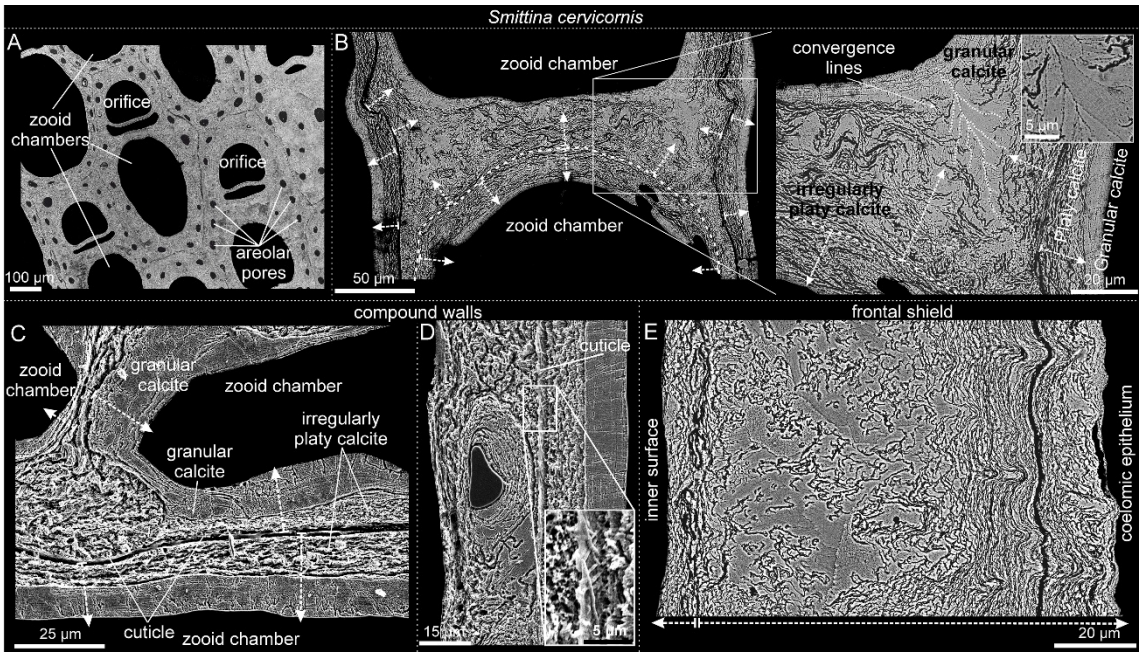

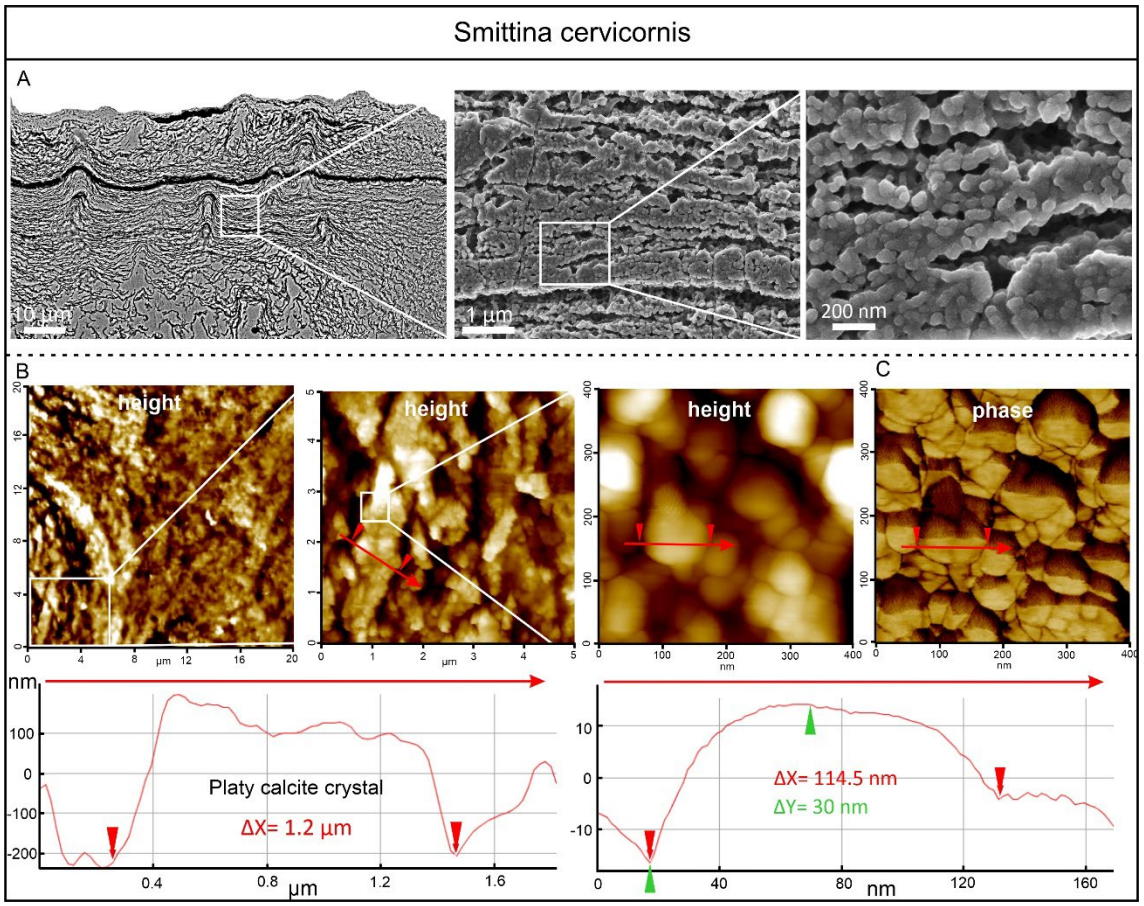

Figure 16. AFM analysis of the irregularly platy calcite of the external wall of *Smittina cervicornis*. A. From left to right, SEM images at different magnifications (see framed areas) of a similar region to that scanned with the AFM. The surface nanoroughness is clearly visible in the right image. B. AFM height images at increased magnifications (framed areas) of the region scanned. The height profiles indicate a width of the selected calcite plate of 1.2 µm (left) and a diameter of 114.5 nm of the selected nano protuberance, with a height of 30 nm (right). C. Phase image showing the presence of a dark phase at the top edges of the nanoprotrusions.

Figure 15. SEM images of the irregularly platy and granular calcites of *Smittina cervicornis.* A. Polished colony fragment. The section plane cuts the zooids longitudinally. B. Polished surface of the compound walls between adjacent zooids. The white dashed arrows indicate the growth direction from the cuticle between the zooids (marked with broken lines) toward the interiors of the chambers (detailed view in the inset). The close-up of the framed area shows the transition from platy to granular calcite. Due to the high curvature of the wall, the grains (growing at high angles to the wall) converge along irregular bisecting lines (thin broken lines). C, D. Polished-etched compound wall in longitudinal section. The growth direction proceeds from the cuticle towards the zooid interior, with the irregularly platy calcite forming first, followed by the granular calcite. The irregularly platy calcite surrounds the areolar pores and their laminae display a concentric disposition (D). The fibrous nature of the cuticle can be appreciated (inset in D). E. Polished cross-section of a frontal shield. Two growth directions are discernible: (1) toward the zooid interior (left) and (2) toward the frontal surface (bottom dashed arrows).

3.5. Microstructures of the aragonitic bryozoans

Rhynchozoon neapolitanum and *Schizomavella cornuta* (Fig. 17) are the only species whose skeletal structures (interior walls, compound walls, and frontal shields; Fig. 9) are made entirely of fibrous aragonite. As described above for bimineralic bryozoans, fibrous aragonite consists of fibrillar crystals arranged into spherulites. The convex, free surfaces of the spherulites produce a nodular aspect to the outer surface of the frontal shield (Fig. 17A). Individual fibers are 2 to ~40 μm long, depending on the size of the spherulite, and 0.5 to 1 μm wide (Fig. 17B, C, E and F). In the interior walls, the fibers nucleate onto an unstructured, granular central layer and spread on both sides toward the inner surfaces. The result is a wall with a sandwiched structure (Fig. 17D). In the compound walls that separate adjacent zooids, the fibers nucleate from the cuticle (placed at the center) toward the interior of the zooecium (Fig. 17E). In both cases, the inner surfaces are relatively smooth. At the frontal shield, the aragonite fibers spread toward the exterior (Fig. 17F-H). During the thickening of the frontal shield, the spherulites merge with each other. In polished sections, nucleation centers are clearly visible (Fig. 17F). The growth surface of the spherulites is convex or straight, depending on whether it grows free or abuts a neighboring spherulite (Fig. 17G and H).

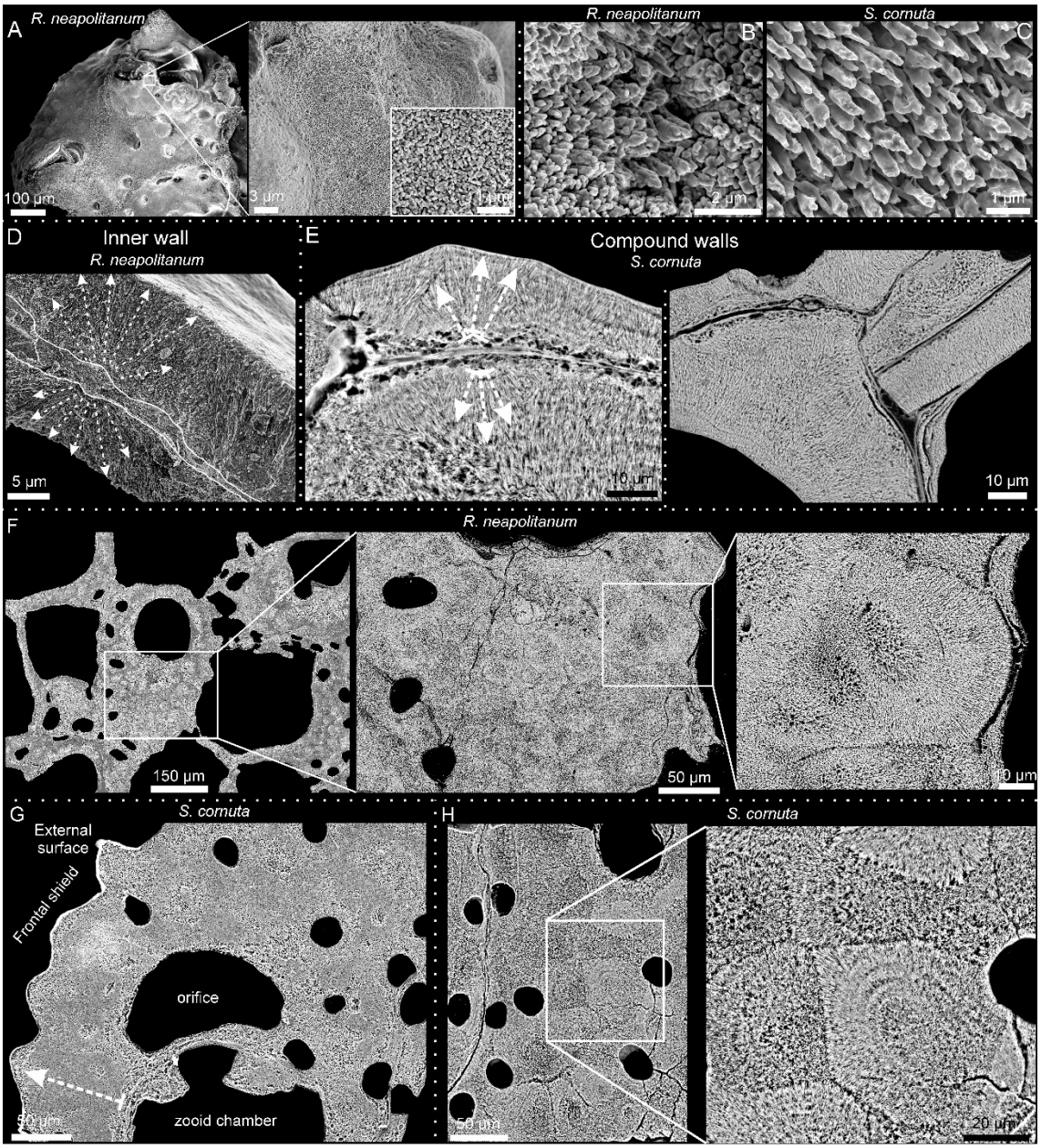

Figure 17. SEM images of the fibrous aragonite of *Rhynchozoon neapolitanum* (A, B, D, F) and *Schizomavella cornuta* (C, E, G, H). A. Autozooid and adventitious avicularia of *R. neapolitanum*. The close-up view to the right shows the nodular reliefs. The small inset shows the granular aspect of the external surface. B, C. Detailed views of the bundles of aragonite fibers of both species. D. Fracture of an interior wall of *R. neapolitanum*. The aragonite crystals grow bidirectionally from a granular center, resulting in a sandwich structure. E. Polished compound wall sections of *S. cornuta*. The aragonite crystals grow from the cuticle toward the zooid interiors in both directions. F. Polished fragment of *R. neapolitanum*. The section plane cuts through the frontal shield, showing the outlines of the spherulites. G. Polished section of a zooid of *S. cornuta*. The spherulites produce a nodular appearance of the frontal shield. H. Polished section along the frontal shield. The close-up of the framed area shows the outlines of the spherulites composed of radiating fibers and displays marked growth increments. White dashed arrows in D, E and G indicate growth direction.

3.6. Crystallography

The crystallography of the tabular and granular calcite of *Calpensia nobilis* is shown in Fig. 18. The selected map was done on the interior walls of a zooid chamber. The boundary between the tabular and granular (on the inner side) microstructures is delineated in the band contrast map (Fig. 18A), demonstrating good signal strength of the measurement. The phase map indicates that the interior walls are made entirely of calcite (Fig. 18B). The entire EBSD color orientation map (IPFz map, Fig. 18C) reveals a broad color variation, which suggests no preferred orientation of the calcite crystals. The pole figures of the map display a scattered distribution of the crystallographic axes (Fig. 18C), due to the curvature of the walls. The MUD value (12) for the map, indicates a low co-orientation of the crystallographic axes. Locally, similar colors extend from the tabular to the granular microstructures, delineating relatively big "crystallographic domains" with a uniform orientation. This indicates crystallographic continuity between the two microstructures. This continuity can be better appreciated in the selected subsets of Fig. 18D and E (MUD values 114 and 64, respectively). If only the tabular calcite layer is selected, the c-axes are roughly parallel to the growth surface (Fig. 18F). The maxima spread in the contour pole figures (with a MUD value of 30), partly due to the c-axes following the curvature of the wall (as indicated by the unit cells, Fig. 18F).

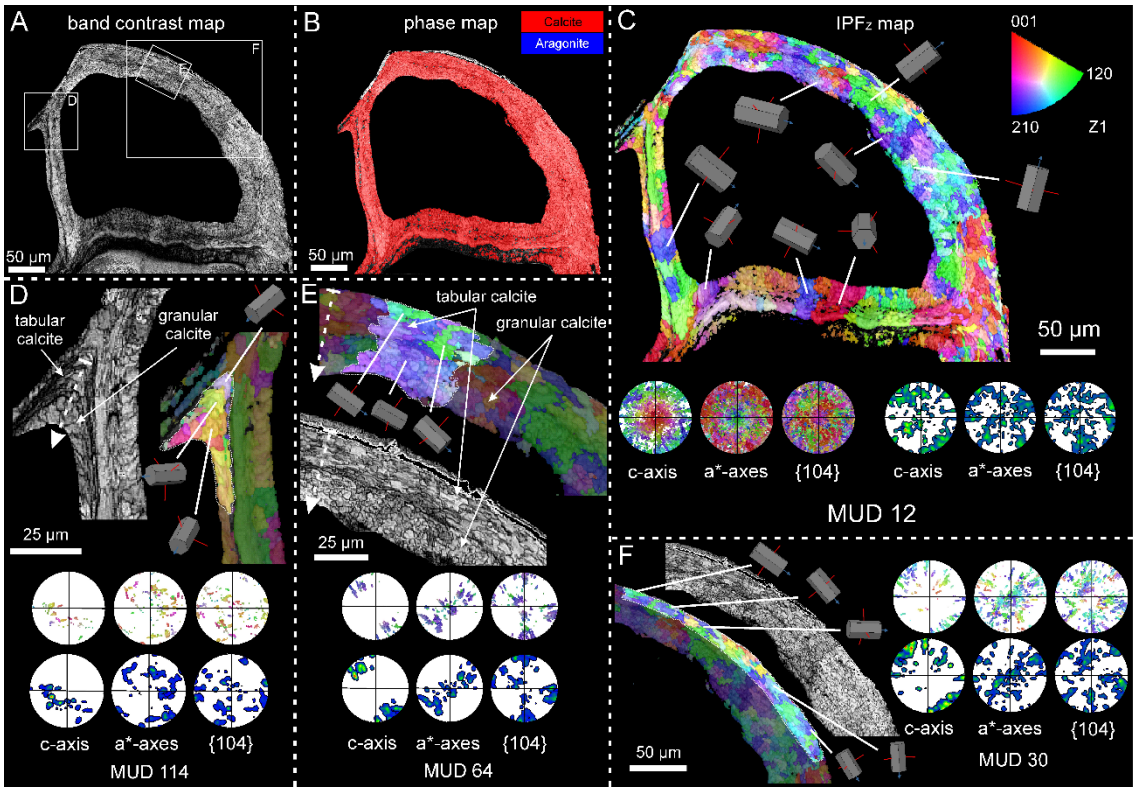

Figure 18. EBSD analysis of the interior walls of a zooid of *Calpensia nobilis*, comprising tabular and granular calcite. A. Band contrast map. The lighter or darker regions correspond to stronger or weaker EBSD diffraction signals, respectively. The framed areas are analyzed in detail in D, E and F. B. Phase map showing that all the interior walls are made of calcite. C. EBSD map. The color triangle is the orientation color key. The varied colors indicate a non-preferred orientation of the crystallographic axes, as shown by the pole figures. The low MUD for the entire map (12) is partly due to the changing orientation of the wall. The orientation of selected grains is also provided by the unit cells. D. Detailed view of an interior wall corner. The tabular calcite grades into granular calcite without a significant change in orientation (note similar colors and unit cell orientations). The pole figures indicate that the c-axes are at a high angle to the section plane. E. Magnified area of the wall cross-section. The selected subset comprises both tabular and granular calcite. No changes in the orientation from one microstructure to the other are observed (as indicated by the unit cells). The pole figures indicate that the c-axes are roughly parallel to the section plane and to the elongation of the wall. F. Subset of the tabular calcite layer only. The c-axes lie parallel to the section plane and to the growth surface, showing a change in orientation coinciding with the curvature of the wall (see the unit cells). Color key to the top right of C, valid for all maps.

The crystallography of the granular calcite and the fibrous aragonite microstructures of bimineralic bryozoans is represented by the *Pentapora fascialis* example (Fig. 19A and B). The selected map was obtained in a cross-section that cuts obliquely through the frontal shield. In the band contrast map (Fig. 19C), the regions corresponding to the fibrous aragonite (composed of smaller crystals) present a lower signal strength (darker areas) than those of the granular calcite (lighter areas). The phase map (Fig. 7J-L) supports the distribution of aragonite surrounding the pores in the outermost layer of the frontal shield (blue color, Fig. 7L). The granular calcite (red color, Fig. 7L) is progressively exposed between the aragonite as the oblique sectioning plane reaches the basal calcitic layers of the frontal shield (see distribution of layers in Fig. 13E-H). An overview of the entire IPFz map (Fig. 19D) reveals a wide color variation for both microstructures, suggesting that the crystals are inconsistently oriented. The contoured versions of the pole figures of the calcitic and aragonitic microstructures show weak axial textures in both cases (Fig. 19E), with scattered maxima for the c-axes, indicating an orientation roughly perpendicular (aragonite) or oblique (calcite) to the section plane. The low MUD values (10 and 5 for calcite and aragonite, respectively) are evidence of the poor texture (Fig. 19E). An analysis of the change in co-orientation of the microstructures with growth is shown in Fig. 19F. We have cropped out areas corresponding to two different developmental stages of the fibrous aragonite. According to the lesser spread of the pole maxima of the contoured pole figures, and to the increase of the MUD values (from 18 to 38), the fibers become more co-oriented with growth.

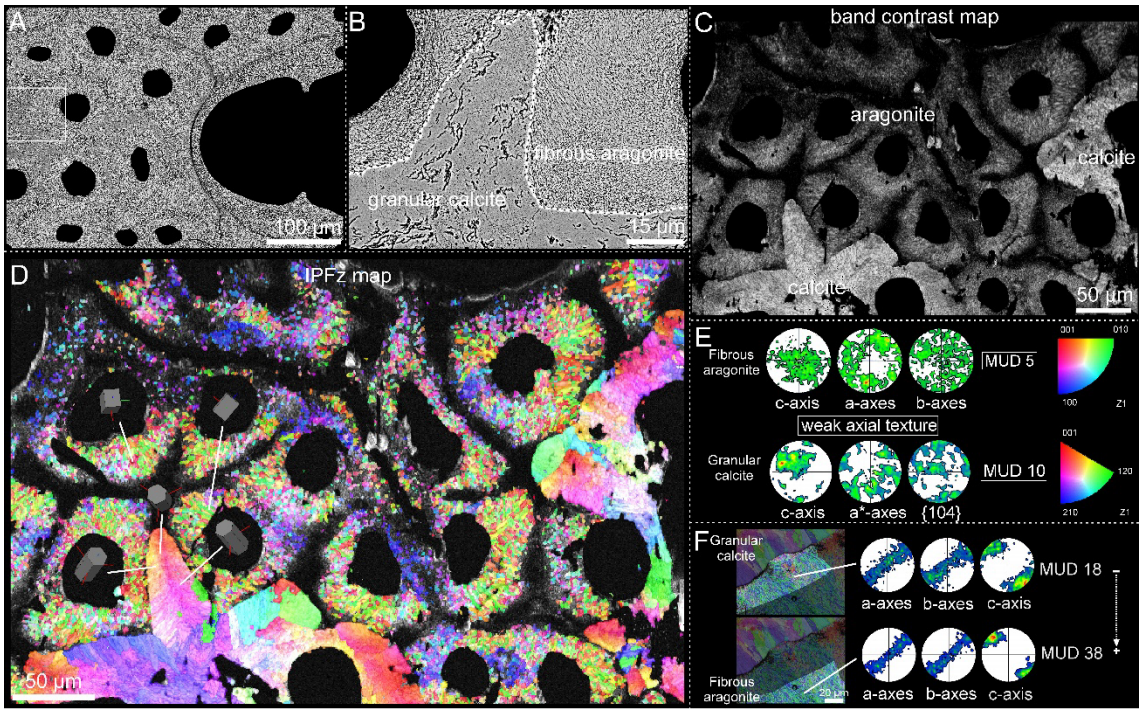

Figure 19. EBSD analysis of the granular calcite and the fibrous aragonite of *Pentapora fascialis*. A, B. SEM images of a region similar to that analyzed for EBSD, corresponding to a longitudinal cross-section of the frontal shield. The middle layer of granular calcite (see Fig. 5E-G) is visible between the fibrous aragonite that surrounds the pores. The boundary between the calcite and the aragonite microstructures is visible (white dashed line). C. Band contrast map. The calcite shows stronger EBSD diffraction signals (lighter colors than the aragonite. D. IPFz map. The broad variety of colors indicates widely scattered orientations of the crystallographic axes for both microstructures. Orientation color keys are provided in E. E. Contour pole figures for the fibrous aragonite (top) and the granular calcite (bottom). The crystallographic axes depict a weak axial texture, with the c-axis as fiber axis. Accordingly, the MUD values are very low. The triangles are orientation color keys for aragonite and calcite. F. Selected subsets for the fibrous aragonite at two different growth stages. The selected area to the top comprises an initial growth stage starting at the boundary with the granular calcite. The region to the bottom belongs to a more advanced growth stage. The contour pole figures and their MUD values (18 and 38) indicate that the texture becomes stronger with growth.

The crystallography of the irregularly platy and granular calcites of *Smittina cervicornis* is shown in Fig. 20. The analysis was performed on a large area comprising a longitudinal cross-section across several zooid chambers (Fig. 20A and B). The bulk of the colony is made of calcite (see the phase map in Fig. 8). The IPFz map (Fig. 20C) reveals a high incidence of reddish colors, which indicates that the c-axes of calcite are at a high angle to the sectioning plane. This is also shown by the contoured pole figures of Fig. 20C. The exceptions are the external walls and the areas adjacent to the cuticles (in green and blue), where

the c-axes lie at a low angle to the surface (subset to the bottom left in Fig. 20C). The crystallographic domains extend the platy and granular calcites, which indicates no distinction in crystallographic orientation. This is shown by the slight color variation and the slight dispersion of the pole figure maxima of the delineated and zoomed areas in Fig. 20C (with MUD values of 21 and 63). All the pole figures in Fig. 20C display an axial texture, with the c-axis as the fiber axis. Similar to the fibrous aragonite, the granular and irregularly platy calcites become more co-oriented with growth, as corroborated by the lesser spread of the pole maxima and the increase of the MUD values of areas corresponding to the different growth stages (Fig. 20D).

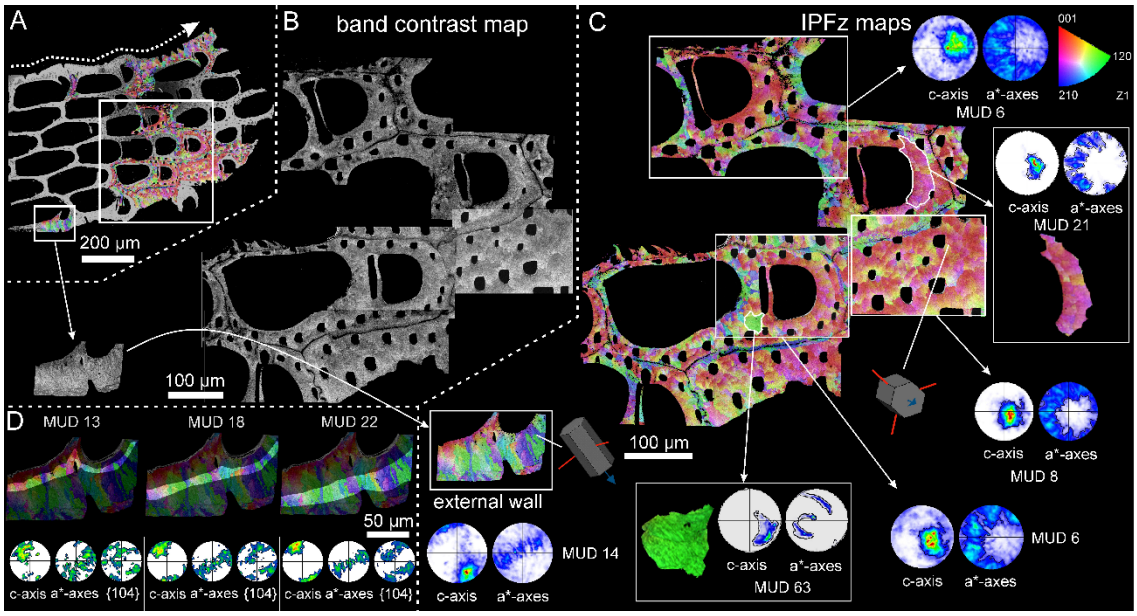

Figure 20. EBSD analysis of the platy and granular calcites of *Smittina cervicornis.* A. SEM image of a longitudinal cross-section of a colony fragment. The section plane cuts throughout different zooid chambers and covers the entire width of the colony. The dashed wavy arrow indicates the colony growth direction. B. Band contrast maps of the areas framed in A, showing a good diffraction signal strength for all the measurements. C. EBSD orientation color maps (IPFz map) for the areas in B and contoured pole figures for framed regions and subsets (delineated with white lines). The MUD values are low (between 6 and 14) for the framed areas. The reddish colors predominate (i.e., the c-axis is at a high angle to the section plane), except in areas adjacent to the cuticle between zooids (compound walls) and at the external walls, where the c-axes are roughly parallel to the sectioned surface (subset to the bottom left). The calcite crystals are organized into big crystallographic domains with relatively high internal misorientations (bottom center selected green subset, with a MUD value of 63). The color triangle is the orientation color key. D. Selected areas along the external wall at increasing growth stages (from left to right). The lesser spread of the maxima in the contour pole figures and the increasing MUD values (from 13 to 22) indicate that the texture becomes stronger with growth.

The crystallography of the predominantly aragonitic bryozoans is represented by the examples of *Rhynchozoon neapolitanum* (Fig. 21A-C) and *Schizomavella cornuta* (Fig. 21D-F). The areas for EBSD measurements were selected on a longitudinal cross-section of the frontal shields (Fig. 21A and D). EBSD phase maps indicate the aragonitic nature of the samples (Fig. 9). The spherulites are discernible in the band contrast maps (Fig. 21B and E; compared to Fig. 17E and G); their centers have a weaker signal strength (darker areas) because the fibers are thinner and are disposed at a high angle to the section plane. The IPFz maps (Fig. 21C and F) show that the fibers are oriented predominantly perpendicular to the section plane (red color). Exceptions were found in *S. cornuta,* where the c-axes of the fibers are locally parallel to the section plane and perpendicular to the inner surface of the orifice of the sub-oral avicularia (top framed area in Fig. 21F). The pole figures display a neat axial texture for both samples, with the c-axis as the fiber axis. The MUD values indicate a weak to medium texture.

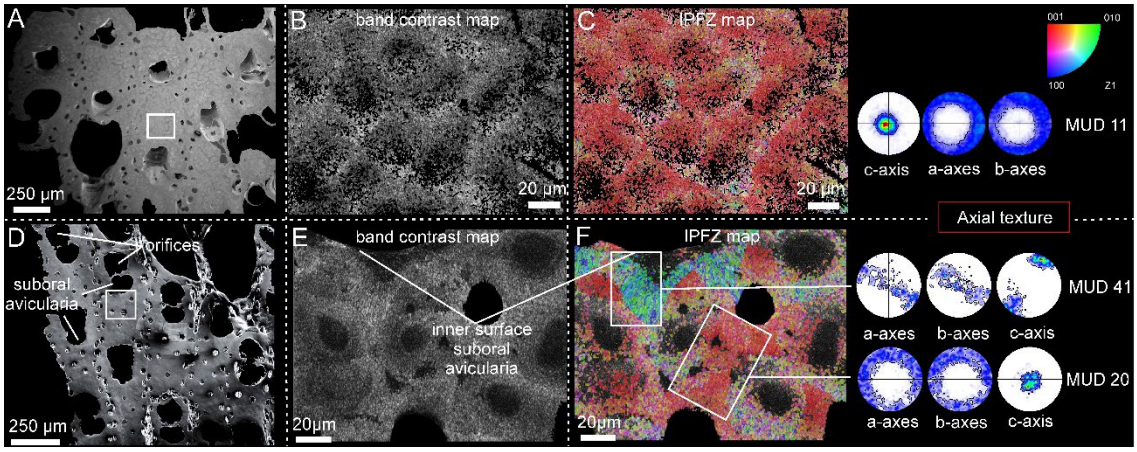

Figure 21. EBSD analysis of the fibrous aragonite of *Rhynchozoon neapolitanum* (A-C) *and Schizomavella cornuta* (D-F). A, D. SEM images of the polished colony fragments. The section planes cut across the frontal shields of the zooids. The framed areas correspond to the regions analysed with EBSD. B, E. Band contrast maps showing darker hues at the centers of the spherulites, where the signal strength of the measurement is weak or absent. C, F. IPFz maps and pole figures (contoured version), displaying clear axial textures. The c-axes are perpendicular to the section plane, with the exception of the region around the sub-oral avicularia orifice in *S. cornuta* (F, top framed area), where the c-axes of the fibers are oriented roughly parallel to the section plane.

4. Discussion

4.1. General structure and mineralogy of cheilostome bryozoans

Cheilostomes develop a complex colony structure with a widespread and high level of zooid polymorphism (Figs. 5 and 6). In addition, feeding autozooids, defensive avicularia, brooding chambers (ovicells and gonozooids), and structural kenozooids are often found (Schack et al. 2019; Taylor 2020). Considering the larger variety of colony forms and functional zooids, and the higher colony growth rates (due to their better ability to obtain food) of cheilostomes compared to cyclostomes, it is not surprising that they have become the most successful bryozoan group from the Late Cretaceous to date (McKinney 1992; Schack et al. 2019; Taylor 2020; Taylor and Waeschenbach 2015).

The organic fraction present in the zooidal skeleton consists of the outer cuticle and the inter- and intra-mineral organic matter. The first studies performed on histological preparations were done with periodic acid Schiff and Mallory triple stain tests and revealed a cuticle composition predominantly of mucopolysaccharides, proteins, and chitin (Tavener-Smith and Williams 1972). Lombardi et al. (2023) demonstrated a similar composition in the intramineral soluble organic matter of three Antarctic calcitic bryozoans' skeletons.

Our samples included calcitic, aragonitic, and bimineralic bryozoans (Figs. 7-9). In all bimineralic species, aragonite was always found in the frontal shield (or cryptocyst in *Calpensia nobilis*), whilst calcite constituted the structure of the interior compound walls and the basal layers of the frontal shield. According to numerous studies summarized by Taylor et al. (2009), there is a strong latitudinal pattern related to the mineralogy of the gymnolaemate bryozoans, since the number of aragonitic and bimineralic species increases towards the equator. This pattern was explained by the different solubilities of the calcium carbonate mineral phases, as high-Mg calcite and aragonite are more vulnerable at high-latitude cold waters. Hence, solubility seems an important factor limiting the

geographical extent of species according to their mineralogy (Kuklinski and Taylor 2009). This latitudinal pattern is consistent with the mineralogy described in our samples, which were collected in the Adriatic Sea (see Material and Methods).

4.2. Relationships between microstructures

In the eight species of cheilostome bryozoans analyzed in this study, we detected five microstructures: three calcitic (tabular, irregularly platy, and granular) and two aragonitic (fibrous and granular-platy). To determine the growth sequences, we used the following criteria: (1) the cuticle is always the first structure to be secreted (Tavener-Smith and Williams 1972); (2) growth fronts can be deduced from the distribution and shape of crystal growth lines (Figs. 13H, 15C-E and 17E, F, H); (3) the contours of platy calcite units are considered as growth surfaces when they are subparallel to each other and, eventually, to the growth lines of granular calcite (Fig. 15E); (4) the grains on both sides of the boundaries between converging growth fronts of the granular calcite point in the growth direction (Fig. 15B, inset); (5) the spherulites spread from the nucleation center outwards in all directions (Fig. 17F-H).

We observed recurrent relationships between the calcitic microstructures of both bimineralic and calcitic cheilostomes. Tabular calcite is the first microstructure secreted in *Calpensia nobilis*, and it grows from the cuticle (at the center of the compound walls) toward the zooecium interior. As the wall thickens, the tablets, which are stacked parallel to each other and surrounded by organics threads (Fig. 10C), gradually shift to a granular layer that ultimately covers the inner surfaces of the zooecium (white dashed arrows in Fig. 11A-C, and Fig. 22A). The same applies to the irregularly platy calcite. It is the first layer secreted at the center of the compound walls in the bimineralic bryozoans *Schizobrachiella sanguinea*, *Schizoretepora serratimargo*, and *Pentapora fascialis* (Fig.

10D-F and 11D-F) and in the calcitic bryozoan *Smittina cervicornis* (Fig. 15). The irregularly platy units grow from the cuticles in opposite directions toward the interiors of both zooids. Similar to the tabular calcite, the irregularly platy calcite gradually changes into granular calcite with growth (see white dashed arrows in Figs. 10D-F, 11D-F, and 15B-D; Fig. 22B).

The crystallographic continuity observed between either the tabular or the irregularly platy calcite and the granular calcite (Figs. 18C-E and Fig. 20C) indicates that the microstructural change is merely due to the disappearance of the organic membranes typical of the former two microstructures. The only explanation we envisage is that, with wall thickening, there is a progressive decrease in the availability of organic components in the solidifying medium (extracellular space). The result is the formation of large calcite grains devoid of occluded organic membranes that are typical of the granular layer. Schoeppler et al. (2019) explained the transition from aragonitic granular to columnar to nacreous layers in different mollusc shells through a process analogous to that of directional solidification, well-known in the field of metallic materials science (Schoeppler et al. 2018). This process in mollusc shells is unlikely to be influenced by shifts in temperature, because biomineralization takes place at ambient temperature. However, supersaturation, the mineral deposition rate and the amount of organic matter have to be considered. Supersaturation would be reflected in the number of crystals (high: many crystals, low: few crystals), which is not observed in the walls of cheilostomes. Accordingly, the transition between microstructures may take place through a reduction in either the growth rate or the amount of available organic matter. At faster growth rates, the organic molecules would tend to be entrapped within the crystals, whereas at slower growth rates, they would be repelled and attach to the growth fronts, eventually forming organic membranes. Although we cannot rule out either possibility, there is neither evidence nor a clear reason why the rate of calcification should decrease during skeletal wall thickening. We opt for the possibility that a

decrease in the number of organic biomolecules released by the mineralizing tissue of the animal over time is responsible for the observed microstructural changes, without affecting the crystallographic continuity. A feasible proxy for growth rate is the Mg content of the calcite crystals (Gabitov et al. 2014; Nielsen et al. 2016). However, this analysis was not carried out in this study.

In the primarily aragonitic cheilostomes *Rhynchozoon neapolitanum*, and *Schizomavella cornuta*, the bulk of the colony is made uniquely of fibrous aragonite (Fig. 17). However, no microstructural variations were observed in the different walls, where the fibers were always organized into spherulites, displaying a strong axial texture (Fig. 21). The same invariance was noted in the fibrous aragonite that forms the frontal shields (or cryptocyst in *C. nobilis*) of the bimineralic cheilostomes studied (Fig. 13A-H).

Regarding the granular-platy aragonite found around the pores in *Adeonella pallasii* (fig. 11H and 13I-K), we observed that the irregularly platy units are often subdivided into granular crystals with angular edges. Similar to the irregularly platy calcite, the platy appearance of aragonite may be due to the intercalation of organic membranes. Despite the lack of crystallographic data on these microstructures, it is possible that both granular and irregularly platy aragonite are crystallographically continuous.

4.3. The relation of the growing crystals with the secretory epithelium

Among the microstructures described in our study, only the tabular calcite of *Calpensia nobilis* looks relatively sophisticated, i.e. far from the morphologies of abiogenic calcites (Fig. 10A-C). It is a material made of well-defined, parallel, flat lamellae. This suggests the existence of a closely adjacent secretory epithelium that levels off the surfaces of the growing crystals (Fig. 22A1). Conversely, the other microstructures (irregularly platy calcite, granular calcite, fibrous

aragonite, granular-platy aragonite) present a characteristic inorganic-like appearance, and evidence that the epithelium is at a distance from the forming crystals (Fig. 22A2, B, C1).

The lamellae of the irregularly platy calcite display uneven boundaries marked by organic membranes. In the likely case that individual organic membranes form at once (i.e. they are parallel or subparallel to growth lines; Figs. 10F and 15E), their sinuous contours and the great variation in shape and extension imply some degree of freedom of the growth surface. This is understandable if there is not a tight connection with an even secretory epithelium surface (Fig. 22B). Otherwise, the lamellae would tend to be flat, regular in size, and well-ordered parallel to the growth surface (as in the tabular calcite of *C. nobilis*; Fig. 22A1). Regarding the granular calcite, the grains show an internal fibrous substructure. Each fiber coincides with a tooth of the serrated growth surface. Clearly, teeth are sectioned small rhombohedra (Fig. 11C, D, and F). Thus, the surfaces of grains are comparable to micro-sized dog-tooth calcite (Fig. 13G, inset). This suggests that the growth fronts of grains are at a distance, even if small, from the epithelium (Fig. 22A2, B2).

The fibrous aragonite microstructure is always made by spherulites (see Figs. 13 and 17) that extend until colliding with their neighbors and then grow on top of each other (Fig. 13C, E-G, and Fig. 17F-H). They give the external surfaces a nodular aspect (Fig. 13C, E and Fig. 17A), which is evidence that their growth surfaces are free to bulge, out of the reach of an epithelium leveling them off (Fig. 22C1). The distribution of growth lines (Fig. 13H) indicates that, when the frontal shield is about to be complete, growth ceases at the depression, but continues at the elevations. This indicates that the biomineralizing epithelium ceases to secrete at the depressions while it is actively secreting at the elevations. When the frontal shield formation is complete, the epithelium adheres all along its surface and becomes inactive (Fig. 22C2).

All the characteristics of the aragonitic and calcitic microstructures of cheilostome bryozoans mentioned above suggest an origin via remote biomineralization, i.e. the process which occurs when the secretory epithelium is not in close contact with the forming crystals (Checa 2000; Chinzei and Seilacher 1993). This is unlike other groups, e.g. bivalves and brachiopods, in which the thicknesses of the extrapallial spaces (i.e. the distance between the cells and the forming crystals) are on the order of 100 nm (Checa et al. 2014) and 50 nm (Simonet Roda et al. 2019), respectively. In stenolaemate bryozoans, the distance increases to 150-200 nm (Nielsen and Pedersen 1979). We cannot give an estimate of the thickness of the extrapallial space in gymnolaemate bryozoans, but it must be well above those dimensions.

4.4. Growth by space competition

Space competition happens in crystal aggregates with a common growth front. The crystals that grow with their fastest growth axes at a high angle to the growth front survive and become larger at the expense of those growing more obliquely, which tend to be extinguished (Grigor'ev 1965; Rodríguez-Navarro and García-Ruiz 2000). Consequently, with time, the spread of crystallographic axes lessens. This applies to a wide variety of molluscan microstructures (Crippa et al. 2020; Stevens et al. 2017; Ubukata 1994), and the chicken eggshell (Hincke et al. 2012).

With EBSD, we supported an increasing crystallographic ordering at subsequent development stages of the irregularly platy-granular calcite association (Fig. 20D) and the fibrous aragonite microstructures (Fig. 19F). This is consistent with a growth process of competition for space and is the first case so far reported in bryozoans.

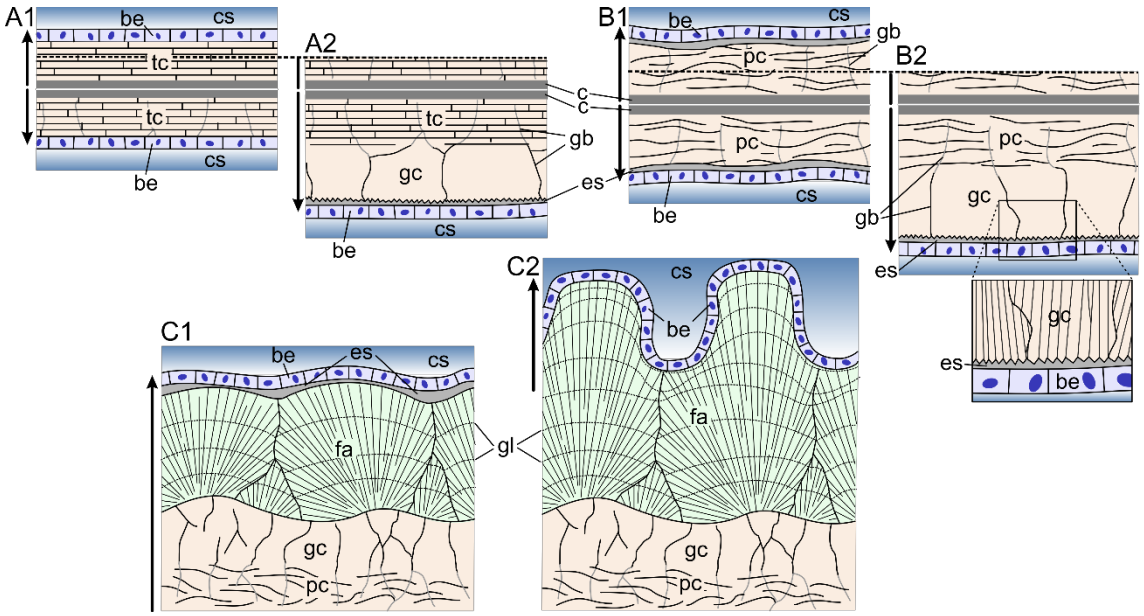

Figure 22. Growth sequences of microstructures and relation with the secreting epithelium in the compound walls (A, B) and frontal shield ©. A. Compound walls of *Calpensia nobilis*. Walls grow from the cuticles in both directions toward the zooecium interiors. During the secretion of the tabular calcite (A1), the biomineralizing epithelium is in close contact with the shell growth surface, although there is always a small, almost negligible, extrapallial space. During subsequent secretion of the granular calcite (A2), there is a wide intervening extrapallial space. B. Compound walls of the rest of either calcitic or bimineralic species. The walls are made by a cuticle followed by irregular platy calcite (B1) and granular calcite (B2). The biomineralizing epithelium is at a certain distance from the shell growth surface. The zoom-up in B2 shows the relationship between the biomineralizing epithelium and the serrated shell growth surface in more detail. C. Formation of the frontal shield in bimineralic species (e.g. *Pentapora fascialis*). It is formed by superposed layers of irregular platy calcite, granular calcite, and spherulites of fibrous aragonite. During active secretion (C1), the soft body is separated from the shell growth surface by a wide intervening extrapallial space. It is a smooth replicate of the shell surface topography. Secretion ceases first at the depressions and continues in the elevations, as indicated by growth lines (compare to Fig. 5H). When secretion of the frontal shield comes to an end, the biomineralizing epithelium adheres to the shell surface and becomes inactive (C2). Arrows indicate the growth directions. In A2 and B2, only the growth of one of the walls is shown (the broken lines are intended as references). be: biomineralizing epithelium; c: cuticle; cs: coelomic space; es: extrapallial space; fa: fibrous aragonite; gb: grain boundary; gc: granular calcite; gl: growth line; pc: irregularly platy calcite; tc: tabular calcite.

4.5. Final remarks

With the exception of tabular calcite, the microstructures present in cheilostomes are much more abiogenic-like compared to those of cyclostomes, which produce tabular and foliated calcite (Grenier et al. 2023; Taylor and Weedon 2000), or to those of other organisms such as brachiopods (tabular, fibrous calcite) (Williams

1970) and molluscs (e.g., foliated, nacre, crossed-lamellar) (Bøggild 1930). In all of these instances, the thickness of the extrapallial space is negligible and there is strict secretory control by an adjoining epithelium (see Checa 2018 for molluscs, and Simonet Roda et al. 2019 for brachiopods). As commented on above, this is not the case in cheilostome bryozoans, where remote biomineralization seems widespread. The question remains, however, whether remote mineralization is favorable in terms of, e.g., a lower metabolic cost (Lowenstam 1981; Lowenstam and Weiner 1989; Mann 1983; Palmer 1983, 1992). Sophisticated microstructures are, in general, highly functional materials and their biomechanical performance is particularly good (e.g., Currey 1977; Currey and Taylor 1974). In this sense, it is possible that cheilostomes make a low investment in high-performance materials, which was not an obstacle to their extraordinary evolutionary success.

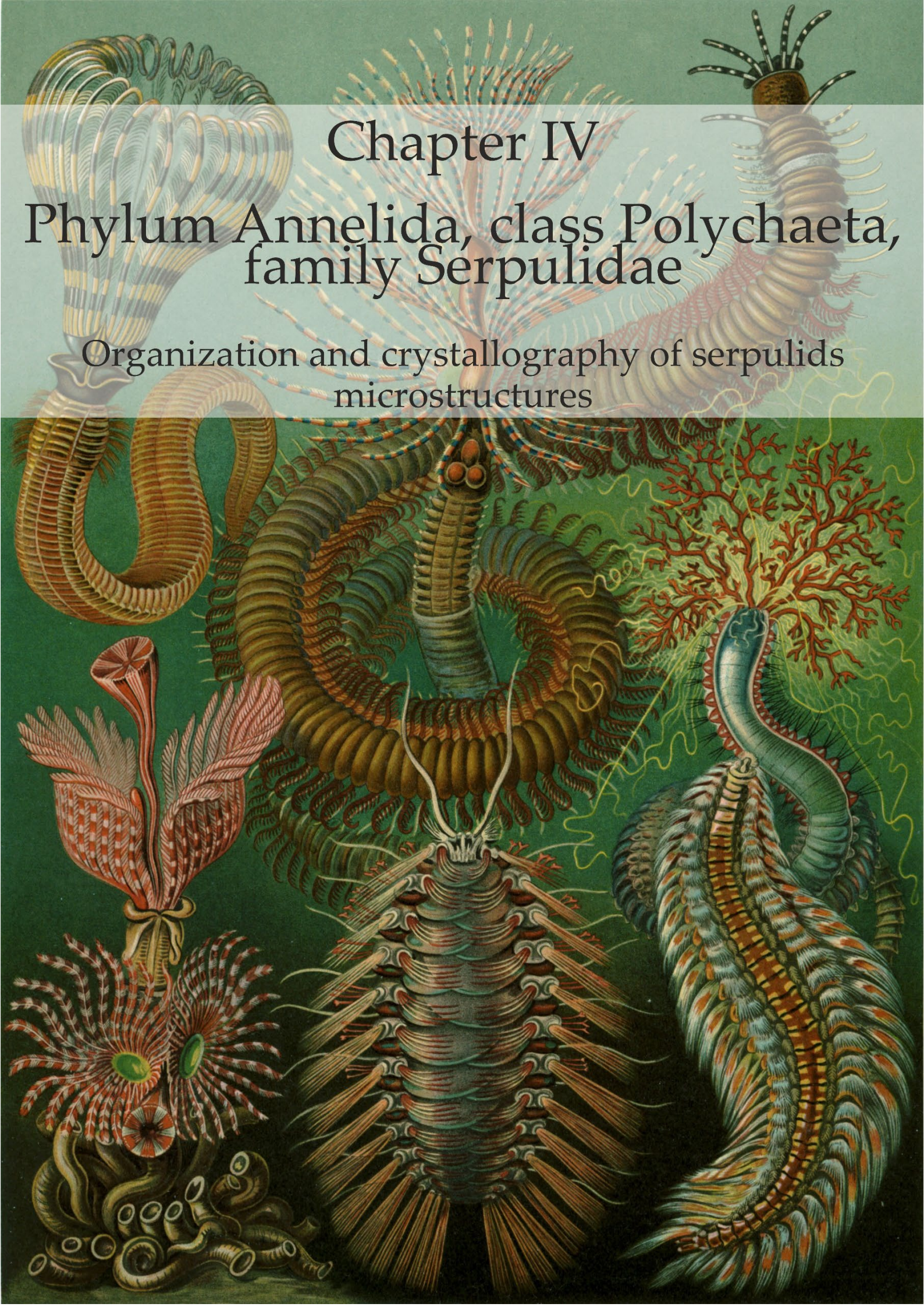

Chapter IV

Phylum Annelida, class Polychaeta, family Serpulidae

Organization and crystallography of serpulids microstructures

Class Polychaeta

Family Serpulidae

Microstructures, crystallography and growth patterns of serpulid tubeworms (Class Polychaeta)

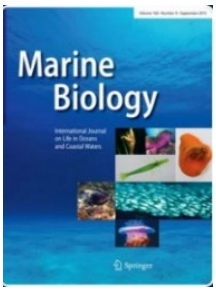

Microstructures, crystallography and growth patterns of serpulid tubeworms (Class Polychaeta)

Christian Grenier[1], Kasia Berent[2], Alejandro B. Rodríguez-Navarro[3], Olev Vinn[4], Antonio G. Checa[1,5]*

[1]Departamento de Estratigrafía y Paleontología, Universidad de Granada, 18071 Granada, Spain.

[2]Academic Centre for Materials and Nanotechnology, AGH University of Science and Technology, 30-055 Kraków, Poland.

[3]Departamento de Mineralogía y Petrología, Universidad de Granada, 18071 Granada, Spain.

[4]Department of Geology, Institute of Ecology and Earth Sciences, University of Tartu, 50411 Tartu, Estonia.

[5]Instituto Andaluz de Ciencias de la Tierra, CSIC-Universidad de Granada, 18100 Armilla, Spain.

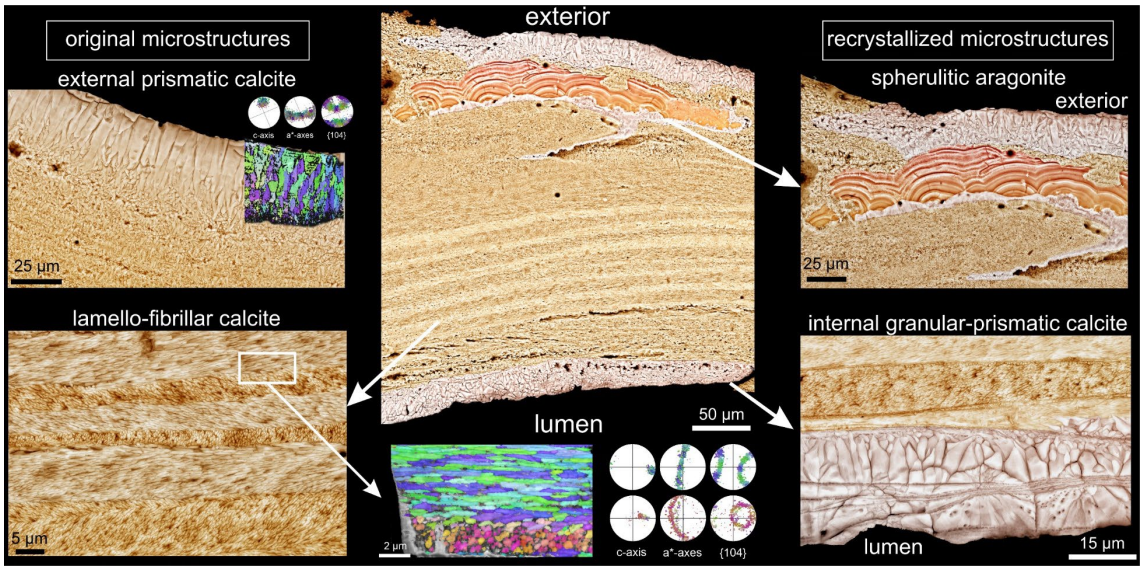

Submitted 13/05/2024
Status: under review

ABSTRACT

Serpulid polychaetes are global marine worms that secrete tubes of calcium carbonate, in which they live. Despite extensive previous research on their microstructures, there are no crystallographic data and their biomineralization process remains unclear. Herein, we review the microstructures of seven different serpulid species and study their chemical composition, mineralogy and crystallography, using X-ray diffraction, Raman and Fourier transform infrared spectroscopy, scanning electron microscopy, energy dispersive X-ray spectroscopy, focused ion beam, electron backscatter diffraction, and thermogravimetric analysis. Generally, serpulid tubes have a high amount of organic matter (~7.5 wt. %), consisting of chitin and proteins, and the calcite is always present as medium to high magnesium calcite. We identified three main microstructures: granular-prismatic and lamello-fibrillar calcite, and fibrous aragonite. They all display an axial texture, which is stronger in the lamello-fibrillar calcite, with the c-axis aligned with the elongation axis of the crystals. Our findings demonstrate that only some instances of the granular-prismatic and the lamello-fibrillar calcite are biogenic (primary) microstructures. Conversely, other instances of the granular-prismatic calcite and the fibrous aragonite are a consequence of a recrystallization process (i.e. secondary). Substitution may occur on either primary or secondary calcitic microstructures (replaced by aragonite). Secondary microstructures retain remnants of the previously substituted microstructures, such as vestigial crystals or major growth increments. The high-Mg nature of the calcite favors the recrystallization processes. We hypothesize that the plywood arrangement of the lamello-fibrillar is obtained by the ordering of a chitin fibrillar precursor into a cholesteric liquid crystal phase. Subsequently, calcite would grow by oriented nucleation onto the organic fibrils.

1. Introduction

Serpulid tubes are made of either calcite, aragonite, or both (Lowenstam 1954; Ten Hove and Van den Hurk 1993; Vinn et al. 2008c, b). Although the mineralogy of most species is unknown, the majority of serpulids studied are calcitic (around 40%), followed by bimineralic (36%) and aragonitic (24%) (Smith et al. 2013). Calcite is always medium- to high-Mg calcite (7-15 wt% $MgCO_3$) (Smith et al. 2013). The tube has a high amount of organic matter, which occurs primarily as membranes marking different growth increments (Vinn 2011). The organic fraction can be separated into soluble and insoluble organic matter (SOM and IOM), which are mainly composed of carboxylated and sulfated polysaccharides (Tanur et al. 2010).

Since the second half of the 20th century, the microstructures of serpulids have been studied by different authors (Hedley 1958; Weedon 1994), who described lath-like crystals arranged in ordered and disordered chevron layers and spherulitic prismatic structures locally distributed (Fig. 1). However, the most extensive research about the ultrastructure and mineral composition of serpulid tubes was conducted by Vinn et al. (2008b), who analyzed 44 recent

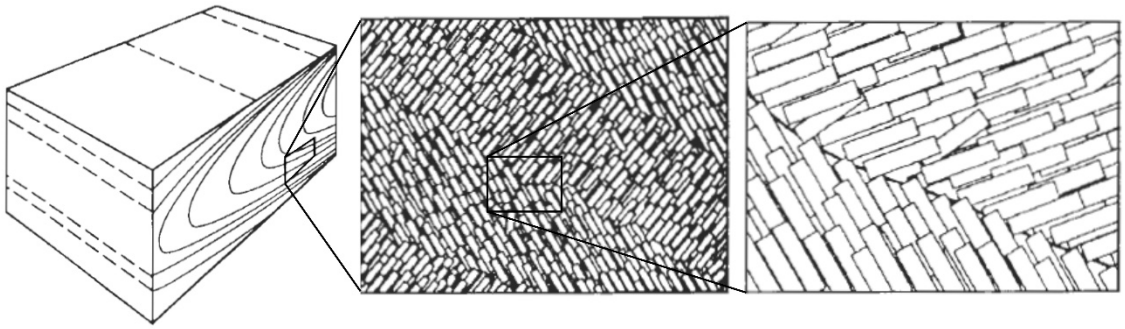

Figure 1. Diagram of the tube structure of *Spirobranchus triqueter* (from Weedon 1994). The longitudinal cross-section shows the concave growth increments. The framed areas are magnified, showing in detail a schematic representation of the lamello-fibrillar microstructure. The change in orientation of the co-oriented fibers between adjacent layers gives rise to a pattern known as a "chevron structure".

species from 36 genera. From SEM images, they described a total of twelve different microstructures based on the mineralogy, morphology, and arrangement of the constituting crystals (some instances are depicted in Fig. 2).

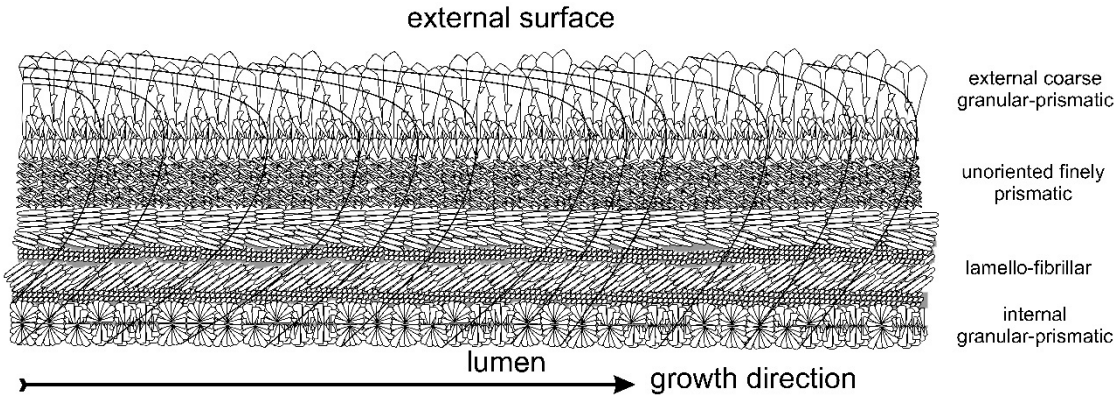

Figure 2. Schematic representation of a longitudinal cross-section tube of *Crucigera websteri.* The main calcitic microstructures found and their ubication from the lumen to the external surface are depicted. The growth direction is indicated by the overlapping concave lines (i.e. growth increments). The straight disposition of the different microstructures is intentional to facilitate their representation within the tube section. Adapted from Vinn (2021).

Summarising, Vinn et al. (2008b) distinguished fibrillar, prismatic, platy, and spherulitic microstructures, each arranged in oriented, semi-oriented, or disoriented manners (all the combinations are depicted in Fig. 3). Other studies also focused on the transitions between microstructures across the different layers of the tube. For instance, Buckman (2015) described in *Spirobranchus triqueter* a progressive change from well-ordered inner and medium layers (chevron layer), constituted by the lamello-fibrillar microstructure, to an outer, less structured layer (pseudo-laminar layer), consisting of the irregularly oriented-prismatic microstructure (Buckman 2015). In summary, in recent decades the tube structure of serpulids has been described in detail, leaving behind a complex and wide variety of microstructures (fifteen until now), which led to the suggestion that serpulids possess a more advanced biomineralization system than previously thought (Vinn 2021).

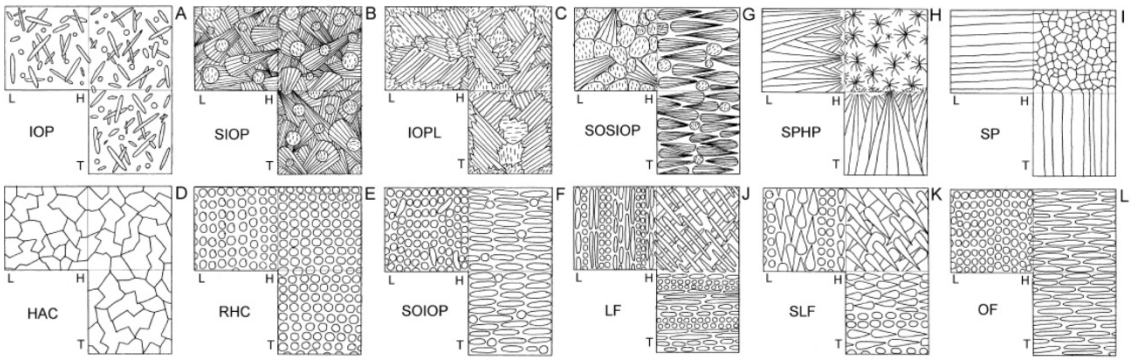

Figure 3. The twelve microstructures described by Vinn et al. (2008). A. irregularly oriented prismatic (IOP). B. spherulitic irregularly oriented prismatic (SIOP). C. irregularly oriented platy (IOPL). D. homogeneous angular crystal (HAC). E. rounded homogeneous crystal (RHC). F. semi-ordered irregularly oriented prismatic (SOIOP). G. semi-ordered spherulitic irregularly oriented prismatic (SOSIOP). H. spherulitic prismatic (SPHP). I. simple prismatic (SP). J. lamello-fibrillar (LF). K. spherulitic lamello-fibrillar (SLF). L. ordered-fibrillar (OF). Abbreviations: H, horizontal section; L, longitudinal section; T, transverse section.

Contrary to other groups of biocalcifiers (e.g. molluscs, Checa and Salas 2017; brachiopods, Coronado et al. 2019; Yin et al. 2021; Simonet Roda et al. 2022), there are no studies on the crystallography of serpulid tubes. In the present study, we analyze the microstructures of seven different serpulid species: *Crucigera websteri*, *Spirobranchus triqueter*, *Serpula vermicularis*, *Spirobranchus giganteus*, *Serpula crenata*, *Crucigera zygophora*, and *Floriprotis sabiuraensis*. We determined the existence of only three main types: granular-prismatic and lamello-fibrillar calcite, and fibrous aragonite. For each microstructure, we determine the mineralogy, the type and arrangement of crystallites, their location within the tube, and, for the first time, their crystallographic arrangement.

To do this, we used Scanning Electron Microscopy (SEM), Energy Dispersive X-ray Spectroscopy (EDS), Electron Backscattered Diffraction (EBSD), and Focused Ion Beam (FIB) techniques. Additional data were obtained with X-ray Diffraction (XRD), Thermogravimetry Analysis (TGA), and Raman and Fourier Transform Infrared Spectroscopy (FTIR). We conclude that only the lamello-fibrillar calcite and some instances of the granular-prismatic calcites are primary microstructures (i.e. directly secreted by the animal). Conversely, other instances of the granular-prismatic calcite and the fibrous aragonite are

secondary microstructures (i.e. a consequence of a recrystallization process). Finally, we explain how the plywood structure of the lamello-fibrillar microstructure is created through the ordering of a chitin fibrillar precursor into a cholesteric liquid crystal phase. Subsequently, calcite would grow by oriented nucleation on the organic fibrils.

2. Materials and Methods

2.1. Material

Seven different serpulid species were analyzed in the present study: *Cruzigera websteri* (Benedict, 1887) [V.Pol.3589, Shelf of Surinam]; *Spirobranchus triqueter* (Linnaeus, 1758) [Atlantic Sea]; *Serpula vermicularis* (Linnaeus, 1767) [V.Pol.3780, Ireland, Ardbear Lough]; *Spirobranchus giganteus* (Pallas, 1766) [Sta.2073Aa, Netherlands Antilles, Curaçao]; *Serpula crenata* (Ehlers, 1908) [V.Pol.1739, Indonesia, Siboga Sta.159], *Floriprotis sabiuraensis* (Uchida, 1978) [V.Pol.3929 Shimoshima Isl., Amakusa, Japan]; and *Crucigera zygophora* (Johnson, 1901) [V.Pol.3287 Canoe Bay, Alaska, USA]. The specimens were all collected alive, either by hand from intertidal zones, or through diving, trawling, or dredging techniques from the subtidal zone. They were initially preserved in 4% formaldehyde solution and subsequently relocated to 70% ethanol for archival storage in museum collections (initially at the Zoological Museum, Amsterdam, and presently at the Naturalis Biodiversity Center, Leiden). Mussels with attached *S. triqueter* were purchased at Granada fish markets. Specimens were cleaned, oven-dried and stored dry.

2.2. Scanning electron microscope (SEM)

Fragments of each of the seven species were cleaned by immersion in commercial bleach (~ 5% active chlorine) for 2 h in a stirring set. Then, the bleach solution was removed by several ultrasonication washes (2-3 min each) in deionized water.

Once oven-dried at 40 °C for 24 h, the fragments were embedded in epoxy resin (EpoFix, Struers). After 48h of hardening, the cross-section of each tube was exposed by successive grinding steps with 360, 600, 1200, and 3000 (ANSI/CAMI US grit numbers) electroplated diamond discs. Subsequently, the surfaces were polished with high-density wool felt pad discs (adding 1 μm and ¼ μm of polycrystalline diamond suspension, Struers), until reaching a mirror surface finish. A Hi-Tech Diamond polishing machine (All-U-Need model) was used for both grinding and polishing. Finally, an etching and decalcifying solution (2.5% glutaraldehyde, 0.25 M HEPES buffer, and 0.05 M EDTA) was applied directly to the exposed surfaces for 1 min in a stirring module. SEM observations were performed after carbon coating (Emitech K975X carbon evaporator) using Secondary Electron (SE) and BackScatter Electron (BSE) detectors in a field emission SEM FEI QemScan 650 F and a Carl Zeiss SMT AURIGA Crossbeam Station. All the equipment is housed in the Centro de Instrumentación Científica (CIC) at the Universidad de Granada (UGR).

2.3. RAMAN microscopy

The analyses were performed on the samples prepared for SEM after repolishing to remove the carbon coating. A dispersive Micro-Raman spectrometer (JASCO NRS-5100/7000 Series) was used. The Light source used was a VIS-NIR red diode that generated a laser beam at 785.11 nm with a spot size of 4 μm. The spectrum analyzed ranged from 100 cm^{-1} to 1200 cm^{-1}, with a data interval of 1 cm^{-1}. The exposure time was 20 s, with 5 accumulations per measurement and a resolution of 6.49 cm^{-1}. All the measurements were taken with the 20x objective at a degree of laser attenuation (aperture) O.D.-1 and with corrected fluorescence. Software Spectra Manager II was used for system control, data acquisition, and data analysis. Analyses were carried out at Centro de Instrumentación Científica (CIC) of the University of Granada (UGR).

2.4. X-ray diffraction (XRD) and Rietveld refinement

Cleaned tube fragments from *S. vermicularis* and *S. triqueter* were ground to a fine powder and heated up to 25°C, 200°C and 400°C in an oven. The samples were analyzed with an X-ray powder diffractometer (PANalytical X'Pert PRO) at the Department of Mineralogy and Petrology, University of Granada, using Cu radiation (λ = 1.5406Å). The data were collected in reflection mode, from 4° to 120° (°2θ) with a step size of 0.017° and 69.85 s integration time per step. Rietveld refinement analyses of XRD profiles were done using TOPAS 5.0 software (Bruker, Germany) to determine the quantitative mineral concentration (at 25 °C). The calcite unit cell parameters were refined to calculate the cationic substitutions (% Mg) in calcite (average of the measurements at each temperature). A small amount of silicon powder was added to the sample as an internal standard to more precisely determine the d-spacings (Dos Santos et al. 2017).

2.5. Electron backscatter diffraction (EBSD)

A total of 12 EBSD maps were performed on *S. crenata*, *S. triqueter*, *S. vermicularis*, and *S. giganteus*. The samples prepared for SEM observation were finished with a manual etch-polishing step (for 3-5 min) by applying alumina suspension (0.3 μm, Buehler). The samples were coated with 4 to 6 nm of carbon (Leica EM ACE200). Measurements were taken on a FEI Versa 3D scanning electron microscope (SEM) equipped with the Symmetry S2 CMOS-based EBSD detector (Oxford Instruments). The data were acquired using Aztec 6.0 software with an accelerating voltage of 20 kV. EBSD measurements were performed in step increments between 20 and 25 nm.

2.6. Focused Ion Beam (FIB) and Transmission-electron backscatter diffraction (t-EBSD)

Transmission Kikuchi Diffraction (TKD), also known as the t-EBSD technique, was conducted with the same FEI Versa 3D SEM equipment as for EBSD measurements. Ultra-thin lamellae for t-EBSD were prepared on a FIE Quanta 200i SEM (gallium FIB column). The sample surface was coated by FIB deposition with a 2 μm thick protective stripe of tungsten, whose length is equal to that of the lamella to be extracted. Trenches were then excavated on both sides of the deposited layer in two steps: rough milling was performed with a 30 kV 15 nA ion beam, followed by finer milling steps using a 30 kV 1 nA beam current. A thin fragment of the sample was separated from the bulk, transferred, and attached to the TEM copper grid by an OmniProbe micromanipulator. Subsequently, the FIB lamella was thinned by Ga+ ions on both sides at 30 kV, with a beam current initially set at 300 pA, which was gradually reduced to 50 pA. The final thinning step (to ~100 nm) was conducted at 5 kV and 50 pA, to minimize surface damage.

2.7. Thermogravimetric Analysis (TGA)

Cleaned and dried tube fragments were ground to a fine, homogeneous powder. Approximately 20 mg of material were analyzed using a METTLER-TOLEDO (TGA/DSC1) equipment, with a heating rate of 20°C/min in air. From the TGA curves, the total amounts of water (weight loss from 25°C to 200°C), organic matter-I (weight loss from 200°C to 400°C, presumably corresponding to intermineral proteins and polysaccharides), and organic matter-II (weight loss from 400°C to 600°C, corresponding to intramineral proteins) were determined for each sample (Rashidi et al. 2012; Rodríguez-Navarro et al. 2006).

2.8. Decalcification and Fourier Transform Infrared Spectroscopy (FTIR)

A fragment of *S. triqueter* (1 cm in length) was treated with commercial bleach and then washed several times with sonicated ultrapure distilled water (milli Q). Once oven-dried at 40°C, the fragment was immersed in a decalcifying solution (0,05M EDTA + 0.1M HEPES + 2,5% Glutaraldehyde). The decalcification process was carried out in an orbital shaker for 24 h at room temperature, and the solution was replaced several times. The resulting loose membranes were gently washed several times with ultrapure distilled water (MilliQ) and oven-dried at 40°C. They were then placed on an attenuated total reflection (ATR) diamond unit (Jasco Pro One) and analyzed by a FTIR spectrometer (Jasco 6600). To calculate the standard deviation and error, four repetitions were performed in different areas of each membrane. The range of the spectrum was 400 cm^{-1} to 4000 cm^{-1}, with a resolution of 2 cm^{-1} and 100 scans. Spectra Manager software was used for system control and data acquisition. IR peaks associated with main chemical components (i.e., proteins, polysaccharides, carbonates) were measured to determine the chemical composition of the samples.

3. Results

3.1. Microstructures: overview and mineralogy

Based on crystal morphology and arrangements, we have identified three main microstructures: granular-prismatic, lamello-fibrillar, and fibrous (Fig. 4A-C). With few exceptions, all of them appear in the different species studied.

The granular-prismatic microstructure may be present in different locations and has varied appearances. In the outermost regions of the tube cross-section, it initiates as a finely prismatic disoriented layer, which changes into a coarsely prismatic layer in the outward direction, with the prisms arranged perpendicularly to the external surface (Figs. 4A, D, and E). The granular-prismatic material is also found as ubiquitous clusters or as discontinuous layers at the innermost part of the tube cross-section (Fig. 4D).

The lamello-fibrillar microstructure consists of layers of thin, elongated, co-oriented fibers separated by membranes (Fig. 4B, D, and E). Fiber orientation changes between layers. It is always found in the central part of the tube cross-section and constitutes the bulk of the tube structure in the majority of the samples analyzed (Fig. 4D and E). The fibrous microstructure is made of needle-like fibers, usually forming spherulites, with a fan-shaped arrangement in section (Fig. 4C). It appears as discontinuous layers, either at the outermost or the innermost part of the tube cross-section (Fig. 4D and E). It is also often found in the form of clusters at any location (Fig. 4F and G).

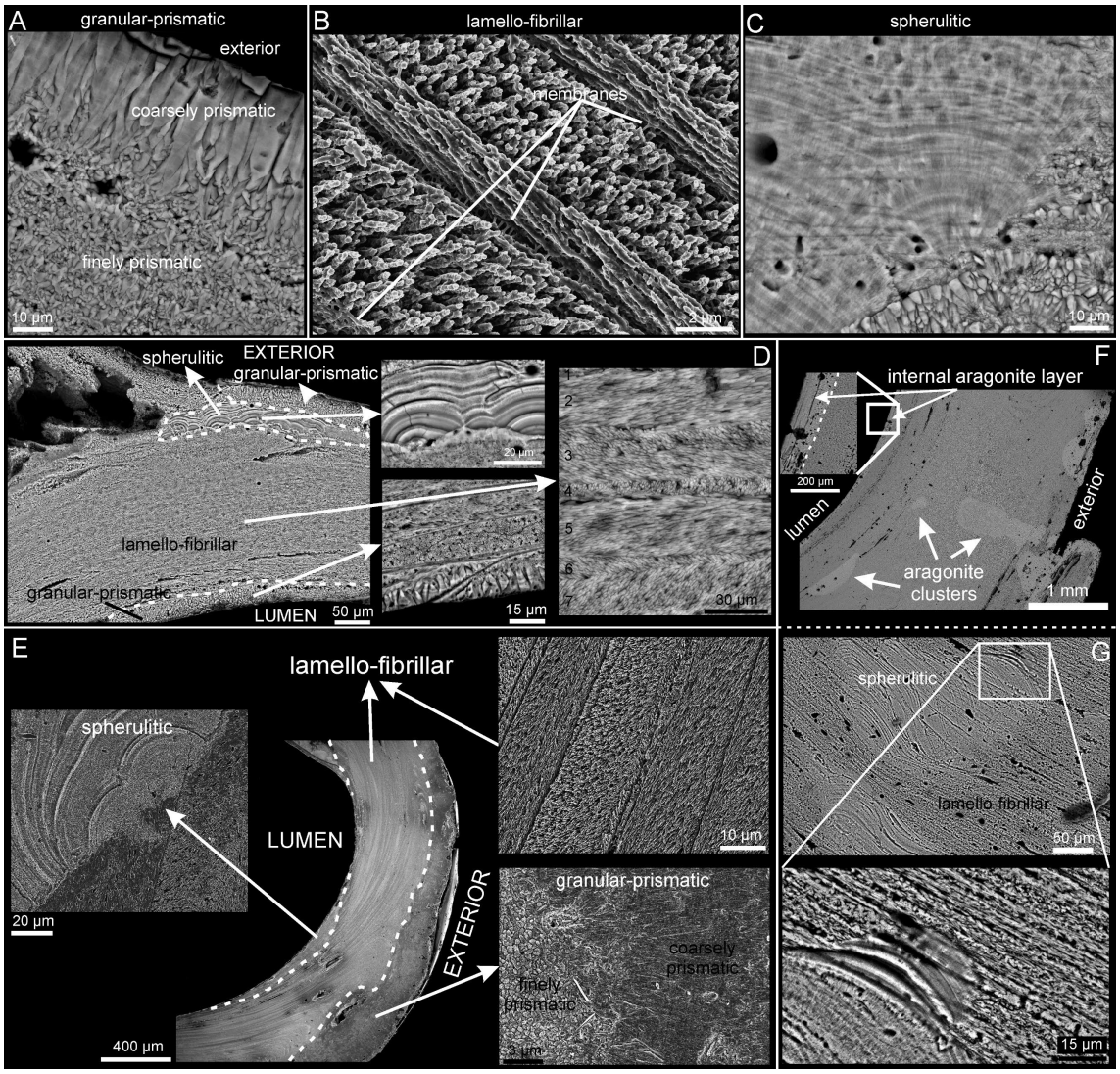

Figure 4. The three microstructures identified (A-C) and their locations (D-G). A. Granular-prismatic microstructure of *C. websteri*. Two types of crystals can be distinguished: fine disoriented prisms (internal) and oriented coarse prisms (external). B. Lamello-fibrillar microstructure of *C. websteri*. It consists of successive layers of thin co-oriented fibers, separated by membranes. The fibers of one layer change their orientation with respect to those of the next layer. C. Fibrous microstructure of *S. giganteus*. The two sectioned spherulites display a fan-like arrangement of acicular fibers, with concentric growth lines, in turn crossed by faint parallel horizontal lines. D. Cross-section of *C. websteri*, showing the location of the microstructures (indicated), magnified to the right. The numbers in the right image indicate the different layers. E. Cross-sectioned tube of *S. vermicularis*. The spherulitic fibrous microstructure appears as a discontinuous internal layer. The lamello-fibrillar microstructure largely comprises the middle part of the tube. The granular-prismatic microstructure is restricted to the outermost region. F. Fibrous internal layer and spherulitic clusters at any location of the tube cross-section of *S. giganteus*. They can be discerned by their lighter contrast. G. View of sectioned fibrous spherulites. The close-up is a detail of a spherulite intersecting the lamello-fibrillar layers. The boundaries of the latter continue into the spherulite.

The mineralogy of the three microstructures was initially determined by RAMAN infrared spectroscopy and XRD (Fig. 5 and Fig. 6). Calcite presents distinctive Raman peaks at around 1084 cm^{-1}, 710 cm^{-1} and 282 cm^{-1} (Kim et al. 2021), whereas aragonite peaks are at around 1082 cm^{-1}, 702 cm^{-1} and 285 cm^{-1} (Badou et al. 2022).

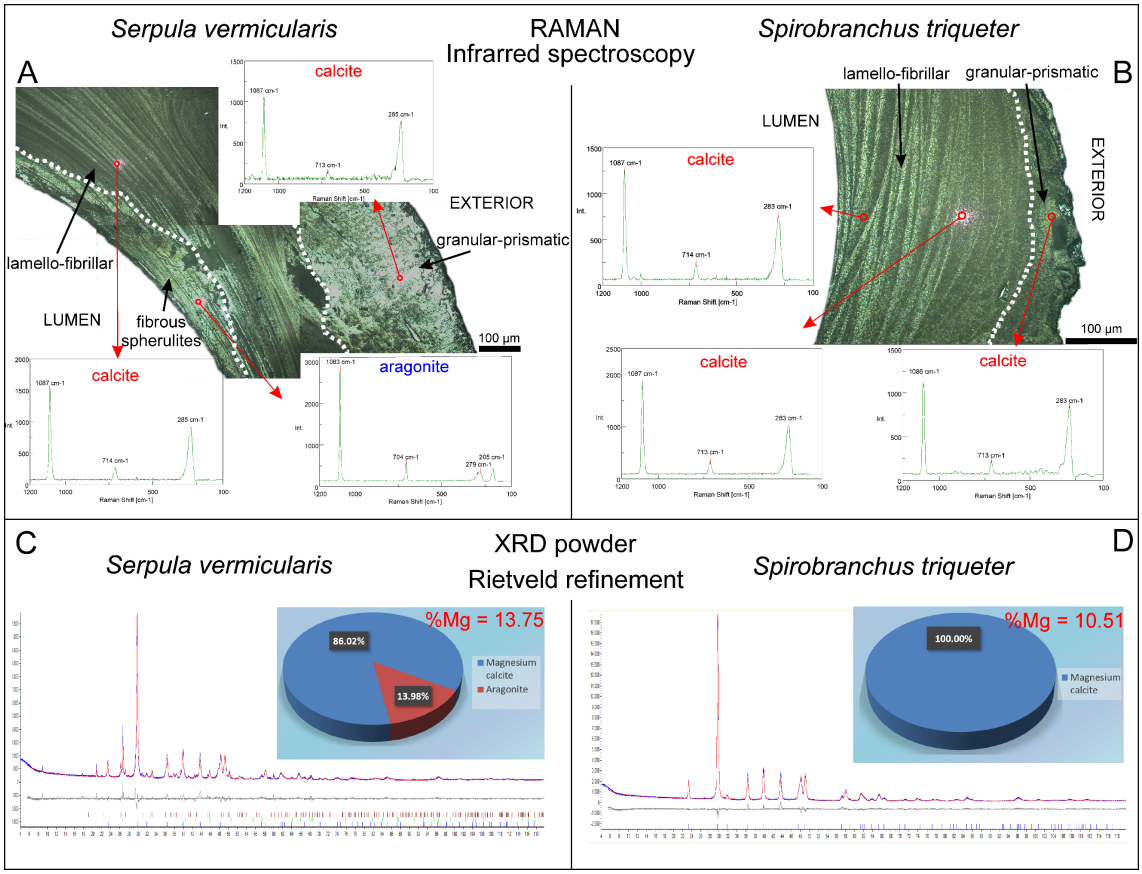

Figure 5. RAMAN and XRD results of *S. vermicularis* and *S. triqueter*. A-B. Raman spectra of *S. vermicularis* (left) and *S. triqueter* (right) from three different positions of the tube cross-sections (indicated in the optical images). A. The external layer (granular-prismatic microstructure) as well as the middle region (lamello-fibrillar microstructure) of *S. vermicularis* are made of calcite. The internal layer (fibrous spherulitic microstructure) is made of aragonite. B. All the different positions analyzed in *S. triqueter* indicated calcite (external granular-prismatic and mid-internal lamello-fibrillar microstructures). C-D. Quantitative mineral composition of tube shell and % of Mg in calcite determined from XRD data analyzed by Rietveld method for *S. vermicularis* (left) and *S. triqueter* (right). C. The tube of *S. vermicularis* is made of 86.02 % high-Mg calcite (13.75 % $MgCO_3$) and 13.98 % aragonite. D. The tube of *S. triqueter* is made entirely of high magnesium calcite (10.51 % Mg_2CO_3).

The granular-prismatic microstructure consists of calcite, as indicated by the spectra obtained from the outermost layers of *S. vermicularis* and *S. triqueter* (Fig. 5A and B, respectively), as well as from *C. websteri* and *S. crenata* (Fig. 6C and E.). The same is true for the lamello-fibrillar layers observed in the middle area of cross sectioned tubes of *S. vermicularis* and *S. triqueter* (Fig. 5A and B, respectively), as well as in *C. websteri*, and *S. giganteus* (Fig. 6C-E). The fibrous microstructure is always made of aragonite, as shown by the analyses performed on the inner layers of *S. vermicularis* (Fig. 5A) and *S. giganteus* (Fig. 6D), as well as on the near external spherulitic clusters of *C. websteri* and in the variously positioned spherulites of *S. giganteus* (Fig. 6C and D, respectively).

The percent of magnesium substitution in the calcite was determined by Rietveld refinement of XRD patterns of tube fragments. In the examples analyzed, calcite has a medium to high magnesium content with 13.75% and 10.51% of $MgCO_3$ for *S. vermicularis* and *S. triqueter*, respectively (Fig. 5C and D).

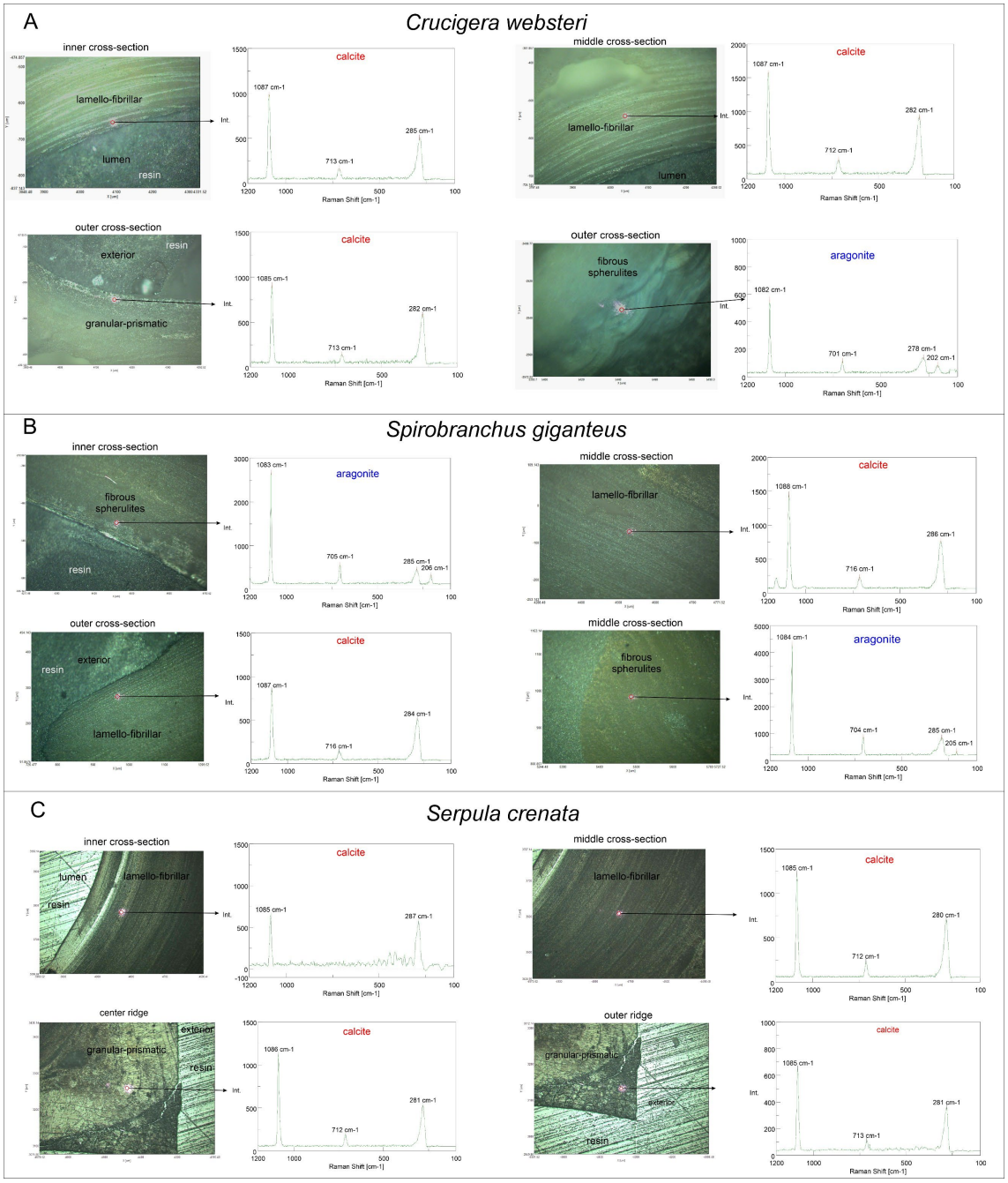

Figure 6. Raman spectroscopy of *Crucigera websteri* (A), *Spirobranchus giganteus* (B) and *Serpula crenata* (C). The analyses were performed on different parts of the tube cross-section (inner, middle, and outer). The mineralogy of the different microstructures analyzed is indicated.

3.2. Granular-prismatic calcite

The granular-prismatic microstructure may present two different varieties according to their location, and to the shape and arrangement of the grains or prisms (Fig. 7):

1) Outer layers of finely prismatic, disoriented crystals that change outward into coarse prisms arranged perpendicularly to the external surface (Figs. 4A and E and 7A-E). Within the coarse vertical prisms, small intra- and intercrystalline grains, either isolated or clustered, are observed (black arrows, Fig. 7B and C). The layer is usually several tens of microns thick, but can reach hundreds of microns at the ribs of some species (e.g. *S. crenata*) (Fig. 7D and E). While most of the prisms increase in diameter as they grow and reach the outer surface, others tend to extinguish at the earliest stages (Fig. 7B and C). They present growth lines parallel to their flat outer surfaces, which are continuous across adjacent prisms (triangles in Fig. 7A and white arrows in D). In some areas, the prisms present arrowhead endings and similarly shaped growth lines (Fig. 7C and D), which correspond to rhombohedral faces in 3D view (Fig. 7C). Under high magnification, the crystal surface nanoroughness can be appreciated (insets in Fig. 7C and D).

☛ **Figure 7** Granular-prismatic calcite. A-E. External layers with granular-prismatic microstructure. A. Sequential magnifications of the external layer of *C. websteri*. The innermost part of the layer is formed by fine, disordered prismatic crystals, which change into coarse prisms arranged perpendicularly to the external surface. Parallel growth lines extend between adjacent prisms (hollow arrows). B. View of the same external granular-prismatic layer, showing small grains within and between the prisms (black arrows). C. Prisms arranged perpendicular to the outer surface, exhibiting rhombohedral endings. The surface nano-roughness can be appreciated (inset). D. Granular-prismatic calcite of *S. crenata.* The prisms are perpendicular to the external surface. Straight and parallel growth lines are continuous across adjacent prisms (arrows). Some prisms of the bottom part show arrowhead endings. The surface nano-roughness is visible (inset to the top). E. External granular-prismatic calcite of *S. vermicularis*, forming layers with very irregular outlines. F-I. Internal granular-prismatic layers in *C. websteri* (F and G) and *S. vermicularis* (H and I). Smaller, disoriented prisms nucleate on the vestiges of the organic membranes between lamello-fibrillar layers penetrating the prismatic-granular layers (particularly evident in G and H). J. Irregularly sized prisms growing across the vestigial membranes in *Crucigera zygophora*. K, L. Two examples of granular-prismatic microstructure in *Floriprotis sabiuraensis*. K. Irregular concretionary growth front within a granular-prismatic layer. L. Granular-prismatic mass containing sparse or clustered smaller fibers. These are co-oriented and distributed in layers (one such layer is indicated by broken lines). Their sizes and mode of co-orientation are typical of the lamello-fibrillar microstructure. M. Lamello-fibrillar layer of *S. giganteus*, including prismatic layers (bottom left part) and a central concretion of granular calcite, with the fibers adapting to its lower contour.

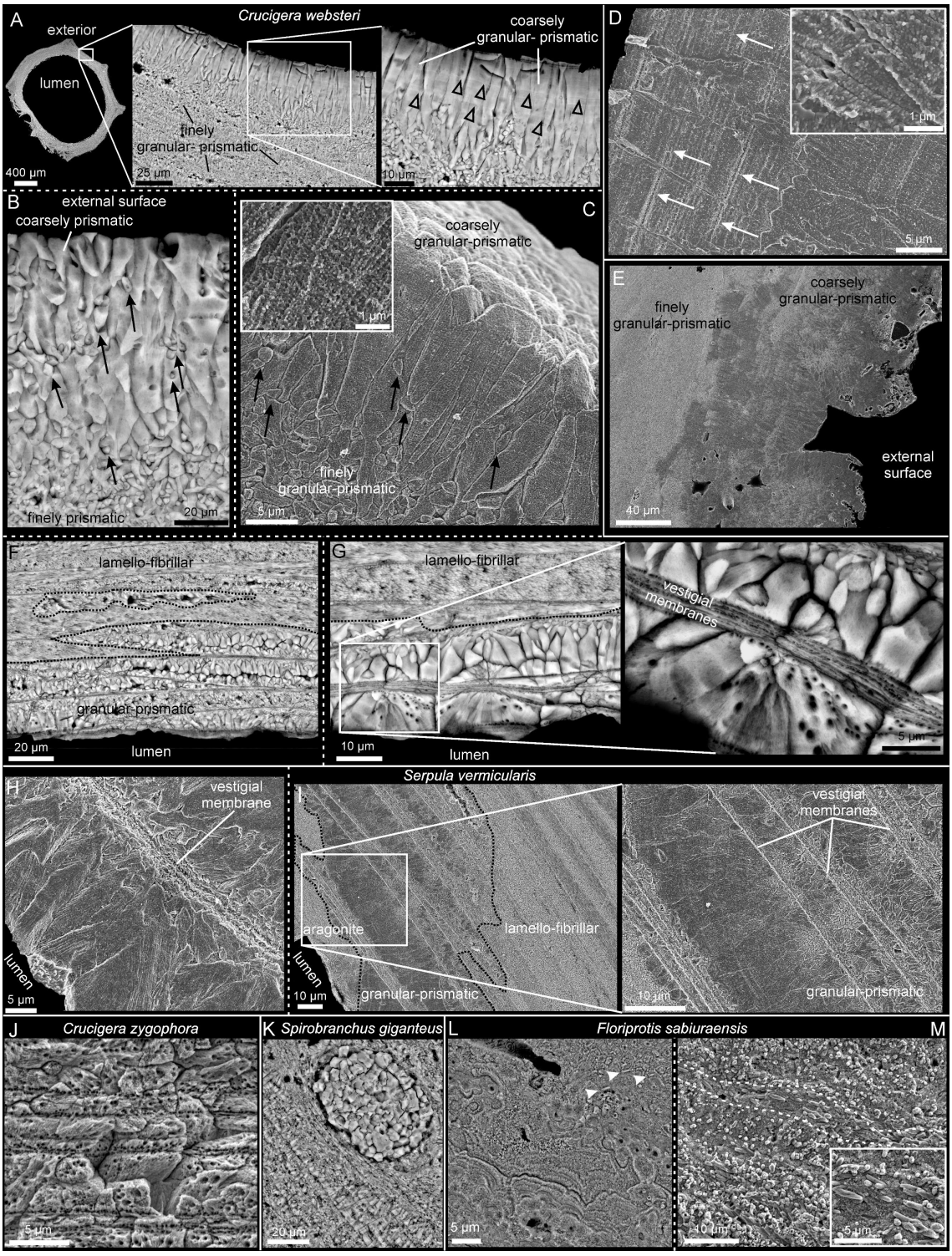
A
Crucigera websteri
exterior
lumen
finely granular- prismatic
coarsely granular- prismatic
400 µm
25 µm
10 µm
B
external surface
coarsely prismatic
finely prismatic
20 µm
C
coarsely granular-prismatic
1 µm
finely granular-prismatic
5 µm
D
1 µm
5 µm
E
finely granular-prismatic
coarsely granular-prismatic
external surface
40 µm
F
lamello-fibrillar
granular-prismatic
20 µm
lumen
G
lamello-fibrillar
vestigial membranes
10 µm
lumen
5 µm
Serpula vermicularis
H
vestigial membrane
lumen
5 µm
I
aragonite
lamello-fibrillar
lumen
10 µm
granular-prismatic
vestigial membranes
10 µm
granular-prismatic
J
Crucigera zygophora
5 µm
K
Spirobranchus giganteus
20 µm
L
Floriprotis sabiuraensis
5 µm
M
10 µm
5 µm

2) Irregular layers or aggregates close or at the innermost part of the tube (Fig. 7F-J), which laterally change into the layers of the lamello-fibrillar microstructure (Fig. 7F and I). The prisms-grains range from less than one to several tens of microns both in length and thickness. Vestiges of the organic membranes that separate the lamello-fibrillar layers continue into the granular-prismatic microstructure. The grains-prisms usually nucleate on the vestigial membranes (Fig. 7F-I), sometimes forming spherulites with well-defined concentric growth lines, which indicate radial growth (detailed view in Fig. 7G). The prisms may continue across the vestigial membranes (Fig. 7J). Exceptionally, round aggregates of granular calcite are found within lamello-fibrillar layers (Fig. 7K). On occasion, the spherulites fuse to form continuous, irregular, concretion-like growth fronts (Fig. 7L). In other instances, the granular-prismatic material constitutes a matrix, which contains oriented isolated fibers or clusters of them, typical of the lamello-fibrillar microstructure (Fig. 7M).

The crystallography of the granular-prismatic calcite, particularly the coarse prisms of the external layer, is shown in Figs. 8 and 9. The EBSD maps showing the mineral distribution and crystal orientation were done on a ridge of *S. crenata*, made entirely of granular-prismatic calcite. The BC map of Fig. 8A depicts well indexed areas on both sides of the ridge, but not in the dark central region, where the diffraction signal is either too weak or absent. The phase maps corroborate that the entire ridge consists of calcite (Figs. 8B and 9B). While the prisms of Fig. 8 were sectioned parallel to their long axes, those of Fig. 9 were sectioned oblique to their axes. The IPFz map of Fig. 8C reveals a predominance of green-purple colors, which suggests that the prisms have their c-axes in plane (see the triangle color key). The PFs are plotted for three separate regions (two lateral and one central) (Fig. 8C). Both raw and contoured PFs display a well-defined axial texture, which is better defined in the lateral regions. The calcite c-axis coincides with the elongation axis of the prisms (Fig. 8C) and remains at a high angle to the external surface (as indicated by the unit cells), adapting to the change in curvature of the ridge. The MUD value of the top lateral region is significantly higher (69) than those of the central (27) and bottom lateral (32) regions, coinciding with the higher spread of the c-axes in the latter regions. Their low MUD values can be attributed to the scarcity of indexed points. To check the change in co-orientation of the prisms with growth, we have cropped three regions of the top area belonging to the progressive developmental stages of the prisms (Fig. 8D). There is a reduction in the dispersion of the maxima in the contour PFs and an increase of the MUD values (from 40 to 60 to 76), indicating that prisms become progressively co-oriented with growth.

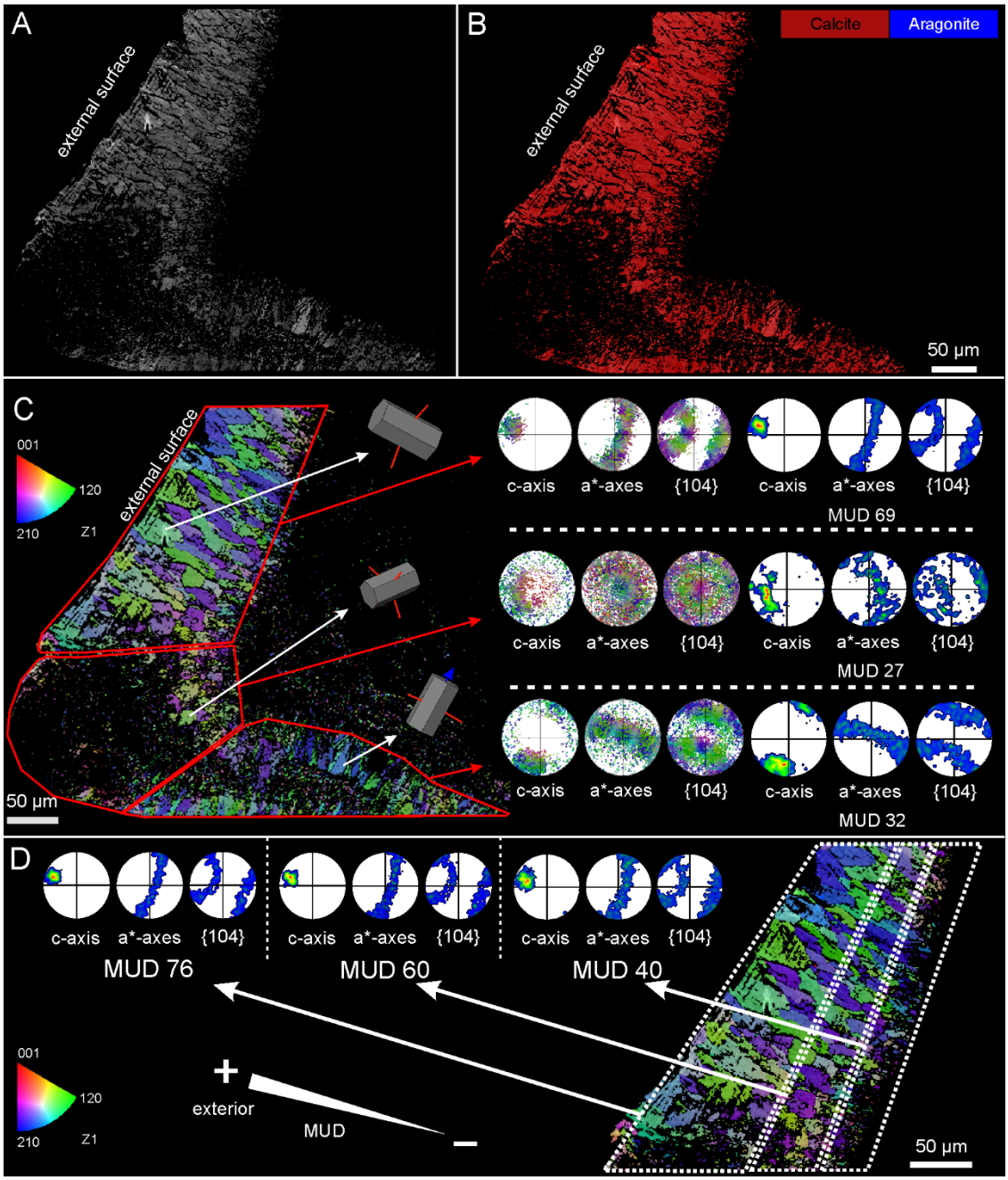

Figure 8. EBSD analysis of the granular-prismatic calcite (coarse prismatic layer) of a ridge of *S. crenata*. A. The BC map (grey color) shows a central area with weak to absent EBSD diffraction signal (dark area). B. The phase map indicates that the whole structure is made of calcite (see legend). C. IPFz map of the ridge and PFs of the three regions differentiated (two lateral and one central). The green-purple colors are predominant, indicating that the c-axes are in plane. The PFs display axial textures (weaker at the central region). The c-axis is roughly perpendicular to the external surface and it changes in orientation coinciding with the curvature of the ridge, as also indicated by the unit cells. The MUD value of the top lateral region is higher than the values of the central and bottom lateral regions. D. IPFz map of the top lateral area of C. The contour PFs are plotted from three different growth stages. There is a progressive reduction in the spread of the maxima of the contour PFs toward the exterior (from right to left), along with an increase of the MUD values (from 40 to 76). This indicates that the texture becomes stronger with growth. The color triangle is the key for orientations.

The EBSD map of Fig. 9 provides similar results. The IPF map displays a wider range of colors and the maxima for the c-axes are displaced from the center due to the oblique cut (Fig. 9C). The subsets indicate that the MUD values also increase from the interior to the exterior (Fig. 9D), although the bottom subsets display lower values because the higher curvature of the area (indicated by the growth lines, Fig. 9A) gives rise to a higher dispersion of the c-axes.

An additional EBSD crystal orientation map was performed directly on the polished surface of the transversal cross-section tube of *S. giganteus* (Fig. 10). The area analyzed contains several layers of granular-prismatic calcite delineated by vestigial membranes in the middle of the tube (Fig. 10A-C). The prisms are, in general, oriented perpendicular to the membranes. As in the previous instances, the IPFz map and the PFs indicate that the calcite c-axes are in plane (Fig. 10D) and parallel to the elongation axes of prisms. The texture is a weak axial texture (MUD value of 23). This arrangement is particularly evident in the central layer (delimited by white broken lines in Fig. 10D), which consists of coarse prisms (see cell lattices). It displays a medium axial texture (MUD value of 56).

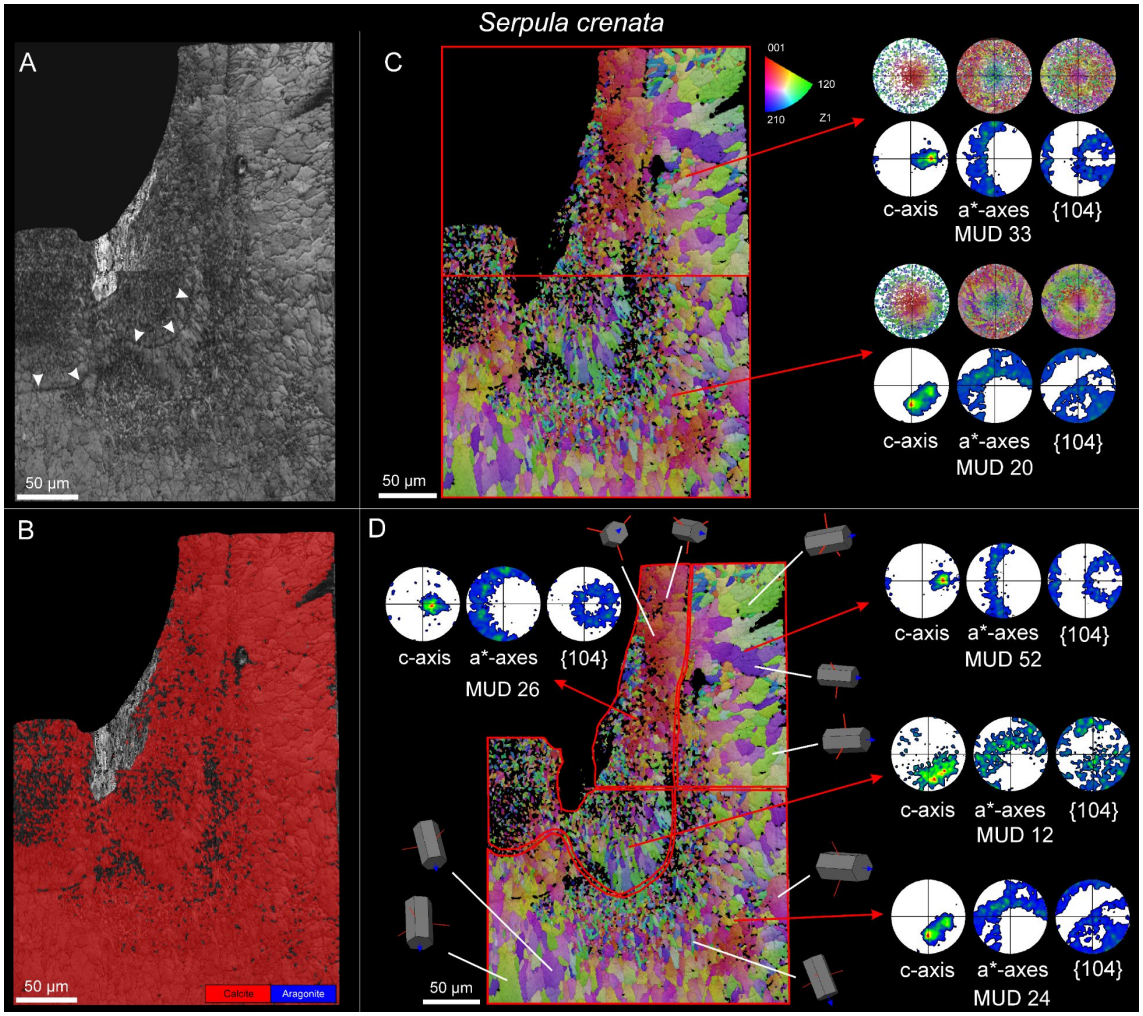

Figure 9. EBSD analysis of the granular-prismatic calcite (coarse prismatic layer) of a ridge of *S. crenata*. Given the large area covered, the analysis was done over two contiguous maps (framed in C). A. The band contrast maps show a good EBSD diffraction signal (light-grey color). Some arc-shaped growth lines are visible in the central part (white arrowheads). B. The phase maps indicate that the entire structure is made of calcite (red color, see legend). C. The two IPFz maps predominantly exhibit green, red, and purple colors, the latter indicating that the prisms' c-axes are roughly oblique to the section plane. Their respective pole figures show a medium axial texture (MUD values of 33 and 20), with the c-axis maxima placed from the center. The c-axis maximum is wider in the pole figures of the bottom map, due to the curvature of the ridge. D. The same IPFz maps with differentiation of the internal and external regions. The pole figure maxima exhibit slightly more perpendicular c-axes (also depicted by the unit cells) in the inner regions. The maxima become narrower and the MUD values increase (from 26 to 52 at the top, and from 12 to 24 at the bottom) toward the exterior. The color triangle is the orientation key.

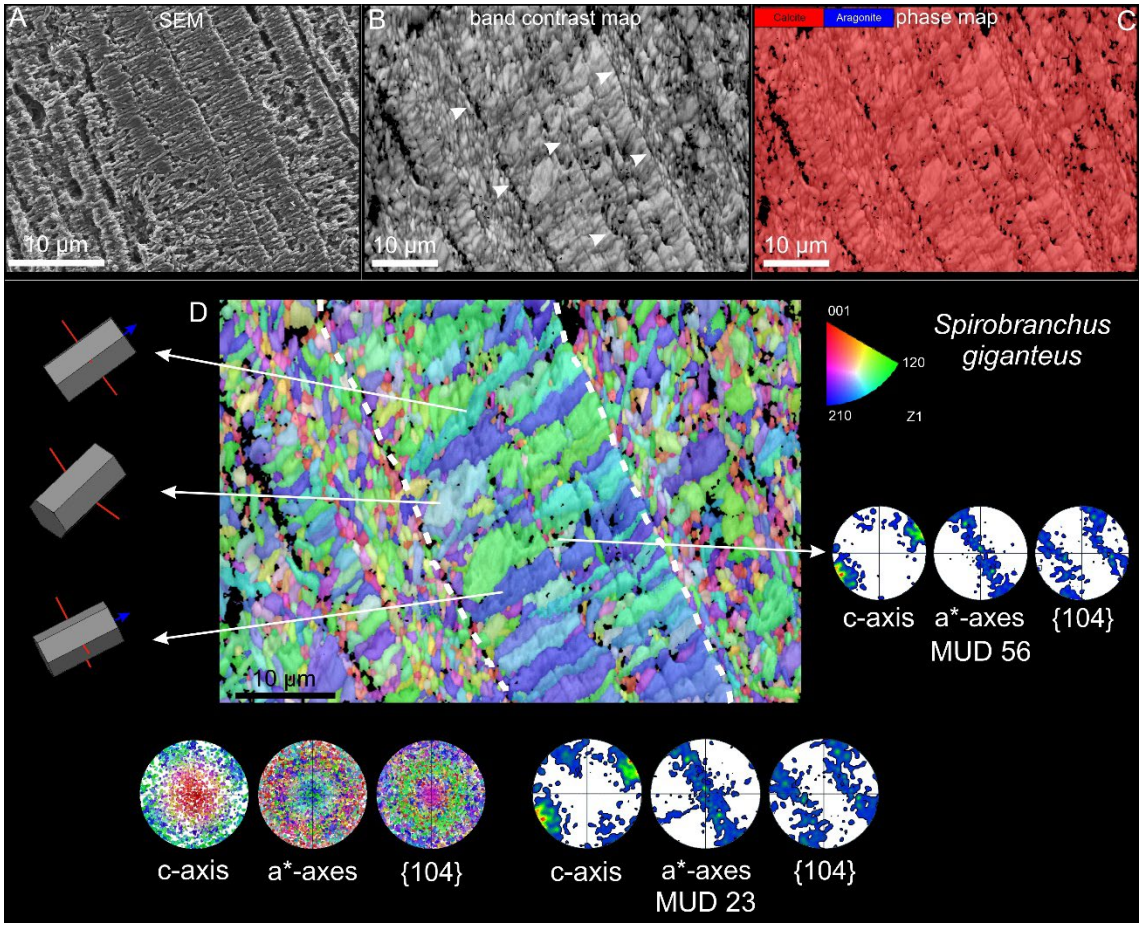

Figure 10. EBSD analysis of a polished surface of the finely granular-prismatic calcite of *S. giganteus*, transversal to the tube. A. SEM image of a surface similar to that analyzed with EBSD. B-D. Surface analyzed. B. Band contrast map. The light-grey color of the whole map denotes a good EBSD signal strength. The contours of the prisms are easily recognizable. They are arranged perpendicular to the vestigial membranes (white arrowheads). There is a central coarse prismatic layer. C. Phase map. The entire map is made of calcite (see legend). D. IPFz map and pole figures. Green-blue-purple colors predominate, indicating that the c-axes of most of the prisms are parallel to the section plane. This is corroborated by the unit cells and the position of the c-axis maximum. The pole figures display a weak axial texture (MUD value 23). The pole figures for the central coarse prismatic layer, delineated by broken lines, give a medium axial texture (MUD value 56). The color triangle is the orientation color key.

The crystallographic data of the finely granular-prismatic calcite underlying the coarse granular prismatic calcite are provided in Fig. 5. The EBSD map was performed in a longitudinal cross-section of the *S. crenata* tube, similar to that in 11A. The BC map (11B) shows a stronger diffraction signal for the coarse prisms. The phase map confirms the calcitic composition of the microstructure (11C). The wide variety of colors of the IPFz map of the finely prismatic grains (top right area of the map of 11D) indicates that their axes are not co-oriented (see cell lattices). The PFs corroborate the lack of texture, with scattered maxima for all axes and a very low MUD value (9). Conversely, the overlying coarse prisms present a predominance of green-purple colors (bottom left area of the map of 11D), which means that they are co-oriented (as also indicated by the cell lattices), with the c-axis along their elongation axes and almost in plane. The coarse prisms have a moderate axial texture (MUD value of 56), with the c-axis as the fiber axis.

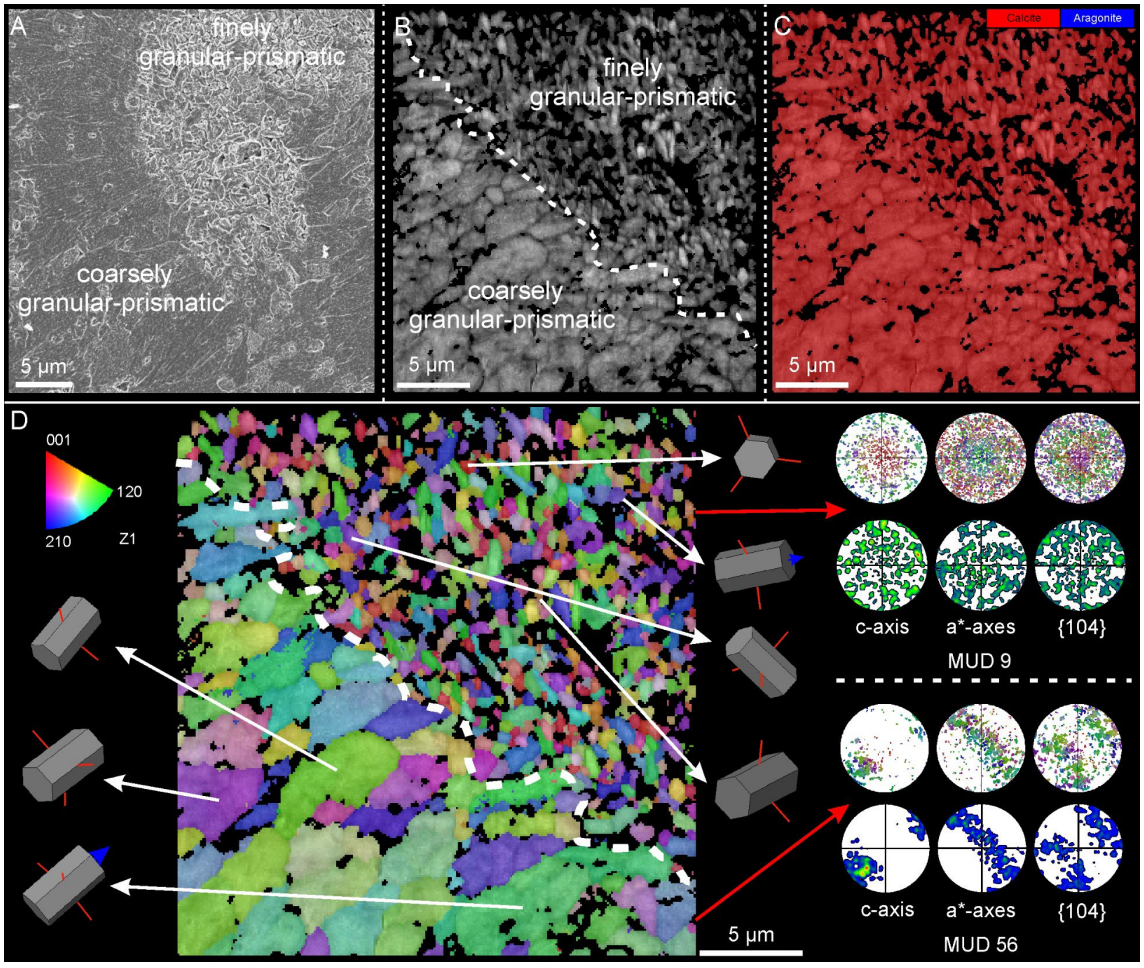

3.3. Lamello-fibrillar calcite

The lamello-fibrillar microstructure is made of successive layers of thin, elongated, and co-oriented calcite fibers, arranged parallel to the growth surfaces (Figs. 4B, D, E, and 12). The layers are not homogeneous in thickness, varying from 2 to more than 10 μm in width (Fig. 12A-C), and they frequently wedge out laterally (Fig. 12F and G). Fiber size ranges from 3-6 μm in length and 400-600 nm in width. Fibers of single layers are strictly co-oriented, although some particularly thick layers show a progressive twisting across the layer thickness (white arrows in Fig. 12A and D). There is always a noticeable change in orientation between superposed layers (Fig. 12A, C, D, G). In all samples studied, the lamello-fibrillar microstructure constitutes the middle and internal parts of the tube, except for intercalated layers or clusters of granular-prismatic calcite or spherulitic fibrous aragonite. Conspicuous organic membranes separate the layers (white triangles in Fig. 12A and B) and organic threads are presented between the calcite fibers (white arrows in Fig. 12A and C). As the lamello-fibrillar microstructure approaches the outer surface, its organic membranes reflect back (Fig. 12B) at the same time that it changes into the disordered, non-layered finely granular-prismatic microstructure (Fig. 12A, B).

☚ **Figure 11.** EBSD analysis of two superposed types of granular-prismatic calcite of *S. crenata* (finely and coarsely prismatic), forming the outer layer of the tube. A. SEM image of an area similar to that analyzed. B. BC map showing the two types of granular-prismatic calcite. C. Phase map indicating that the microstructure is made of calcite (see legend). D. IPFz map depicting a broader color variation of the finely granular-prismatic calcite compared to the coarsely prismatic calcite. The PFs of the finely granular calcite present scattered maxima for all the axes, while the coarsely prismatic calcite displays a moderate axial texture, with the c-axis (fiber axis) oriented at a small angle to the sectioning plane (also indicated by the unit cells). The color triangle is the orientation key.

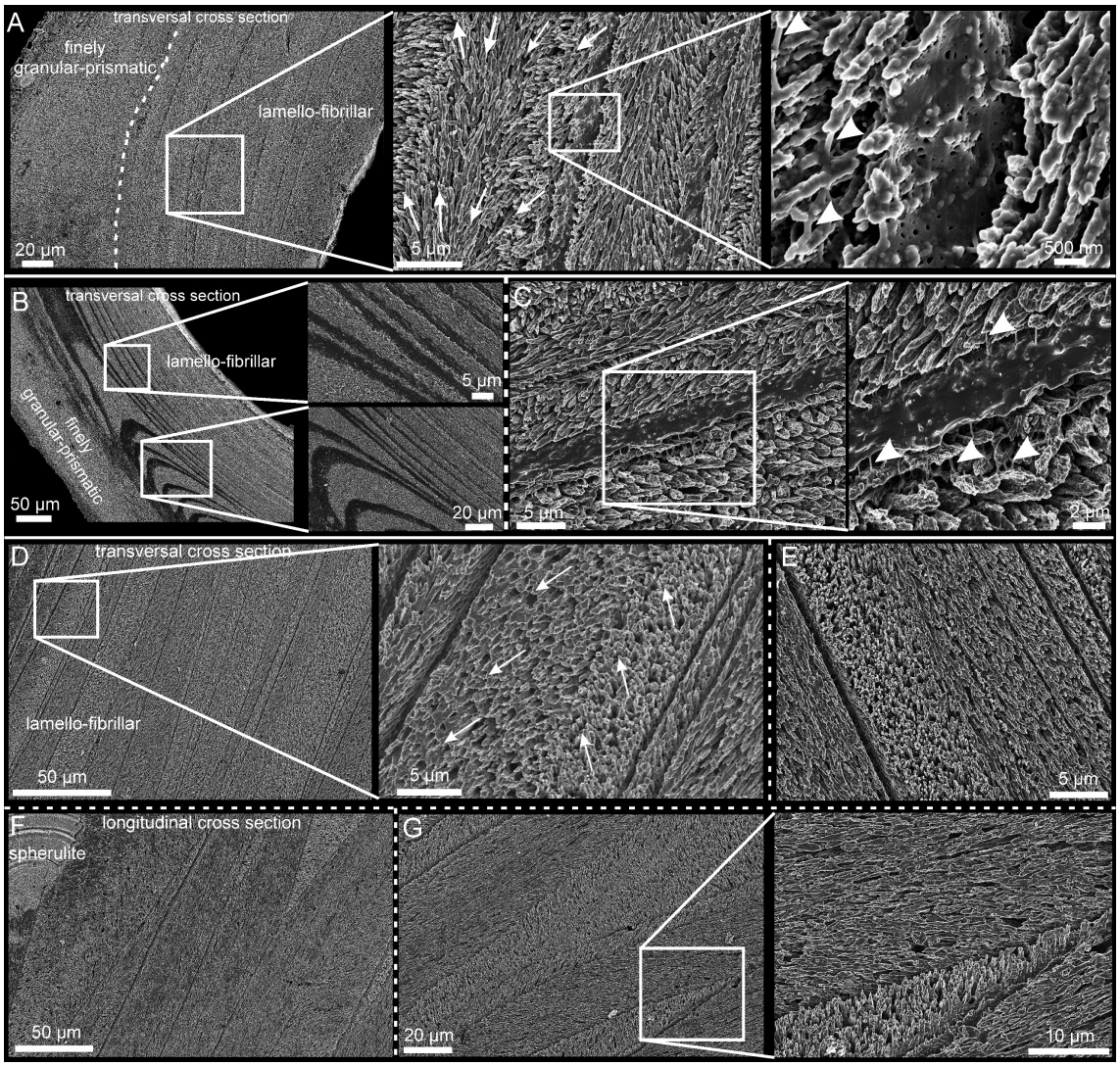

Figure 12. The lamello-fibrillar calcite of polychaetes. A. Lamello-fibrillar microstructure of *C. websteri*. The boundary with the finely granular-prismatic material is indicated. The progressive magnifications show the changing orientations of the fibers in different layers (arrows in the central image), bounded by organic membranes. The arrowheads of the right image point to organic threads between fibers. B-C. Lamello-fibrillar calcite of *S. triqueter*. B. The different layers are clearly marked by organic membranes (see zoomed views of the framed areas). These disappear into the external finely granular prismatic layer. C. Detail of an organic membrane between the layers. The organic threads between calcite fibers are indicated with arrowheads. D-E. Lamello-fibrillar microstructure of the middle cross-section tube of *S. vermicularis*. D. Note the changing thicknesses of the layers. The close-up view shows the change in the orientation of the fibers between layers and the rotation of fibers inside the central layer (white arrows). E. View similar to the close-up in D. F-G. Longitudinal cross-sections of the tube of *S. vermicularis*. Lamello-fibrillar layers have varied thicknesses and wedge out frequently.

Crystallographic data on the lamello-fibrillar microstructure of *S. triqueter* (Figs. 13 and 14) and *S. vermicularis* (Fig. 14) have been obtained with t-EBSD. Maps are either perpendicular (Fig. 13) or parallel (Fig. 14) to the longitudinal direction of the fibers within single layers (see lamellae preparation in Fig. 15). The BC map of *S. triqueter* (Fig. 14A) shows well-defined fiber contours, indicating a good EBSD diffraction signal for the entire lamella, whereas for *S. vermicularis*, the BC map shows gaps in the left area due to damage by ion beam during sample preparation (dark area in Fig. 14D). In *S. triqueter*, the fibers are arranged in two different directions: longitudinally at the top and transversely at the bottom. In *S. vermicularis*, the fibers are coaligned and belong to a single layer although there is some spread of the axes. The phase maps corroborate that the only phase is calcite (Fig. 14B and E). The EBSD color maps (IPFz maps, Figs. 14C and F) reveal a predominance of green-purple colors for the longitudinally cut fibers and reddish for the transversally cut fibers. This indicates that, in the first instance, the fibers have been cut close to their c-axis, whereas in the latter case, the c-axes are at a high angle to the image plane (see the triangle color key). The PFs (Figs. 14C and F) display a strong axial texture, with the c-axis as the fiber axis (depicted by the unit cells). In *S. triqueter*, the maximum for the c-axis is well-clustered and the MUD values are very high (176 for the longitudinal fibers and 90 for the transversal fibers) (Fig. 14C). In *S. vermicularis*, the c-axis maximum is broader and the MUD value is significantly lower (41) (Fig. 14C), likely due to the progressive change in orientation of the c-axes (see also cell lattices).

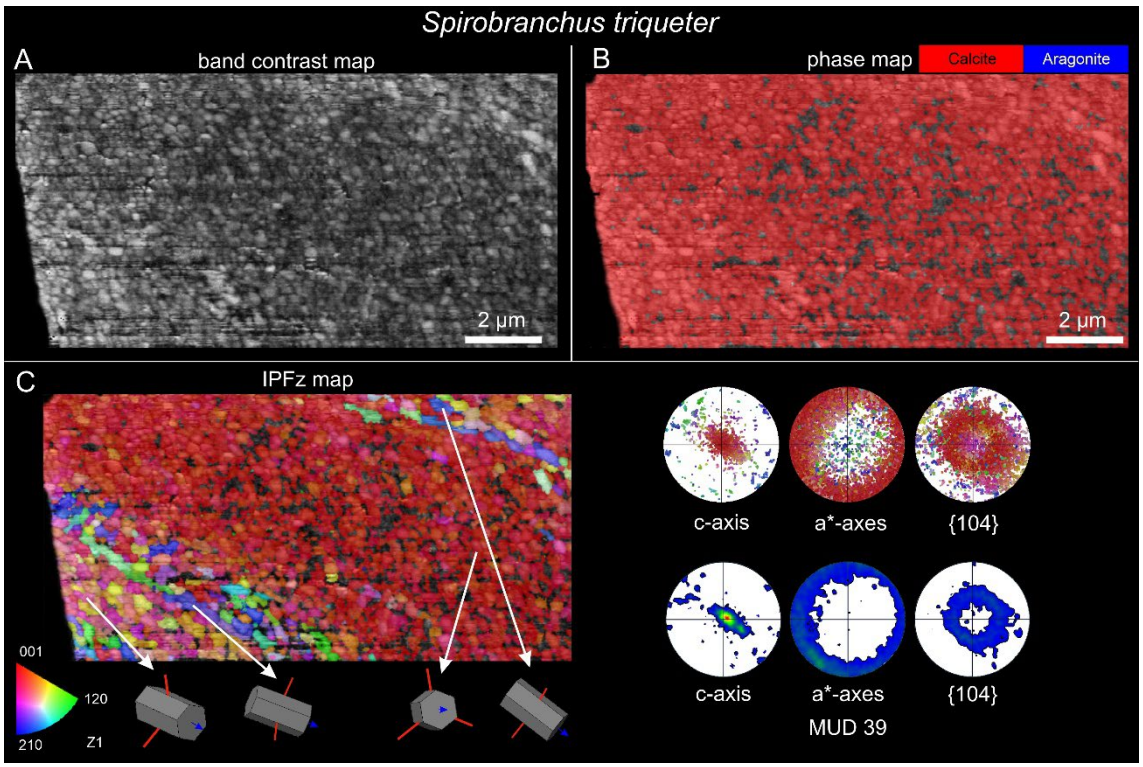

Figure 13. EBSD analysis of a FIB-prepared lamella of the lamello-fibrillar calcite of *S. triqueter*. A. Band contrast map. The contours of the transversely sectioned fibers are recognizable. B. Phase map. The entire structure is made of calcite (see legend). C. The IPFz map shows a predominant red color in the central oblique band, indicating that the fibers have their c-axis at a high angle to the sectioning plane. Given the high surface contribution of this band, the c-axis pole figures have prevalent central maxima. The MUD value (39) indicates a medium axial texture. Some fibers of the oblique stripes at the top and bottom are roughly parallel to the plane (see the unit cells). The color triangle is the orientation color key.

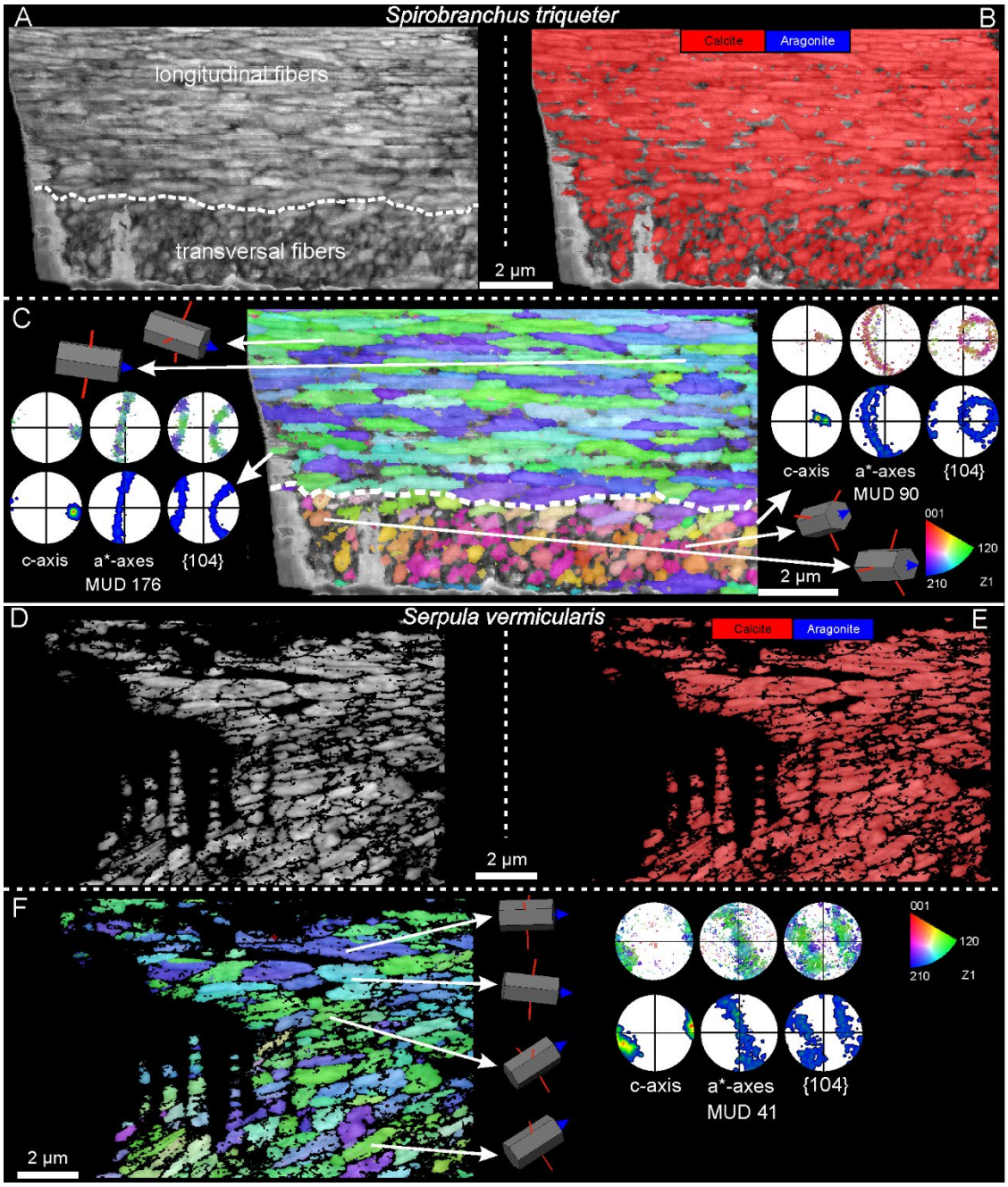

Figure 14. EBSD analysis of the lamello-fibrillar calcite of *S. triqueter* (A-C) and *S. vermicularis* (D-F). A. BC map. The contours of the fibers are easily recognizable. They are arranged longitudinally at the top and transversely at the bottom. B. The phase map indicates that the entire structure is made of calcite (see legend). C. The IPFz map shows that the fibers' c-axis is co-oriented within each layer (note similar colors). The PFs for each layer show a strong axial texture, where the calcite c-axis is the fiber axis, aligned in the elongation direction of the fibers (as also indicated by the unit cells). The high MUD values of the two superposed layers (176 and 90) indicate high co-orientations. D. BC map. Some areas of the left side (in black) could not be indexed due to damaging of the lamella. E. Phase map. The red color indicates the calcitic nature of the sample. F. IPFz map. The purple-green colors show that the fibers were cut approximately parallel to the c-axis. There is evident fiber spread (indicated by the cell lattices). The PFs show an axial texture, in which the calcite c-axis is the fiber axis, aligned in the elongation direction of the fibers (see also unit cells). The MUD value (41) is well below those of *S. triqueter* (see C). The color triangle is the orientation color key.

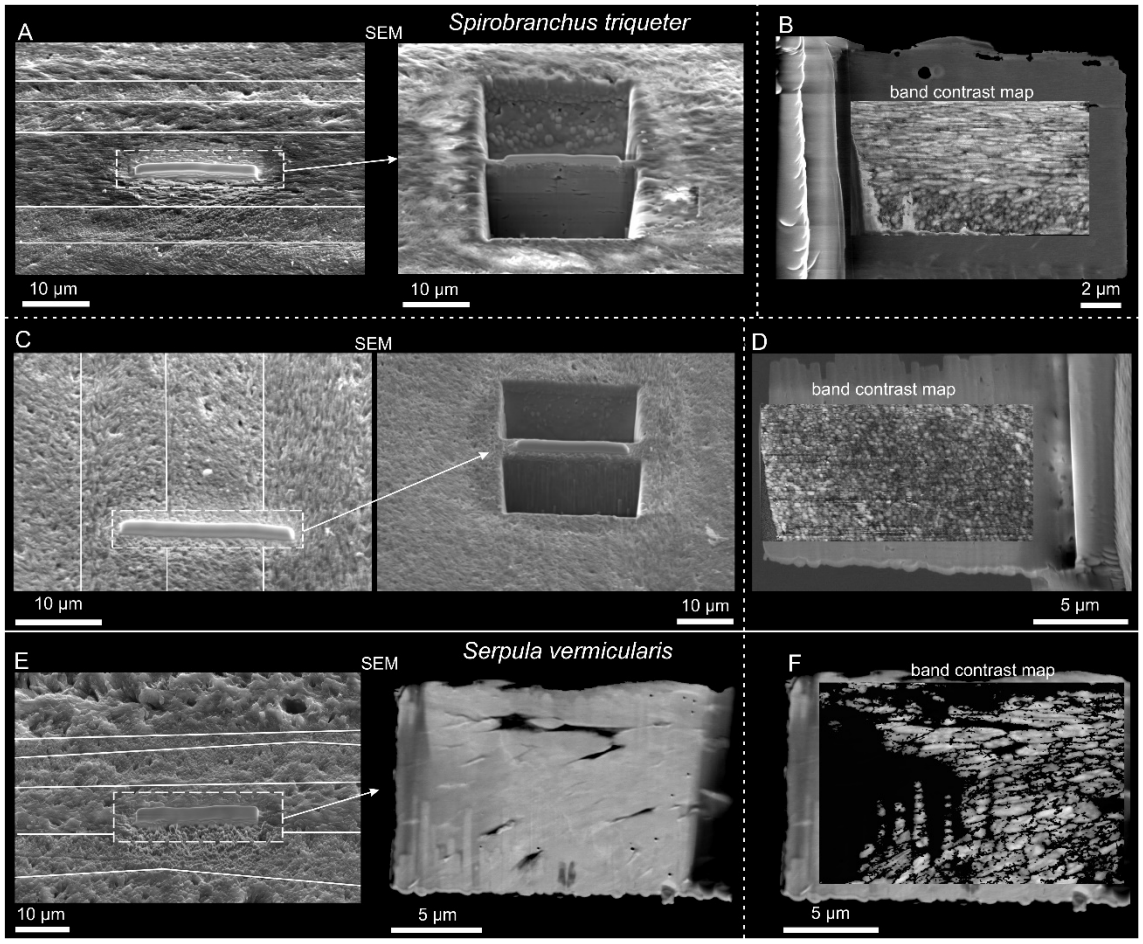

Figure 15. Thin foil lamellae prepared by the FIB technique on the lamello-fibrillar microstructure in *S. triqueter* (A-D) and *S. vermicularis* (E-F). The examples correspond to the EBSD results shown in Figs. 13 (C, D) and 14 (A, B, E, F). A, C, and E are SEM images of the areas selected, either along (A, E) or transversal (C) to the growth increments (arrows). Intermediate stages of the preparation are shown in A and C, and a SEM view of the lamella is provided in E. B, D, and F. The extracted lamellae with their respective band contrast maps superimposed, indicating the areas analyzed by EBSD.

An additional EBSD map of the lamello-fibrillar calcite of *S. triqueter* was directly performed on the middle part of a polished cross-section (Fig. 16). Three different layers can be distinguished on the BC map (Fig. 16 B), with fibers of each layer displaying different orientations and sizes, however all made of calcite according to the phase map (Fig. 16C). The IPFz map and the PFs indicate that the c-axes of most fibers are roughly parallel to the viewing plane in the lateral layers, and at a high angle in the central layer (see also cell lattices for each layer, Fig. 16D). The right layer demonstrates thin and well co-oriented fibers (medium

axial texture, MUD value of 62), characteristic of the lamello-fibrillar microstructure. In the central and left layers, there is an increase in size and a decrease in co-orientation (MUD values of 25 and 31 for the central and left layers respectively), thus being more typical of the granular-prismatic microstructure.

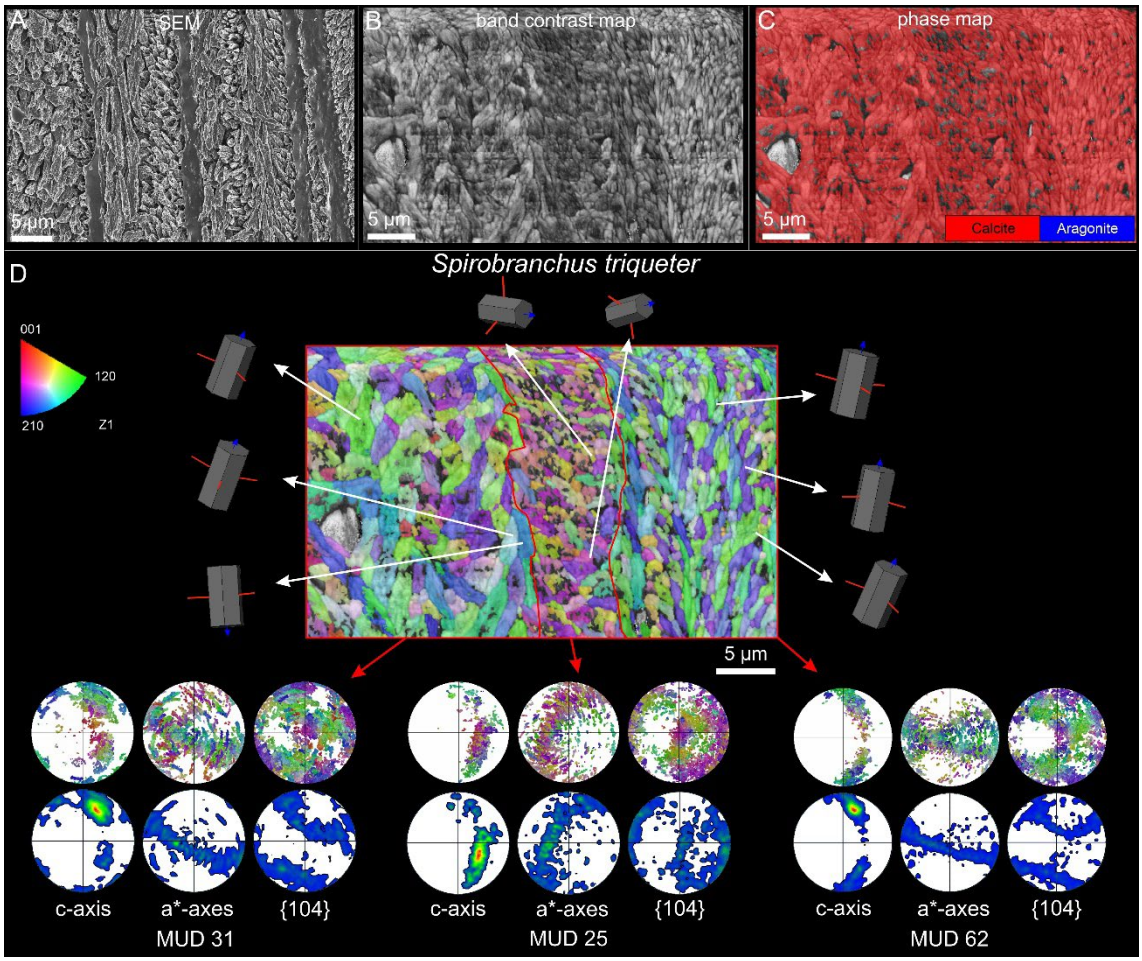

Figure 16. EBSD analysis of a polished surface of the lamello-fibrillar calcite of *S. triqueter*. A. SEM image of a surface from a transversal tube cross-section, similar to that analyzed by EBSD. B. Band contrast map, exhibiting a good EBSD signal strength (light-grey color). The contours of the fibers are easily recognizable, being smaller and thinner in the right area. C. Phase map. It is entirely made of calcite (see legend). D. IPFz map and pole figures. Three different layers were analyzed. In the lateral layers, the c-axes of the fibers are roughly in plane, while in the central layer, the c-axes are at a high angle (see cell lattices). The pole figures display a better co-orientation of the fibers of the right layer (medium axial texture, MUD value 62), than those of the central and left layers (MUD values 25 and 31, respectively). The color triangle is the orientation color key.

Decalcification with EDTA of the lamello-fibrillar microstructure of *S. triqueter* (Fig. 17) exposes the arrangement of curved organic membranes (Fig. 17A right), with changes in thickness of the intervening layers similar to those observed in non-decalcified samples (Figs. 12A, B, D, F, and 17A left). The

thermogravimetric analysis reveals that the total amount of organic matter is ~7.5% of the total weight (weight loss between 200°C and 600°C, Fig. 17B). The organic membrane chemical composition was analyzed by FTIR-ATR analysis, indicating that it contains mainly proteins and sulfated polysaccharides (Fig. 17C).

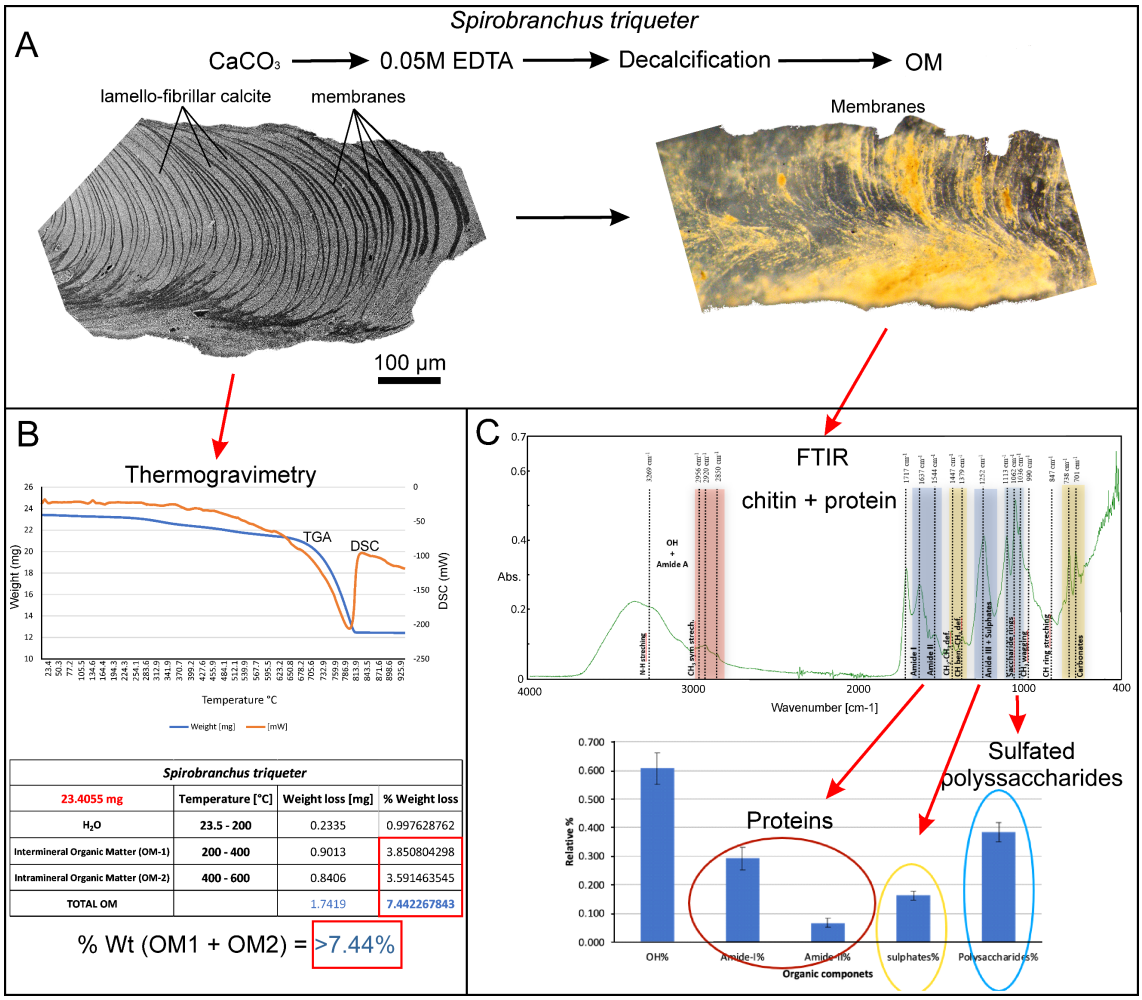

Spirobranchus triqueter			
23.4055 mg	Temperature [°C]	Weight loss [mg]	% Weight loss
H_2O	23.5 - 200	0.2335	0.997628762
Intermineral Organic Matter (OM-1)	200 - 400	0.9013	3.850804298
Intramineral Organic Matter (OM-2)	400 - 600	0.8406	3.591463545
TOTAL OM		1.7419	7.442267843

% Wt (OM1 + OM2) = >7.44%

Figure 17. Characterization of the organic matrix of the *S. triqueter* shell by TGA and FTIR. A. Stages in the decalcification of a tube fragment with EDTA. B. TGA analysis of shell powder. The main weight loss events corresponding to different chemical components were determined between 25°C and 600°C and are indicated in the table. C. Results of the analysis of the decalcified organic membranes by FTIR showing the main chemical components.

3.4. Fibrous aragonite

The fibrous aragonite microstructure consists of needle-like aragonite fibers, usually arranged into spherulites, where the fibers radiate from a nucleation center (Figs. 4C-G and 18). They have rounded (Fig. 18A, C-E) or, rarely, angular outlines (Fig. 18B). Aragonite spherulites can be found as discontinuous layers with highly variable thicknesses, either at the innermost or the outermost part of the tube (Fig. 18A-F). When internal layers become particularly thick, the growth front of coalescing spherulites may become increasingly flat (Fig. 18D, G). Spherulites can also be found as clusters of variable sizes in any region within the tube (Fig. 18E and F). Then, they exhibit well-defined concentric growth lines (Figs. 18C-H and 19A-C), whose shapes indicate growth either toward the lumen or the exterior of the tube (Fig. 18A, B, D, E and F). The fibrous aragonite can be found in contact with either the lamello-fibrillar or the granular-prismatic microstructures.

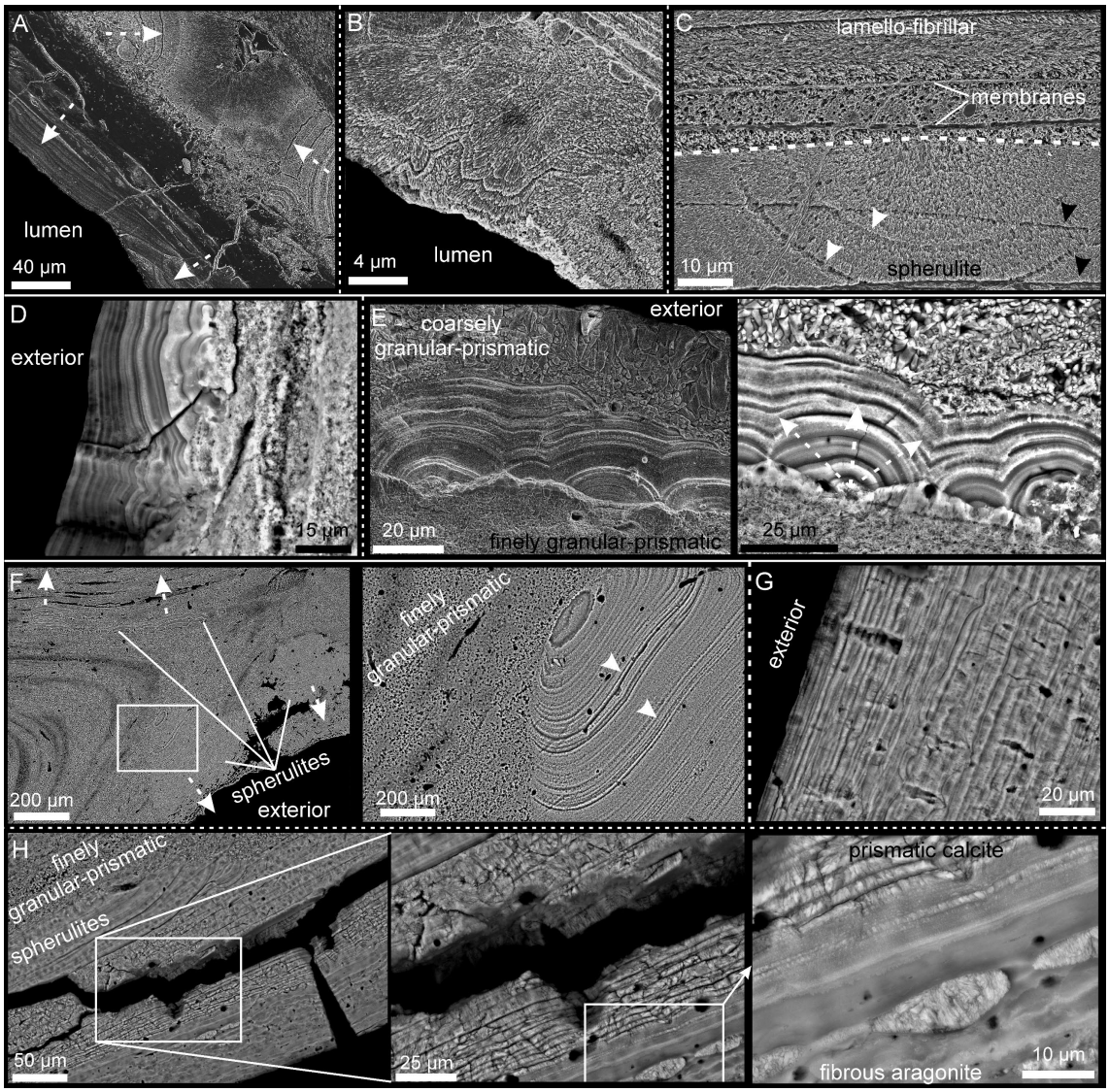

Figure 18. Fibrous aragonite microstructure. A-C. Spherulites in *S. vermicularis*. A. Spherulites at the innermost layers. Some of them grow toward the lumen, whereas others spread laterally toward each other (growth directions indicated by the white dashed arrows). B. Coalescing aggregates of fibrous aragonite with angular outlines. Concentric growth lines are visible. C. Spherulite in the interior of the tube, underlying lamello-fibrillar layers. Its concentric growth lines extend across the relict organic membranes of the lamello-fibrillar calcite (black triangles). D, E. Spherulitic aragonite of *C. websteri*. D. Fibrous aragonite at the outermost layer. Initially, it consists of spherulites which fuse outward and form a roughly continuous layer. E. Layer of coalescing spherulites located between the finely granular-prismatic and the external prismatic calcite (see enlarged view). The concentric growth lines of the spherulites are visible, indicating growth toward the external surface (white dashed arrows). F-H. Fibrous aragonite of *S. giganteus*. F, G. Spherulites scattered within the tube cross-section (F) or constituting internal discontinuous layers (G). H. Innermost layer. The fibrous aragonite intersects the finely granular-prismatic calcite (see sequential magnifications).

In the first instance, the spherulite growth lines occasionally overprint the relicts of the membranes between the lamello-fibrillar layers (triangles in Figs.

4G, 18C, F, G and 19C). The interface between the aragonitic and calcitic microstructures was further analyzed using EDX in *S. giganteus* (Fig. 19A-C), which allows for the identification of calcite grains according to their Mg^{2+} content (blue color in Fig. 19). This procedure reveals the existence of relict calcite grains within the aragonite fibers close to the interface with the calcitic microstructure.

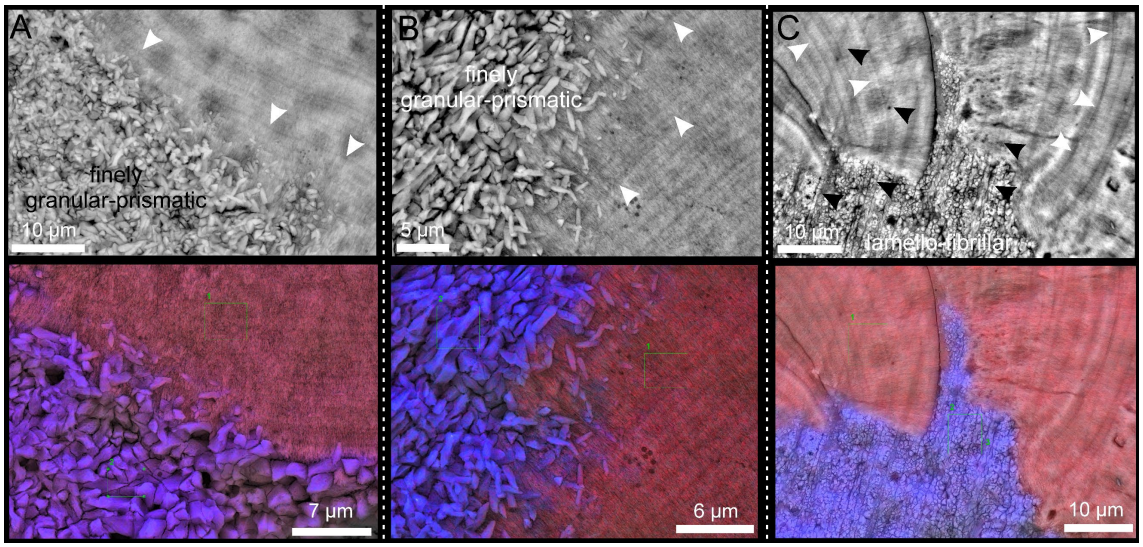

Figure 19. EDX analysis of the interface between calcite and aragonite spherulites in *S. giganteus*. A-C. SEM views of the interfaces (top) and their respective EDX maps (red= Ca^{2+}; blue= Mg^{2+}) (bottom). The white arrowheads indicate the marked growth lines of the aragonite spherulites. The black triangles (C) point to relict organic membranes continuing into the spherulites.

The crystallography of the spherulitic microstructure is shown in Fig. 20. The analysis was performed on a polished cross-section of *S. giganteus*, at the boundary between the finely granular-prismatic calcite and the fibrous aragonite microstructures, located in the middle of the tube (Fig. 20A). The BC map (Fig. 20B left) shows a better diffraction signal of the calcite grains (lighter areas) than of the fibrous aragonite. The phase map (Fig. 20B right) corroborates the polymorph distribution (see legend). The EBSD map (IPFz maps, Fig. 20C) reveals a predominance of green-orange colors for the aragonitic fibers and a wider variety of colors (orientations) for the granular-prismatic calcite, suggesting that the former are better co-oriented. The cell lattices for the

aragonite fibers (Fig. 20C, right bottom) indicate that their c-axes are parallel to their long axis. The fibrous aragonite has a moderate axial texture (MUD value 65), with the c-axis as the fiber axis, while the calcite grains-prisms are randomly oriented (MUD value 17).

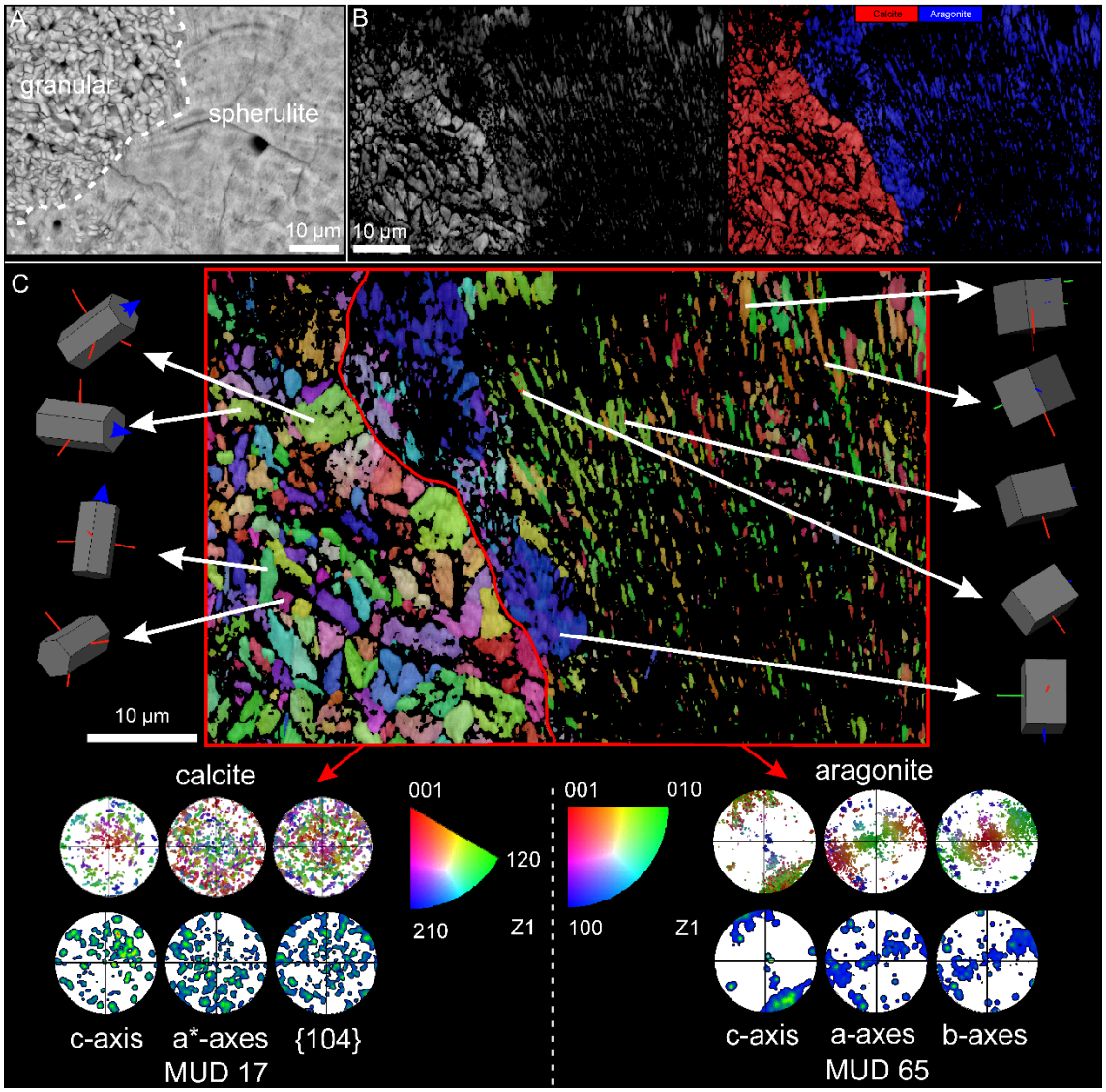

Figure 20. EBSD analysis of the spherulitic aragonite in *S. giganteus*. A. SEM image of the border between the granular-prismatic calcite and the fibrous aragonite, similar to the region analyzed in B to C. B. The BC map (left) shows a stronger EBSD diffraction signal for the calcite (lighter grey). The phase map (right) indicates the distribution of calcite and aragonite (see legend). C. The IPFz map shows a higher variety of colors for the calcite grains than for the aragonite fibers. Large grains of aragonite unrelated to the spherulite (blue/purple in color) appear at the boundary between the two microstructures. The PFs show a loose texture for the calcite, and a moderate axial texture for the aragonite, with the c-axis as the fiber axis, aligned in the elongation direction of the fibers (see unit cells). The co-orientation of the aragonite concurs with the relatively high MUD value (65), whereas the almost absence of orientation of the calcite grains is indicated by the low MUD value (17). The color triangle is the orientation color key.

4. Discussion

4.1. Microstructures and mineralogy

We have identified three different microstructures in seven species of serpulids: granular-prismatic calcite, lamello-fibrillar calcite, and fibrous aragonite. For each one, we have determined their morphological details, distribution within the tube, and mineralogy (Figs. 4, 5, and 6). The lamello-fibrillar calcite forms the bulk of the tube structure in all the samples studied, except in *S. crenata*. The granular-prismatic calcite and the fibrous aragonite are relegated to internal or external layers or appear in the form of ubiquitous (sometimes large) clusters within the tube cross-section. The calcite of the serpulids consistently occurs as medium to high Mg calcite (Smith et al. 2013), also confirmed by our analyses (more than 10% of $MgCO_3$, Fig. 5C, D).

Our observations allow us to conclude that only the lamello-fibrillar and external prismatic microstructures are primary (i.e. directly secreted by the animal), whereas the rest results from processes of substitution-recrystallization of these original microstructures. This is supported by the following observations:

4.1.1. Original microstructures

Lamello-fibrillar layers:

1. It constitutes well-defined and relatively continuous layers parallel to the growth surface (Figs. 4B, D, E and 12).
2. Homogeneous dimensions and co-orientation of the constituent fibers within single layers (parallel to the intervening membranes) (Figs. 4B and 12A-C).
3. Presence of organic membranes between microstructure layers, together with minor organics between fibers (Figs. 4B and 12A-D).

External prismatic layers:

4. They have consistent orientations perpendicular to the external surface (Figs. 4A and 7A, B, C, and D).
5. With growth, there is competition for space, such that some elements become thicker at the expense of others (Grigor'ev 1965; Rodríguez-Navarro and García-Ruiz 2000) (Figs. 4A and 7A, B, C, and D) and the aggregate becomes better co-oriented (e.g. increasing MUD values in Fig. 8D).
6. Growth lines are flat and continuous across the different crystals, indicating the existence of an epithelium lining the growth surface (Fig. 7D).

In the lamello-fibrillar and the external prismatic layers, these features are consistent across the different species.

4.1.2. Secondary (substitution) microstructures

Secondary granular-prismatic materials:

1. Prisms with rhombohedral endings enclosed within or forming part of the external primary prismatic layers. In these instances, the growth lines change from flat to angular. This indicates that the growth surfaces were not bounded by a secretory epithelium (Fig. 7C and D at the bottom).
2. Small intra- or extra prismatic grains associated with the same external layers, at any growth stage (Fig. 7B and C). If they were original, they should be interpreted as new crystallization nuclei. Nevertheless, in columnar prismatic materials growing by crystal selection and competition, there is no opportunity for new crystals to appear (Crippa et al. 2020a, b; Stevens et al. 2017).
3. Highly irregular internal layers or clusters of coarse prisms or grains that laterally continue into lamello-fibrillar layers (Fig. 7F, G, and I). Within these layers, the prismatic units have varied orientations and intersect, what seem to be remnants of organic membranes, similar and continuous into those separating the lamello-fibrillar layers. The membranes clearly did not

belong to the prismatic layers but to the previous lamello-fibrillar layers (Fig. 7J).

4. Associated with the previous instance (3.), prismatic grains may form spherulitic arrangements which nucleate on the relict organic membranes (Fig. 7G). In addition to the membranes predating the calcitic grains, this arrangement indicates centrifugal growth, while in primary materials, growth must always proceed toward the interior of the tube.
5. The secondary grains sometimes fuse, producing either isolated aggregates (Fig. 7K), or spherulitic and concretional structures (Fig. 7L) without defined growth directions, which is contrary to primary materials.
6. In some cases, scattered or clustered, much thinner fibers oriented according to the layers are still present within these materials (Fig. 7M). We interpret the former as remains of the original lamello-fibrillar microstructure being substituted by granular-prismatic materials.

Fibrous aragonite:

1. The shapes of the growth surfaces of spherulites do not conform to the shape of the overall growth surface of the tube (Fig. 18). In some instances, according to the convexity of the growth lines, growth is inferred to proceed toward the tube's exterior (spherulitic clusters in Figs. 18E, F, G). In any case, the growth fronts of the fibrous aragonite indicate that it is invading previous calcitic microstructures, either primary (Fig. 18C) or secondary (Fig. 18H). In high magnification, relict grains, either from the original or secondary calcitic microstructures, persist within the advancing aragonite spherulite (Fig. 19).
2. Organic membranes of the lamello-fibrillar microstructure continue as ghosts into the spherulites (spherulitic clusters in Figs. 4G, 18C, 19C), which is indicative of substitution of the lamello-fibrillar microstructure by aragonite.

All the above features clearly indicate that the fibrous aragonite comes from the substitution of the previous calcitic microstructures.

In all species analyzed, and independently of the microstructures previously described in the literature, only the lamello-fibrillar microstructure and the non-secondary granular-prismatic microstructures described above are original, while the rest are substitution microstructures. Since the studied specimens were collected alive, these substitution processes happened *in vivo*.

A summary of the different instances in which substitution microstructures can be found in Fig. 21.

According to our observations, the primary microstructures may be substituted by either secondary calcite (Fig. 7F, G) or, directly, by aragonite (Fig. 18C). Transformation of the secondary calcite into aragonite has also been observed (Fig. 18H). We suggest that the replacement is likely induced by the high solubility of the primary high-Mg calcite and must occur via dissolution-

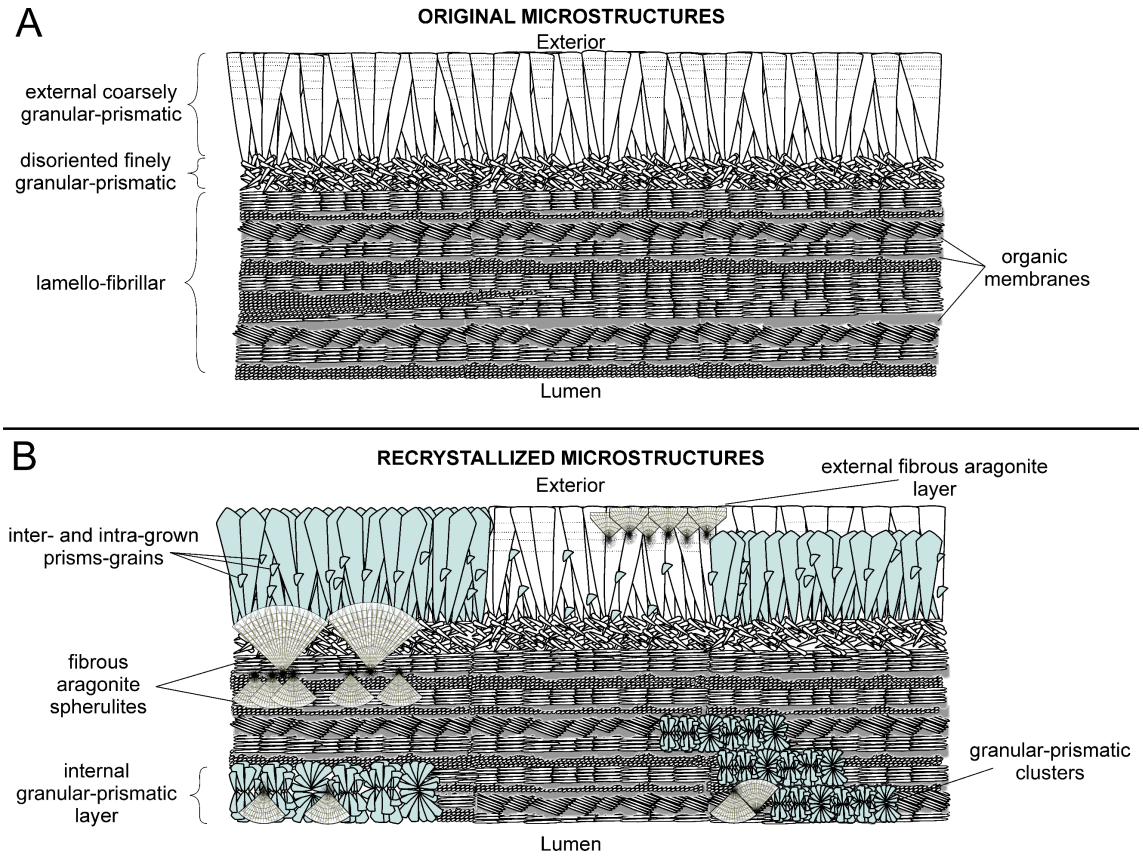

recrystallization processes (Morse and Mackenzie 1990). This process will favor the crystallization of less soluble calcites (i.e., with slightly

lower Mg contents), with the consequent accumulation of Mg^{2+} at the transformation interface. At some point, Mg^{2+} concentration may inhibit the formation of calcite and promote the precipitation of aragonite, which does not incorporate Mg^{2+} (see EDX maps in Fig. 19) (Burton and Walter 1987; Morse et al. 1997). This theoretical sequence can vary depending on local conditions, and aragonite could be produced directly, without the need for a secondary Mg calcite precursor. These substitution processes will be investigated in detail in the future.

4.2. Growth patterns of the external prismatic and lamello-fibrillar layers

Considering that in serpulids, secreting glands, of both calcium carbonate and organic matter, are principally located in the folds of the peristomial collar, just beneath the radiolar crown (Hedley 1956), the deposition of new material occurs when the serpulid is in feeding mode (with the radiolar crown protruding outwards). At this point, the collar folds would adapt to the edge of the tube, facilitating the addition of new material. The secretion of a new layer would stop each time the serpulid retracts inside the tube.

The distribution of growth lines of the primary external prismatic layers indicates that growth proceeds with the addition of closely spaced (submicron thick) growth increments (Fig. 7D). The flat, parallel, and continuous growth lines across the prisms mark the positions where the soft body adhered to the tube's growth surface to continue calcification. This pattern is similar to that found in other calcifying invertebrates, such as e.g. molluscs, brachiopods, and corals.

☚ **Figure 21** Schematic representation of a serpulid tube cross-section, with indication of the original microstructures, before (A) and after (B) substitution by secondary microstructures.

On the contrary, in the lamello-fibrillar microstructure, we have not found any evidence of growth lines within the layers, despite the different preparation protocols applied. The only evidence of periodicity is constituted by the organic membranes delineating the lamello-fibrillar layers. Accordingly, we assume that these membranes correspond to the different growth episodes and delineate the contour of the mineralizing epithelium (the collar fold). This distribution pattern is suggestive of a rather episodic growth, with increments between a few microns to several tens of microns (Fig. 12D-G).

To reconcile the relatively continuous growth of the external prismatic layer with the seemingly episodic growth of the lamello fibrillar layers, we envisage two possibilities: (1) Mineralization of the lamello-fibrillar layer takes place continuously, with the addition of sublayers one to several fibers thick; when the layer is complete, secretion of the organic membrane takes place (Fig. 22A). (2) The animal isolates a space with a new membrane at a distance of the previous membrane, enriched in the mineralization precursors of the calcitic fibers; mineralization of a fresh lamello-fibrillar layer takes place at once within this space (Fig. 22B). Whatever the exact process, this growth mode leads to the production of the characteristic pattern of unequal, sometimes slightly offset, growth wedges of lamello-fibrillar material (Fig. 12).

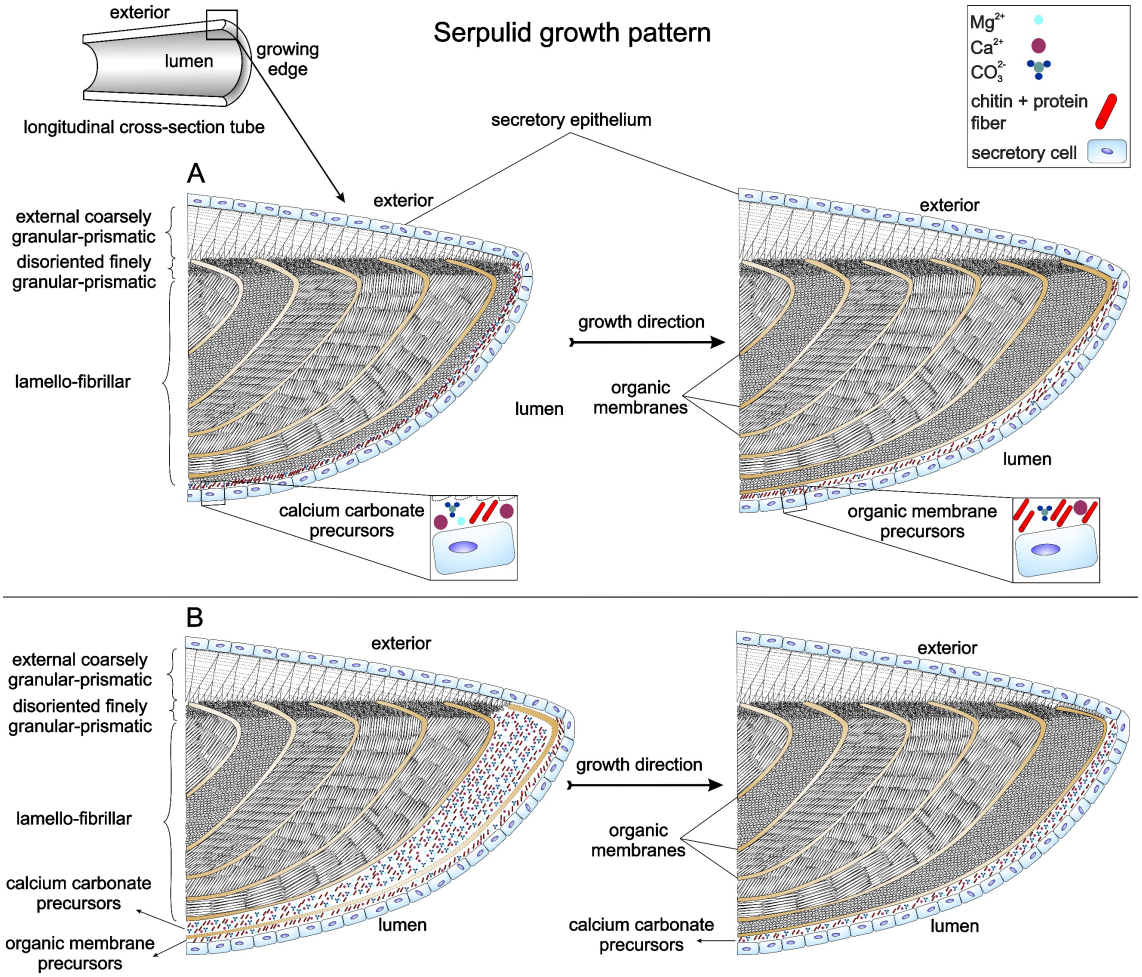

Figure 22. Two possible growth modes for the outer granular-prismatic and lamello-fibrillar microstructures. A. Both the granular-prismatic and the lamello-fibrillar microstructures grow continuously toward the tube exterior and interior, respectively. When the lamello-fibrillar layer is complete, it is covered by an organic membrane. B. While the granular-prismatic layer grows continuously toward the external surface, the space corresponding to the future lamello-fibrillar layer is filled with the precursor components and sealed by a membrane. Subsequently, mineralization of the enclosed space takes place at once. In both cases (A and B), the chitin+protein fibers organize as a cholesteric liquid crystal phase and calcite nucleate orientally.

Other biocalcifiers, such as molluscs, bryozoans or brachiopods, can control the chemistry of the precipitation medium and the production of particular mineral phases (low-Mg calcite, aragonite). This is likely due to the fact that this occurs in a very thin space (much less that one micron thick) between the mantle cells and the shell growth surface, called the extrapallial space (Nielsen and Pedersen 1979, Checa et al. 2014, Simonet Roda et al. 2019). This is isolated from the environment by an organic membrane, the periostracum in molluscs and brachiopods, and the cuticle in bryozoans. Serpulids, conversely,

lack such an isolating membrane, and the growing edge of the tube is exposed to the environment, particularly when the animal is retracted inside its tube. This could explain the high-Mg calcite mineralogy of the serpulid microstructures, whose original microstructures are particularly prone to substitution processes, as explained above.

4.3. Assimilation of the plywood structure of the lamello-fibrillar calcite to a chiral nematic liquid crystal phase

The characteristic plywood arrangement of the lamello-fibrillar material, made of co-oriented fibers that twist their orientation across successive layers, is known in the literature as a "chevron pattern" (Weedon 1994). It was initially explained as being induced by swirling movements of the collar folds, which mold the material (still in a slurry state) through forward and backward applications before hardening (also Weedon 1994). However, this hypothesis fails to explain three critical issues: (1) how traction forces induce fiber orientations, (2) why the fibers achieve co-orientation across the whole thickness of a single layer, made of many superposed, co-oriented fibers (Fig. 12), and, as we reveal here, (2) how the crystallographic c-axis becomes co-oriented with the long axis of the fibers (see EBSD results in Figs. 13, 14, 16 and 17). Out of Hedley's hypothesis, no specific mechanism has been proposed to explain the plywood-like arrangement of the lamello-fibrillar calcite.

The changing orientation of fibers across the different layers is reminiscent of the plywood structures of many organic fibrous biocomposites in plants and animals (Neville 1993). Many such cases have been interpreted as resulting from a process of liquid crystallization, in particular, from the formation of the so-called cholesteric or chiral-nematic phase. In this phase configuration, polar nanofibers or molecules arrange in planes, and the fibers in each plane are

parallel to each other and slightly rotated with respect to those of the contiguous plane. After a certain distance (called pitch), the orientation of the fibers b

ecomes the same. In other instances, the change in orientation is abrupt, resulting in superposed lamellae of fibers with marked differences in orientation.

The most archetypal example of biological plywood materials attributed to cholesteric liquid crystallization is the arthropod exoskeleton, consisting of α-chitin+protein fibers (Bouligand 1972; Neville 1993). In molluscs (β-chitin+protein), similar patterns have been recognized in the periostracum of some gastropods (Hunt and Oates 1984), the squid pen (Levi-Kalisman et al. 2001), the chambers and septa of *Sepia* (Checa et al. 2015), and the septa of *Spirula* (Checa et al. 2022; Griesshaber et al. 2023). In all these instances, growth proceeds with the addition of successive layers. This is the opposite of in vitro-formed liquid crystals, in which all layers develop at once from a suspension.

Out of the above examples, the plywood structures of *Sepia* and *Spirula* are calcified with aragonite but there is no correspondence between the crystallographic c-axes of aragonite (perpendicular to the layers; Griesshaber et al. 2023) and the organic fibers of chitin protein (parallel to the layers). If we assimilate the formation of the lamello-fibrillar microstructure of serpulids to a liquid crystallization process, the calcite should nucleate onto previous organic fibrils, with its c-axis parallel to the long axis of the fibers (see EBSD data, Figs. 13, 14, and 16). This would constitute a unique case of oriented nucleation. The putative fibers would be made of chitin (in its β-polymorph; Chamoy et al. 2001; Choi et al. 2022; Hausen 2005; Hunt and Oates 1984; Merz 2015) and proteins, two components we have identified within the tubes with FTIR (Fig. 17) (Tsurkan et al. 2021). We do not know if intra-layer growth proceeds sequentially (i.e. layer by layer, as in the previous biological examples) or all at once (see previous section). Unfortunately, we have not yet identified the organic precursor scaffold of the lamello-fibrillar material. Further research will be done in this area.

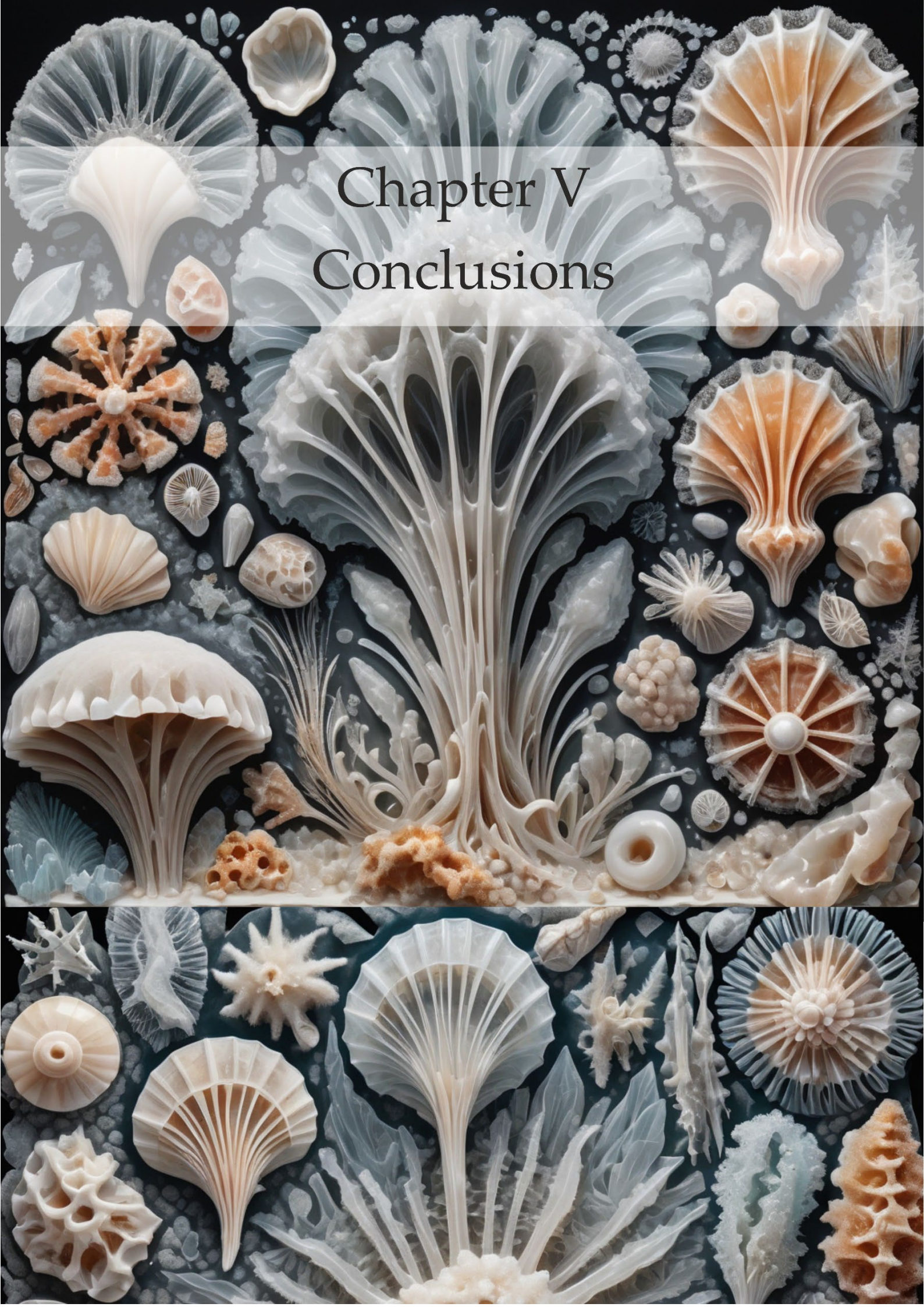

Chapter V
Conclusions

5. Conclusions

5.1. Stenolaemata bryozoans

1. Micro-CT results demonstrate that *C. elegans* builds erect cylindrical colonies where the zooid chambers are arranged concentrically, whereas *H. robusta* constructs erect branched colonies with long tubular zooids, which are oriented towards the front. We confirm the existence of a complex system of communicative channels, the funicular system, between the zooids in both species.
2. Foliated calcite is the microstructure that makes up the bulk of the colony skeleton of both *F. ramosa* and *C. elegans*. Tabular calcite is the principal microstructure of the colony skeleton of *H. robusta.*
3. Both microstructures share a high ability to adapt to the irregularities of the surface produced by the different structures, such as inner walls, communicative pores, external pustules, and internal spines. Bends, bifurcations, and changes in the morphology of the laths of foliated calcite occur without changes in the orientation of the crystallographic axes.
4. The calcite crystals forming both microstructures present a surface nanoroughness. In the case of foliated calcite, the nanoprotrusions are preferentially oriented along the crystallographic directions with the strongest bonds (PBCs).
5. The crystallography of the foliated calcite of *F. ramosa* and *C. elegans* exhibits a characteristic sheet texture, which is weaker in *C. elegans*. The c-axis is along the growth axis of the laths, whereas their main surfaces are roughly of the {100} type.
6. The crystallography of the tabular calcite from *H. robusta* exhibits an axial texture, with the c-axis as fiber axis, and perpendicular to the surface of the tablets.

5.2. Gymnolaemata bryozoans

1. We have identified five basic microstructures in cheilostome bryozoans: Tabular, irregularly platy, and granular calcite, as well as fibrous and granular-platy aragonite.
2. The three calcitic microstructures form recurrent associations. The SEM and EBSD results indicate that both tabular and irregularly platy calcite are structurally continuous into granular calcite. The differences can be attributed to a significant reduction of the observed organic matrix.
3. Both SEM and EBSD data allowed us to reconstruct the growth directions of the microstructures, filling in the interior walls and frontal shields (or cryptocyst). Depending on the species, either tabular or irregularly platy calcite is secreted first and later transformed into granular calcite. In bimineralic cheilostomes, fibrous aragonite is always the last microstructure to be secreted.
4. The granular-platy microstructure was only found in *A. pallasii*, around the pores of the frontal shield.
5. The increase in the MUD values (derived from the contoured pole figures) for both the calcitic and aragonitic microstructures suggests competitive growth, which is described for the first time in cheilostome bryozoans.
6. Apart from tabular calcite, the rest of the microstructures show evidence that the epithelium is not in direct contact with the surfaces of the growing crystals. This demonstrates a case of remote growth, which seems widespread in cheilostome bryozoans but is very uncommon among invertebrates.

5.3. Serpulid Polychaeta

1. We have identified three different microstructures: granular-prismatic calcite, lamello-fibrillar calcite, and fibrous aragonite. For each one, we have characterized their distribution, mineralogy, and crystallography.
2. The granular-prismatic microstructure may be present either as (1) an outer layer of long prisms perpendicular to the external surface, or as (2) ubiquitous clusters or discontinuous layers in different parts of the tube cross-section.
3. The lamello-fibrillar microstructure has a plywood structure of thin fibers arranged in successive layers separated by membranes. It is found in the central and internal parts of the tube.
4. The fibrous aragonite usually forms spherulites and appears as discontinuous layers or clusters at any location in the tube.
5. Serpulid tubes incorporate a high amount of organic matter, consisting primarily of chitin plus protein. Calcite is always medium to high Mg calcite (>10%).
6. From the crystallographic viewpoint, the calcitic external prismatic and lamello-fibrillar layers, and the fibrous aragonite present an axial texture, with either the calcite or the aragonite c-axis as the fiber axis. The lamello-fibrillar calcite displays the strongest texture. The long prisms of the external prismatic calcite become better co-oriented with growth, a characteristic indicative of competition for space.
7. Only the external prismatic and the lamello-fibrillar microstructures are secreted by the animal. All the other instances of granular-prismatic and fibrous aragonite microstructures result from the *in vivo* substitution of original microstructures. The fibrous aragonite can also substitute the secondary calcite. Substitution is likely triggered by the high Mg^{2+} content of the original calcites.

8. The external granular-prismatic layer exhibits continuous growth, while the lamello-fibrillar layers grow either: (1) by continuous addition of sublayers one to several fibers thick, until, upon completion of the layer, an organic membrane is secreted; or (2) by isolating a space sealed by a new membrane, where mineralization occurs at once.
9. We hypothesize that the plywood configuration of the lamello-fibrillar calcite occurs by the ordering of a precursor made of organic fibrils into a cholesteric liquid crystal phase. Subsequently, calcite would grow by oriented nucleation onto the organic fibrils. We have not identified the organic precursor.

5. Conclusiones

5.1. Bryozoos stenolemados

1. Los resultados de micro-TC demuestran que *C. elegans* construye colonias cilíndricas erectas en las que las cámaras de los zooides están dispuestas concéntricamente, mientras que *H. robusta* construye colonias ramificadas erectas con largos zooides tubulares, que están orientados hacia delante. Confirmamos la existencia de un complejo sistema de canales comunicativos, el sistema funicular, entre los zooides de ambas especies.
2. La calcita foliada es la microestructura que constituye la mayor parte del esqueleto de las colonias tanto de *F. ramosa* como de C. elegans. La calcita tabular es la principal microestructura del esqueleto de la colonia de *H. robusta*.
3. Ambas microestructuras comparten una gran capacidad de adaptación a las irregularidades de la superficie producidas por las diferentes estructuras, como paredes internas, poros comunicantes, pústulas externas y espinas internas. Las curvaturas, bifurcaciones y cambios en la morfología de las láminas de calcita foliada se producen sin cambios en la orientación de los ejes cristalográficos.
4. Los cristales de calcita que forman ambas microestructuras presentan una nanorrugosidad superficial. En el caso de la calcita foliada, las nanoprotrusiones se orientan preferentemente a lo largo de las direcciones cristalográficas con los enlaces más fuertes (PBCs).
5. La cristalografía de la calcita foliada de *F. ramosa* y *C. elegans* exhibe una "textura de lámina" característica, que es más débil en *C. elegans*. El eje c está a lo largo del eje de crecimiento de las láminas, mientras que sus superficies principales son aproximadamente del tipo {100}.

6. La cristalografía de la calcita tabular de *H. robusta* exhibe una "textura axial", con el eje c como eje de fibra, perpendicular a la superficie de las tabletas.

5.2. Briozoos gimnolemados

1. Hemos identificado cinco microestructuras básicas en los briozoos queilostomados: calcita tabular, irregularmente laminar y granular, así como aragonito fibroso y granular-laminar.
2. Las tres microestructuras calcíticas forman asociaciones recurrentes. Los resultados SEM y EBSD indican que tanto la calcita tabular como la irregularmente laminar se continúan estructuralmente en la calcita granular. Las diferencias pueden atribuirse a una reducción significativa de la matriz orgánica observada.
3. Tanto los datos de SEM como los de EBSD nos permitieron reconstruir las direcciones de crecimiento de las microestructuras, rellenando las paredes interiores y los "escudos frontales" (o criptocisto). Dependiendo de la especie, primero se segrega calcita tabular o irregularmente laminar, que posteriormente se transforma en calcita granular. En los queilostomados biminerales, el aragonito fibroso es siempre la última microestructura en ser secretada.
4. La microestructura granular-laminar sólo se encontró en *A. pallasii*, alrededor de los poros del escudo frontal.
5. El aumento de los valores de MUD (derivados de las figuras de polos), tanto para las microestructuras calcíticas como aragoníticas, sugiere un crecimiento competitivo que se describe por primera vez en briozoos queilostomados.
6. Aparte de la calcita tabular, el resto de las microestructuras muestran evidencias de que el epitelio no está en contacto directo con las superficies

de los cristales en crecimiento. Esto demuestra un caso de crecimiento remoto, que parece muy extendido en los briozoos queilostomados pero es muy poco común entre los invertebrados.

5.3. Serpúlidos poliquetos

1. Hemos identificado tres microestructuras diferentes: calcita granular-prismática, calcita lamelo-fibrilar y aragonito fibroso. Para cada una de ellas, hemos caracterizado su distribución, mineralogía y cristalografía.
2. La microestructura granular-prismática puede estar presente como (1) una capa externa de prismas largos perpendicular a la superficie externa, o como (2) agrupaciones ubicuas o capas discontinuas en diferentes partes de la sección transversal del tubo.
3. La microestructura lamelo-fibrilar tiene una estructura contrachapada de fibras finas dispuestas en capas sucesivas separadas por membranas. Se encuentra en las partes central e interna del tubo.
4. El aragonito fibroso suele formar esferulitas y aparece como capas discontinuas o agrupaciones en cualquier lugar del tubo.
5. Los serpúlidos incorporan una gran cantidad de materia orgánica en la estructura del tubo, compuesta principalmente por quitina y proteínas. La calcita contiene siempre un contenido en Mg medio/alto (>10%).
6. Desde el punto de vista cristalográfico, las capas externas prismáticas y lamelo-fibrilar de calcita y el aragonito fibroso presentan una textura axial, con el eje c tanto de la calcita como del aragonito como eje de fibra. La calcita lamello-fibrilar presenta la textura más fuerte. Los prismas largos de la calcita prismática externa se co-orientan mejor con el crecimiento, una característica indicativa de competencia por el espacio.
7. Sólo las microestructuras prismáticas externa y lamelo-fibrilar son secretadas por el animal. Todos los demás casos de microestructuras

granulares-prismáticas y fibrosas de aragonito resultan de la sustitución in vivo de las microestructuras originales. El aragonito fibroso también puede sustituir a la calcita granular-prismática secundaria. La sustitución es probablemente provocada por el alto contenido en Mg^{2+} de las calcitas originales.

8. La capa de calcita granular-prismática externa presenta un crecimiento continuo, mientras que las capas de calcita lamelo-fibrilar crecen: (1) por adición continua de subcapas de una a varias fibras de grosor, hasta que, al completarse la capa, se segrega una membrana orgánica; o (2) aislando un espacio sellado por una nueva membrana, donde la mineralización se produce de inmediato.
9. Nuestra hipótesis es que la configuración contrachapada de la calcita lamelo-fibrilar se produce por el ordenamiento de un precursor formado por fibrillas orgánicas en una fase de cristal líquido colestérico. Posteriormente, la calcita crecería por nucleación orientada sobre las fibrillas orgánicas. No hemos identificado el precursor orgánico.

References

Addadi L, Weiner S (1992) Control and design principles in biological mineralization. Angew Chem Int Ed Engl 31:153-69. https://doi.org/10.1002/anie.199201531

Almagro I, Cartwright JHE, Checa AG, Macías-Sánchez E, Sainz-Díaz CI (2021) Evidence for a liquid-crystal precursor involved in the formation of the crossed-lamellar microstructure of the mollusc shell. Acta Biomater 120:12-19. https://doi.org/10.1016/j.actbio.2020.06.018

Aquilano D, Bruno M, Massaro FR, Rubbo M (2011) Theoretical equilibrium shape of calcite. 2.[441] zone and its role in biomineralization. Cryst Growth Des 11:3985-3993. https://doi.org/10.1021/cg2005584

Bader B, Schäfer P (2004) Skeletal morphogenesis and growth check lines in the Antarctic bryozoan *Melicerita obliqua*. J Nat Hist 38:2901-2922. https://doi.org/10.1080/00222930310001657685

Badou A, Pont S, Auzoux-Bordenave S, Lebreton M, Bardeau J-F (2022) New insight on spatial localization and microstructures of calcite-aragonite interfaces in adult shell of *Haliotis tuberculata*: Investigations of wild and farmed abalones by FTIR and Raman mapping. J Struct Biol 214:107854. http://doi.org/10.1016/j.jsb.2022.107854

Batson PB, Tamberg Y, Gordon DP, Negrini M, Smith AM (2021) *Hornera currieae* n. sp. (Cyclostomatida: Horneridae): a new bathyal cyclostome bryozoan with reproductively induced skeletal plasticity. Zootaxa 5020:257-287. https://doi.org/10.11646/zootaxa.5020.2.2

Batson PB, Tamberg Y, Taylor PD (2022) Composite branch construction by dual autozooidal budding modes in hornerids (Bryozoa: Cyclostomatida). J Morphol 283:783-804. https://doi.org/10.1002/jmor.21469

Benedix G, Jacob DE, Taylor PD (2014) Bimineralic bryozoan skeletons: a comparison of three modern genera. Facies 60:389-403. https://doi.org/10.1007/s10347-013-0380-2

Boardman RS, Cheetham AH (1969) Skeletal growth, intracolony variation, and evolution in Bryozoa: a review. J Paleontol 205-233.

Boardman RS, McKinney FK, Taylor PD (1992) Morphology, anatomy, and systematics of the Cinctiporidae, new family (Bryozoa: Stenolaemata). Smithsonian Contr Paleobiol 70:1-81. https://doi.org/10.5479/si.00810266.70.1

Bobin G (1977) Interzooecial communications and the funicular system. In: Woolacott RM, Zimmer RL (ed) Biology of bryozoans. Academic Press, New York City, pp 307-333.

Bøggild OB (1930) The shell structure of the mollusks. Kongel Danske Vidensk Selsk Skr Naturvidensk Math Afd 9 2:231-326.

Bone EK, Keough MJ (2010) Does polymorphism predict physiological connectedness? A test using two encrusting bryozoans. Biol Bull 219:220-30. https://doi.org/10.1086/BBLv219n3p220

Bouligand Y (1972) Twisted fibrous arrangements in biological materials and cholesteric mesophases. Tissue Cell 4:189–217. http://doi.org/10.1016/S0040-8166(72)80042-9

Brand U, Gao Y (2003) Chemostratigraphy and correlation of the late Pennsylvanian Madera Formation, Cañon de San Diego, New Mexico, USA. Carbonates Evaporites. 18:151-70. https://doi.org/10.1007/BF03176235

Brood K (1976) Wall structure and evolution in cyclostomate Bryozoa. Lethaia 9:377-389. https://doi.org/10.1111/j.1502-3931.1976.tb00977.x

Bruet BJF, Qi HJ, Boyce MC, Panas R, Tai K, Frick L, Ortiz C (2055) Nanoscale morphology and indentation of individual nacre tablets from the gastropod mollusc *Trochus niloticus*. J Mater Res 20:2400-2419. https://doi.org/10.1557/jmr.2005.0273

Buckman JO (2015) An overview of the tube fabric of *Pomatoceros* (Polychaeta, Serpulidae), illustrated by examples from the British Isles. Zool Anz 259:54–60. http://doi.org/10.1016/j.jcz.2014.11.005

Burton EA, Walter LM (1987) Relative precipitation rates of aragonite and Mg calcite from seawater: Temperature or carbonate ion control? Geology 15:111–114. http://doi.org/10.1130/0091-7613(1987)15<111:RPROAA>2.0.CO;2

Carle KJ, Ruppert EE (1983) Comparative ultrastructure of the bryozoan funiculus: a blood vessel homologue. J Zool Syst Evol Res 21:181-93. https://doi.org/10.1111/j.1439-0469.1983.tb00286.x

Carter JG, Clark GR (1985) Classification and phylogenetic significance of molluscan shell microstructure. Ser Geol Notes Short Course 13:50-71. https://doi.org/10.1017/S0271164800001093

Cartwright JHE, Checa AG, Escribano B, Sainz-Díaz CI (2009) Spiral and target patterns in bivalve nacre manifest a natural excitable medium from layer growth of a biological liquid crystal. PNAS 106:10499-10504. http://doi.org/10.1073/pnas.0900867106

Chamoy L, Nicolaï M, Ravaux J, Quennedey B, Gaill F, Delachambre J (2001) A novel chitin-binding protein from the vestimentiferan *Riftia pachyptila* interacts specifically with β-Chitin: Cloning, expression, and characterization. J Biol Chem 276:8051–8058. http://doi.org/10.1074/jbc.M009244200

Chan VBS, Li C, Lane AC, Wang Y, Lu X, Shih K, Zhang T, Thiyagarajan V (2012) CO_2-driven ocean acidification alters and weakens integrity of the calcareous tubes produced by the serpulid tubeworm, *Hydroides elegans*. PLoS ONE 7:e42718. http://doi.org/10.1371/journal.pone.0042718

Charles M, Faillettaz R, Desroy N, Fournier J, Costil K (2018) Distribution, associated species and extent of biofouling "reefs" formed by the alien species *Ficopomatus enigmaticus* (Annelida, Polychaeta) in marinas. Estuar Coast Shelf Sci 212:164–175. http://doi.org/10.1016/j.ecss.2018.07.007

Checa A, Salas C (2017) Treatise Online no. 93: Part N, Revised, Volume 1, Chapter 3: Periostracum and shell formation in the Bivalvia. Treat Online 1:1-51. http://doi.org/10.17161/to.v0i0.6650

Checa AG (2000) Remote biomineralization in divaricate ribs of *Strigilla* and *Solecurtus* (Tellinoidea: Bivalvia). J Molluscan Stud 66:457-466. https://doi.org/10.1093/mollus/66.4.457

Checa AG (2018) Physical and biological determinants of the fabrication of molluscan shell microstructures. Front Mar Sci 5:353. https://doi.org/10.3389/fmars.2018.00353

Checa AG, Cartwright JHE, Sánchez-Almazo I, Andrade JP, Ruiz-Raya F (2015) The cuttlefish Sepia officinalis (Sepiidae, Cephalopoda) constructs cuttlebone from a liquid-crystal precursor. Sci Rep 5:11513. https://doi.org/10.1038/srep11513

Checa AG, Esteban-Delgado FJ, Rodríguez-Navarro AB (2007) Crystallographic structure of the foliated calcite of bivalves. J Struct Biol 157:393-402. https://doi.org/10.1016/j.jsb.2006.09.005

Checa AG, Gaspard D, González-Segura A, Ramírez-Rico J (2009) Crystallography of the calcitic foliated-like and seminacre microstructures

of the brachiopod *Novocrania*. Cryst Growth Des 9:2464-2469. https://doi.org/10.1021/cg801372j

Checa AG, Grenier C, Griesshaber E, Schmahl WW, Cartwright JHE, Salas C, Oudot M (2022) The shell structure and chamber production cycle of the cephalopod *Spirula* (Coleoidea, Decabrachia). Mar Biol 169:132. http://doi.org/10.1007/s00227-022-04120-0

Checa AG, Linares F, Grenier C, Griesshaber E, Rodríguez-Navarro AB, Schmahl WW (2021) The argonaut constructs its shell via physical self-organization and coordinated cell sensorial activity. iScience 24:103288. https://doi.org/10.1016/j.isci.2021.103288

Checa AG, Linares F, Grenier C, Griesshaber E, Rodríguez-Navarro AB, Schmahl WW (2021) The argonaut constructs its shell via physical self-organization and coordinated cell sensorial activity. iScience 24:103288. https://doi.org/10.1016/j.isci.2021.103288

Checa AG, Macías-Sánchez E, Rodríguez-Navarro AB, Sánchez-Navas A, Lagos NA (2020) Origin of the biphase nature and surface roughness of biogenic calcite secreted by the giant barnacle *Austromegabalanus psittacus*. Sci Rep 10:1-14. https://doi.org/10.1038/s41598-020-73804-8

Checa AG, Salas C, Harper EM, Bueno-Pérez J de D (2014) Early stage biomineralization in the periostracum of the 'living fossil' bivalve *Neotrigonia*. PLoS One 9:e90033. https://doi.org/10.1371/journal.pone.0090033

Checa AG, Salas C, Varela-Feria FM, Rodríguez-Navarro AB, Grenier C, Kamenev GM, Harper EM (2022) Crystallographic control of the fabrication of an extremely sophisticated shell surface microornament in the glass scallop *Catillopecten*. Sci Rep 12:1-15. https://doi.org/10.1038/s41598-022-15796-1

Checa AG, Yáñez-Ávila ME, González-Segura A, Varela-Feria F, Griesshaber E, Schmahl WW (2019) Bending and branching of calcite laths in the foliated microstructure of pectinoidean bivalves occurs at coherent crystal lattice orientation. J Struct Biol 205:7-17. https://doi.org/10.1016/j.jsb.2018.12.003

Cheetham AH, Rucker JB, Carver RE (1969) Wall structure and mineralogy of the cheilostome bryozoan *Metrarabdotos*. J Paleontol 43:129-135.

Chinzei K, Seilacher A (1993) Remote biomineralization I: fill skeletons in vesicular oyster shells. N Jb Geol Paläontol Abh 190:185-197.

Choi H, Kim SL, Jeong M-K, Yu OH, Eyun S (2022) Identification and phylogenetic analysis of chitin synthase genes from the deep-sea polychaete *Branchipolynoe onnuriensis* genome. J Mar Sci Eng 10:598. http://doi.org/10.3390/jmse10050598

Coronado I, Fine M, Bosellini FR, Stolarski J (2019) Impact of ocean acidification on crystallographic vital effect of the coral skeleton. Nat Commun 10:2896. https://doi.org/10.1038/s41467-019-10833-6

Crippa G, Griesshaber E, Checa AG, Harper EM, Roda MS, Schmahl WW (2020a) Orientation patterns of aragonitic crossed-lamellar, fibrous prismatic and myostracal microstructures of modern *Glycymeris* shells. J Struct Biol 212:107653. https://doi.org/10.1016/j.jsb.2020.107653

Crippa G, Griesshaber E, Checa AG, Harper EM, Simonet Roda M, Schmahl WW (2020b) SEM, EBSD, laser confocal microscopy and FE-SEM data from modern *Glycymeris* shell layers. Data Brief 33:106547. http://doi.org/10.1016/j.dib.2020.106547

Currey JD (1976) Further studies on the mechanical properties of mollusc shell material. J Zool 180:445-453. https://doi.org/10.1111/j.1469-7998.1976.tb04690.x

Currey JD (1977) Mechanical properties of mother of pearl in tension. Proc R Soc Lond B 196:443-463. https://doi.org/10.1098/rspb.1977.0050

Currey JD, Taylor JD (1974) The mechanical behaviour of some molluscan hard tissues. J Zool 173:395-406. https://doi.org/10.1111/j.1469-7998.1974.tb04122.x

Dauphin Y (2001) Nanostructures de la nacre des tests de céphalopodes actuels. Paläontol Z 75:113-122. http://dx.doi.org/10.1007%2FBF03022601

Dauphin Y (2006) Structure and composition of the septal nacreous layer of *Nautilus macromphalus* L. (Mollusca, Cephalopoda). Zoology 109:85-95. https://doi.org/10.1016/j.zool.2005.08.005

Dauphin Y (2008) The nanostructural unity of mollusc shells. Mineral Mag 72:243-246. https://doi.org/10.1180/minmag.2008.072.1.243

Davis KJ, Dove PM, De Yoreo JJ (2000) Resolving the control of magnesium on calcite growth: thermodynamic and kinetic consequences of impurity incorporation for biomineral formation. MRS Online Proc Libr (OPL) 620:M9.5.1. https://doi.org/10.1557/PROC-620-M9.5.1

De Yoreo JJ, Gilbert PU, Sommerdijk NA, Penn RL, Whitelam S, Joester D, Zhang H, Rimer JD, Navrotsky A, Banfield JF, Wallace AF, Michel FM, Meldrum F. C, Cölfen H, Dove PM (2015) Crystallization by particle attachment in synthetic, biogenic, and geologic environments. Science 349:aaa6760. https://doi.org/10.1126/science.aaa6760

Dick MH, Lidgard S, Gordon DP, Mawatari SF (2009) The origin of ascophoran bryozoans was historically contingent but likely. Proc R Soc B 276:3141-3148. https://doi.org/10.1098/rspb.2009.0704

Dos Santos HN, Neumann R, Ávila CA (2017) Mineral quantification with simultaneous refinement of Ca-Mg Carbonates non-stoichiometry by X-ray

diffraction, Rietveld method. Minerals 7:164. http://doi.org/10.3390/min7090164

Fischer R, Pernet B, Reitner J (2000) Organomineralization of cirratulid annelid tubes-fossil and recent examples. Facies 42:35–49. http://doi.org/10.1007/BF02562565

Gabitov RI, Sadekov A, Leinweber A (2014) Crystal growth rate effect on Mg/Ca and Sr/Ca partitioning between calcite and fluid: An in situ approach. Chem Geol 367:70-82. https://doi.org/10.1016/j.chemgeo.2013.12.019

Gal A, Kahil K, Vidavsky N, DeVol RT, Gilbert PU, Fratzl P, Weiner S, Addadi L (2014) Particle accretion mechanism underlies biological crystal growth from an amorphous precursor phase. Adv Funct Mater 24:5420-5426. https://doi.org/10.1039/C4CE01474J

Grant HE, Ostrovsky AN, Jenkins HL, Vieira LM, Gordon DP, Foster PG, Kotenko ON, Smith AM, Berning B, Porter JS, Souto J, Florence WK, Tilbrook KJ, Waeschenbach A (2023) Multiple evolutionary transitions of reproductive strategies in a phylum of aquatic colonial invertebrates. Proc R Soc B 290:20231458. https://doi.org/10.1098/rspb.2023.1458

Grenier C, Griesshaber E, Schmahl WW, Checa AG (2023) Microstructure and crystallographic characteristics of stenolaemate bryozoans (Phylum Bryozoa and Class Stenolaemata). Cryst Growth Des 23:965–979. https://doi.org/10.1021/acs.cgd.2c01149

Griesshaber E, Checa AG, Salas C, Hoffmann R, Yin X, Neuser R, Rupp U, Schmahl WW (2023) Biological light-weight materials: The endoskeletons of cephalopod mollusks. J Struct Biol 215:107988. http://doi.org/10.1016/j.jsb.2023.107988

Grigor'ev DP (1965) Ontogeny of Minerals. Israel Program for Scientific Translations, Jerusalem.

Hageman SJ, Lukasik J, McGowran B, Bone Y (2003) Paleoenvironmental significance of *Celleporaria* (Bryozoa) from modern and Tertiary cool-water carbonates of southern Australia. Palaios 18:510-527. https://doi.org/10.1669/0883-1351(2003)018%3C0510:PSOCBF%3E2.0.CO;2

Hardie LA, Stanley SM (1997) Secular biotic trends in skeletal secretion and sedimentary carbonate production resulting from oscillations in seawater chemistry driven by plate tectonics. Eos Trans Am Geophys Union 17:S179.

Harper DA (2006) The Ordovician biodiversification: Setting an agenda for marine life. Palaeogeogr Palaeoclimatol Palaeoecol 232:148-166. https://doi.org/10.1016/j.palaeo.2005.07.010

Hausen H (2005) Comparative structure of the epidermis in polychaetes (Annelida). Hydrobiologia 535:25–35. http://doi.org/10.1007/s10750-004-4442-x

Hedley RH (1956) Studies of serpulid tube formation: I. The secretion of the calcareous and organic components of the tube by *Pomatoceros triqueter*. J Cell Sci 3:411–419

Hedley RH (1958) Tube formation by *Pomatoceros triqueter* (Polychaeta). J Mar Biol Ass 37:315–322. http://doi.org/10.1017/S0025315400023717

Hincke MT, Nys Y, Gautron J, Mann K, Rodríguez-Navarro AB, McKee MD (2012) The eggshell: structure, composition and mineralization. Front Biosci 17:1266-1280.

Hudson JH, Shinn EA, Halley RB, Lidz B (1976) Sclerochronology: a tool for interpreting past environments. Geology 4:361-4. https://doi.org/10.1130/0091-7613(1976)4%3C361:SATFIP%3E2.0.CO;2

Hunt S, Oates K (1984) Chitin helicoids accompany protein helicoids in the periostracum of a whelk, *Buccinum*. Tissue Cell 16:565–575. http://doi.org/10.1016/0040-8166(84)90031-4

Hüssy K, Limburg KE, De Pontual H, Thomas OR, Cook PK, Heimbrand Y, Blass M, Sturrock AM (2021) Trace element patterns in otoliths: the role of biomineralization. Rev Fish Sci Aquac 29:445-77. https://doi.org/10.1080/23308249.2020.1760204

Jablonski D, Lidgard S, Taylor PD (1997) Comparative ecology of bryozoan radiations: origin of novelties in cyclostomes and cheilostomes. Palaios 505-523. https://doi.org/10.2307/3515408

Jacob DE, Ruthensteiner B, Trimby P, Henry H, Martha SO, Leitner J, Otter LM, Scholz J (2019) Architecture of *Anoteropora latirostris* (Bryozoa, Cheilostomata) and implications for their biomineralization. Sci Rep 9:11439. https://doi.org/10.1038/s41598-019-47848-4

Jewett EB, Hines AH, Ruiz GM (2005) Epifaunal disturbance by periodic low levels of dissolved oxygen: native vs. invasive species response. Mar Ecol Prog Ser 304:31–44. http://doi.org/10.3354/meps304031

Kamenev GM (2018) Four new species of the family Propeamussiidae (Mollusca: Bivalvia) from the abyssal zone of the northwestern Pacific, with notes on *Catillopecten squamiformis* (Bernard, 1978). Mar Biodivers 48:647-676. https://doi.org/10.1007/s12526-017-0821-1

Kim Y, Caumon M-C, Barres O, Sall A, Cauzid J (2021) Identification and composition of carbonate minerals of the calcite structure by Raman and infrared spectroscopies using portable devices. Spectrochim Acta A 261:119980. http://doi.org/10.1016/j.saa.2021.119980

Kovacs CS, Chaussain C, Osdoby P, Brandi ML, Clarke B, Thakker RV (2021) The role of biomineralization in disorders of skeletal development and tooth formation. Nat Rev Endocrinol 17:336-49. https://doi.org/10.1038/s41574-021-00488-z

Kuklinski P, Taylor PD (2009) Mineralogy of Arctic bryozoan skeletons in a global context. Facies 55:489-500. https://doi.org/10.1007/s10347-009-0179-3

Kupriyanova E, Hutchings P, Wong E (2016) A fully illustrated web-based guide to distinguish native and introduced polychaetes of Australia. Manag Biol Invasions 7:305–312. http://doi.org/10.3391/mbi.2016.7.3.10

Kupriyanova EK, Vinn O, Taylor PD, Schopf JW, Kudryavtsev AB, Bailey-Brock J (2014) Serpulids living deep: calcareous tubeworms beyond the abyss. Deep Sea Res I: Oceanogr Res Pap 90:91–104. http://doi.org/10.1016/j.dsr.2014.04.006

Lacoste E, Gaertner-Mazouni N (2015) Biofouling impact on production and ecosystem functioning: a review for bivalve aquaculture. Rev Aquacult 7:187–196. http://doi.org/10.1111/raq.12063

Levi-Kalisman Y, Falini G, Addadi L, Weiner S (2001) Structure of the nacreous organic matrix of a bivalve mollusk shell examined in the hydrated state using cryo-TEM. J Struct Biol 135:8–17. http://doi.org/10.1006/jsbi.2001.4372

Levy-Lior A, Pokroy B, Levavi-Sivan B, Leiserowitz L, Weiner S, Addadi L (2008) Biogenic guanine crystals from the skin of fish may be designed to enhance light reflectance. Cryst Growth Des 8:507-11. https://doi.org/10.1021/cg0704753

Lombardi C, Kuklinski P, Spirandelli E, Bruzzone G, Raiteri G, Bordone A, Mazzoli C, López Correa M, van Geldern R, Plasseraud L (2023) Antarctic bioconstructional bryozoans from Terra Nova Bay (Ross Sea): Morphology, skeletal structures and biomineralization. Minerals 13:246. https://doi.org/10.3390/min13020246

Lowenstam HA (1954) Factors affecting the aragonite: calcite ratios in carbonate-secreting marine organisms. J Geol 62:284–322. http://doi.org/10.1086/626163

Lowenstam HA (1981) Minerals formed by organisms. Science 211:1126-1131. https://www.jstor.org/stable/1685216

Lowenstam HA, Weiner S (1989) On biomineralization. Oxford University Press, New York, USA

Macías-Sánchez E, Willinger MG, Pina CM, Checa, AG (2017) Transformation of ACC into Aragonite and the Origin of the Nanogranular Structure of Nacre. Sci Rep 7:1-11. https://doi.org/10.1038/s41598-017-12673-0

Maloof AC, Porter SM, Moore JL, Dudás FÖ, Bowring SA, Higgins JA, Fike DA, Eddy MP (2010) The earliest Cambrian record of animals and ocean geochemical change. Geol Soc Am Bull 122:1731-1774. https://doi.org/10.1130/B30346.1

Mann S (1983) Mineralization in biological systems. In: Inorganic elements in biochemistry. Springer Berlin, Heidelberg, pp 125-174. https://doi.org/10.1007/BFb0111320

Mann S. (2001) Biomineralization: principles and concepts in bioinorganic materials chemistry. Oxford University Press. https://doi.org/10.1093/oso/9780198508823.001.0001

Massaro FR, Pastero L, Rubbo M, Aquilano D (2008) Theoretical surface morphology of {011-2} acute rhombohedron of calcite: A comparison with experiments and {101-4} cleavage rhombohedron. J Cryst Growth 310:706-715. https://doi.org/10.1016/j.jcrysgro.2007.11.086

McKinney FK (1992) Competitive interactions between related clades: evolutionary implications of overgrowth interactions between encrusting cyclostome and cheilostome bryozoans. Mar Biol 114:645-652. https://doi.org/10.1007/BF00357261

Merz RA (2015) Textures and traction: how tube-dwelling polychaetes get a leg up. Invertebr Biol 134:61–77. http://doi.org/10.1111/ivb.12079

Montefalcone M, Oprandi A, Azzola A, Morri C, Bianchi CN (2022) Serpulid reefs and their role in aquatic ecosystems: A global review. Adv Mar Biol 92:1–54. https://doi.org/10.1016/bs.amb.2022.06.001

Morse JW, Mackenzie FT (1990) Geochemistry of Sedimentary Carbonates. Elsevier, Amsterdam.

Morse JW, Wang Q, Tsio MY (1997) Influences of temperature and Mg:Ca ratio on CaCO3 precipitates from seawater. Geology 25:85–87. http://doi.org/10.1130/0091-7613(1997)025<0085:IOTAMC>2.3.CO;2

Neff JM (1969) Mineral regeneration by serpulid polychaete worms. Biol Bull 136:76-90. https://doi.org/10.2307/1539670

Negrini M, Batson PB, Smith AM, Smith SAF, Prior DJ, Henry H, Li KC, Tamberg Y (2022) Understanding the crystallographic and nanomechanical properties of bryozoans. J Struct Biol 214:107882. https://doi.org/10.1016/j.jsb.2022.107882

Nelson KS, Liddy M, Lamare MD (2017) Embryology, larval development, settlement and metamorphosis in the New Zealand serpulid polychaete *Galeolaria hystrix*. Invertebr Reprod Dev 61:207–217. http://doi.org/10.1080/07924259.2017.1318183

Neville AC (1993) Biology of fibrous composites: development beyond the cell membrane. Cambridge University Press, Cambridge, UK

Nielsen C, Pedersen KJ (1979) Cystid structure and protrusion of the polypide in *Crisia* (Bryozoa, Cyclostomata). Acta Zool 60:65–88. https://doi.org/10.1111/j.1463-6395.1979.tb00599.x

Nielsen MR, Sand KK, Rodriguez-Blanco JD, Bovet N, Generosi J, Dalby KN, Stipp SLS (2016) Inhibition of calcite growth: Combined effects of Mg^{2+} and SO_4^{2-}. Cryst Growth Des 16:6199-6207. https://doi.org/10.1021/acs.cgd.6b00536

O'Dea A, Håkansson E, Taylor PD, Okamura B (2011) Environmental change prior to the K–T boundary inferred from temporal variation in the morphology of cheilostome bryozoans. Palaeogeogr Palaeoclimatol Palaeoecol 308:502-512. https://doi.org/10.1016/j.palaeo.2011.06.001

Orr RJS, Di Martino E, Ramsfjell MH, Gordon DP, Berning B, Chowdhury I, Craig S, Cumming RL, Figuerola B, Florence W, Harmelin J-G, Hirose M, Huang D, Jain SS, Jenkins HL, Kotenko ON, Kuklinski P, Lee HE, Madurell T, McCann L, Mello HL, Obst M, Ostrovsky AN, Paulay G, Porter JS, Shunatova NN, Smith AM, Souto-Derungs J, Vieira LM, Voje KL, Waeschenbach A, Zágoršek K, Warnock RCM, Liow LH (2022) Paleozoic origins of cheilostome bryozoans and their parental care inferred by a new genome-skimmed phylogeny. Sci Adv 8:eabm7452. https://doi.org/10.1126/sciadv.abm7452

Palmer AR (1983) Relative cost of producing skeletal organic matrix versus calcification: Evidence from marine gastropods. Mar Biol 75:287-292. https://doi.org/10.1007/BF00406014

Palmer AR (1992) Calcification in marine molluscs: how costly is it? PNAS 89:1379-1382. https://doi.org/10.1073/pnas.89.4.1379

Peharda M, Schöne BR, Black BA, Correge T (2021) Advances of sclerochronology research in the last decade. Palaeogeogr Palaeoclimatol Palaeoecol 570:110371. https://doi.org/10.1016/j.palaeo.2021.110371

Porter SM (2007) Seawater chemistry and early carbonate biomineralization. Science 316:1302-1302. https://doi.org/10.1126/science.1137284

Rashidi NA, Mohamed M, Yusup S (2012) The kinetic model of calcination and carbonation of *Anadara granosa*. Int J Renew Energy Res 2:497–503

Rodríguez-Navarro AB, Cabral de Melo C, Batista N, Morimoto N, Álvarez-Lloret P, Ortega-Huertas M, Fuenzalida VM, Arias JI, Wiff JP, Arias JL

(2006) Microstructure and crystallographic texture of giant barnacle (*Austromegabalanus psittacus*) shell. J Struct Biol 156:355–362. http://doi.org/10.1016/j.jsb.2006.04.009

Rodríguez-Navarro AB, García-Ruiz JM (2000) Model of textural development of layered crystal aggregates. Eur J Mineral 12:609–614. http://doi.org/https://doi.org/10.1127/0935-1221/2000/0012-0609

Rodríguez-Navarro AB, Marie P, Nys Y, Hincke MT, Gautron J (2015) Amorphous calcium carbonate controls avian eggshell mineralization: a new paradigm for understanding rapid eggshell calcification. J Struct Biol 190:291-303. https://doi.org/10.1016/j.jsb.2015.04.014

Rossbach FI, Casoli E, Beck M, Wild C (2021) Mediterranean red macro algae mats as habitat for high abundances of serpulid polychaetes. Diversity 13:265. http://doi.org/10.3390/d13060265

Ryland JS (1977) Physiology and ecology of marine bryozoans. Adv Mar Biol. 14:285-443. https://doi.org/10.1016/S0065-2881(08)60449-6

Sandberg PA (1971) Scanning electron microscopy of cheilostome bryozoan skeletons; techniques and preliminary observations. Micropaleontology 17:129-151. https://doi.org/10.2307/1484946

Sandberg PA (1977) Ultrastructure, mineralogy, and development of bryozoan skeletons. In: Woollacott RM, Zimmer RL (eds) Biology of bryozoans. Academia Press, New York, pp 43-181

Sandberg PA (1983) An oscillating trend in Phanerozoic non-skeletal carbonate mineralogy. Nature 305:19-22. https://doi.org/10.1038/305019a0

Schack CR, Gordon DP, Ryan KG (2019) Modularity is the mother of invention: a review of polymorphism in bryozoans. Biol Rev 94:773-809. https://doi.org/10.1111/brv.12478

Schoeppler V, Gránásy L, Reich E, Poulsen N, De Kloe R, Cook P, Rack A, Pusztai T, Zlotnikov I (2018) Biomineralization as a paradigm of directional solidification: a physical model for molluscan shell ultrastructural morphogenesis. Adv Mater 30:1803855. https://doi.org/10.1002/adma.201803855

Schoeppler V, Lemanis R, Reich E, Pusztai T, Gránásy L, Zlotnikov I (2019) Crystal growth kinetics as an architectural constraint on the evolution of molluscan shells. PNAS 116:20388-20397. https://doi.org/10.1073/pnas.1907229116

Schöne BR, Gillikin DP (2013) Unraveling environmental histories from skeletal diaries—advances in sclerochronology. Palaeogeography, Palaeoclimatology, Palaeoecology 373:1-5. https://doi.org/10.1016/j.palaeo.2012.11.026

Sethmann I, Hinrichs R, Wörheide G, Putnis A (2006) Nano-cluster composite structure of calcitic sponge spicules—A case study of basic characteristics of biominerals. J Inorg Biochem 100:88-96. https://doi.org/10.1016/j.jinorgbio.2005.10.005

Simonet Roda M, Griesshaber E, Angiolini L, Rollion-Bard C, Harper EM, Bitner MA, Milner Garcia S, Ye F, Henkel D, Häussermann V, Eisenhauer A, Gnägi H, Brand U, Logan A, Schmahl WW (2022) The architecture of Recent brachiopod shells: diversity of biocrystal and biopolymer assemblages in rhynchonellide, terebratulide, thecideide and craniide shells. Mar Biol 169:4. http://doi.org/10.1007/s00227-021-03962-4

Simonet Roda M, Griesshaber E, Ziegler A, Rupp U, Yin X, Henkel D, Häussermann V, Laudien J, Brand U, Eisenhauer A (2019) Calcite fibre formation in modern brachiopod shells. Sci Rep 9:598. https://doi.org/10.1038/s41598-018-36959-z

Simonet Roda M, Ziegler A, Griesshaber E, Yin X, Rupp U, Greiner M., Henkel D, Häussermann V, Eisenhauer A, Laudien J, Schmahl WW (2019) Terebratulide brachiopod shell biomineralization by mantle epithelial cells. J Struct Biol 207:136-157. https://doi.org/10.1016/j.jsb.2019.05.002

Smith AM, Girvan E (2010) Understanding a bimineralic bryozoan: Skeletal structure and carbonate mineralogy of *Odontionella cyclops* (Foveolariidae: Cheilostomata: Bryozoa) in New Zealand. Palaeogeogr Palaeoclimatol Palaeoecol 289:113-122. https://doi.org/10.1016/j.palaeo.2010.02.022

Smith AM, Key Jr MM, Gordon DP (2006) Skeletal mineralogy of bryozoans: taxonomic and temporal patterns. Earth Sci Rev 78:287-306. https://doi.org/10.1016/j.earscirev.2006.06.001

Smith AM, Riedi MA, Winter DJ (2013) Temperate reefs in a changing ocean: skeletal carbonate mineralogy of serpulids. Mar Biol 160:2281–2294. http://doi.org/10.1007/s00227-013-2210-z

Söderqvist T (1968) Observations on extracellular body wall structure in *Crisia eburnea*. Atti Soc Ital Sci Nat Mus Civico Storia Nat Milano 108:115-118.

Stevens K, Griesshaber E, Schmahl W, Casella LA, Iba Y, Mutterlose J (2017) Belemnite biomineralization, development, and geochemistry: The complex rostrum of *Neohibolites minimus*. Palaeogeogr Palaeoclimatol Palaeoecol 468:388–402. http://doi.org/https://doi.org/10.1016/j.palaeo.2016.12.022

Tanur AE, Gunari N, Sullan RMA, Kavanagh CJ, Walker GC (2010) Insights into the composition, morphology, and formation of the calcareous shell of the serpulid *Hydroides dianthus*. J Struct Biol 169:145–160. http://doi.org/10.1016/j.jsb.2009.09.008

Tavener-Smith R, Williams A (1972) The secretion and structure of the skeleton of living and fossil Bryozoa. *Philos Trans R Soc* 264:97-160. https://doi.org/10.1098/rstb.1972.0010

Taylor PD (1994) An early cheilostome bryozoan from the Upper Jurassic of Yemen. N Jb Geol Palaeontol Abh 191:331-344.

Taylor PD (2020) Bryozoan paleobiology. Wiley Blackwell, Oxford, 320 pp.

Taylor PD, Allison PA (1998) Bryozoan carbonates throgugh time and space. Geology 26:459-462. https://doi.org/10.1130/0091-7613(1998)026<0459:BCTTAS>2.3.CO;2

Taylor PD, James NP, Bone Y, Kuklinski P, Kyser TK (2009) Evolving mineralogy of cheilostome bryozoans. Palaios 24:440-452. https://doi.org/10.2110/palo.2008.p08-124r

Taylor PD, Jones CG (1993) Skeletal ultrastructure in the cyclostome bryozoan Hornera. Acta Zool 74:135-143. https://doi.org/10.1111/j.1463-6395.1993.tb01230.x

Taylor PD, Kudryavtsev AB, Schopf JW (2008) Calcite and aragonite distributions in the skeletons of bimineralic bryozoans as revealed by Raman spectroscopy. Invertebr Biol 127:87-97. https://doi.org/10.1111/j.1744-7410.2007.00106.x

Taylor PD, Lombardi C, Cocito S (2015) Biomineralization in bryozoans: present, past and future. Biol Rev 90:1118-1150. https://doi.org/10.1111/brv.12148

Taylor PD, Waeschenbach A (2015) Phylogeny and diversification of bryozoans. Palaeontology 58:585-599. https://doi.org/10.1111/pala.12170

Taylor PD, Weedon MJ (2000) Skeletal ultrastructure and phylogeny of cyclostome bryozoans. Zool J Linn Soc 128:337-399. https://doi.org/10.1111/j.1096-3642.2000.tb01521.x

Ten Hove HA, Kupriyanova EK (2009) Taxonomy of Serpulidae (Annelida, Polychaeta): the state of affairs. Zootaxa 2036:1–126. http://doi.org/10.11646/zootaxa.2036.1.1

Ten Hove HA, Van den Hurk P (1993) A review of Recent and fossil serpulid reefs; actuopalaeontology and Upper Malm serpulid limestones in NW Germany. Geol Mijnbouw 72:23-67

Tilic E, Rouse GW, Bartolomaeus T (2021) Comparative ultrastructure of the radiolar crown in Sabellida (Annelida). Zoomorphology 140:27–45. http://doi.org/10.1007/s00435-020-00509-x

Tsurkan MV, Voronkina A, Khrunyk Y, Wysokowski M, Petrenko I, Ehrlich H (2021) Progress in chitin analytics. Carbohydr polym 252:117204. https://doi.org/10.1016/j.carbpol.2020.117204

Ubukata T (1994) Architectural constraints on the morphogenesis of prismatic structure in Bivalvia. Palaeontology 37:241-261

Urey HC, Lowenstam HA, Epstein S, McKinney CR (1951) Measurement of paleotemperatures and temperatures of the Upper Cretaceous of England, Denmark, and the southeastern United States. Geol Soc Am Bull 62:399-416. https://doi.org/10.1130/0016-7606(1951)62[399:MOPATO]2.0.CO;2

Veizer J, Ala D, Azmy K, Bruckschen P, Buhl D, Bruhn F, Carden GA, Diener A, Ebneth S, Godderis Y, Jasper T (1999) 87Sr/86Sr, δ13C and δ18O evolution of Phanerozoic seawater. Chem Geol 161:59-88. https://doi.org/10.1016/S0009-2541(99)00081-9

Veizer J, Godderis Y, François LM (2000) Evidence for decoupling of atmospheric CO2 and global climate during the Phanerozoic eon. Nature 408:698-701. https://doi.org/10.1038/35047044

Vinn O (2009) The ultrastructure of calcareous cirratulid (Polychaeta, Annelida) tubes. Estonian J Earth Sci 58:153. http://doi.org/10.3176/earth.2009.2.06

Vinn O (2011) The role of an internal organic tube lining in the biomineralization of serpulid tubes. Carnets Géol 2011:01. http://doi.org/10.4267/2042/38798

Vinn O (2021) Biomineralization in polychaete annelids: A review. Minerals 11:1151. http://doi.org/10.3390/min11101151

Vinn O, Mutvei H, Ten Hove HA, Kirsimäe E K (2008c) Unique Mg-calcite skeletal ultrastructure in the tube of the serpulid polychaete *Ditrupa*. N Jb Geol Paläont Abh 248:79–89. http://doi.org/10.1127/0077-7749/2008/0248-0079

Vinn O, Ten Hove HA, Mutvei H (2008a) On the tube ultrastructure and origin of calcification in sabellids (Annelida, Polychaeta). Palaeontology 51:295–301. http://doi.org/10.1111/j.1475-4983.2008.00763.x

Vinn O, Ten Hove HA, Mutvei H, Kirsimäe K (2008b) Ultrastructure and mineral composition of serpulid tubes (Polychaeta, Annelida). Zool J Linn Soc 154:633–650. http://doi.org/10.1111/j.1096-3642.2008.00421.x

von Buch L. Über den Jura in Deutschland. Dümmler; 1839.

Wasylenki LE, Dove PM, De Yoreo JJ (2005) Effects of temperature and transport conditions on calcite growth in the presence of Mg2+: Implications for paleothermometry. Geochimica et Cosmochimica Acta 69:4227-4236. http://doi.org/10.1016/j.gca.2005.04.006

Weedon MJ (1994) Tube microstructure of Recent and Jurassic serpulid polychaetes and the question of the Palaeozoic 'spirorbids'. Acta Palaeontol Pol 39:1–15.

Weedon MJ, Taylor PD (2000) Skeletal ultrastructure of primitive cheilostome bryozoans. In: Proceedings of the 11th International Bryozoology Association conference. Smithsonian Tropical Research Institute, Balboa, Panama, pp 400-411.

Weiner S, Dove PM (2003) An overview of biomineralization processes and the problem of the vital effect. Rev Mineral Geochem 54:1-29. https://doi.org/10.2113/0540001

Weiner S, Mahamid J, Politi Y, Ma Y, Addadi L (2009) Overview of the amorphous precursor phase strategy in biomineralization. Front Mater Sci China 3:104-108. https://doi.org/10.1007/s11706-009-0036-x

Williams A (1970) Spiral growth of the laminar shell of the brachiopod Crania. Calcif Tissue Res 6:11-19. https://doi.org/10.1007/BF02196180

Williams A, Wright AD (1970) Shell structure of the Craniacea and other calcareous inarticulate Brachiopoda. Spec Papers Palaeontol 7:1-51.

WoRMS Editorial Board (2024). World Register of Marine Species. Available from https://www.marinespecies.org at VLIZ. http://doi.org/doi:10.14284/170

Xie Z, Wong N, Qian P, Qiu J (2005) Responses of polychaete *Hydroides elegans* life stages to copper stress. Mar Ecol Prog Ser 285:89–96. http://doi.org/10.3354/meps285089

Yin X, Griesshaber E, Checa A, Nindiyasari-Behal F, Sánchez-Almazo I, Ziegler A, Schmahl WW (2021) Calcite crystal orientation patterns in the bilayers of laminated shells of benthic rotaliid foraminifera. J Struct Biol 213:107707. https://doi.org/10.1016/j.jsb.2021.107707

Zhang G, Hirsch A, Shmul G, Avram L, Elad N, Brumfeld V, Pinkas I, Feldman Y, Ben Asher R, Palmer BA, Kronik L (2019) Guanine and 7, 8-dihydroxanthopterin reflecting crystals in the Zander fish eye: crystal locations, compositions, and structures. J Am Chem Soc 141:19736-45. https://doi.org/10.1021/jacs.9b08849

Zhang Z, Zhang Z, Ma J, Taylor PD, Strotz LC, Jacquet SM, Skovsted CB, Chen F, Han J, Brock GA (2021) Fossil evidence unveils an early Cambrian origin

for Bryozoa. Nature 7884:251-255. https://doi.org/10.1038/s41586-021-04033-w

Appendix: publications

Grenier C, Griesshaber E, Schmahl WW, Checa AG (2023) Microstructure and crystallographic characteristics of stenolaemate bryozoans (Phylum Bryozoa and Class Stenolaemata). Cryst Growth Des 23:965–979. https://doi.org/10.1021/acs.cgd.2c01149

Impact factor: 3.8; 5/26 (Q1) in the category Crystallography (JCR 2022).

CRYSTAL GROWTH & DESIGN

pubs.acs.org/crystal Article

Microstructure and Crystallographic Characteristics of Stenolaemate Bryozoans (Phylum Bryozoa and Class Stenolaemata)

Christian Grenier, Erika Griesshaber, Wolfgang W. Schmahl, and Antonio G. Checa*

Cite This: https://doi.org/10.1021/acs.cgd.2c01149 Read Online

ACCESS | Metrics & More | Article Recommendations | Supporting Information

ABSTRACT: The bryozoan Cass Stenolaemata is currently represented by the Order Cyclostomata. They produce skeletons made exclusively of calcite crystals assembled into different microstructures. Despite extensive previous research, no appropriate crystallographic techniques have been applied to decipher their crystallographic organization. We present an in-depth crystallographic study of the microstructures of three extant species (*Fasciculipora ramosa*, *Hornera robusta*, and *Cinctipora elegans*) using scanning electron microscopy and associated techniques (energy-dispersive spectroscopy and electron backscatter diffraction), together with atomic force microscopy and micro-computed tomography. We differentiate two microstructures, foliated and tabular calcite, and establish consistent models of their crystallography. Foliated calcite of *F. ramosa* and *C. elegans* consists of co-oriented laths arranged with their *c*-axes parallel to their elongation axis and to their main surfaces, and one *a**-axis perpendicular to the latter (sheet texture). Tabular calcite of *H. robusta* consists of polygonal tablets with the *c*-axis as fiber axis (axial texture), perpendicular to the tablet surface. The foliated calcite of bryozoans is homeomorph to that of bivalves but has a significantly different crystallography. The tabular calcite of bryozoans lacks the spiral morphology of the tablet-shaped calcite of craniiformis brachiopods and has a different orientation of the *c*-axis with respect to the constituent tablets.

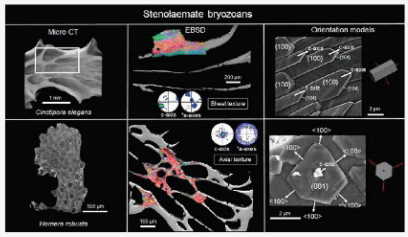

1. INTRODUCTION

The Phylum Bryozoa is the only one among invertebrates composed exclusively of aquatic colonial animals. They are found worldwide in both continental and marine waters, although the vast majority are found in the latter environment. Almost all marine bryozoans secrete calcium carbonate skeletons to build their colonies.[1] Together with their importance in the fossil record, they also register the effects of climate change in the marine environment and constitute a significant CO_2 fixation reservoir, along with many other marine calcifying proto- and metazoans (e.g., corals, mollusks, and foraminifera).[2] Currently, the estimated number of living bryozoan species is 6451 (WoRMS, accessed Oct 10, 2022),[3] distributed within three Classes. The Class Stenolaemata, which is the subject of this present study, contains 652 extant species, all of which inhabit marine environments and produce mineralized skeletons. They are currently represented by a single Order, Cyclostomata. Stenolaematans were the first bryozoans to appear, as early as in the Early Cambrian (Cambrian Age 3) and participated in the Cambrian radiation.[4] They spread their diversity during the Great Ordovician Biodiversity Event[5] and remained as the dominant group of bryozoans until the Upper-Jurassic radiation of the gymnolaematans.[6]

Bryozoans form colonies composed of clone individuals, called zooids. Depending on the species, each colony can be formed by a few to many thousands of zooids. Nevertheless, despite their identical genetic pool, zooids can have diverse morphologies (polymorphism) due to either a different developmental stage (ontogeny and astogeny) or because of functional differentiation depending on their role within the colony: feeding lophophorate zooids (autozooids), brooding zooids (gonozooids), defensive zooids (avicularia), and structural zooids (kenozooids).[1] This phenotypic plasticity has played a fundamental role in the evolutionary and adaptive success of this phylum throughout its history.[7]

Bryozoans build their skeletons of calcium carbonate. They first form a thin organic periostracum, mainly composed of chitin and mucopolysaccharides, secreted by a stratum of palisade cells.[8] Then, the periostracum becomes the seeding sheet for the calcium carbonate layers, which are secreted by

Received: October 11, 2022
Revised: December 29, 2022

Grenier C, Griesshaber E, Schmahl WW, Berning B, Checa AG (2024) Skeletal microstructures of cheilostome bryozoans (phylum Bryozoa, class Gymnolaemata): crystallography and secretion patterns. Mar Life Sci Technol. https://doi.org/10.1007/s42995-024-00233-1

Impact factor: 5.7; 5/109 (Q1) in the category Marine and Freshwater Biology (JCR 2022).

Marine Life Science & Technology
https://doi.org/10.1007/s42995-024-00233-1

RESEARCH PAPER

Skeletal microstructures of cheilostome bryozoans (phylum Bryozoa, class Gymnolaemata): crystallography and secretion patterns

Christian Grenier[1] · Erika Griesshaber[3] · Wolfgang Schmahl[3] · Björn Berning[4] · Antonio G. Checa[1,2]

Received: 30 November 2023 / Accepted: 30 April 2024

Abstract
Gymnolaemata bryozoans produce $CaCO_3$ skeletons of either calcite, aragonite, or both. Despite extensive research, their crystallography and biomineralization patterns remain unclear. We present a detailed study of the microstructures, mineralogy, and crystallography of eight extant cheilostome species using scanning electron microscopy, electron backscatter diffraction, atomic force microscopy, and micro-computed tomography. We distinguished five basic microstructures, three calcitic (tabular, irregularly platy, and granular), and two aragonitic (granular-platy and fibrous). The calcitic microstructures consist of crystal aggregates that transition from tabular or irregularly platy to granular assemblies. Fibrous aragonite consists of fibers arranged into spherulites. In all cases, the crystallographic textures are axial, and stronger in aragonite than in calcite, with the c-axis as the fiber axis. We reconstruct the biomineralization sequence in the different species by considering the distribution and morphology of the growth fronts of crystals and the location of the secretory epithelium. In bimineralic species, calcite formation always predates aragonite formation. In interior compound walls, growth proceeds from the cuticle toward the zooecium interior. We conclude that, with the exception of tabular calcite, biomineralization is remote and occurs within a relatively wide extrapallial space, which is consistent with the inorganic-like appearance of the microstructures. This biomineralization mode is rare among invertebrates.

Keywords Biomineralization · Bryozoan · Skeleton · Calcite · Aragonite · Electron backscatter diffraction

Introduction

Bryozoans comprise an entire phylum of aquatic, colonial animals that occur worldwide in fresh and marine waters, from shallow to deep waters (Ryland 1977; Taylor 2020). The colonies are made of clonal units, called zooids, which differentiate during their development (ontogeny) into various types (polymorphs) according to their function in the colony: feeding autozooids, structural kenozooids, defensive avicularia, and brooding chambers called gonozooids (see Ryland 1977; Taylor 2020) for a biological introduction to the phylum). The total number of living bryozoan species is estimated at ~ 6500, distributed among the classes Gymnolaemata (> 85% of the extant bryozoan species), Phylactolaemata (< 100 species), and Stenolaemata (654 species) (WoRMS Editorial Board 2024).

More than 98% of bryozoans live in seawater and secrete calcium carbonate skeletons, which makes them an important fossil group (Hageman et al. 2003; O'Dea et al. 2011; Taylor and Allison 1998). The non-marine bryozoans (Phylactolaemata) are unmineralized. The order Cheilostomatida, which appeared in the Late Jurassic (Taylor 1994) and diversified from the mid-Cretaceous on (Jablonski et al. 1997), became the current, dominant group of bryozoans (Taylor 2020).

Cheilostomatida is the major order of gymnolaemates, comprising more than 94% of the species. They all live in marine environments (except a few species that occur in brackish waters) and produce mineralized skeletons that are

Edited by Jiamei Li.

✉ Antonio G. Checa
acheca@ugr.es

[1] Departamento de Estratigrafía y Paleontología, Universidad de Granada, 18071 Granada, Spain

[2] Instituto Andaluz de Ciencias de La Tierra, CSIC-Universidad de Granada, 18100 Armilla, Spain

[3] Department of Earth and Environmental Sciences, Ludwig-Maximilians Universität, 80333 Munich, Germany

[4] Institute for Geology, University of Hamburg, 20146 Hamburg, Germany

Published online: 07 June 2024

Grenier C, Berent K, Rodríguez-Navarro AB, Vinn O, Checa AG (under review) Microstructures, crystallography and growth patterns of serpulid tubeworms (Class Polychaeta). Mar Biol.

Impact factor: 2.4; 29/109 (Q2) in the category Marine and Freshwater Biology (JCR 2022).

Marine Biology

Microstructures, crystallography and growth patterns of serpulid tubeworms (Class Polychaeta)

--Manuscript Draft--

Manuscript Number:	
Full Title:	Microstructures, crystallography and growth patterns of serpulid tubeworms (Class Polychaeta)
Article Type:	Original paper
Keywords:	serpulids; microstructures; biomineralization; crystallography; episodic growth; recrystallization
Corresponding Author:	Antonio G Checa, PhD Universidad de Granada Granada, SPAIN
Corresponding Author Secondary Information:	
Corresponding Author's Institution:	Universidad de Granada
Corresponding Author's Secondary Institution:	
First Author:	Christian Grenier
First Author Secondary Information:	
Order of Authors:	Christian Grenier
	Katarzyna Berent
	Alejandro B. Rodríguez-Navarro
	Olev Vinn
	Antonio G Checa, PhD

UNIVERSIDAD
DE GRANADA